REPORT DOCUMENTATION PAGE

Form Approved
OMB No. 0704-0188

Public reporting burden for this collection of information is estimated to average 1 hour per response, including the time for reviewing instructions, searching existing data sources, gathering and maintaining the data needed, and completing and reviewing this collection of information. Send comments regarding this burden estimate or any other aspect of this collection of information, including suggestions for reducing this burden to Department of Defense, Washington Headquarters Services, Directorate for Information Operations and Reports (0704-0188), 1215 Jefferson Davis Highway, Suite 1204, Arlington, VA 22202-4302. Respondents should be aware that notwithstanding any other provision of law, no person shall be subject to any penalty for failing to comply with a collection of information if it does not display a currently valid OMB control number. **PLEASE DO NOT RETURN YOUR FORM TO THE ABOVE ADDRESS.**

1. REPORT DATE *(DD-MM-YYYY)*
February 2012

2. REPORT TYPE
Thesis Dissertation

3. DATES COVERED *(From - To)*
February 2012 – April 2012

4. TITLE AND SUBTITLE
Droplet Combustion and Non-Reactive Shear-Coaxial Jets with and without Transverse Acoustic Excitation

5a. CONTRACT NUMBER
In-House

5b. GRANT NUMBER

5c. PROGRAM ELEMENT NUMBER

6. AUTHOR(S)
Sophonias Teshome

5d. PROJECT NUMBER

5e. TASK NUMBER

5f. WORK UNIT NUMBER
23080533

7. PERFORMING ORGANIZATION NAME(S) AND ADDRESS(ES)

Air Force Research Laboratory (AFMC)
AFRL/RQRC
10 E. Saturn Blvd.
Edwards AFB CA 93524-7680

8. PERFORMING ORGANIZATION REPORT NO.

9. SPONSORING / MONITORING AGENCY NAME(S) AND ADDRESS(ES)
Air Force Research Laboratory (AFMC)
AFRL/RQR
5 Pollux Drive
Edwards AFB CA 93524-7048

10. SPONSOR/MONITOR'S ACRONYM(S)

11. SPONSOR/MONITOR'S REPORT NUMBER(S)
AFRL-RZ-ED-TP-2012-118

12. DISTRIBUTION / AVAILABILITY STATEMENT
Distribution A: Approved for Public Release; Distribution Unlimited. PA#12298

13. SUPPLEMENTARY NOTES

14. ABSTRACT

This experimental study focused on the coupling of transverse acoustic flow perturbations with two different fundamental phenomena that take place in combustion chambers: reactive, condensed-phase droplet combustion, and non-reactive shear-coaxial injection flows. The study on fuel droplet combustion characteristics examined the response and behavior of various burning fuel droplets during exposure to external acoustical perturbations. These liquid fuels included ethanol, methanol, aviation fuel (JP-8), liquid synthetic fuel derived from natural gas, and a blend of JP-8 and synfuel. The study examined combustion during excitation conditions in a closed waveguide in which the droplet was situated at or near a pressure node, where the droplet experienced the greatest effects of velocity perturbations, and at or near a velocity node (pressure antinode), where the droplet was exposed to minimal velocity fluctuations but maximum pressure fluctuations. A two-speaker configuration provided the means to produce a fairly symmetric acoustic field in the waveguide. In the absence of acoustic excitation, values of the measured droplet burning rate constant *K* were generally consistent with available values for the different fuels explored. During acoustic excitation of droplets situated in the vicinity of a pressure node or antinode, flame orientation was consistent with the sign of an acoustic radiation force acting on the burning system, creating conditions where the flame deflection switched, depending on the relative location of the droplet.

The acceleration associated with the acoustic radiation force was estimated by measuring the degree of deflection that the flame underwent relative to an unforced flame. Although overall there were no significant variations in the measured *K* values with changing acoustic excitation, in some cases, locally increased *K* values were observed to be associated with larger measured acoustic accelerations. This study also examined the extinction characteristics and made preliminary estimations of the extinction strain rates of the different fuels.

15. SUBJECT TERMS

16. SECURITY CLASSIFICATION OF:

a. REPORT	**b. ABSTRACT**	**c. THIS PAGE**	**17. LIMITATION OF ABSTRACT**	**18. NUMBER OF PAGES**	**19a. NAME OF RESPONSIBLE PERSON** Doug Talley
Unclassified	**Unclassified**	**Unclassified**	SAR	275	**19b. TELEPHONE NO** *(include area code)* 661-525-6174

Standard Form 298 (Rev. 8-98)
Prescribed by ANSI Std. 239.18

University of California
Los Angeles

Droplet Combustion and Non-Reactive Shear-Coaxial Jets with and without Transverse Acoustic Excitation

A dissertation submitted in partial satisfaction
of the requirements for the degree
Doctor of Philosophy in Mechanical Engineering

by

Sophonias Teshome

2012

Distribution A, approved for public release; distribution unlimited.

© Copyright by
Sophonias Teshome
2012

Abstract of the Dissertation

Droplet Combustion and Non-Reactive Shear-Coaxial Jets with and without Transverse Acoustic Excitation

by

Sophonias Teshome

Doctor of Philosophy in Mechanical Engineering

University of California, Los Angeles, 2012

Professor Ann R. Karagozian, Co-chair

Professor Owen I. Smith, Co-chair

This experimental study focused on the coupling of transverse acoustic flow perturbations with two different fundamental phenomena that take place in combustion chambers: reactive, condensed-phase droplet combustion, and non-reactive shear-coaxial injection flows.

The study on fuel droplet combustion characteristics examined the response and behavior of various burning fuel droplets during exposure to external acoustical perturbations. These liquid fuels included ethanol, methanol, aviation fuel (JP-8), liquid synthetic fuel derived from natural gas, and a blend of JP-8 and synfuel. The study examined combustion during excitation conditions in a closed waveguide in which the droplet was situated at or near a pressure node, where the droplet experienced the greatest effects of velocity perturbations, and at or near a velocity node (pressure antinode), where the droplet was exposed to minimal velocity fluctuations but maximum pressure fluctuations. A two-speaker configuration provided the means to produce a fairly symmetric acoustic field in the waveguide. In the absence of acoustic excitation, values of

the measured droplet burning rate constant K were generally consistent with available values for the different fuels explored. During acoustic excitation of droplets situated in the vicinity of a pressure node or antinode, flame orientation was consistent with the sign of an acoustic radiation force acting on the burning system, creating conditions where the flame deflection switched, depending on the relative location of the droplet. The acceleration associated with the acoustic radiation force was estimated by measuring the degree of deflection that the flame underwent relative to an unforced flame. Although overall there were no significant variations in the measured K values with changing acoustic excitation, in some cases, locally increased K values were observed to be associated with larger measured acoustic accelerations. This study also examined the extinction characteristics and made preliminary estimations of the extinction strain rates of the different fuels.

The non-reactive flow study investigated the mixing behavior and characteristics of dynamic flow structures of shear-coaxial nitrogen jets under varying flow conditions, with and without the presence of pressure perturbations due to acoustic forcing transverse to the flow direction. The role of injector geometry was examined using two shear-coaxial injectors with different outer to inner jet area ratios, A_o/A_i, and different inner jet post thickness to inner jet diameter ratios, t/D_1. Flow conditions under chamber pressures spanning high subcritical pressures (reduced pressure or chamber to critical pressure, P_r, of 0.44) to nearcritical pressures ($P_r = 1.05$), with varying outer to inner jet momentum flux ratios ($J = 0.1 - 21$), and maximum or minimum amplitude in the pressure perturbation at the jet axis location were considered. The inner and outer jet temperatures were independently controlled so that the inner and outer flows were in liquid and gaseous states at $P_r = 0.44$, respectively, and in transcritical and supercritical states at $P_r = 1.05$, respectively. Back-lighting the coaxial jets resulted in a silhouette of the dense inner jet, which appeared as a dark column. This distinguished it from the outer jet, and thus, enabled high speed images to capture the its flow dynamics. Dark-core

length, pertaining to the axial length of the unmixed portion of the inner flow, measurements were used to indicate the extent of mixing under the different flow conditions and injector geometries. In general, for baseline flows at both P_r, the dark-core length to inner jet diameter L_B/D_1 ratio decreased with increasing J and t/D_1, and decreasing A_o/A_i. During a maximum pressure perturbation forcing condition, the forced to baseline flow dark-core length ratio, which stayed constant around one for $J < 10$ for the small A_o/A_i, large t/D_1 injector flows, also underlined the influence of geometry on the mixing and response to external pressure disturbances. A basic application of proper orthogonal decomposition on the intensity fluctuation of the high-speed images enabled the extraction of the spatial and temporal characteristics of the dominant flow structures that existed in the flow field during exposure to acoustic forcing. With increasing J, the flow response to forcing depended on the injector geometry. A comparison of the spatio-temporal characteristics of the baseline flows and their corresponding acoustically forced flows revealed that for the $J > 5$ flows of the large A_o/A_i, small t/D_1 injector, the baseline flow behavior was retained in the forced flow, thereby indicating a flow regime that was less sensitive to external pressure disturbances.

The dissertation of Sophonias Teshome is approved.

Russel E. Caflisch
Xiaolin Zhong
Ivett A. Leyva
Owen I. Smith, Committee Co-chair
Ann R. Karagozian, Committee Co-chair

University of California, Los Angeles
2012

Table of Contents

1 Introduction . . . 1

1.1 Fuel Droplet Combustion . . . 2

1.1.1 Alternative Fuels . . . 2

1.1.2 Related Works in Droplet Combustion . . . 3

1.1.3 Effects of Acoustics on Droplet Combustion . . . 4

1.2 Shear-Coaxial Jets . . . 8

1.2.1 Near-Field Mixing of Same and Different Density Shear-Coaxial Jets . . . 9

1.2.2 Stability Consideration of Coaxial Jets . . . 14

1.2.3 Transverse Acoustic Excitation of Coaxial Jets . . . 16

1.2.4 Objectives . . . 19

2 Experimental Facility and Methods . . . 23

2.1 Acoustic Waveguide . . . 23

2.2 Droplet Generation and Ignition . . . 26

2.3 Measurement Methods . . . 27

2.3.1 Burning Rate Constant . . . 27

2.3.2 Acoustic Acceleration . . . 27

2.3.3 Extinction Strain Rate Estimation . . . 28

2.4 Experimental Procedure . . . 29

2.5 Measurement Uncertainties . . . 30

2.5.1 Precision Uncertainty 30

2.5.2 Bias Uncertainty 31

3 Results - Acoustically Coupled Fuel Droplet Combustion 38

3.1 Baseline Burning Rate Constants 38

3.2 Flame Alterations under Acoustic Excitation 39

3.3 Effect of Acoustic Acceleration on Burning Rate Constants 43

3.4 Fuel Extinction Studies 44

3.5 Preliminary Conclusions 45

4 Experimental Set-Up and Methodology 68

4.1 High Pressure Chamber and Flow Facility 69

4.2 Shear-Coaxial Injectors 70

4.3 Inner Chamber: Acoustic Waveguide and Characterization 72

4.4 Measurement of Physical Properties 73

4.5 Jet Visualization 74

4.6 Measurement of Dark-Core Length 74

4.7 Proper Orthogonal Decomposition of Pixel Intensity Data Array 75

4.8 Measurement Uncertainty 79

5 Shear-Coaxial Jets: Results and Discussion 90

5.1 Shear-Coaxial Jets without Acoustic Forcing 91

5.1.1 Qualitative Characteristics of Baseline Flows 91

5.1.2 Baseline Dark-Core Length Measurements 94

5.1.3 Characterization of Dominant Behavior of Baseline Flow Structures 98

5.2 Transverse Acoustic Forcing of Shear-Coaxial Jets 132
    5.2.1 Qualitative Characteristics of Acoustically Forced Flows 133
    5.2.2 Acoustically Forced Dark-Core Length Measurements 138
    5.2.3 Characterization of Dominant Dynamic Flow Structures 140

6 Summary, Conclusions and Recommendations for Future Work . . . 186

6.1 Droplet Combustion 186
6.2 Non-Reactive Shear-Coaxial Jets 188

A Shear-Coaxial Jets Experimental Facility:
Piping and Instrumentation Diagram 193

B Shear-Coaxial Jets Experiment:
Standard Operating Procedures 199

C Shear-Coaxial Jets Experiment:
Summary Tables of Flow Conditions 224

References 228

List of Figures

2.1 Experimental setup of the acoustic waveguide and droplet feed system. . 32

2.2 Acoustic characterization of the waveguide (S&R configuration) as measured by pressure transducers at P1 and P2. Local maxima for both pressure transducers corresponds to a pressure antinode location. A local minimum at P1 and maximum at P2 corresponds to a pressure node. The distance between the speaker and reflector is approximately 62 cm. . . . 33

2.3 Measurements of relative local perturbation velocity (made by the hot wire anemometer) and the relative local perturbation pressure (made by the pressure transducer), both at the geometric center of the waveguide, for the Speaker-Reflector configuration ("S & R"). The displacement of the speaker and reflector is indicated on the abscissa, relative to their original locations as determined from the geometric center of the waveguide. Positive displacement refers to the S & R moved to the right. Results are shown for acoustic excitation at an applied frequency of: (a) 784 Hz (for a pressure node condition) and (b) 544 Hz (for a pressure antinode condition). 34

2.4 Measurements of relative local perturbation velocity (made by the hot wire anemometer) and the relative local perturbation pressure (made by the pressure transducer P1), both at the geometric center of the waveguide, for the two Speaker configuration ((”S & S”). The displacement of the two speakers is indicated on the abscissa, relative to their original locations as determined from the geometric center of the waveguide and a maximum or minimum in the pressure transducer. Positive displacement refers to the S & S moved to the right. Results are shown for acoustic excitation at an applied frequency of: (a) 784 Hz (for a pressure node condition) and (b) 544 Hz (for a pressure antinode condition). 35

2.5 Ethanol droplet burning with and without acoustic excitation or forcing. In the absence of acoustic forcing, the flame orientation is only influenced by force of buoyancy F_B, while with acoustic excitation, both F_B and acoustic radiation force F_R affect its orientation: (a) Unforced flame orientation (b) Forced flame orientation 36

2.6 A schematic of the flow and relevant parameters used in estimating extinction strain rate. The flame assumes a nearly horizontal orientation at the instant before extinction. 37

3.1 Images of various fuel droplets burning in the absence of acoustic excitation. 48

3.2 Schematic showing the relative displacement between a pressure node (velocity antinode) and the droplet. *Top*: Location of the speakers in the waveguide relative to a velocity antinode (pressure node) situated at $x' = 0$, with the droplet located at $x = 0$ relative to the velocity antinode. *Middle*: Location of velocity antinode at $x' > 0$ relative to the droplet (and of the droplet at $x < 0$ relative to the velocity antinode),resulting from displacement of the speakers to the right as compared with the original condition. *Bottom*: Location of velocity antinode at $x' < 0$ relative to the droplet (and of the droplet at $x > 0$ relative to the velocity antinode), resulting from displacement of the speakers to the left as compared with the original condition. 49

3.3 Photographs of a burning ethanol droplet with acoustic excitation at an applied frequency of 784 Hz (for a pressure node condition). The positions of the two speakers ("S & S") are indicated, relative to their original locations as determined from the geometric waveguide center and minimum in measured pressures. "S & S X cm to left" refers to the case where the speakers were moved by X cm to the left as compared with their original positions, etc. The true pressure node was likely coincident with the droplet located between cases (c) and (d), very close to the pressure node. 50

3.4 Photographs of a burning JP-8 droplet with acoustic excitation at an applied frequency of 784 Hz (for a pressure node condition). The positions of the two speakers ("S & S") are indicated, relative to their original locations as determined from the geometric waveguide center and minimum in measured pressures. "S & S X cm to left" refers to the case where the speakers were moved by X cm to the left as compared with their original positions, etc. The true pressure node was likely coincident with the droplet located between cases (c) and (d), very close to the pressure node. 51

3.5 Photographs of a burning JP-8/FT blend droplet with acoustic excitation at an applied frequency of 784 Hz (for a pressure node condition). The positions of the two speakers ("S & S") are indicated, relative to their original locations as determined from the geometric waveguide center and minimum in measured pressures. "S & S X cm to left" refers to the case where the speakers were moved by X cm to the left as compared with their original positions, etc. The true pressure node was likely coincident with the droplet located between cases (c) and (d), very close to the pressure node. 52

3.6 Photographs of a burning FT droplet with acoustic excitation at an applied frequency of 784 Hz (for a pressure node condition). The positions of the two speakers ("S & S") are indicated, relative to their original locations as determined from the geometric waveguide center and minimum in measured pressures. "S & S X cm to left" refers to the case where the speakers were moved by X cm to the left as compared with their original positions, etc. The true pressure node was likely coincident with the droplet located between cases (c) and (d), very close to the pressure node. 53

3.7 Photographs of a burning ethanol droplet with acoustic excitation at an applied frequency of 1340 Hz (for a pressure node condition). The positions of the two speakers (“S & S”) are indicated, relative to their original locations as determined from the geometric waveguide center and minimum in measured pressures. “S & S X cm to left” refers to the case where the speakers were moved by X cm to the left as compared with their original positions, etc. The true pressure node was likely coincident with the droplet located between cases (c) and (d), very close to the pressure node. 54

3.8 Photographs of a burning JP-8 droplet with acoustic excitation at an applied frequency of 1340 Hz (for a pressure node condition). The positions of the two speakers (“S & S”) are indicated, relative to their original locations as determined from the geometric waveguide center and minimum in measured pressures. “S & S X cm to left” refers to the case where the speakers were moved by X cm to the left as compared with their original positions, etc. The true pressure node was likely coincident with the droplet located between cases (c) and (d), very close to the pressure node. 55

3.9 Photographs of a burning FT droplet with acoustic excitation at an applied frequency of 1340 Hz (for a pressure node condition). The positions of the two speakers (“S & S”) are indicated, relative to their original locations as determined from the geometric waveguide center and minimum in measured pressures. “S & S X cm to left” refers to the case where the speakers were moved by X cm to the left as compared with their original positions, etc. The true pressure node was likely coincident with the droplet located between cases (c) and (d), very close to the pressure node. 56

3.10 Pressure perturbations, estimated theoretical and actual acoustic accelerations g_a, and average burning rate constant K as a function of the displacement of the speakers with respect to the original position (0 cm) for the ethanol droplet burning in the vicinity of a pressure node at a frequency of approximately 784 Hz. 57

3.11 Pressure perturbations, estimated theoretical and actual acoustic accelerations g_a, and average burning rate constant K as a function of the displacement of the speakers with respect to the original position (0 cm) for the JP-8 droplet burning in the vicinity of a pressure node at a frequency of approximately 784 Hz. 58

3.12 Pressure perturbations, estimated theoretical and actual acoustic accelerations g_a, and average burning rate constant K as a function of the displacement of the speakers with respect to the original position (0 cm) for the JP-8/FT blend droplet burning in the vicinity of a pressure node at a frequency of approximately 784 Hz. 59

3.13 Pressure perturbations, estimated theoretical and actual acoustic accelerations g_a, and average burning rate constant K as a function of the displacement of the speakers with respect to the original position (0 cm) for the FT droplet burning in the vicinity of a pressure node at a frequency of approximately 784 Hz. 60

3.14 Pressure perturbations, estimated theoretical and actual acoustic accelerations g_a, and average burning rate constant K as a function of the displacement of the speakers with respect to the original position (0 cm) for the ethanol droplet burning in the vicinity of a pressure node at a frequency of approximately 1340 Hz. 61

3.15 Pressure perturbations, estimated theoretical and actual acoustic accelerations g_a, and average burning rate constant K as a function of the displacement of the speakers with respect to the original position (0 cm) for the JP-8 droplet burning in the vicinity of a pressure node at a frequency of approximately 1340 Hz. 62

3.16 Pressure perturbations, estimated theoretical and actual acoustic accelerations g_a, and average burning rate constant K as a function of the displacement of the speakers with respect to the original position (0 cm) for the FT droplet burning in the vicinity of a pressure node at a frequency of approximately 1340 Hz. 63

3.17 A sequence of images showing the extinction process of the flame surrounding an ethanol fuel droplet. The time span between the consequetive images was approximately 33 ms. The sound pressure level was 142.3 dB, and the estimated strain rate at extinction for this case was 260 s^-1. 64

3.18 A sequence of images showing the extinction process of the flame surrounding a JP-8 fuel droplet. The time span between the consequetive images was approximately 33 ms. The sound pressure level was 140.8 dB, and the estimated strain rate at extinction for this case was 230 s^-1. . . 65

3.19 A sequence of images showing the extinction process of the flame surrounding a JP-8/FT fuel blend droplet. The time span between the consequetive images was approximately 33 ms. The sound pressure level was 141.8 dB, and the estimated strain rate at extinction for this case was 350 s^-1. 66

3.20 A sequence of images showing the extinction process of the flame surrounding an FT fuel droplet. The time span between the consequetive images was approximately 33 ms. The sound pressure level was 141.6 dB, and the estimated strain rate at extinction for this case was 360 s^-1. . . 67

4.1 A schematic of the chamber and peripheral lines. 82

4.2 A schematic of the shear-coaxial injector assembly (expanded view of **A**: See Figure 4.3). 83

4.3 A schematic of the shear-coaxial injector exit. 83

4.4 Pictures of the acoustic elements. Acoustic waves generated by the piezosiren enter the end of the waveguide of circular cross-section and propagate down to the test-section of rectangular cross-section 84

4.5 Back-lit images of baseline LAR-thin injector flows at $J = 0.1$ where the chamber pressure, and the chamber, outer jet and inner jet temperatures were: (a) 1.5 MPa, 243 K, 198 K, 107 K, and (b) 3.57 MPa, 252 K, 195 K, 114 K, respectively. 84

4.6 Measurement of dark-core length: (a) original image (b) black and white image after thresholding (c) Contour used to define the dark-core length (L). 85

4.7 Illustration of (a) how pixel intensity values from a single image are arranged into a row vector; (b) the construction of **A**, data matrix of pixel intensities. 85

4.8 PN forced ($f_F = 3.12$ kHz) LAR-thin injector flow at $P_r = 0.44$, $J = 5.2$: (a) a snapshot image captured at 25 kHz; (b) a time-averaged image from 1000 consecutive images. 86

4.9 Singular values for PN forced ($f_F = 3.12$ kHz) LAR-thin injector flow at $P_r = 0.44$, $J = 5.2$. 86

4.10 Proper orthogonal mode (POM) image and power spectral density (PSD) of the temporal amplitude coefficients for PN forced ($f_F = 3.12$ kHz) LAR-thin injector flow at $P_r = 0.44$, $J = 5.2$: mode-1 (a) POM, (b) PSD; mode-2 (c) POM (d) PSD. 87

4.11 A time sequence of POM images for PN forced ($f_F = 3.12$ kHz) LAR-thin injector flow at $P_r = 0.44$, $J = 5.2$: (a) mode-1 only, (b) superposition of mode-1 and mode-2. 88

4.12 Cross-power spectral density (CPSD) of mode-1 and mode-2 for PN forced ($f_F = 3.12$ kHz) LAR-thin injector flow at $P_r = 0.44$, $J = 5.2$: (a) magnitude, (b) phase. 89

5.1 Back-lit images of the LAR-thin injector baseline flow at $P_r = 0.44$ and varying J. The image framing rate was 25 kHz. At subcritical chamber pressure, the inner jet was in liquid state while the outer jet was in gaseous state. Table C.1 gives a summary of the flow conditions. 104

5.2 Back-lit images of the LAR-thin injector baseline flow at $P_r = 1.05$ and varying J. The image framing rate was 25 kHz. At nearcrtical chamber pressure, the inner jet was in liquid state while the outer jet was supercritical. Table C.1 gives a summary of the flow conditions. 105

5.3 Back-lit images of the SAR-thick injector baseline flow at $P_r = 0.44$ and varying J. The image framing rate was 25 kHz. At subcritical chamber pressure, the inner jet was in liquid state while the outer jet was in gaseous state. Table C.2 gives a summary of the flow conditions. 106

5.4 Back-lit images of the SAR-thick injector baseline flow at $P_r = 1.05$ and varying J. The image framing rate was 25 kHz. At nearcrtical chamber pressure, the inner jet was in liquid state while the outer jet was supercritical. Table C.2 gives a summary of the flow conditions. 107

5.5 Measurements of the LAR-thin injector baseline flows dark-core lengths, L_B normalized by the inside diameter of the inner injector, D_1. The vertical error bars represent the uncertainty in a single measurement to within 2σ of the mean for 1000 measurements. The horizontal error bars represent the bias errors in the measurement of J. The large errors at higher J values were mainly due to the large relative uncertainties $(\delta\dot{m}_i/\dot{m}_i)$ in the low inner jet flowrate measurements. 108

5.6 Measurements of the SAR-thick injector baseline flows dark-core lengths, L_B normalized by the inside diameter of the inner injector, D_1. The vertical error bars represent the uncertainty in a single measurement to within 2σ of the mean for 1000 measurements. The horizontal error bars represent the bias errors in the measurement of J. 109

5.7 A power-law curve-fit to the L_B/D_1 data plotted in Figures 5.6 and 5.5. The variation of L_B/D_1 with J was similar for both injector flows in the same pressure regime. In addition, the SAR-thick injector L_B/D_1 were consistently lower than the LAR-thin injector, and those at $P_r = 1.05$ were lower than at $P_r = 0.44$. 110

5.8 Measured L_B/D_1 at $P_r = 0.44$ using different injector configurations including those used by Rodriguez, Graham *et al.*, and Leyva *et al.*. The dimensions of the LAR-thick and SAR-thin injectors are given in Table 1.2.111

5.9 Measured L_B/D_1 at $P_r = 1.05$ using different injector configurations including those used by Rodriguez, Graham *et al.*, and Leyva *et al.*. The dimensions of the LAR-thick and SAR-thin injectors are given in Table 1.2. 112

5.10 Measured L_B/D_1 for the different injectors at $P_r = 0.44$ plotted versus $G = c_1 J^{c_2}(t/D_1)^{c_3}(A_o/A_i)^{c_4}$, where the constants were obtained using non-linear regression, and whose values are listed in Table 5.1.2. The nearly linear line with a unit slope indicated that L_B/D_1 may be predicted with knowledge of the flow J and the injector geometry. 113

5.11 Measured L_B/D_1 for the different injectors at $P_r = 1.05$ plotted versus $G = c_1 J^{c_2}(t/D_1)^{c_3}(A_o/A_i)^{c_4}$, where the constants were obtained using non-linear regression, and whose values are listed in Table 5.1.2. The nearly linear line with a unit slope indicated that L_B/D_1 may be predicted with knowledge of the flow J and the injector geometry. 114

5.12 See caption on page 118. 115

5.12 See caption on page 118. 116

5.12 See caption on page 118. 117

5.12 A back-lit image of the LAR-thin injector baseline flow at $P_r = 0.44$ similar to those in Figure 5.1, a time-averaged image and an image of the superposed conjugate proper orthogonal modes (POMs) are shown for each J. The averaged image consisted of 1000 frames sampled at 25 kHz. The corresponding plots are the cross-power spectral density (CPSD) magnitude of the time-dependent amplitude cofficients of the conjugate modes. The peaks in the spectra are the characteristic frequencies of the periodic flow structures identified in the POM images. 118

5.13 See caption on page 121. 119

5.13 See caption on page 121. 120

5.13 A back-lit image of the LAR-thin injector baseline flow at $P_r = 1.05$ similar to those in Figure 5.2, a time-averaged image and an image of the superposed conjugate proper orthogonal modes (POMs) are shown for each J. The averaged image consisted of 1000 frames sampled at 25 kHz. The corresponding plots are the cross-power spectral density (CPSD) magnitude of the time-dependent amplitude cofficients of the conjugate modes. The peaks in the spectra are the characteristic frequencies of the periodic flow structures identified in the POM images. 121

5.14 See caption on page 125. 122

5.14 See caption on page 125. 123

5.14 See caption on page 125. 124

5.14 A back-lit image of the SAR-thick injector baseline flow at $P_r = 0.44$ similar to those in Figure 5.3, a time-averaged image and an image of the superposed conjugate proper orthogonal modes (POMs) are shown for each J. The averaged image consisted of 500 frames sampled at 25 kHz. The corresponding plots are the cross-power spectral density (CPSD) magnitude of the time-dependent amplitude cofficients of the conjugate modes. The peaks in the spectra are the characteristic frequencies of the periodic flow structures identified in the POM images. 125

5.15 See caption on page 129. 126

5.15 See caption on page 129. 127

5.15 See caption on page 129. 128

5.15 A back-lit image of the SAR-thick injector baseline flow at $P_r = 1.05$ similar to those in Figure 5.4, a time-averaged image and an image of the superposed conjugate proper orthogonal modes (POMs) are shown for each J. The averaged image consisted of 500 frames sampled at 25 kHz. The corresponding plots are the cross-power spectral density (CPSD) magnitude of the time-dependent amplitude cofficients of the conjugate modes. The peaks in the spectra are the characteristic frequencies of the periodic flow structures identified in the POM images. 129

5.16 Plots of the outer jet exit velocities, U_o, inner jet exit velocities, U_i, their corresponding mean velocities, U_{mean}, and the estimated convection velocities of the dominant flow structures, U_s for the LAR-thin and SAR-thick injector flows at $P_r = 0.44$. It can be seen that the LAR-thin injector outer jet flow had more influence on the inner shear layer flow than did the SAR-thick outer jet flow. 130

5.17 Plots of the outer jet exit velocities, U_o, inner jet exit velocities, U_i, their corresponding mean velocities, U_{mean}, and the estimated convection velocities of the dominant flow structures, U_s for the LAR-thin and SAR-thick injector flows at $P_r = 1.05$. Again, it is clear that the LAR-thin injector outer jet flow had more influence on the inner shear layer flow than did the SAR-thick outer jet flow. 131

5.18 See caption on page 147. 145

5.18 See caption on page 147. 146

5.18 Back-lit images of the LAR-thin injector PAN flow at $P_r = 0.44$ and varying J. The image framing rate was 25 kHz. Table C.3 gives a summary of the acoustic forcing frequencies and amplitudes. 147

5.19 See caption on page 149. 148

5.19 Back-lit images of the LAR-thin injector PAN flow at $P_r = 1.05$ and varying J. The image framing rate was 25 kHz. Table C.3 gives a summary of the acoustic forcing frequencies and amplitudes. 149

5.20 A time-sequence of images during PAN forcing ($f_F = 3.14$ kHz) of the $J = 0.5$ LAR-thin injector flow at $P_r = 0.44$. The images were captured at 40 μs intervals, and show formation of the outer shear layer vortices, which grow and dominate the inner shear layer and inner jet flow dynamics. 150

5.21 A time-sequence of images during PAN forcing ($f_F = 3.11$ kHz) of the $J = 14$ LAR-thin injector flow at $P_r = 0.44$. The images were captured at 40 μs intervals. Unlike the $J = 0.5$ flow in Figure 5.20, the large convection speed of the shear layer vortices prevented their interaction with the inner shear layer. 151

5.22 Synchronized acoustic pressure perturbation measurements during PAN forcing ($f_F = 3.14$ kHz) of the $J = 0.5$ LAR-thin injector flow at $P_r = 0.44$. The numbers next to the data points refer to the amplitudes measured corresponding to the image numbers in Figure 5.20. 152

5.23 Synchronized acoustic pressure perturbation measurements during PAN forcing ($f_F = 3.11$ kHz) of the $J = 14$ LAR-thin injector flow at $P_r = 0.44$. The numbers next to the data points refer to the amplitudes measured corresponding to the image numbers in Figure 5.21. 152

5.24 See caption on page 155. 153

5.24 See caption on page 155. 154

5.24 Back-lit images of the SAR-thick injector PAN flow at $P_r = 0.44$ and varying J. The image framing rate was 25 kHz. Table C.4 gives a summary of the acoustic forcing frequencies and amplitudes. 155

5.25 See caption on page 158. 156

5.25 See caption on page 158. 157

5.25 Back-lit images of the LAR-thin injector PAN flow at $P_r = 1.05$ and varying J. The image framing rate was 25 kHz. Table C.4 gives a summary of the acoustic forcing frequencies and amplitudes. 158

5.26 Measurements of the PAN forced flow dark-core length, L_PAN normalized by the corresponding baseline flow dark-core length, L_B. 158

5.27 Measurements of the PN forced flow dark-core length, L_PN normalized by the corresponding baseline flow dark-core length, L_B. 159

5.28 A back-lit image of the LAR-thin injector forced ($f_F = 3.13$ kHz) flows at $P_r = 0.44$ similar to that in Figure 5.18, a time-averaged image and an image of the superposed conjugate proper orthogonal modes (POMs). The averaged image consisted of 1000 frames sampled at 25 kHz. The corresponding plots are the cross-power spectral density (CPSD) magnitude of the time-dependent amplitude cofficients of the conjugate modes. The peak characteristic frequencies of the periodic flow structures were identical to f_F. For the purpose of comparison, the baseline spectra are shown in dots. Under both the PAN and PN forcing conditions, the forced spectra were completely different from that of the baseline. (.........Baseline, ———Forced) 160

5.29 A back-lit image of the LAR-thin injector forced ($f_F = 3.14$ kHz) flows at $P_r = 0.44$ similar to that in Figure 5.18, a time-averaged image and an image of the superposed conjugate proper orthogonal modes (POMs). The averaged image consisted of 1000 frames sampled at 25 kHz. The corresponding plots are the cross-power spectral density (CPSD) magnitude of the time-dependent amplitude cofficients of the conjugate modes. The peak characteristic frequencies of the periodic flow structures were identical to f_F. For the purpose of comparison, the baseline spectra are shown in dots. Under both the PAN and PN forcing conditions, the forced spectra were completely different from that of the baseline. (.........Baseline, ———Forced) 161

5.30 A back-lit image of the LAR-thin injector forced ($f_F = 3.12$ kHz) flows at $P_r = 0.44$ similar to that in Figure 5.18, a time-averaged image and an image of the superposed conjugate proper orthogonal modes (POMs). The averaged image consisted of 1000 frames sampled at 25 kHz. The corresponding plots are the cross-power spectral density (CPSD) magnitude of the time-dependent amplitude cofficients of the conjugate modes. The peak characteristic frequencies of the periodic flow structures were identical to f_F. For the purpose of comparison, the baseline spectra are shown in dots. Under both the PAN and PN forcing conditions, the forced spectra were still different from that of the baseline. (.........Baseline, ———Forced) 162

5.31 A back-lit image of the LAR-thin injector forced ($f_F = 3.12$ kHz) flows at $P_r = 0.44$ similar to that in Figure 5.18, a time-averaged image and an image of the superposed conjugate proper orthogonal modes (POMs). The averaged image consisted of 1000 frames sampled at 25 kHz. The corresponding plots are the cross-power spectral density (CPSD) magnitude of the time-dependent amplitude cofficients of the conjugate modes. The peak characteristic frequencies of the periodic flow structures were identical to f_F. For the purpose of comparison, the baseline spectra are shown in dots. (.........Baseline, ———Forced) 163

5.32 A back-lit image of the LAR-thin injector forced ($f_F = 3.10$ kHz) flows at $P_r = 0.44$ similar to that in Figure 5.18, a time-averaged image and an image of the superposed conjugate proper orthogonal modes (POMs). The averaged image consisted of 1000 frames sampled at 25 kHz. The corresponding plots are the cross-power spectral density (CPSD) magnitude of the time-dependent amplitude cofficients of the conjugate modes. The peak characteristic frequencies of the periodic flow structures were identical to f_F. For the purpose of comparison, the baseline spectra are shown in dots. Under the PAN forcing condition, the forced spectrum retained the baseline spectrum. (.........Baseline, ———Forced) 164

5.33 A back-lit image of the LAR-thin injector forced ($f_F = 3.11$ kHz) flows at $P_r = 0.44$ similar to that in Figure 5.18, a time-averaged image and an image of the superposed conjugate proper orthogonal modes (POMs). The averaged image consisted of 1000 frames sampled at 25 kHz. The corresponding plots are the cross-power spectral density (CPSD) magnitude of the time-dependent amplitude cofficients of the conjugate modes. The peak characteristic frequencies of the periodic flow structures were identical to f_F. For the purpose of comparison, the baseline spectra are shown in dots. Under the PAN forcing condition, the forced spectrum retained the baseline spectrum. (.........Baseline, ———Forced) 165

5.34 A back-lit image of the LAR-thin injector forced ($f_F = 3.11$ kHz) flows at $P_r = 0.44$ similar to that in Figure 5.18, a time-averaged image and an image of the superposed conjugate proper orthogonal modes (POMs). The averaged image consisted of 1000 frames sampled at 25 kHz. The corresponding plots are the cross-power spectral density (CPSD) magnitude of the time-dependent amplitude cofficients of the conjugate modes. The peak characteristic frequencies of the periodic flow structures were identical to f_F. For the purpose of comparison, the baseline spectra are shown in dots. Under the PAN forcing condition, the forced spectrum retained the baseline spectrum. (.........Baseline, ———Forced) 166

5.35 A back-lit image of the LAR-thin injector forced ($f_F = 3.10$ kHz) flows at $P_r = 1.05$ similar to that in Figure 5.19, a time-averaged image and an image of the superposed conjugate proper orthogonal modes (POMs). The averaged image consisted of 1000 frames sampled at 25 kHz. The corresponding plots are the cross-power spectral density (CPSD) magnitude of the time-dependent amplitude cofficients of the conjugate modes. The peak characteristic frequencies of the periodic flow structures were identical to f_F. For the purpose of comparison, the baseline spectra are shown in dots. Under both the PAN and PN forcing conditions, the forced spectra were completely different from that of the baseline. (.........Baseline, ———Forced) 167

5.36 A back-lit image of the LAR-thin injector forced ($f_F = 3.10$ kHz) flows at $P_r = 1.05$ similar to that in Figure 5.19, a time-averaged image and an image of the superposed conjugate proper orthogonal modes (POMs). The averaged image consisted of 1000 frames sampled at 25 kHz. The corresponding plots are the cross-power spectral density (CPSD) magnitude of the time-dependent amplitude cofficients of the conjugate modes. The peak characteristic frequencies of the periodic flow structures were identical to f_F. For the purpose of comparison, the baseline spectra are shown in dots. Under the PAN forcing condition, the forced spectrum was completely different from that of the baseline. (.........Baseline, ———Forced) 168

5.37 A back-lit image of the LAR-thin injector forced ($f_F = 3.41$ kHz) flows at $P_r = 1.05$ similar to that in Figure 5.19, a time-averaged image and an image of the superposed conjugate proper orthogonal modes (POMs). The averaged image consisted of 1000 frames sampled at 25 kHz. The corresponding plots are the cross-power spectral density (CPSD) magnitude of the time-dependent amplitude cofficients of the conjugate modes. The peak characteristic frequencies of the periodic flow structures were identical to f_F. For the purpose of comparison, the baseline spectra are shown in dots. Under both the PAN and PN forcing conditions, the forced spectra were completely different from that of the baseline. (.........Baseline, ———Forced) 169

5.38 A back-lit image of the LAR-thin injector forced ($f_F = 3.10$ kHz) flows at $P_r = 1.05$ similar to that in Figure 5.19, a time-averaged image and an image of the superposed conjugate proper orthogonal modes (POMs). The averaged image consisted of 1000 frames sampled at 25 kHz. The corresponding plots are the cross-power spectral density (CPSD) magnitude of the time-dependent amplitude cofficients of the conjugate modes. The peak characteristic frequencies of the periodic flow structures were identical to f_F. For the purpose of comparison, the baseline spectra are shown in dots. Under the PAN forcing condition, the forced spectrum retained the baseline spectrum. (.........Baseline, ———Forced) 170

5.39 A back-lit image of the LAR-thin injector forced ($f_F = 3.10$ kHz) flows at $P_r = 1.05$ similar to that in Figure 5.19, a time-averaged image and an image of the superposed conjugate proper orthogonal modes (POMs). The averaged image consisted of 1000 frames sampled at 25 kHz. The corresponding plots are the cross-power spectral density (CPSD) magnitude of the time-dependent amplitude cofficients of the conjugate modes. The peak characteristic frequencies of the periodic flow structures were identical to f_F. For the purpose of comparison, the baseline spectra are shown in dots. Under the PAN forcing condition, the forced spectrum retained the baseline spectrum. (.........Baseline, ———Forced) 171

5.40 A back-lit image of the SAR-thick injector forced ($f_F = 3.10$ kHz) flows at $P_r = 0.44$ shown in Figure 5.24, a time-averaged image and an image of the superposed conjugate proper orthogonal modes (POMs). The averaged image consisted of 500 frames sampled at 25 kHz. The corresponding plots are the cross-power spectral density (CPSD) magnitude of the time-dependent amplitude cofficients of the conjugate modes. The low frequency peak associated with the periodic flow structures was not identical to f_F. For the purpose of comparison, the baseline spectra are shown with dots. (.........Baseline, ———Forced) 172

5.41 A back-lit image of the SAR-thick injector forced ($f_F = 3.04$ kHz) flows at $P_r = 0.44$ shown in Figure 5.24, a time-averaged image and an image of the superposed conjugate proper orthogonal modes (POMs). The averaged image consisted of 500 frames sampled at 25 kHz. The corresponding plots are the cross-power spectral density (CPSD) magnitude of the time-dependent amplitude coefficients of the conjugate modes. The low frequency peak associated with the periodic flow structures was not identical to f_F. For the purpose of comparison, the baseline spectra are shown with dots. (.........Baseline, ———Forced) 173

5.42 A back-lit image of the SAR-thick injector forced ($f_F = 3.07$ kHz) flows at $P_r = 0.44$ shown in Figure 5.24, a time-averaged image and an image of the superposed conjugate proper orthogonal modes (POMs). The averaged image consisted of 500 frames sampled at 25 kHz. The corresponding plots are the cross-power spectral density (CPSD) magnitude of the time-dependent amplitude coefficients of the conjugate modes. The low frequency peaks associated with the periodic flow structures was not identical to f_F. For the purpose of comparison, the baseline spectra are shown with dots. (.........Baseline, ———Forced) 174

5.43 A back-lit image of the SAR-thick injector forced ($f_F = 3.11$ kHz) flows at $P_r = 0.44$ shown in Figure 5.24, a time-averaged image and an image of the superposed conjugate proper orthogonal modes (POMs). The averaged image consisted of 500 frames sampled at 25 kHz. The corresponding plots are the cross-power spectral density (CPSD) magnitude of the time-dependent amplitude coefficients of the conjugate modes. The peak frequencies of the periodic flow structures were identical to f_F. For the purpose of comparison, the baseline spectra are shown with dots. (.........Baseline, ———Forced) 175

5.44 A back-lit image of the SAR-thick injector forced ($f_F = 3.11$ kHz) flows at $P_r = 0.44$ shown in Figure 5.24, a time-averaged image and an image of the superposed conjugate proper orthogonal modes (POMs). The averaged image consisted of 500 frames sampled at 25 kHz. The corresponding plots are the cross-power spectral density (CPSD) magnitude of the time-dependent amplitude coefficients of the conjugate modes. The peak frequencies of the periodic flow structures were identical to f_F. For the purpose of comparison, the baseline spectra are shown with dots. (.........Baseline, ———Forced) 176

5.45 A back-lit image of the SAR-thick injector forced ($f_F = 3.04$ kHz) flows at $P_r = 0.44$ shown in Figure 5.24, a time-averaged image and an image of the superposed conjugate proper orthogonal modes (POMs). The averaged image consisted of 500 frames sampled at 25 kHz. The corresponding plots are the cross-power spectral density (CPSD) magnitude of the time-dependent amplitude cofficients of the conjugate modes. The peak frequencies of the periodic flow structures were identical to f_F. For the purpose of comparison, the baseline spectra are shown with dots. (.........Baseline, ———Forced) 177

5.46 A back-lit image of the SAR-thick injector forced ($f_F = 3.11$ kHz) flows at $P_r = 0.44$ shown in Figure 5.24, a time-averaged image and an image of the superposed conjugate proper orthogonal modes (POMs). The averaged image consisted of 500 frames sampled at 25 kHz. The corresponding plots are the cross-power spectral density (CPSD) magnitude of the time-dependent amplitude cofficients of the conjugate modes. The peak frequencies of the periodic flow structures were identical to f_F. For the purpose of comparison, the baseline spectra are shown with dots. (.........Baseline, ———Forced) 178

5.47 A back-lit image of the SAR-thick injector forced ($f_F = 3.12$ kHz) flows at $P_r = 1.05$ shown in Figure 5.25, a time-averaged image and an image of the superposed conjugate proper orthogonal modes (POMs). The averaged image consisted of 500 frames sampled at 25 kHz. The corresponding plots are the cross-power spectral density (CPSD) magnitude of the time-dependent amplitude cofficients of the conjugate modes. The low frequency peak associated with the periodic flow structures was not identical to f_F. For the purpose of comparison, the baseline spectra are shown with dots. (.........Baseline, ———Forced) 179

5.48 A back-lit image of the SAR-thick injector forced ($f_F = 3.00$ kHz) flows at $P_r = 1.05$ shown in Figure 5.25, a time-averaged image and an image of the superposed conjugate proper orthogonal modes (POMs). The averaged image consisted of 500 frames sampled at 25 kHz. The corresponding plots are the cross-power spectral density (CPSD) magnitude of the time-dependent amplitude cofficients of the conjugate modes. The low frequency peaks associated with the periodic flow structures were not identical to f_F. For the purpose of comparison, the baseline spectra are shown with dots. (.........Baseline, ———Forced) 180

5.49 A back-lit image of the SAR-thick injector forced ($f_F = 3.04$ kHz) flows at $P_r = 1.05$ shown in Figure 5.25, a time-averaged image and an image of the superposed conjugate proper orthogonal modes (POMs). The averaged image consisted of 500 frames sampled at 25 kHz. The corresponding plots are the cross-power spectral density (CPSD) magnitude of the time-dependent amplitude cofficients of the conjugate modes. The low frequency peaks associated with the periodic flow structures were not identical to f_F. For the purpose of comparison, the baseline spectra are shown with dots. (.........Baseline, ———Forced) 181

5.50 A back-lit image of the SAR-thick injector forced ($f_F = 3.08$ kHz) flows at $P_r = 1.05$ shown in Figure 5.25, a time-averaged image and an image of the superposed conjugate proper orthogonal modes (POMs). The averaged image consisted of 500 frames sampled at 25 kHz. The corresponding plots are the cross-power spectral density (CPSD) magnitude of the time-dependent amplitude cofficients of the conjugate modes. The peak frequencies of the periodic flow structures were identical to f_F. For the purpose of comparison, the baseline spectra are shown with dots. (.........Baseline, ———Forced) 182

5.51 A back-lit image of the SAR-thick injector forced ($f_F = 3.11$ kHz) flows at $P_r = 1.05$ shown in Figure 5.25, a time-averaged image and an image of the superposed conjugate proper orthogonal modes (POMs). The averaged image consisted of 500 frames sampled at 25 kHz. The corresponding plots are the cross-power spectral density (CPSD) magnitude of the time-dependent amplitude cofficients of the conjugate modes. The peak frequencies of the periodic flow structures were identical to f_F. For the purpose of comparison, the baseline spectra are shown with dots. (.........Baseline, ———Forced) 183

5.52 A back-lit image of the SAR-thick injector forced ($f_F = 3.05$ kHz) flows at $P_r = 1.05$ shown in Figure 5.25, a time-averaged image and an image of the superposed conjugate proper orthogonal modes (POMs). The averaged image consisted of 500 frames sampled at 25 kHz. The corresponding plots are the cross-power spectral density (CPSD) magnitude of the time-dependent amplitude cofficients of the conjugate modes. The peak frequencies of the periodic flow structures were identical to f_F. For the purpose of comparison, the baseline spectra are shown with dots. (.........Baseline, ———Forced) 184

5.53 A back-lit image of the SAR-thick injector forced ($f_F = 3.12$ kHz) flows at $P_r = 1.05$ shown in Figure 5.25, a time-averaged image and an image of the superposed conjugate proper orthogonal modes (POMs). The averaged image consisted of 500 frames sampled at 25 kHz. The corresponding plots are the cross-power spectral density (CPSD) magnitude of the time-dependent amplitude coefficients of the conjugate modes. The peak frequencies of the periodic flow structures were identical to f_F. For the purpose of comparison, the baseline spectra are shown with dots. (.........Baseline, ———Forced) 185

A.1 Experimental facility piping and instrumentation diagram. 194

A.2 Expanded view of section A in Figure A.1. 195

A.3 Expanded view of section B in Figure A.1. 196

A.4 Expanded view of section C in Figure A.1. 197

A.5 Expanded view of section D in Figure A.1. 198

List of Tables

1.1 Summary of flow conditions used in the literature 21

1.2 Summary of injector exit dimensions used in the literature 22

3.1 Comparison of measured values of burning rate constant K for various fuel droplets in the absence of acoustic excitation. Comparisons with available established values for K are also given. 47

3.2 Acoustic conditions of various fuels at extinction. The corresponding sound pressure levels in decibels (dB) and rough estimates of the strain rates are also shown. 47

4.1 Injector exit dimensions (mm) 72

5.1 Values of the constants in Equation 5.4 obtained from non-linear regression of the L_B/D_1 data. 97

C.1 Summary table of flow conditions for the LAR-thin injector. 225

C.2 Summary table of flow conditions for the SAR-thick injector. 226

C.3 Summary table of acoustic forcing conditions and dark-core length measurements for the LAR-thin injector. 227

C.4 Summary table of acoustic forcing conditions and dark-core length measurements for the SAR-thick injector. 227

NOMENCLATURE

Symbols

$\mathbf{A}$	matrix of image pixel intensities
A	area
a	vector of time-dependent amplitude coefficients
c	speed of sound
D	injector diameter, jet diameter
d	droplet diameter
f	acoustic frequency
F_R	acoustic radiation force
g_a	acoustic acceleration
g_o	gravitational acceleration
I	acoustic intensity
J	outer to inner jet momentum flux ratio, $\rho_o U_o^2/\rho_i U_i^2$
K	burning rate constant
L	distance between speakers
M	momentum flux
$\dot{m}$	mass flow rate
P	pressure
p'	pressure perturbation
P_r	reduced pressure, P/P_{cr}
Q	volume flow rate
R	outer to inner jet velocity ratio, U_o/U_i
Re	Reynolds number
r	droplet radius
S	outer to inner jet density ratio, ρ_o/ρ_i

T	temperature
t	time, inner jet injector post thickness
U	flow velocity
u'	velocity perturbation
V	volume
x	displacement of droplet relative to PN
x'	displacement of PN relative to droplet
z	impedance

Greek Symbols

α	density difference correction factor
δX	uncertainty in quantity X
ϵ	strain rate
θ	flame deflection angle
λ	acoustic wavelength
ϕ	proper orthogonal mode
ρ	density
σ	standard deviation
ψ	streamfunction

Subscripts

1	inner jet injector inside diameter
2	inner jet injector outside diameter
3	outer jet injector inside diameter
4	outer jet injector outside diameter
a	acoustic
c	chamber
cr	critical
eqvs	equivalent volume of a sphere
exp	experimental
f	flame
i	inner jet
o	outer jet
p	hot combustion products
th	theoretical
∞	ambient flow, bulk flow

CHAPTER 1

Introduction

The present experimental studies focus on condensed phase combustion processes and non-reactive shear injection flows in the presence of transverse acoustic excitation. Combustion in the presence of and with coupling to acoustic instabilities is widely known to occur in airbreathing as well as rocket engines, particularly in the latter, where large scale combustion instabilities in liquid rocket engines (LREs) can lead to strong vehicle vibrations, as occurs in the "pogo" instability, or in catastrophic failure. The ability to understand the implications of combustion coupled acoustic instabilities on burning rates and other combustion processes such as localized extinction is critical for the operation and design of current and future engine systems. As a means of contributing to this understanding, the experimental studies presented consists of two independent investigations. The first set of studies, conducted in the UCLA Energy and Propulsion Research Laboratory, explores the combustion of alternative liquid fuel droplets while exposed to acoustic excitation in a cylindrical acoustic waveguide. The second set of studies, conducted in an experimental facility at the Air Force Research Laboratory in Edwards AFB, CA, explores cryogenic, non-reactive shear-coaxial jets in a high pressure chamber with and without the presence of acoustic excitation.

1.1 Fuel Droplet Combustion

1.1.1 Alternative Fuels

A rapid increase in worldwide demand for fossil fuels and fluctuating prices of crude oil has enhanced the search for alternative sources of fuels for transportation systems and power generation. Associated with this increase in the consumption of fossil fuels is the alarming rise of environmentally harmful emissions, including carbon dioxide and nitrogen oxides. This being the case, however, the near term feasible solutions for replacement fuels mainly involve hydrocarbons [1].

Among the different types of fuels under consideration for automotive applications, alcohols and biodiesel are receiving the most attention. Alcohol fuels such as methanol and ethanol exhibit favorable combustion characteristics such as clean burning and higher octane performance over gasoline [2]. However, realization of these features of pure alcohols require significant design changes to the present engines to attain higher compression ratio than that used for gasoline. Moreover, the mass production and distribution costs do not make pure alcohols the ideal substitutes for gasoline. Blends of gasoline and alcohol fuels, on the other hand, require only minimal to none engine modifications and less production costs while delivering some of the beneficial features of alcohol fuels. At the present, many gas stations around the world provide a blend of gasoline and 10% ethanol (E10), which is certified to be used in gasoline engines without any modification, whereas a blend of gasoline and 85% ethanol (E85) is only certified to be used in flexible fuel vehicles (FFVs) with engines specifically designed for this fuel.

As for possible aviation fuel replacements, liquid synthetic fuels derived from natural gas or coal gasification via the Fischer-Tropsch (FT) [3] process show the most promise. In 2006, flight tests using a 50-50% by volume blend of JP-8 and FT fuel in a B-52H aircraft were conducted at Edwards Air Force Base, and later the Air Force certified the blend fuel to be used in this aircraft [4, 5]. Similar flight tests have been conducted using the C-17 Globemaster III, the KC-135 tanker, and others, until the entire Air Force fleet is certified for this alternative fuel blend.

With the potential to use such alternative fuels comes the need to understand, from a fundamental perspective, the performance of such fuels in a typical engine environment. One arena that is not particulary understood is the performance and response of these fuels when the combustion environment is itself acoustically resonant. The differing reactive, diffusive, and convective time scales associated with combustion processes when one changes from one fuel to another could alter the coupling to acoustic resonances and ultimately alter the combustion performance of the device. Thus, it is of interest to examine at a fundamental level the differing behaviors of various fuels when combustion is coupled to acoustic instabilities.

1.1.2 Related Works in Droplet Combustion

Spray injection systems commonly employed in internal combustion and gas turbine engines involve a dilute spray of fuel droplets with the combustion of individual droplets that make up the spray [6, 7]. For non-dilute sprays, on the other hand, the flame structures can surround the entire spray field. Despite the complexity that is present in an actual fuel spray combustion where interaction between neigboring burning droplets has a significant impact on the combustion characteristic of the ensemble, studying the fundamental character of a single isolated burning fuel droplet is important to the whole understanding of spray combustion. Fuel droplet combustion is a heterogeneous and reactive process whereby the droplet evaporates and acts as a source of fuel vapor that reacts with an oxidizer, typically air, to form a diffusion flame front surrounding the droplet. The fuel droplet is also commonly used as a fundamental model for condensed-phase combustion processes in general [8].

For a quasi-steady burning spherical droplet in a quiescent oxidizing environment, classical studies have shown that the variation in the diameter of the droplet d varies linearly with time t following the d^2-Law [9, 10]:

$$d^2(t) = d^2(t = 0) - Kt \tag{1.1}$$

The d^2-Law has been shown to be applicable to essentially spherical burning droplets in a microgravity environment [8], and approximately valid for burning droplets in a gravitational environment, even under non-quiescent conditions [11, 12].

In a microgravity environment, the burning droplet maintains a spherical geometry, thus enabling a direct application of the d^2-Law to obtain the burning rate constant K. Such an environment also allows the study of fundamental droplet combustion phenomena, which would otherwise be difficult, if at all possible, to study in a normal gravity environment, where buoyant motions complicate the flowfield around the droplet [8].

In normal gravity conditions, a suspended burning droplet can no longer maintain a spherical geometry due to gravitational and surface tension forces. In order to determine K using Equation 1.1, the non-spherical droplet diameter is determined by equating the effective volume of the actual droplet to the volume of a spherical droplet of diameter d_{eqvs} as done by Struk *et. al* [13].

1.1.3 Effects of Acoustics on Droplet Combustion

Several experimental studies have shown that there can be an increase in the burning rate constant of droplets under the influence of an external acoustical field. This effect is mainly thought to occur as a result of steepening reactant species concentration and temperature gradients, which in turn, lead to increased mass and heat transfer rates at the droplet surface [11, 14, 15]. Saito *et. al* [14, 15], examine the effects of acoustic waves on single evaporating and burning kerosene droplets in 1g, observing that when the fuel droplet is situated at or near a pressure node (velocity antinode), there can be a two to three-fold increase in evaporative or burning rate constants, while if the droplet is located at a pressure antinode, there is no change in the evaporation and combustion rates. Other experiments have involved acoustical excitation of burning droplets in microgravity, where the absence of natural convection arising from buoyancy force allows isolation of the influence of acoustic radiation forces. Okai *et. al* [16], investigate the effect of the amplitude and frequency on the disturbance of n-octane single droplets and droplet pairs. At a forcing frequency of 2000 Hz and under conditions where the droplets lie at the pressure node of the standing acoustic wave, the burning rate constants increase monotonically with increasing acoustic intensity until the flame extinguishes.

Microgravity droplet burning experiments of Tanabe *et al.* [17, 18] present further evidence of the enhancing effect of acoustics on burning rates. Their studies involve a burning n-decane droplet situated at a pressure node, or between a pressure node and antinode of a standing acoustic wave. They observe significant increases in the burning rate constant as the amplitude of the velocity perturbation is increased, resulting in burning rate constants that are almost double that for a quiescent or an unforced value. In addition, these researchers observe characteristic flame distortions whereby the flame is consistently deflected toward the pressure node when the droplet is situated between a node and antinode. They interpret burning rate increases and flame deflections in terms of the phenonmenon of acoustic streaming, a term which they used to describe the time-averaged motion that is induced in a fluid flow dominated by its fluctuating components [19], such as one which occurs in the presence of standing acoustic waves. Tanabe *et al.* explain the cause of flame deflection in terms of the magnitude and direction of an acoustic radiation force F_R, a body force, acting on the sphere of hot gases surrounding the burning droplet. They propose an expression for this force as

$$F_R = \alpha(\rho_p - \rho_o)V\frac{\partial\overline{u'^2}}{\partial x} \tag{1.2}$$

where ρ_p is the density of the hot combustion products situated about the diffusion flame and the droplet, ρ_o is the density of ambient air surrounding the flame, V is the volume of the sphere containing the hot products, x is the displacement of the droplet from the pressure node or antinode location, and $\overline{u'^2}$ is the mean of the square of the amplitude of the local perturbation velocity, u', inside the waveguide. The coefficient α takes the form

$$\alpha \equiv \frac{3\rho_o}{2(2\rho_p + \rho_o)} \tag{1.3}$$

The acoustic radiation force in Equation 1.2 has the same form as the net buoyant force acting on an object of density ρ_p and volume V submerged in a fluid of density ρ_o. This led Tanabe *et al.* to propose that the influence of the acoustic radiation force on the droplet combustion and flame deformation is similar to that of a gravitational force. The observed flame deflections are consistent with this theory when the droplet is situated away from a pressure node or antinode. They even state that when the droplet is situated precisely at the pressure node, there is no droplet deflection, but there is limited evidence for this.

Recent studies at UCLA and at NASA Glenn Research Center by Dattarajan *et al.* [20, 21] have focused on methanol droplet combustion characteristics during exposure to external acoustical perturbations in both normal gravity and microgravity. The waveguide used in these experiments consisted of a cylindrical tube bounded at one end by a loudspeaker and at the other end by a reflector plate. Emphasis is placed on excitation conditions in which the droplet is situated at or near a velocity antinode (pressure node), where the droplet experiences the greatest effects of velocity perturbations, or at a velocity node (pressure antinode), where the droplet is exposed to minimal velocity fluctuations. In microgravity, for sound pressure levels exceeding about 135 dB, droplet burning rates are seen to increase by over 75% and 200% for droplets situated near pressure antinode and pressure node locations, respectively. In contrast, in normal gravity, acoustic excitation of droplets situated near abpressure node produce only very moderate increases in burning rate (about 11-15% higher during 138 dB forcing than for non-acoustically excited, burning droplets) and produce no significant change in burning rate near a pressure antinode for pressure perturbations in the same range of sound pressure level. Observed flame deformation for droplets situated to one side or the other of pressure nodes or antinodes in microgravity are generally consistent with the notion of acoustic radiation forces per Equation 1.2, yet both velocity and pressure perturbations are seen to affect flame behavior, even when the droplet appears to be situated precisely at or extremely close to node or antinode locations. While displacements of the droplet with respect to node or antinode locations are observed to have a measurable effect on droplet burning rates, acoustic accelerations associated with such displacements, as an analogy to gravitational acceleration, do not completely explain the significant increases in burning rate resulting from the excitation in microgravity.

Further experimental investigations by Rodriguez [**?**] using the same apparatus from the Dattarajan *et al.* studies, explore the combustion behavior of methanol, ethanol, pure FT, and JP-8/FT blend fuel droplet combustion in the presence of acoustic disturbances in normal gravity. The droplet is placed both near and at successively increasing displacements away from a pressure node or antinode. This is accomplished by moving the speaker and reflector to the left or right within the waveguide, maintaining the distance between the two. A general trend of increasing burning rate constants is observed when the droplet is further away from the node or antinode, with increases of up to 20% in the burning rate constant of the alcohol fuels. Extinction studies of the burning fuel droplets are also conducted by exposing them to increasing acoustic intensities. At sufficiently high forcing amplitudes, flame extinction (blow-out) is observed, and the extinction strain rates for the different fuels are roughly estimated based on velocity perturbation amplitudes.

Other several studies of the flame extinction phenomena associated with burning droplets use porous spheres wetted with fuel [22, 23]. In these studies, the point of extinction is marked by the condition in which the leading half of the sphere is no longer inside the flame envelope, but where the flame is stabilized in the wake region of the sphere. The extinction velocities show an increase with increasing sphere diameters. For droplet sizes encountered in industrial fuel sprays, Agnoston *et al.* [23] predict an extinction velocity of about 0.5 m/s.

1.2 Shear-Coaxial Jets

Shear-coaxial injectors have proven to be one of the most effective and simple means of delivering propellants in combustion devices such as in liquid rocket engines (LREs). Their application in LREs in the United States was seen as early as the development of the J-2 engine for the Saturn I and Saturn V launch vehicles, and as recently as the space shuttle main engine (SSME), both of which utilized liquid hydrogen (LH_2) and liquid oxygen (LOX) as propellants. While LREs are highly efficient in terms of specific impulse or thrust per weight flow rate of propellants, and are the most commonly used type of rocket engine today, there are nevertheless technical challenges associated with them, namely combustion instabilities.

Combustion instability is a phenomenon that can destroy an LRE in less than a second. It is primarily a result of feedback interactions between unsteady combustion rates and pressure fluctuations from acoustic modes in the combustion chamber (Harrje and Reardon [24], Schadow *et al.* [25]). This feedback cycle may be described as one where pressure fluctuations in the combustion chamber enhance injector flow perturbations, which in turn give rise to unsteady combustion heat release rates. The by-product of unsteady heat production is density fluctuation, or equivalently pressure and velocity fluctuation, which can become so large as to destroy the engine. Athough LOX/hydrocarbon LREs are most susceptible to combustion instabilities, LOX/LH_2

engines are also known to experience such problems.

Since injector flows are directly involved in the flow processes that take place inside combustors, it is crucial to understand how they contribute to, as well as how they are affected by, these unsteady physical mechanisms that lead to combustion instabilities. However, a successful understanding at a fundamental level of these interactions between injector flows and chamber phenomena can be aided by first isolating the fluid dynamics aspect from the reactive flow processes, and studying the coupling of non-reactive coaxial injector flow instabilities with external pressure perturbations.

1.2.1 Near-Field Mixing of Same and Different Density Shear-Coaxial Jets

Shear-coaxial jets consist of a circular core or inner jet and an annular or outer jet. In the near-field region, where the potential cores of both the inner and outer jets exist, two shear-layers exist: an inner shear layer between the inner and outer jets, and an outer shear layer between the outer jet and the ambient fluid. As such, the mixing of the coaxial jets primarily depends on the development of the inner shear layer, which is governed by their velocity ratio, for same density jets, or their momentum flux ratio, for different density jets, as well as their exit area ratio and inner jet post thickness. However, the dynamics of the inner shear layer is also influenced by the development and dynamics of the outer shear layer.

Several extensive studies explore the effect of outer to inner jet velocity ratio, $R \equiv U_o/U_i$ (Chigier and Beer [26], Forstall and Shapiro [27], Ko and Kwan [28], Wicker and Eator [29], Villermaux *et al.* [30]) and outer to inner nozzle exit area ratio, $AR \equiv A_o/A_i$, (Champagne and Wygnanski [31], Rehab *et al.* [32]) on the potential core length of the inner jet and the near-field flow structure of isodensity coaxial jets. Chigier and Beer [26] present one of the pioneering experimental works on uniform density coaxial jets by making detailed velocity and static pressure measurements of fully developed turbulent coaxial air jets issuing into stationary air. A summary of the exit configuration of the injection elements used in their and other works is given in Table 1.1. They investigate R values ranging from infinite to 0.024 in order to span the limiting cases of an annular jet to an axisymmetric single jet, respectively. For $R = 2.35$, they measure an inner potential core length of about half the inner jet nozzle diameter, D_1, and report that the outer jet completely absorbs the inner jet by $3D_1$, where reverse flow occurs. This reverse flow occurs due to the lack of sufficient entrainment fluid with increasing outer jet mass flow. In the other extreme, for $R = 0.085$, they show that inner jet completely absorbs the outer jet within one hydraulic diameter of the annular nozzle.

Unlike the fully developed turbulent flow exit velocity profile in the Chigier and Beer [26] study, a majority of the studies done on shear-coaxial jets has been on top-hat exit velocity profiles, which are attained using contraction nozzles. Champagne and Wygnanski [31] present one of such studies where they investigate the effect of varying both velocity ratio, R $(0 < R < 10)$, and area ratio, AR $(1.28, 2.94)$, on coaxial air jets. Hot-wire anemometer measurements reveal that the outer potential core length is independent of R as confirmed by Au and Ko [33], and is about 8 times the annular gap width. However, the outer potential core length is shown to increase with AR. The inner jet potential core length, on the other hand, is strongly dependent on both R and AR. For $0 < R < 1$, the inner potential core length is longer than that for a single jet since the presence of the outer jet creates a decreased shear between the inner jet and the surrounding. For $R > 1$, the inner core length decreases with R. The dependence of the core length with AR is due to the fact that the pressure gradient, which exists between the inner jet flow and the ambient fluid, is smaller with thicker outer jets, thereby, inducing less convergence of the jets towards the centerline. Champagne and Wygnanski [31] conclude that for a fixed AR, R should be greater than one for enhanced mixing between the inner and outer jets.

Further studies on the near-field region of coaxial air jets by Ko and Kwan [28] reveal that in the initial merging zone, the region upstream of the end of the outer jet potetial core, there is good agreement between the outer jet mean velocity profile and that of a single jet. Their study examines three velocity ratios, $R = 0.37, 0.5, 0.7$, where they made detailed velocity measurements using a constant temperature hot-wire anemometer and pressure measurements using a microphone. The agreement between their velocity profiles reaffirms the notion that the outer jet behaves similar to a single jet. The inner jet behaves more like a single jet discharging into a coflowing ambient fluid (equivalent to an infinite diameter outer jet). The authors, however, do not make a clear distinction between a coflowing ambient fluid and a finite diameter outer jet flow. The existence of an "outer shear layer" in the latter plays a key role in the mixing and stability characteristics of the inner jet (Sevilla *et al.* [34]). Ko and Kwan [28] also indicate the presence of vortical or coherent flow structures by identifying peaks in the overall pressure profile measured in the inner and outer shear layers. The dominance of the vortices in the inner and outer shear layers are found to depend with R, whereby, the vortices in the outer shear layer become more dominant with increasing R.

While these observations hold for lower outer to inner jet velocity ratios, $R < 1$, studies in the velocity ratio regime $1 < R < 6.7$ (Ko and Au [35], Au and Ko [33]) also reveal the presence of coherent structures in inner and outer shear layers. The coherent structures in the outer shear layer form outward rolling vortices similar to those for the $R < 1$ flows, resembling the same single jet behavior independent of R. The nature of the vortex structures that form in the inner shear layer is dependent on R. For $R > 2$, shear layer vortices, which the authors label as "coflowing-wake-vortices", form with a mean sense of rotation opposite to that of the outer shear layer dominate the flow region. Dahm *et al.* [36] identify these vortices as shear-layer type of instabilities, which occur when a large velocity jump across the interface of the two jets exists. As R approaches one ($R < 1.25$), negligible or no velocity jump across the interface exists, resulting in more dominant "alternate-shedding" or wake-like vortices. These give clear evidence that velocity ratio has a major impact on the dynamics and interaction of vortex structures in the two shear layers, thus affecting the potential core length, or equivalently the extent of mixing of the two jets.

Rehab *et al.* [32, 37] and Villermaux *et al.* [30] conducted similar investigations using same density coaxial water jets. They show that increasing the outer to inner nozzle diameter ratio results in a longer outer potental core, delaying the pinching of the inner jet after the outer potential core ends. Although the inverse proportionality between the inner potential core length to inner jet diameter ratio, L_p/D_1, and R is preserved regardless of the diameter ratio, the constant of proportionality, however, is altered (Rehab *et al.* [32, 37]). In addition, Rehab *et al.* [32] show that a top-hat exit velocity profile results in a longer inner potential core length than a fully developed turbulent flow velocity profile. This is the case since the jet momentum in the latter is less and velocity gradient exists across the entire cross-section of the jet rather than just the edges as in a top-hat profile.

A vast majority of shear-coaxial jet studies have a uniform density flow field with an outer to inner jet density ratio of one ($S = 1$). When that no longer holds, the effect of S on the coaxial jet mixing characteristics comes into play in addition to R. Thus, the effect of both density and velocity ratios may be captured in the outer to inner jet momentum flux ratio, $J \equiv SR^2$. The work by Gladnick *et al.* [38], which studies the near-field evolution of the velocity field of an inner CFC-12 jet with an outer air jet, deals with different density coaxial jets. However, it does not discuss the effects of varying S on the shear layer growth and consequently on the potential core length of the inner jet.

Favre-Marinet *et al.* [39, 40] make a systematic exploration of varying S for low-speed, high-density inner jets and high-speed, low-density outer jets using air-air, He-air, air-SF_6, and He-SF_6, where air and He are used as the outer jets in each coaxial jet pair.

For isodensity air-air jets, the inner potential core length varies as $J^{-1/2}$ or equivalently as R^{-1}. This is in agreement with the R^{-1} dependence for coaxial water jets (Rehab *et al.* [32, 37]). Reducing the density ratio to $S \approx 0.2$ using air-SF_6 jets results in a shorter inner potential core length for a given J. This may be attributed to the increased shear layer growth rate due to the enhanced entrainment velocity of the inner jet by the outer jet. Favre-Marinet *et al.* [39] propose the relation $V_E/U_i \propto (J^{1/2} - S^{1/2})/(1 + S^{1/2})$ for the normalized entrainment velocity based on the estimation for the convection velocity of the vortical structures in a two-dimensional mixing layer (Dimotakis [41]). As this relation shows, lower density ratios translate into increased shear layer growth rates, and hence, shorter core length. However, they find this is only valid up to density ratios of about an order of magnitude below isodensity cases. Larger density differences, such as with He-SF_6 ($S = 0.028$), the potential core length is slightly increased relative to the isodensity case of the same J. Although Favre-Marinet *et al.* [39, 40] do not put forth an explanation as to why this happens, this phenomenon might be attributed to the considerable reduction in the momentum diffusivity of the inner fluid leading to a relatively retarded growth of the inner shear layer.

Other studies involving different density or two-phase coaxial jets include those by Eroglu *et al.* [42], Lasheras *et al.* [43], Davis and Chehroudi [44], Leyva *et al.* [45], and Rodriguez [46]. Lasheras *et al.* [43] examine the break-up and atomization of an inner water jet by a high-speed outer air jet. They found that for high Weber number and high Reynolds number flows, J is the dominant parameter. The liquid intact length, break-up length or cone length, defined as the distance from the exit to where the liquid fraction is close to 1 along the axis, is found to vary as $J^{-1/2}$. This is again in agreement with the dependence of isodensity coaxial air and coaxial water jets (Rehab *et al.* [32, 37], Favre-Marinet *et al.* [39]).

1.2.2 Stability Consideration of Coaxial Jets

The influence of the coherent shear layer flow structures on the overall dynamics of the flow field calls for an understanding of the factors leading to their formation. Detailed studies on the development and growth of natural instabilities in a single circular jet (Cohen and Wygnanski [47]) or a single circular jet with coflow (Michalke and Hermann [48]) reveal two of the most significant natural modes of instability: the axisymmetric mode and the first azimuthal or helical mode. These modes have comparable amplification rates over most of the core region downstream of the exit, with the helical mode eventually dominating the flow field farther downstream. As Ko and Kwan [28] show, the development of the outer shear layer of a coaxial jet behaves as the shear layer of a single jet, while the development of the inner shear layer behaves as that of a single jet issuing into an external coflow. Thus, the axisymmetric and helical modes of instability, along with natural as well as externally imposed flow conditions such as pressure or velocity perturbations that can affect their development, may be used to assess the stability of the coaxial jet.

The theoretical and experimental investigation of Cohen and Wygnanski [47] on the evolution of instabilities in a single, axisymmetric jet shows that very close to the nozzle exit, where the jet diameter to the shear layer momentum thickness ratio is very large ($D/\theta \gg 1$), the axisymmetric and all azimuthal modes of instability have the same amplification rates. As the shear layer grows, all azimuthal modes except the first (helical) mode become negligible within two jet diameters from the exit, while the amplification rate of the axisymmetric mode dominates at high frequencies and that of the helical mode at low frequencies. Near the end of the potential core and beyond, the helical mode dominates at all frequencies, and is shown to govern the evolution of the fully developed axisymmetric jet. External excitation of the axisymmetric and helical mode also reveals that the amplitude of the excited mode can be an order of magnitude larger than the unexcited mode.

The linear, inviscid instability analysis of a circular jet issuing into a coflowing ambient fluid of the same density by Michalke and Hermann [48] examines the effect of the presence of a coflow on the natural instabilities of a single jet. For zero coflow velocity, they also find that the helical mode is more unstable than the axisymmetric mode at large enough downstream location from the exit. A finite coflow velocity shows a stabilizing effect on the jet since the spatial growth rate decreases at all frequencies. Increasing the coflow velocity increases the region of unstable frequencies, and results in a shift of the peak of the spatial growth rates to higher frequencies.

In lieu of a coflow with an infinite cross-stream extent, a coaxial jet configuration has a finite diameter coflow, so that outer to inner jet diameter ratio comes into play in determining the stability characteristics of the flow (Sevilla *et al.* [34], Perrault-Joncas and Maslowe [49]). Sevilla *et al.* [34] investigate the effect of outer to inner jet diameter ratio as well as S on the convective and absolute instability of coaxial jets with $S \geq 1$, $R \leq 1$. They consider how the variation in these parameters factors into the transition from a convectively unstable flow to an absolutely unstable flow. When $R = 1$, increasing the diameter ratio, equivalent to pushing the outer shear layer farther out from the jets' interface, reduces the critical outer to inner jet density ratio, S, at which transition to an absolutely unstable flow occurs, thereby inhibiting absolute instability. In addition, for a diameter ratio larger than 1.03, unlike the axisymmetric mode, the helical mode stays in the convectively unstable regime for all $S > 1$. For $R < 1$, the transition from a convectively to absolutely unstable flow may be due to instabilities in the inner or outer shear layers. They show that the transition to absolutely unstable flow due to inner shear layer instabilities is only possible for very small outer jet velocities (approximately $R < 0.3$), and the transition due to the outer shear layer instability occurs at larger R for a given S and diameter ratio. For a given R, increasing the diameter ratio again reduces the range of S for which the flow is absolutely unstable.

The effect of inner nozzle wall thickness is discussed in the linear instability analysis of isodensity coaxial jets by Talamelli and Gavarini [50]. Their analysis shows that the absolutely unstable flow region may be enlarged by reducing the shear-layer thickness at the jet exit for a given R. In addition, the range of R for which an absolute instability occurs decreases with increasing shear-layer thickness. As a thicker wall delays the development of a shear layer, it may be the case that thick-walled nozzles are more likely to promote absolutely unstable flows.

1.2.3 Transverse Acoustic Excitation of Coaxial Jets

The earliest investigations of the effect of ambient pressure oscillations on free jets includes those by Miesse [51], Newman [52], and Heidmann and Groeneweg [53]. Miesse's experimental study examines how transverse ambient pressure oscillations, generated from a sound source directed perpendicular to the flow axis, alters the disintegration and dispersion behavior of a liquid jet. The results show that acoustic forcing decreases the length of liquid stream, and affected the dispersion pattern in a way so that increasing the frequency of pressure oscillation results in decreased dispersion. Transverse waves also prove to aid in the mixing of parallel streams.

Newman [52] explores how the jet break-up is affected under pressure antinode and velocity antinode conditions in a transverse acoustic field. His results show that both pressure and velocity oscillations are equally efffective in promoting jet break-up although they have entirely different mechanisms. A pressure antinode condition induces periodic variation in the flow rate, which in turn, promotes break-up by inducing cyclic thickenings in the jet column. A velocity antinode condition, on the other hand, produces lateral displacement of the jet column due to tranverse motion of the ambient fluid, thereby, again producing surface irregularities on the jet. His results, however, show pressure oscillations are more effective than velocity oscillations at higher chamber pressure, and both appear less effective in breaking up the jet than at lower chamber pressure.

A majority of the studies done on acoustically excited coaxial jets involve in-flow, axial or longitudinal forcing, where the acoustic source is placed upstream of the nozzle exit. Wicker and Eaton [29] study the effect of the outer jet on the near-field dynamics of the inner jet with axial excitation of each jet independently for $0.55 < R < 1.45$. Axial forcing of the outer jet show formation of periodic axisymmetric vortex rings at the forcing frequency. For $R > 1$, vortex structures in the outer shear layer completely controlled the inner flow within $4D_1$. Forcing the inner jet flow alone does not have a significant effect on the development of structures in the outer shear layer. However, both forcing types result in a reduction of the inner potential core.

Balarac *et al.* [54] analyze numerically the mixing behavior of isodensity coaxial jets when a pure axisymmetric forcing is applied to the outer shear layer. Their analysis shows that strongly axisymmetric vortex rings in the outer shear layer undergo rapid amplification inducing a similar amplification of the inner shear layer rings. Streamwise vortices also appear earlier compared to the natural case. Moreover, this forcing condition reduces both the inner and outer potential core lengths.

In the interest of gaining a better understanding of how acoustic instabilities play a role in combustion instabilities that occur in liquid rocket engine combustion chambers Richecoeur *et al.* [55] investigate the interaction of transverse acoustic waves with multiple shear-coaxial injector cold flows. The nonreactive flow experimental study uses liquid oxygen inner jets and gaseous nitrogen outer jets flowing out of five shear-coaxial injectors in a 3 MPa pressure chamber. Forcing at the first transverse mode of the chamber, at a frequency of 585 Hz, produces measurably shorter jets, whose dark-core regions are as much as 17% shorter than that of the unforced jet. The sinusoidal undulation of the jet due to velocity fluctuation aids in breaking up the jet into filaments, which enhances primary atomization and increases the vaporization rate of the inner oxygen jet.

The dependence of flame-acoustic interactions on density ratio ($1 < S^{-1} < 16$) and velocity ratio ($3.02 < R < 5.27$) is discussed by Ghosh *et al.* [56], and in more detail by Ghosh [57], where they use a planar shear-coaxial injector with an inner gaseous oxygen jet and two outer gaseous hydrogen jets to produce two diffusion flames fronts. Acoustic drivers produce transverse acoustic waves in a chamber at atmospheric pressure. An acoustic frequency of 1.15 kHz used in these experiments is comparable to the high frequency or screeching instabilities that are known to be the most destructive form of instability. Reducing the density gradient (as $S^{-1} \rightarrow 1$) shows a greater resistance to flame-acoustic coupling. This is attributed to the reduced effect of the baroclinic torque due to the density gradient across the flame front and the imposed acoustic pressure perturbation. For the narrow range of R considered in this study, negligible changes in the flame-acoustic interactions are observed.

Earlier studies in the present AFRL experimental facility by Davis [58] and Rodriguez [46] study shear-coaxial nitrogen jets in a high pressure, cryogenic flow facility. With chamber pressures spanning subcritical to supercritical pressures, these studies investigate cryogenic inner nitrogen jets with less dense outer nitrogen jets with and without the presence of a transverse acoustic field. They make dark-core length measurements of the denser inner jet flow for a range of J values. Davis [58] uses an injector with a large outer to inner jet area ratio, and a large inner post thickness to diameter ratio (see Table [**?**]). He reports shorter dark-core length measurements at nearcritical and supercritical pressures than at subcritical chamber pressure. This is in agreement with reports by Favre-Marinet *et al.* [39] in that at the elevated chamber pressures, S is on the order of 0.1 or larger. The normalized dark-core lengths under subcritical pressure are found to vary as $J^{-0.2}$, while they vary as $J^{-0.5}$ under near- and supercritical pressures. The mean dark-core length also shortens with acoustic forcing.

Rodriguez [46] continues the study with the same injector as Davis [58] and another injector with a small outer to inner jet area ratio and a small post thickness to diameter ratio. Tranverse acoustic forcing using two acoustic sources enabled exposure of the coaxial jet flow to various portions of a standing acoustic field including pressure antinode and pressure node conditions. During acoustic forcing, both injector types show maximum reduction in their dark-core lengths relative to the baseline cases at lower momentum flux ratios ($1 < J < 5$) in all chamber pressure regimes. However, Rodriguez [46] reports that the large area ratio injector flow attains the largest reduction of dark-core length at or near a pressure node (velocity antinode) condition, while the small area ratio injector flow does so at or near a pressure antinode condition.

1.2.4 Objectives

The present work continues the series of experimental studies done in the same facility, which have examined the behavior of shear-coaxial N_2 jets at elevated chamber pressures spanning subcritical to supercritcal pressure with and without the presence of a transverse acoustic field. As stated earlier, Davis [58], Davis and Chehroudi [44], Leyva *et al.* [45], and part of the study by Rodriguez [46] uses a shear-coaxial injector with a large outer to inner jet area ratio, $AR \equiv A_o/A_i$ (see Table [**?**]), and a large inner jet injector post thickness to inside diameter ratio, t/D_1. As stated earlier, the study by Rodriguez [46] also uses an injector with a small AR and small t/D_1. The magnitude of AR is one of the factors that dictate the interaction between the outer and inner shear layers; that is, larger AR delays their interaction, therefore, limiting the influence of outer shear layer structures on the development of the inner shear layer. Moreover, the flow recirculation region that is established for a configuration with a large t/D_1 creates a delayed onset and growth of the inner shear layer region. In consideration of such geometric influences, the present study investigates two other injector exit configurations: a large AR with a small t/D_1 and a small AR with a large t/D_1. It also employs different methods of analyzing high-speed image data to examine differences among various flow conditions.

Therefore, the main objectives of this study are:

1. to measure baseline flow dark-core lengths of the inner jets from high-speed back-lit images in order to characterize the mixing behavior using the two injectors under subcritical (reduced pressure, $P_r = 0.44$) and nearcritical ($P_r = 1.05$) chamber pressure conditions for a range of J values. Here, the reduced pressure is defined as the ratio of the chamber pressure to the critical pressure of nitrogen ($P_r \equiv P_c/P_{cr}$).
2. to identify the dependence of baseline flow dark-core lengths on J, and injector geometric parameters, t/D_1 and AR.
3. to evaluate the flow response to pressure antinode and pressure node acoustic forcing conditions by comparing the forced flow dark-core lengths to their baseline counterparts.
4. to apply a proper orthogonal decomposition (POD) analysis to extract coherent, periodic flow structures captured in the high-speed images. This will aid in characterizing the spatial and temporal behavior of the dominant flow structures in the inner shear layer of the baseline and acoustically forced flows. Using this approach, a better understanding may be gained of the critical differences and evolution of flow instability characteristics brought about as a result of simple design alterations in the shear-coaxial injector.

Table 1.1: Summary of flow conditions used in the literature

Ref.	Author(s)	Outer-Inner Jet	R or J	Exit Flow*
[26]	Chigier & Beer	Air-Air	$0.024 < R < \infty$	FDTF
[31]	Champagne & Wygnanski	Air-Air	$0 < R < 10$	TH
[28]	Ko & Kwan	Air-Air	$R = 0.37, 0.5, 0.7$	TH
[35, 33]	Ko & Au, Au & Ko	Air-Air	$1 < R < 6.7$	TH
[36]	Dahm *et al.*	Water-Water	$0.59 < R < 4.16$	TH
[32]	Rehab *et al.*	Water	$1 < R < 8$	TH
[37]	Rehab *et al.*	Water-Water	$1 < R < 8$	FDTF
[37]	Rehab *et al.*	Water-Water	$1 < R < 8$	TH
[38]	Gladnick *et al.*	Air-CFC12	$R = 0.64, 1, 2$	FDTF
[39]	Favre-Marinet *et al.*	Air,He,SF_6^{**}	$1 < J < 200$	TH
[42]	Eroglu *et al.*	Air-Water	$10 < R < 164$	FDTF
[43]	Lasheras *et al.*	Air-Water	$2.5 < J < 40$	FDTF
[44]	Davis & Chehroudi	N_2-N_2^{***}	$0.2 < J < 11.2$	FDTF
[45]	Leyva *et al.*	N_2-N_2^{***}	$0.2 < J < 23$	FDTF
[46]	Rodriguez	N_2-N_2^{***}	$0.1 < J < 23$	FDTF
[29]	Wicker & Eaton	Air-Air	$0.55 < R < 1.45$	TH
[55]	Richecoeur *et al.*	N_2-LOx	$5 < J < 12$	FDTF
-	Present Work	N_2-N_2^{***}	$0.1 < J < 21$	FDTF

* Fully developed turbulent flow (FDTF) or top-hat (TH) velocity profile

** Air-Air, He-Air, Air-SF_6, He-SF_6

*** Inner jet is denser: liquid or transcritical fluid

Table 1.2: Summary of injector exit dimensions used in the literature

Ref.	t (mm)	D_1 (mm)	D_2 (mm)	D_3 (mm)	t/D_1	A_o/A_i or D_3/D_1^*
[26]	19.5	25	64	97	0.78	8.5
[31]	-	25.4	-	-	-	1.28, 2.94
[28]	0.78	21	22.6	40	0.04	2.67
[35, 33]	1	20	22	40	0.05	2.73
[36]	1.27	53.3	55.9	76.4	0.02	0.94 or 1.4^*
[32]	-	20	-	27	-	1.82
[37]	-	-	-	-	-	1.37^*, 2.29^*
[37]	-	-	-	-	-	1.35^*
[38]	0.7	18	19.4	56	0.04	8.5 or 3.1^*
[39]	0.2	20	20.4	27	0.01	1.53^*
[42]	0.15	0.971	1.262	10.36	0.15	112.1 or 10.7^*
[43]	0.2	3.8	4.2	5.6	0.05	0.95 or 1.47^*
[44]	0.53	0.51	1.59	2.42	1.05	12.9
[45]	0.53	0.51	1.59	2.42	1.05	12.9
[46]	0.53, 0.13	0.51, 1.40	1.59, 1.65	2.42, 2.44	1.05, 0.09	12.9, 1.65
[29]	-	20	-	60	-	8 or 3^*
[55]	0.3	5.78	-	7	-	1.21^*
-	0.09, 1.24	0.7, 1.47	0.89, 3.96	2.44, 4.70	0.13, 0.84	10.6, 2.9

CHAPTER 2

Experimental Facility and Methods

The present studies were performed using the same experimental apparatus, with some modifications, used by Dattarajan [21] to analyze the behavior of methanol burning droplets under microgravity and normal gravity conditions, and later on by Rodriguez [46] to study the combustion behavior of methanol and various liquid alternative fuels in the presence of acoustic disturbances under normal gravity conditions.

2.1 Acoustic Waveguide

In the present experiments, standing acoutic waves were generated by two loudspeakers placed at either end of a closed cylindrical waveguide, which operated at background atmospheric pressure and at room temperature. The frequency and amplitude of the acoustic drivers were controlled via a function generator and amplifier. Prior experiments by Dattarajan [21] and by Rodriguez [?] used a speaker and reflector, as will be discussed below. A continuosly fed, burning fuel droplet was situated at the center of the waveguide. A detailed schematic diagram of the experimental apparatus is shown in Figure 4.1. The waveguide was constructed of aluminum, with an inner diameter of 11.4 cm and a maximum length of 90 cm. Quartz windows were situated at either side of the center of the waveguide to provide optical access. A woofer type 8-Ω loudspeaker with a maximum power output of 40 W was placed at each end of the waveguide. A rod assembly connecting the two speakers was used to fix the distance between them to a distance L as they were both moved to the left or to the right. Accordingly, to create a standing acoustic wave in the waveguide, the applied frequency f, of acoustic excitation was chosen such that L was an integral multiple of half the acoustic wavelength, $\frac{1}{2}\lambda = \frac{1}{2}c/f$, where c is the speed of sound in the waveguide.

The standing acoustic waves generated by this configuration allowed the droplet to be exposed to either a pressure node (PN) or pressure antinode (PAN) condition or an intermediate condition, depending on the applied f and positions of the speakers. In order to examine the response of the burning droplet to different acoustic conditions, the speakers were moved relative to the droplet to produce a relative displacement between the droplet and the PN or PAN. At the location of the droplet at the waveguide center, a flush-mounted pressure transducer with a sensitivity rating of 73 mV/kPa revealed approximate PN and PAN conditions based on minima and maxima of the local pressures, respectively. It is important to note that the length L and the position of the droplet relative to a PN or PAN were approximate, since the loudspeaker consisted of a vibrating diaphragm as opposed to a solid wall, and the diameter of the pressure transducer, about 1 cm, introduced ambiguity in the precise location of the minimum and maximum pressure.

The experimental apparatus used by Dattarajan [21], and later on by Rodriguez [46], employed a configuration whereby a speaker was placed at one end of the waveguide, and a wave reflector, consisting of a flat aluminum disc, was placed at the opposite end. A pressure transducer was placed within the reflector plate to provide additional data for determination of standing wave conditions. A sample plot of the variation in pressure measurements at the center and end of the waveguide for a fixed length L and different forcing frequencies is shown in Figure 2.2.

In order to compare the actual acoustic perturbation fields in the waveguide for the speaker and reflector (S&R) configuration with the present two-speaker (S&S) configuration, hot wire anemometry in addition to pressure transducer measurements were used. A single component hot wire anemometer (Dantec StreamLine with a 55P15 probe), placed at the location of the droplet, measured velocity perturbations at the waveguide center. Such velocity perturbations were measured for acoustic excitation with the S&R and with the S&S situated at different locations but with a constant waveguide length L. Simultaneously, the pressure at the center of the waveguide was measured using the pressure transducer. Symmetry in both velocity and pressure perturbations would be expected as one moved the S&R or S&S to the left and right about the geometric center, with a maximum in velocity and minimum in pressure expected about the center for the PN case, and the reverse expected for the PAN conditions.

Figures 2.3ab show the measured pressure and velocity perturbations for the S&R configuration (with their movement at a constant waveguide length) at applied frequencies of 784 Hz (PN condition) and 544 Hz (PAN condition), respectively. The speakers were operated 180^o out-of-phase at 784 Hz, and in-phase at 544 Hz. Figures 2.4ab show similar profiles, but for the S&S configuration. Clearly, the S&R configuration produced an asymmetry in the velocity field about the waveguide center for the pressure node condition, albeit with a relatively symmetric pressure field (Fig. 2.3a), while the S&S configuration under these conditions produced symmetric variation in pressure as well as velocity (Fig. 2.4a). The S&R configuration produced an asymmetry in both the velocity field and pressure field for the pressure antinode condition (Fig. 2.3b), while the S&S configuration under these conditions produced symmetric measurements (Fig.2.4b).

It is not known why the asymmetry should be so pronounced when the S&R are moved to the right for the PN case and when they are moved to the left for the PAN case, but proximity of the reflector to a peak pressure location could have caused this behavior. In any event, the improved symmetry with the two-speaker configuration led us to use this system in the subsequent experiments.

2.2 Droplet Generation and Ignition

The fuel delivery system consisted of a hollow borosilicate glass capillary and a KDS Model 100 syringe pump. The fuel droplet was suspended within the waveguide from the tip of the glass capillary of approximately 0.37 mm outer diameter. An unusual feature of the present experiments was that the liquid fuel could be continuously delivered during the droplet combustion. The syringe pump provided a controlled fuel delivery to the capillary. The volume flow rates Q_v and the droplet size were used to determing the burning rate constant K, as will be described below. A protective copper shroud was placed above the end of the glass capillary in order to prevent vaporization of the fuel within the glass capillary just above the droplet. As described in [20], the distance between the end of the shroud and the end of the tip of the capillary was fixed at 3.2 mm, a regime for which the droplet burning rate constant did not depend on this length.

The droplet was ignited by means of a resistive heating Ni-Cr wire mounted on a push-type solenoid. A TattleTale Model 8 data logger/controller board was used to synchronize the extenstion of the solenoid arm and the passage of current in the ignitor wires. This mechanism created an efficient means for igniting the droplet remotely without having to open, manually ignite, and close the waveguide, thus avoiding the risk of over-heating the capillary by reducing the time span between ignition and the start of data acquisition.

2.3 Measurement Methods

2.3.1 Burning Rate Constant

From continuity for a *spherical* droplet of diameter d, the instantaneous burning rate constant K may be evaluated according to:

$$K = \frac{4Q_v}{\pi d\,(t)} - 2d\dot{d} \tag{2.1}$$

A direct input of the volume flow rate Q_v on the syringe pump provided a constant rate of fuel delivery to the burning droplet. It can noted that the preceding equation for K reduces to that of a typical "non-fed" burning droplet (the "d-squared law" described in Turns [10]) when $Q_v = 0$. Since the burning droplet in the present experiments was not always completely spherical, digitized video images of the burning droplet were used to determine an equivalent diameter of a sphere. An image processing Matlab^{TM} algorithm incorporating specially written edge-detection software [21] was used, so that the effective volume of the actual oblong droplet could be estimated and equated to that of a spherical droplet of equivalent diameter d_{eqvs}, as done by Struk, et al. [13]. Droplet burning rate constants based on d_{eqvs} in (2.1) were then determined, and time-averaged K values were computed.

2.3.2 Acoustic Acceleration

In the absense of acoustic excitation, the net force acting on the hot products of density ρ_p surrounding the burning droplet would be only the buoyancy force, $F_B = (\rho_p - \rho_o)\,V g_o$, which resulted in a vertically oriented, symmetric flame as shown in Figure 2.5a. Here, g_o is normal gravitational acceleration on the earth's surface, 9.81 m/s^2, ρ_o is the density of the surrounding (cooler) air, and V is the volume of the hot gases.

With acoustic excitation, the flame orientation was such that it became aligned with the resultant force due to buoyancy and an analogous acoustic radiation force, $F_R = (\rho_p - \rho_o)\, V g_a$, where g_a is the acoustic acceleration. A sample deflected flame is shown in Figure 2.5b. According to the theory suggested by Tanabe, *et al* [18], based on the work of Nyborg [59], the acoustic acceleration g_a depends on the relative position of the droplet with respect to the PN or PAN. The actual acoustic acceleration at the location of the droplet could be estimated from the measured deflection angle, θ, and the gravitational acceleration:

$$g_a = g_o tan\theta \tag{2.2}$$

The degree of flame deflection θ was estimated by measuring the average change in angle between the tangent lines to an unforced and forced flame edge, as shown in Figures 2.5ab. In most cases, the flame tangent measured on the side to which the deflection occurs was used to represent θ.

2.3.3 Extinction Strain Rate Estimation

A schematic showing the different parameters used in estimating the strain rate experienced by the flame in the vicinity of the droplet stagnation point is shown in Figure 2.6. The strain rate associated with extreme acoustic forcing conditions that induced extinction was estimated based on Oseen's solution for flow over a sphere. The streamfunction for this flow is given as [60]

$$\psi = \frac{U_\infty r_o^2}{4}\left[2\left(\frac{r}{r_o}\right)^2 - 3\left(\frac{r}{r_o}\right) + \left(\frac{r_o}{r}\right)\right] sin^2\theta \tag{2.3}$$

The resulting extension strain rate is

$$\epsilon_{\theta\theta} = \frac{3U_\infty}{4r}\left[2\left(\frac{r_o}{r}\right)^3 - \left(\frac{r_o}{r}\right)\right] cos\theta \approx -\frac{3U_\infty}{4r}\left(\frac{r_o}{r}\right) cos\theta \tag{2.4}$$

where the radius of the droplet equivalent to a sphere radius of r_o is less than r. Here, U_∞ is the effective bulk flow velocity in the vicinity of the droplet. In the stagnation region ($\theta \rightarrow \pi$), where the flame front is located at a distance r_f (as shown in Figure 2.6), the strain rate was estimated to be

$$\epsilon \approx \frac{3U_\infty r_o}{4r_f^2} \tag{2.5}$$

The bulk flow velocity U_∞ was estimated based on the assumption that the kinetic energy of the hot gases is equal to the work done on these gases by the resultant force due to buoyancy and acoustic radiation forces. Thus, the velocity U_∞ of the hot gases was estimated as

$$U_\infty = \sqrt{2gH\frac{T_f - T_\infty}{T_\infty}} \tag{2.6}$$

where g is the resultant acceleration, $H = 2r_f$, and T_f is the stoichiometric, constant pressure, adiabatic flame temperature.

2.4 Experimental Procedure

The pre-experimental set-up involved loading the fuel on the syringe pump, connecting the syringe with the glass capillary via a rubber tube, and eliminating any trapped air pockets out of the fuel line. The acoustic waveguide was also purged of combustion products from a prior experiment. After the fuel was introduced, the ignitor was used to ignite the fuel droplet and the value of Q_v was adjusted until a quasi-steady burning was attained. For all fuels under investigation, this value of Q_v was determined to be 0.9 ± 0.05 mm^3/s. A video camera was used to capture images of the burning droplet, and to store these images on a video cassette. These video images were later digitized and processed by the edge detection software to obtain an equivalent diameter d_{eqvs} and calculate K values according to Equation 2.1.

For cases with acoustic excitation, the S&S were displaced so that the droplet was situtated at some desired location with respect to the PN or PAN. At each such displacements of the S&S, three to four sets of burning droplet video and pressure transducer data were acquired. Then, the waveguide was purged with air to remove the combustion products accumulated. When conducting later extinction experiments, the S&S were set at a displacement where the flame surrounding the burning droplet experienced the maximum deflection. Then, the amplitude of forcing was was systematically increased until flame extinction was achieved.

2.5 Measurement Uncertainties

2.5.1 Precision Uncertainty

The sources of the precision uncertainties in the measured values of the burning rate constant K computed using Equation 2.1 were those associated with the equivalent volume of a sphere diameter d_{eqvs} and the flowrate Q_v. The method of determining d_{eqvs} employed in the present experiments was identical to those used previously by Dattarajan, *et al.* [21]. Accordingly, the precision uncertainty in d_{eqvs} of 10% determined by Dattarajan based on an uncertainity in edge detection of 5 pixels at both edges of the droplet out of an average droplet width of 50 pixels was applied. On the other hand, the uncertainty in Q_v was based on the precision uncertainty of the syringe pump. Hence, the manufacturer's reproducibility rating of the syringe pump at ± 0.1% was taken as the precision uncertainity in Q_v. Since this precision uncertainty in Q_v is very small compared to that in d_{eqvs}, it was not accounted for.

Therefore, applying the propagation of precision uncertainties proposed by Mills and Chang [67], the precision uncertainty in the burning rate constant K was computed as

$$\Delta K = \sqrt{\left(\frac{4\Delta Q_v}{\pi d\left(t\right)}\right)^2 + \left(\frac{\partial K}{\partial d}\Delta d\right)^2} \tag{2.7}$$

$$
\begin{aligned}
&\approx \sqrt{\left(\frac{-4Q_v\Delta d}{\pi d}\right)^2} \\
&= \frac{4Q_v}{\pi d}\left(\frac{\Delta d}{d}\right) \\
&= \frac{4Q_v}{\pi d}(0.1) \\
&\approx 0.1K
\end{aligned}
$$

In this analysis, the transient term in Equation 2.1 was determined from data to be negligible. The measured K values displayed in subsequent sections were averaged over 60 points. Thus, the precision uncertainty in the average K values was estimated to be $10\%/\sqrt{60} \approx 1.3\%$.

2.5.2 Bias Uncertainty

The source of bias uncertainties in the measured values of K was mainly attributed to those associated with Q_v. The syringe pump manufacturer rates the accuracy at $\pm$ 1%. This gave a bias uncertainty in K to be of the order 1%.

As pointed out by Dattarajan, *et al.* [21], a possible overestimation of the size of the actual droplet diameter might have occurred depending on the number of pixels that defined the droplet edge. However, based on repeated measurements of known actual sizes such as the the outer diameter of the tip of the shroud or the glass capillary, the uncertainty introduced due to the pixel representation was deemed insignificant.

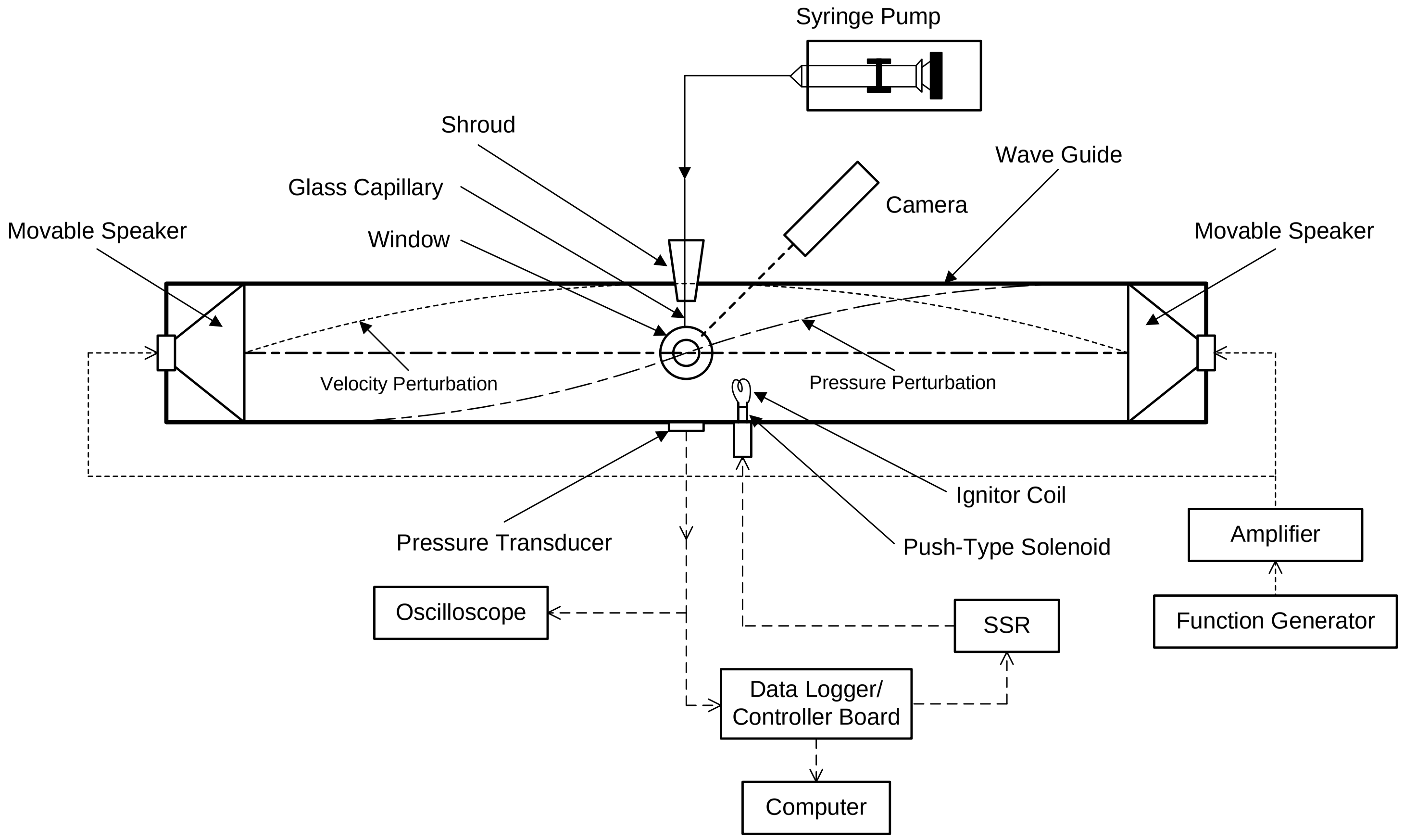
Syringe Pump
Shroud
Glass Capillary
Wave Guide
Camera
Movable Speaker
Window
Movable Speaker
Velocity Perturbation
Pressure Perturbation
Ignitor Coil
Pressure Transducer
Push-Type Solenoid
Amplifier
Oscilloscope
SSR
Function Generator
Data Logger/
Controller Board
Computer

Figure 2.1: Experimental setup of the acoustic waveguide and droplet feed system.

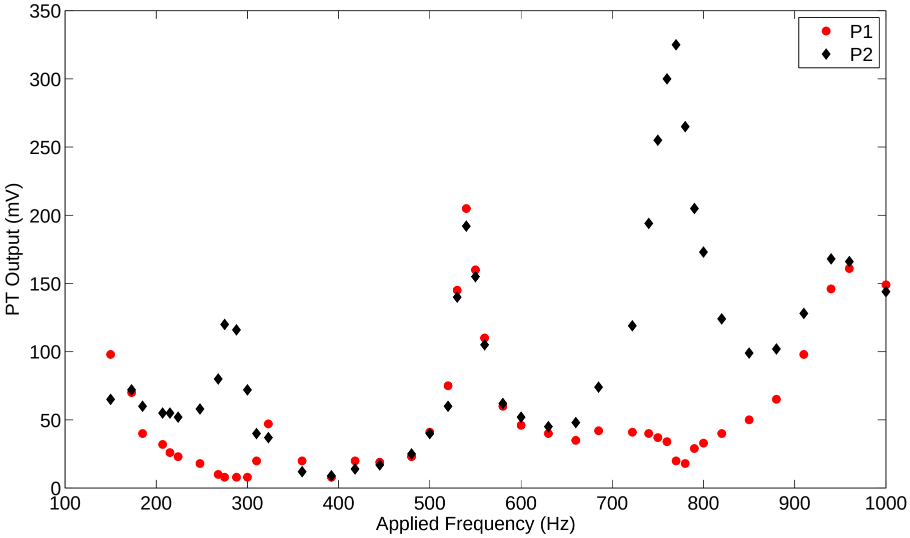

Figure 2.2: Acoustic characterization of the waveguide (S&R configuration) as measured by pressure transducers at P1 and P2. Local maxima for both pressure transducers corresponds to a pressure antinode location. A local minimum at P1 and maximum at P2 corresponds to a pressure node. The distance between the speaker and reflector is approximately 62 cm (Dattarajan, *et. al* [20])

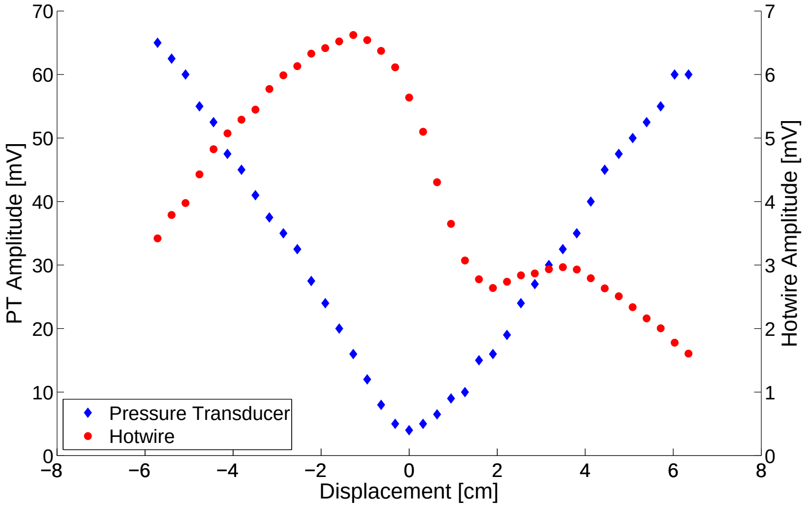

(a) 784 Hz PN

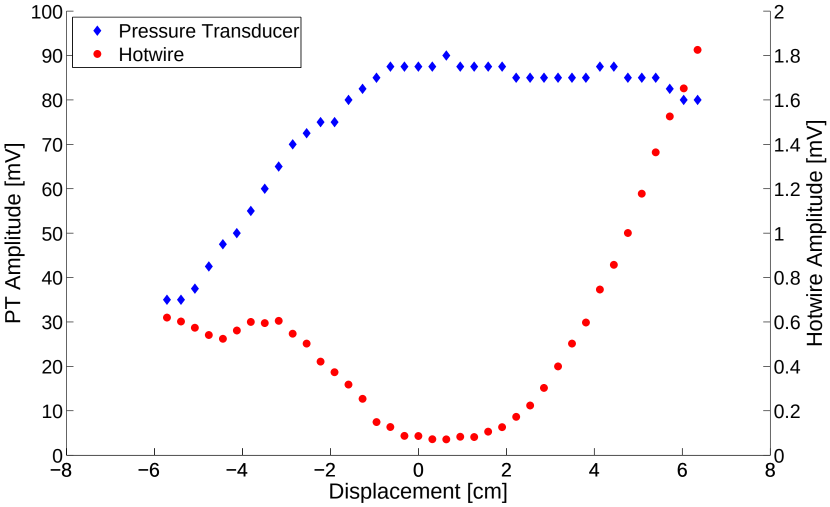

(b) 544 Hz PAN

Figure 2.3: Measurements of relative local perturbation velocity (made by the hot wire anemometer) and the relative local perturbation pressure (made by the pressure transducer), both at the geometric center of the waveguide, for the Speaker-Reflector configuration (”S & R”). The displacement of the speaker and reflector is indicated on the abscissa, relative to their original locations as determined from the geometric center of the waveguide. Positive displacement refers to the S & R moved to the right. Results are shown for acoustic excitation at an applied frequency of: (a) 784 Hz (for a pressure node condition) and (b) 544 Hz (for a pressure antinode condition).

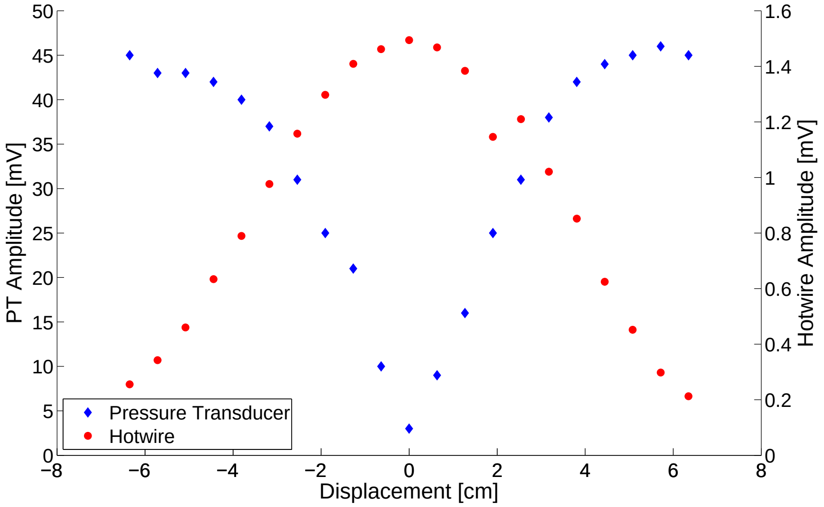

(a) 784 Hz PN

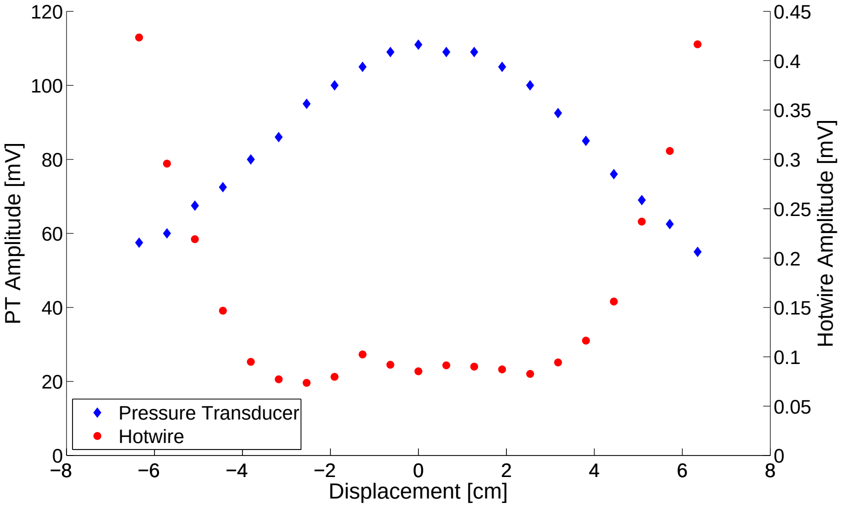

(b) 544 Hz PAN

Figure 2.4: Measurements of relative local perturbation velocity (made by the hot wire anemometer) and the relative local perturbation pressure (made by the pressure transducer P1), both at the geometric center of the waveguide, for the two Speaker configuration ((”S & S”). The displacement of the two speakers is indicated on the abscissa, relative to their original locations as determined from the geometric center of the waveguide and a maximum or minimum in the pressure transducer. Positive displacement refers to the S & S moved to the right. Results are shown for acoustic excitation at an applied frequency of: (a) 784 Hz (for a pressure node condition) and (b) 544 Hz (for a pressure antinode condition).

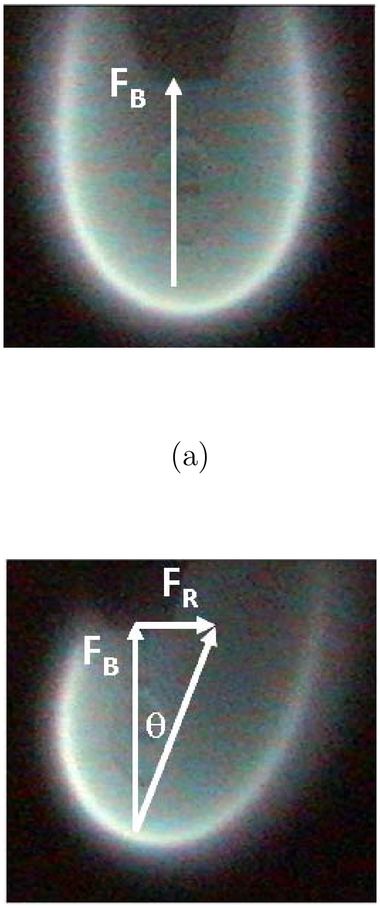

(a)

(b)

Figure 2.5: Ethanol droplet burning with and without acoustic excitation or forcing. In the absence of acoustic forcing, the flame orientation is only influenced by force of buoyancy F_B, while with acoustic excitation, both F_B and acoustic radiation force F_R affect its orientation: (a) Unforced flame orientation (b) Forced flame orientation

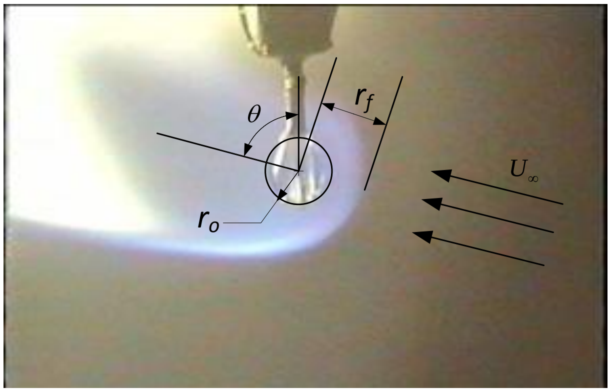

Figure 2.6: A schematic of the flow and relevant parameters used in estimating extinction strain rate. The flame assumes a nearly horizontal orientation at the instant before extinction.

CHAPTER 3

Results - Acoustically Coupled Fuel Droplet Combustion

3.1 Baseline Burning Rate Constants

Fuel droplet combustion experiments were first conducted in the absence of acoustic excitation. Images of some of the burning fuel droplets without acoustic forcing are shown in Figure 3.1. The effects of gravitational and surface tension forces gave the droplets a characteristic oblong shape. The symmetric but rather elongated diffusion flames surrounding the droplets were also a result of buoyancy force acting on the hot species. For the hydrocarbon fuels, the presence of soot gave the flame an orange or yellow appearance.

These studies were designed to evaluate "baseline" droplet combustion features for comparison with droplets burning in the presence of acoustic excitation. Determination of the droplet diameter d_{eqvs} via video imaging allowed for extraction of K values that were roughly constant over time for constant fuel flow rates. Average K values based on d_{eqvs} were close to available data for various fuel droplets burning in normal gravity, as indicated in Table 3.1.

It should be noted that in the present experiments, the potential influence of water absorption on the alcohol droplet burning rates was likely reduced or eliminated, since there was continual replenishment of the droplet with fresh fuel via continuous delivery through the capillary. Dattarajan [21] has shown that alterations in the capillary length between 2.0 mm and 3.2 mm did not yield significant or systematic changes in K. A capillary length of 3.2 ± 0.2 mm was thus selected for these experiments since this produced a minimal influence of the shroud on droplet and flame characteristics, while simultaneously preventing fuel boiling in the capillary.

3.2 Flame Alterations under Acoustic Excitation

The influence of acoustic excitation or forcing on the combustion of the fuel droplets was explored by causing the pressure node to tbe situated at various locations relative to the location of the droplet. With the distance between the two speakers fixed to approximately 62 cm, forcing frequencies of approximately 784 Hz and 1340 Hz produced a standing wave with a pressure node at the waveguide center, while a forcing frequency of approximately 1088 Hz produced a pressure antinode at the center, as verified from pressure transducer measurements. Such estimates of the standing wave were obtained within the waveguide in the absence of combustion, at room temperature.

For a standing wave, the acoustic radiation force equation can be expressed per the analysis of Tanabe, *et al.* [17, 18], as

$$F_R = (\rho_p - \rho_o)V\left[\mp 4\alpha\left(\frac{I}{z_a}\right)\left(\frac{2\pi f}{c}\right)\sin\left(\frac{2\pi x}{\lambda}\right)\cos\left(\frac{2\pi x}{\lambda}\right)\right]. \tag{3.1}$$

Here I represents the acoustic intensity, which depends on the maximum sound pressure level inside the waveguide, $z_a = \rho c$ represents the acoustic impedance, and c represents the speed of sound ($= f\lambda$). The term in square brackets represents an equivalent acoustic acceleration term, $g_a \equiv \alpha\frac{\partial\overline{u'^2}}{\partial x}$, for a condition where a standing wave is present in the waveguide. The coefficient α defined in Equation (1.3) was approximated to be equal to one in subsequent analyses. The minus sign in the bracketed term corresponds to the case where a pressure node or velocity antinode was positioned at the center of the waveguide ($x = 0$); the plus sign corresponds to a pressure antinode or velocity node at that location. Thus, if the droplet were situated to the right ($x > 0$) or left ($x < 0$) of the waveguide center, the flame and hot gas zone surrounding the droplet would experience a nonzero acoustic acceleration g_a, which in turn would result in a finite acoustic radiation force that deflected the flame in a direction opposite to that of g_a. These phenomena were observed for n-decane droplet combustion in microgravity by Tanabe, *et al.* [17, 18], for methanol droplet combustion in microgravity and normal gravity by Dattarajan, *et al.* [20, 21], and in normal gravity for several fuels by Rodriguez [**?**]. It is noted that the latter two sets of experiments were conducted in the present waveguide but with a speaker-reflector configuration.

A schematic diagram of the displacements of the two speakers is shown in Figure 3.2, where x' corresponds to the location of the pressure node (PN) relative to the position of the droplet, and x corresponds to the location of the droplet relative to the PN. Hence, during an acoustic forcing that produced a PN at the waveguide center, when the two speakers ("S&S") were moved substantially to the right, one approached a condition where the PN lay to the right of the droplet, or the droplet lay to the left of the PN ($x < 0$). In this case, if the droplet lay to the left of the PN, then the sign of the acoustic radiation force in Equation 3.1 would become negative, shifting the flame and hot gases toward the left side of the waveguide, away from the PN. On the other hand, when the S&S were moved substantially to the left, so that $x > 0$, the opposite would occur, causing the flame to deflect to the right, away from the PN. For the case of a standing wave with an established pressure antinode (PAN) in the waveguide, e.g., 1088 Hz, the opposite behaviors should take place when the S&R or S&S are moved. In general, the direction of the acoustic radiation force was oriented towards the nearest PAN.

The influence of relative droplet-node displacements on the flame surrounding a burning fuel droplet was explored using different fuels. Figures 3.3-3.6 show images captured from video of the burning droplets of the different fuels during acoustic forcing. Images of a burning ethanol droplet at different locations relative to the estimated pressure node location, which coincides with the waveguide center and is designated as the location of 0 cm displacement, are shown in Figures 3.3a-f. It can be seen from these images that when the speakers were displaced to the left, resulting in a left displacement of the PN relative to the droplet (so that $x' < 0$), or equivalently, a right displacement of the droplet relative to the PN (so that $x > 0$), the flames were deflected to the right, away from the PN location or towards the PAN. This observation was consistent with the direction of the acoustic radiation force as predicted in the above discussion. However, a switch in the direction of the flame deflection occurred between the original location (0 cm) and 0.6 cm (Fig. 3.3d) to the right of the original or PN location. Thus, in Figures 3.3d-f, the droplet probably lay slightly to the left of the PN (so that $x < 0$). Similar types of flame shifts were observed during exposure of a burning JP-8, JP-8/FT fuel blend, and pure FT droplets near a PN at 784 Hz forcing frequency, as shown in Figures 3.4a-f, 3.5a-f, and 3.6a-f, respectively. Forcing conditions that produced a PAN at the waveguide center, such as 1088 Hz, also resulted in directions of flame deflection that were in agreement with the expectation that the acoustic radiation force always acts towards the nearest PAN, thus producing flame deflections towards the 0 cm displacement location or waveguide center.

The location of the flame switch, however, was consistently offset by up to 0.5 cm, or 1 cm in some cases, from the PN location. Plots of local (at the droplet location) pressure measurements taken for a range of speaker displacements during a 784 Hz forcing frequency are shown in Figures 3.3-3.6. These pressure profiles show that a minimum in the pressure perturbations occurred at the waveguide center. This being the case, the locations of the flame switch were nevertheless observed to occur anywhere between 0.5 cm to 1 cm displacement of the speakers to the right of the PN. Similar plots of pressure measurements (Figures 3.7 - 3.9) during a 1340 Hz forcing frequency show a PN situated at about 0.5 cm to the left of the waveguide center. Despite this, the flame switch locations corresponding to these cases were still within 1 cm to the right of the PN location. One possible cause for this offset of the flame switch location, which did not show any quantifiable dependency on the fuel type, may be attributable to the uncertainties in the precise location of the PN. This is mainly due to the fact that the pressure transducer diaphragm has a diameter of about 1 cm, thus giving rise to a measurement uncertainty in the location of the PN of about 0.5 cm.

The idea of acoustic acceleration in the vicinity of the burning droplet, related to the acoustic radiation force in Equation 3.1 was explored experimentally. The fuel droplet burning in the absence of acoustic forcing did so under the sole influence of gravitational acceleration, g_o, which gave rise to the buoyancy force, resulting in the characteristic vertically symmetric, yet elongated flame structure. When acoustics was imposed on the burning droplet, the flame was deflected from its original vertically symmetric orientation to one where it aligned itself with the resultant force due to buoyancy and an analogous acoustic radiation force. As shown in Figure 2.5, the actual acoustic accelerations, $g_{a,exp}$, were quantified based on the geometry of the angular deflection of the flames using the relation given in Equation 2.2. The theoretical acoustic accelerations, $g_{a,th}$, were computed based on Equation 3.1, where the "true" PN location ($x = 0$) was set at the flame switch location. Plots comparing the $g_{a,exp}$ and $g_{a,th}$ profiles for the different 784 Hz cases are shown in Figures 3.3 - 3.6, and similar plots for the 1340 Hz cases are shown in Figures 3.7 - 3.9. It is evident that the direction of $g_{a,exp}$, depicted by its sign, was consistent with the $g_{a,th}$. However, the magnitudes of $g_{a,exp}$ showed a rather large deviation from the theoretical estimation.

In theory, the magnitude of the acoustic radiation force is the largest at a midpoint location between a node and antinode (or equivalently, $\lambda/8$ from a node or antinode), since that is where $\frac{\partial \overline{u'^2}}{\partial x}$ is maximized [18]. Farther away from this midpoint, the gradient term decreases finally reaching zero at a node or antinode, thus resulting in a zero acoustic acceleration. This theoretical scenario should be reflected with maximum flame deflections at the halfway location between a node and antinode, and no deflection at a node or antinode. On the other hand, experimental observations showed a steep profile of the acoustic acceleration as shown in Figures 3.10 - 3.16, whereby the flame deflections were rather steep in the immediate region of the PN, and became less deflected farther from the PN.

3.3 Effect of Acoustic Acceleration on Burning Rate Constants

Average burning rate constants based on time averages over the period of experimentation that lasted 2 seconds were obtained for various fuels for pressure node conditions and for a range of different positions of the speakers. Sample K values for different positions of the speakers are plotted in Figures 3.10, 3.11, 3.12, and 3.13 for ethanol, pure JP-8, JP-8/FT blend, and pure FT, respectively. A 784 Hz (PN) forcing was employed, and the positions of the speakers relative to their original locations are plotted on the abscissa. On the upper plots of these figures, the local pressure measured at the center of the wageguide is compared with the theoretical values for different speaker positions. The middle plots show the acoustic acceleration $g_{a,exp}$ measured from the flame deflection as compared with the theoretical $g_{a,th}$ from Equation 3.1. Placed on the bottom plots are measured K values as well as the estimates of the magnitudes of the theoretical and experimental acoustic accelerations at different speaker displacements. Similar plots are shown for the 1340 Hz (PN) forcing condition for ethanol, pure JP-8, and pure FT in Figures 3.14, 3.15, and 3.16, respectively.

The pressure measurements were generally consistent with theory, except in some cases for the amplitude. As discussed previously, it is evident from the plots for the 784 Hz cases that the magnitude of the actual acoustic acceleration, $g_{a,exp}$, increased as the speakers' displacement approached the flame switch location, which coincides with the supposed "true" PN location. Although the flame switch near the zero displacement indicated the same qualitative behavior for g_a as in the theory, the magnitudes of the flame deflection near the zero location were considerably larger than suggested by theory. Accordingly, variations in the K values were observed to follow more closely the magnitudes of $g_{a,exp}$ rather than the theory. These effects were more pronounced in the ethanol (Figure 3.10) and pure JP-8 (Figure 3.11) cases, where the K values near the PN increased by up to 15% above the lower limit of the unforced K values for these fuels. The trends in K values obtained for the 1340 Hz case did not show as large a variation from the unforced. There was nevertheless a general trend in K that followed the magnitude $g_{a,exp}$ more closely than the theory.

Dattarajan's [21] studies on the combustion of methanol fuel droplet combustion in microgravity revealed significant increases in K values (up to 200%) while the droplet was placed at or near a PN. Similar studies in normal gravity, however, showed a severe limitation on the effects of acoustics on the K values (11-15% increase). In the present studies, the same limitations were observed despite significant changes in the acoustic accelerations.

3.4 Fuel Extinction Studies

An exploration of the extinction phenomenon was performed whereby burning droplets in the absence of acoustic forcing were abruptly exposed to successively increasing acoustic intensities. At high enough acoustic intensities, extinction (flame blowout) occurred. Sample sets of consecutive image frames showing the extinction process of ethanol, pure JP-8, JP-8/FT fuel blend, and pure FT are shown in Figures 3.17, 3.18, 3.19 and 3.20, respectively. It can be seen that the instant before extinction, the acoustic radiation force acting on the hot products was the dominant force as was evident in the extreme degree of deflection that the flames underwent. Under such conditions, it was estimated that the hot gases experience magnitudes of $g_{a,exp}$ that were up to eight fold that of g_o.

The flame extinction strain rates on the stagnation side of the droplets were estimated for some of the fuels under consideration. The preliminary results including the extinction sound pressure levels (SPLs) are shown in Table 3.2. As given in Equation 2.5, the strain rate is directly proportional to the droplet radius, and bulk flow velocity induced in the vicinity of the droplet due to the action of the acoustic radiation force on the hot gases, and inversely proportional to the flame standoff distance. The bulk flow velocity, in turn, is proportional to the acoustic acceleration and flame temperature. In the current estimations, this velocity was found to be on the order 1 m/s. In general, extinction occurs when the reaction time scale becomes very long or the diffusion time scale becomes very short. Thus, the effect of increased acoustic intensities was in decreasing the diffusion time scale so that the finite rate chemical kinetics could no longer maintain the temperature that could sustain the reaction. This argument may be used to explain why fuels with higher flame temperature are harder to extinguish that those with relatively lower ones. Current limits on the knowledge of a complete thermochemical data for the hydrocarbon fuels rendered rather crude flame extinction strain rate estimates for those fuels. However, based on just SPL of extinction, it was observed that the alcohols had a slightly larger resistance to extinction.

3.5 Preliminary Conclusions

The present experiments allowed for the exploration of alternative fuel combustion characteristics in the presence of acoustic perturbations. These included changes that can occur in the mean burning rates associated with a single burning fuel droplet, and flame extinction limits for a range of acoustic excitation conditions . The flame deflections observed at moderate acoustic intensities were qualitatively in accordance with the predictions of the acoustic radiation force theory. The directions of the theoretical and measured acoustic accelerations were consistent with each other. However, the magnitudes of the measured acoustic accelerations were larger and steeper in the vicinity of the pressure node than predicted by theory. This was contrary to the expected profile, where a maximum acceleration was expected to occur at approximately $\lambda/8$ away from the pressure node. The variation in magnitude of the burning rate constants, despite not being significantly larger than the measurement uncertainties, showed a closer correspondence to the variation in magnitude of the measured acoustic accelerations than the theoretical acoustic accelerations.

Conducting the experiments in normal gravity resulted in natural convection being a significant factor in the magnitude of the burning rate constants at moderate levels of acoustic forcing, thereby diminishing the impact of the acoustic radiation force. At very high amplitudes of forcing, however, the nearly horizontal deflected flames indicated that g_a exceeded gravitational acceleration by a significant degree.

Based on preliminary extinction strain rate results obtained thus far, there was no significant difference between the alcohols and the hydrocarbon fuels. The current method of evaluating strain rates involved estimating an equivalent bulk flow velocity due to the strong acoustic acceleration and gravitation accleration. Since the acoustic acceleration was measured based on the degree of flame deflection, and the flame orientation was nearly horizontal at the instant before extinction, the estimated bulk flow velocity was thus very sensitive to measured angles of flame deflection. As little as two to three degrees of uncertainity in the measured flame deflection angle brought about changes in the estimated strain rates of more than $40s^{-1}$. A more refined method of estimating the extinction strain rates for the flames of the different fuels is ongoing.

Table 3.1: Comparison of measured values of burning rate constant K for various fuel droplets in the absence of acoustic excitation. Comparisons with available established values for K are also given.

Fuel	K, present (mm^2/s)	K, established (mm^2/s)
Ethanol	0.78-0.88	0.81-0.86
Methanol	0.83-0.95	0.85-1.2
JP-8	0.88-1.05	0.87,1.04 (JP-4)
JP-8/FT	0.78-0.90	-
Pure FT	0.80	-

Table 3.2: Acoustic conditions of various fuels at extinction. The corresponding sound pressure levels in decibels (dB) and rough estimates of the strain rates are also shown.

Fuel	SPL (dB)	Strain Rate ($s^{-}1$)
Ethanol	142.3 ± 0.6	260
Methanol	142.0 ± 0.6	220
JP-8	140.8 ± 0.7	230
JP-8/FT	141.8 ± 0.5	360
Pure FT	141.6 ± 0.4	350

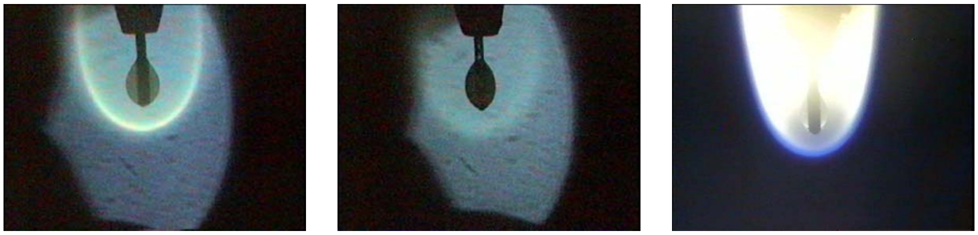

(a) Ethanol (b) Methanol (c) JP-8

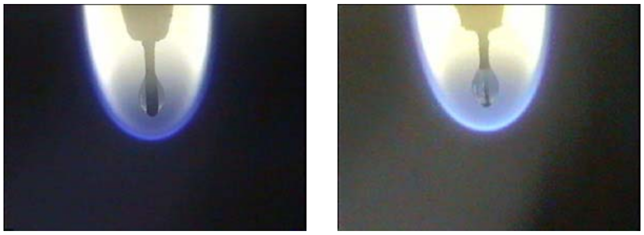

(d) JP-8/FT Blend (e) FT

Figure 3.1: Images of various fuel droplets burning in the absence of acoustic excitation.

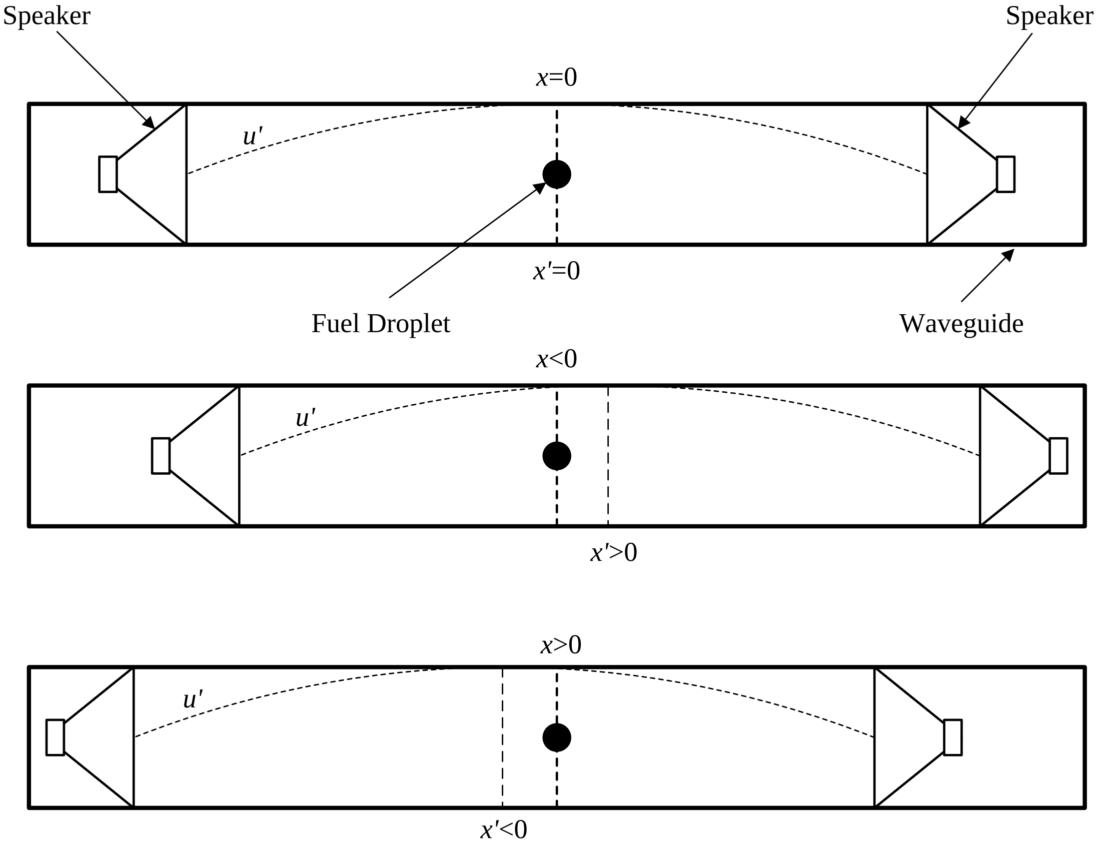

Figure 3.2: Schematic showing the relative displacement between a pressure node (velocity antinode) and the droplet. *Top*: Location of the speakers in the waveguide relative to a velocity antinode (pressure node) situated at $x' = 0$, with the droplet located at $x = 0$ relative to the velocity antinode. *Middle*: Location of velocity antinode at $x' > 0$ relative to the droplet (and of the droplet at $x < 0$ relative to the velocity antinode),resulting from displacement of the speakers to the right as compared with the original condition. *Bottom*: Location of velocity antinode at $x' < 0$ relative to the droplet (and of the droplet at $x > 0$ relative to the velocity antinode), resulting from displacement of the speakers to the left as compared with the original condition.

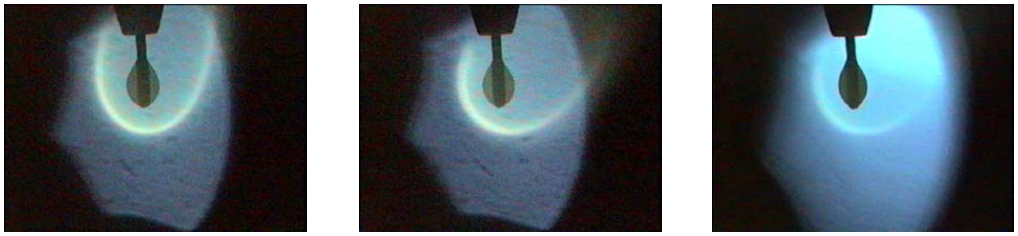

(a) S&S 3.8 cm to left (b) S&S 2.5 cm to left (c) S&S 0 cm

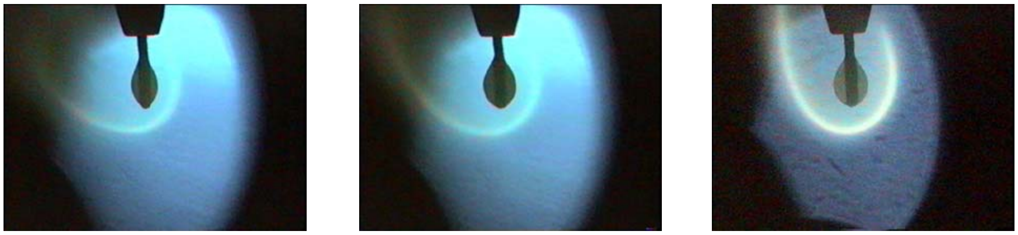

(d) S&S 0.6 cm to right (e) S&S 2.5 cm to right (f) S&S 3.8 cm to right

Figure 3.3: Photographs of a burning ethanol droplet with acoustic excitation at an applied frequency of 784 Hz (for a pressure node condition). The positions of the two speakers ("S & S") are indicated, relative to their original locations as determined from the geometric waveguide center and minimum in measured pressures. "S & S X cm to left" refers to the case where the speakers were moved by X cm to the left as compared with their original positions, etc. The true pressure node was likely coincident with the droplet located between cases (c) and (d), very close to the pressure node.

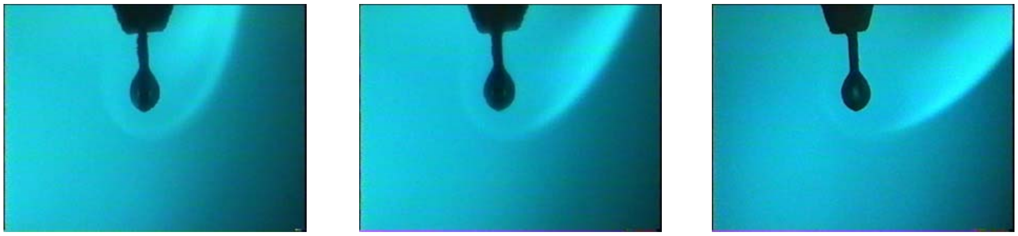

(a) S&S 3.8 cm to left (b) S&S 2.5 cm to left (c) S&S 0 cm

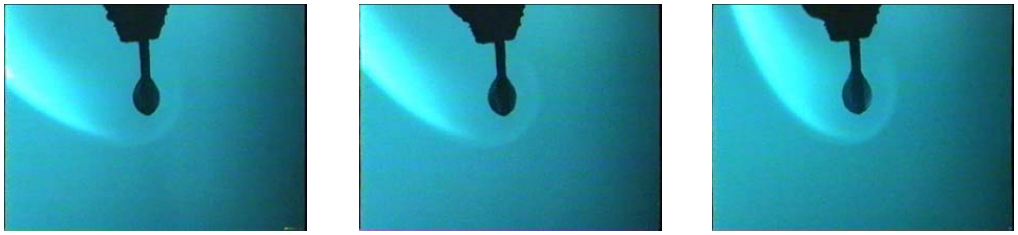

(d) S&S 0.6 cm to right (e) S&S 2.5 cm to right (f) S&S 3.8 cm to right

Figure 3.4: Photographs of a burning JP-8 droplet with acoustic excitation at an applied frequency of 784 Hz (for a pressure node condition). The positions of the two speakers ("S & S") are indicated, relative to their original locations as determined from the geometric waveguide center and minimum in measured pressures. "S & S X cm to left" refers to the case where the speakers were moved by X cm to the left as compared with their original positions, etc. The true pressure node was likely coincident with the droplet located between cases (c) and (d), very close to the pressure node.

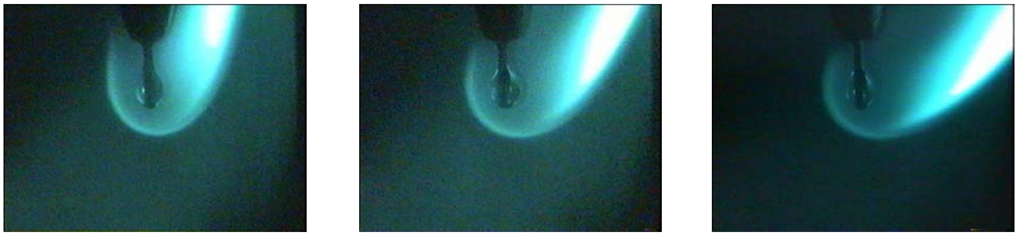

(a) S&S 3.8 cm to left (b) S&S 2.5 cm to left (c) S&S 0 cm

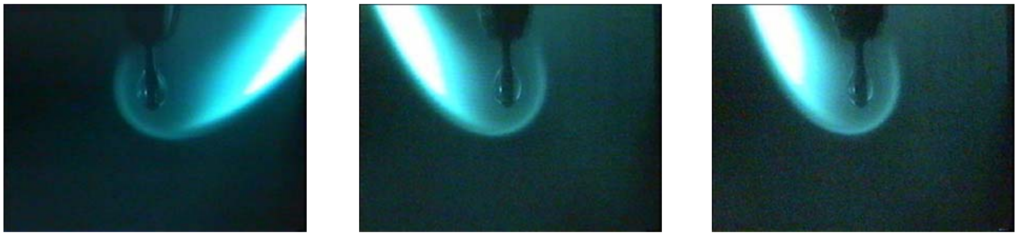

(d) S&S 0.6 cm to right (e) S&S 2.5 cm to right (f) S&S 3.8 cm to right

Figure 3.5: Photographs of a burning JP-8/FT blend droplet with acoustic excitation at an applied frequency of 784 Hz (for a pressure node condition). The positions of the two speakers ("S & S") are indicated, relative to their original locations as determined from the geometric waveguide center and minimum in measured pressures. "S & S X cm to left" refers to the case where the speakers were moved by X cm to the left as compared with their original positions, etc. The true pressure node was likely coincident with the droplet located between cases (c) and (d), very close to the pressure node.

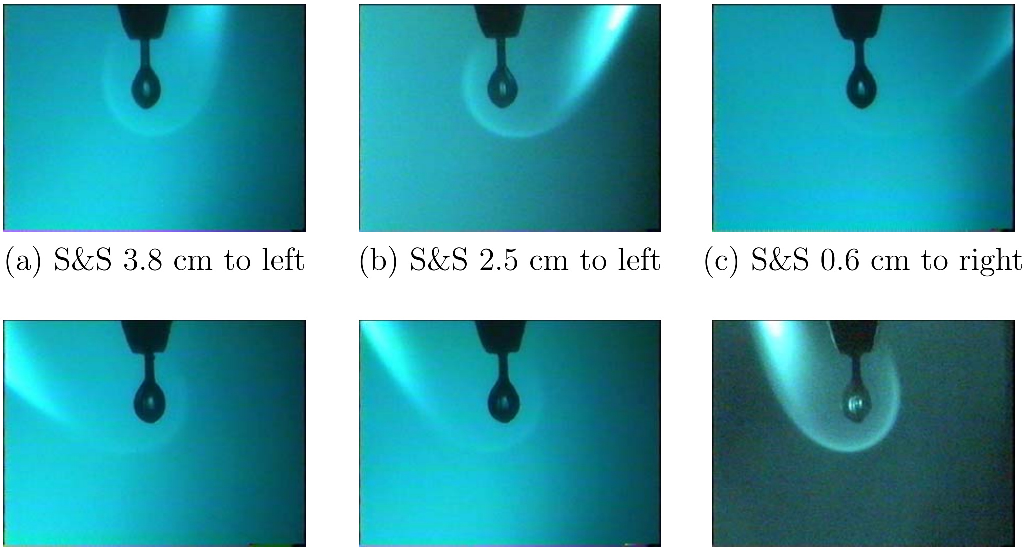

(a) S&S 3.8 cm to left (b) S&S 2.5 cm to left (c) S&S 0.6 cm to right

(d) S&S 1.9 cm to right (e) S&S 2.5 cm to right (f) S&S 3.8 cm to right

Figure 3.6: Photographs of a burning FT droplet with acoustic excitation at an applied frequency of 784 Hz (for a pressure node condition). The positions of the two speakers ("S & S") are indicated, relative to their original locations as determined from the geometric waveguide center and minimum in measured pressures. "S & S X cm to left" refers to the case where the speakers were moved by X cm to the left as compared with their original positions, etc. The true pressure node was likely coincident with the droplet located between cases (c) and (d), very close to the pressure node.

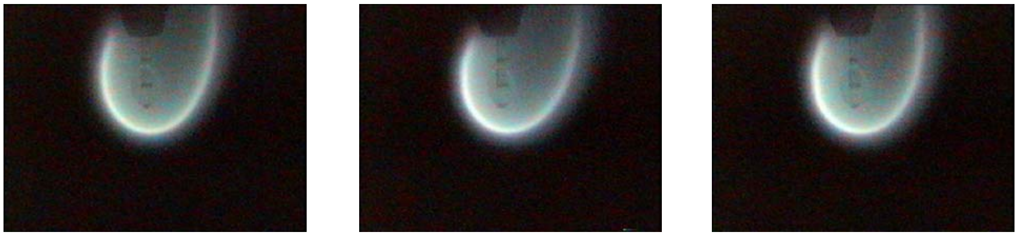

(a) S&S 3.8 cm to left (b) S&S 2.5 cm to left (c) S&S 0 cm

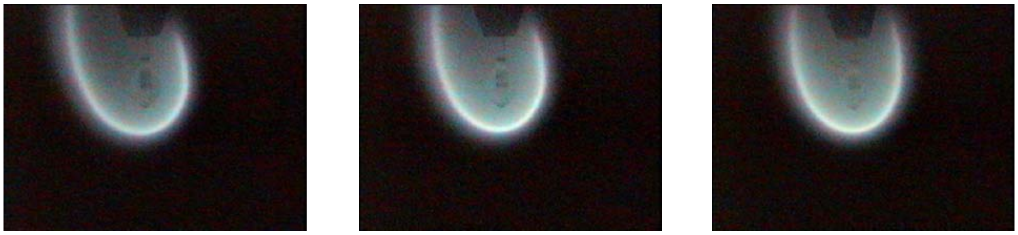

(d) S&S 0.6 cm to right (e) S&S 2.5 cm to right (f) S&S 3.8 cm to right

Figure 3.7: Photographs of a burning ethanol droplet with acoustic excitation at an applied frequency of 1340 Hz (for a pressure node condition). The positions of the two speakers ("S & S") are indicated, relative to their original locations as determined from the geometric waveguide center and minimum in measured pressures. "S & S X cm to left" refers to the case where the speakers were moved by X cm to the left as compared with their original positions, etc. The true pressure node was likely coincident with the droplet located between cases (c) and (d), very close to the pressure node.

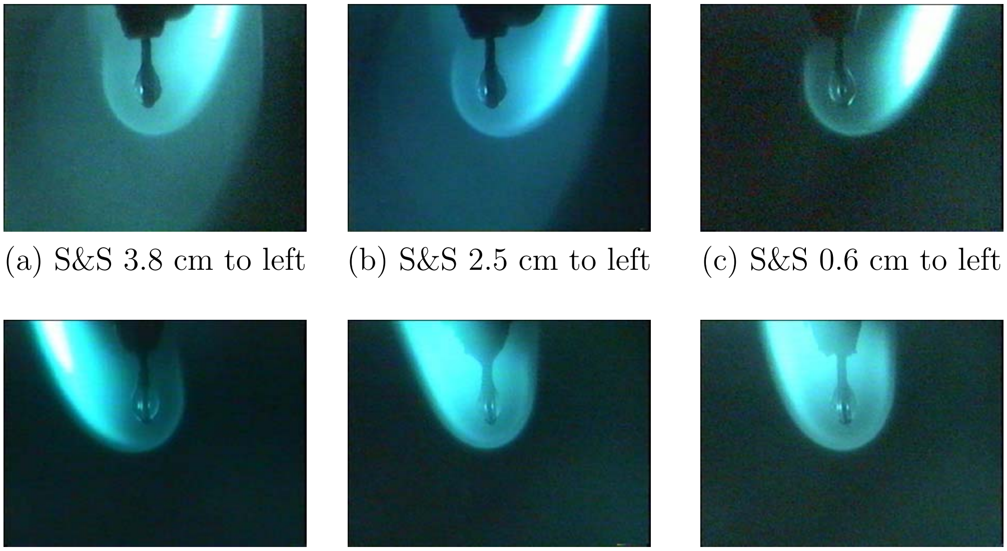

(a) S&S 3.8 cm to left (b) S&S 2.5 cm to left (c) S&S 0.6 cm to left

(d) S&S 0 cm (e) S&S 2.5 cm to right (f) S&S 3.8 cm to right

Figure 3.8: Photographs of a burning JP-8 droplet with acoustic excitation at an applied frequency of 1340 Hz (for a pressure node condition). The positions of the two speakers ("S & S") are indicated, relative to their original locations as determined from the geometric waveguide center and minimum in measured pressures. "S & S X cm to left" refers to the case where the speakers were moved by X cm to the left as compared with their original positions, etc. The true pressure node was likely coincident with the droplet located between cases (c) and (d), very close to the pressure node.

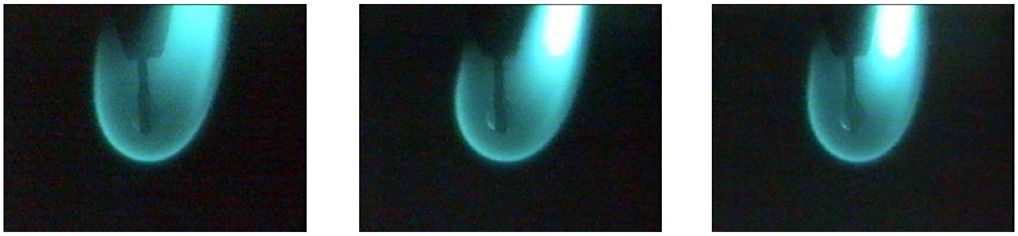

(a) S&S 3.8 cm to left (b) S&S 2.5 cm to left (c) S&S 0 cm

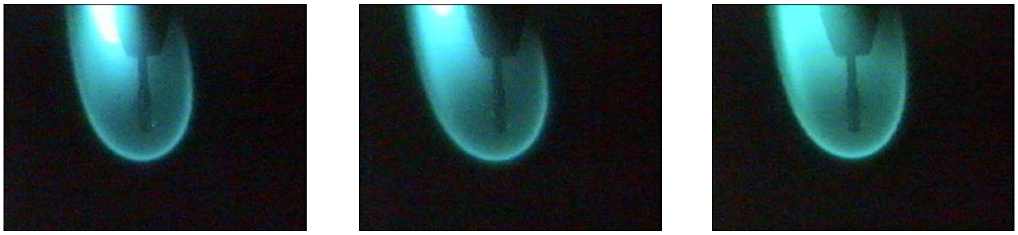

(d) S&S 0.6 cm to right (e) S&S 2.5 cm to right (f) S&S 3.8 cm to right

Figure 3.9: Photographs of a burning FT droplet with acoustic excitation at an applied frequency of 1340 Hz (for a pressure node condition). The positions of the two speakers ("S & S") are indicated, relative to their original locations as determined from the geometric waveguide center and minimum in measured pressures. "S & S X cm to left" refers to the case where the speakers were moved by X cm to the left as compared with their original positions, etc. The true pressure node was likely coincident with the droplet located between cases (c) and (d), very close to the pressure node.

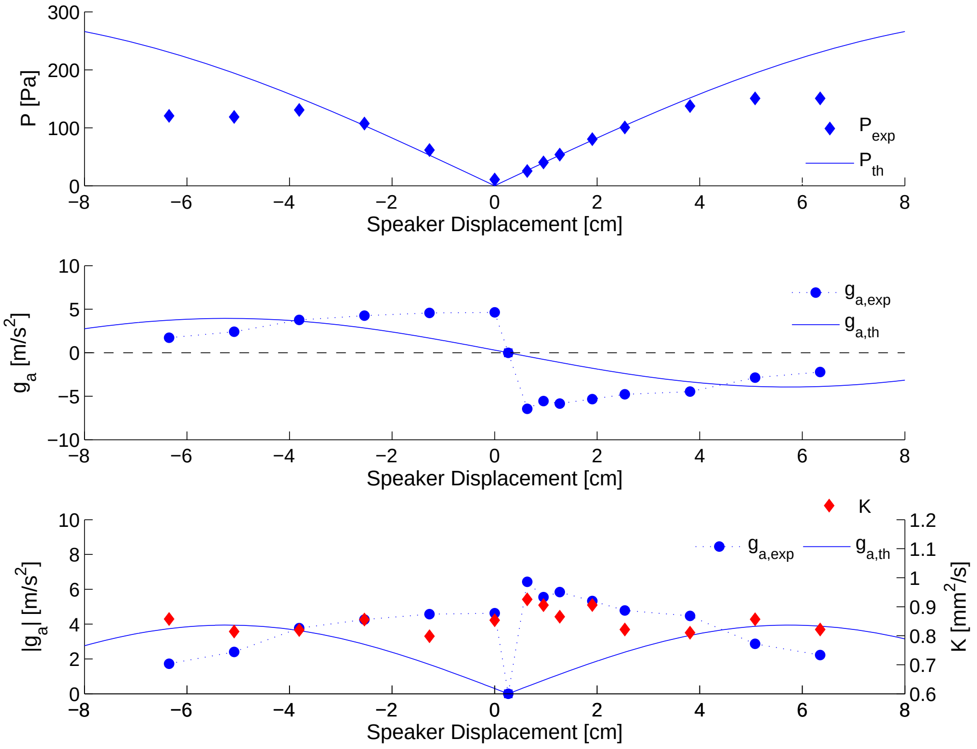

Figure 3.10: Pressure perturbations, estimated theoretical and actual acoustic accelerations g_a, and average burning rate constant K as a function of the displacement of the speakers with respect to the original position (0 cm) for the ethanol droplet burning in the vicinity of a pressure node at a frequency of approximately 784 Hz.

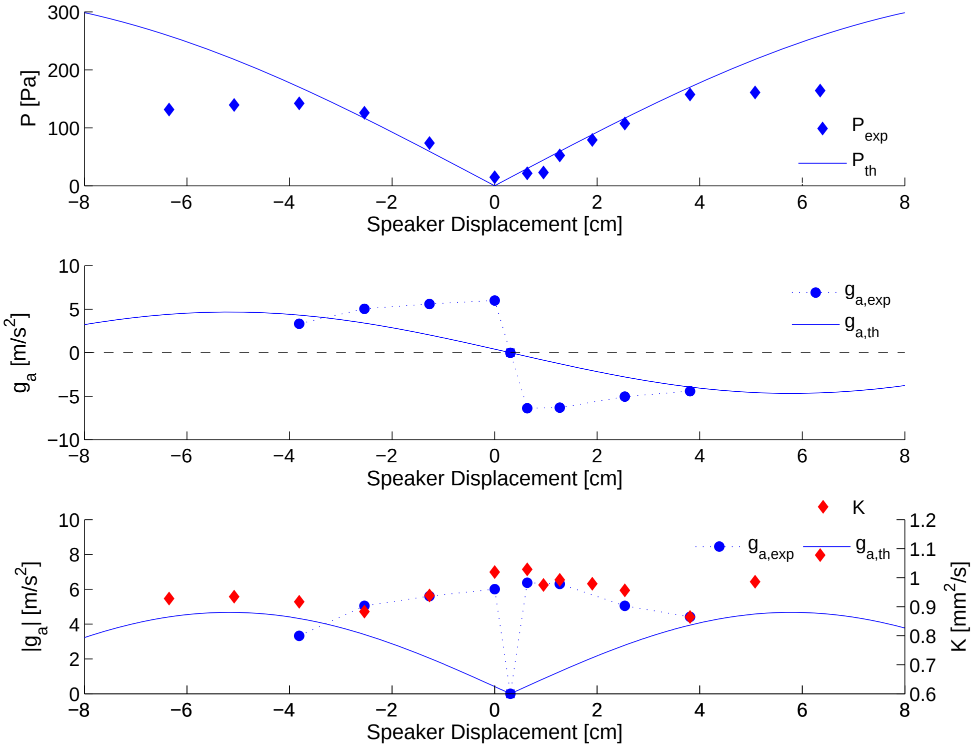

Figure 3.11: Pressure perturbations, estimated theoretical and actual acoustic accelerations g_a, and average burning rate constant K as a function of the displacement of the speakers with respect to the original position (0 cm) for the JP-8 droplet burning in the vicinity of a pressure node at a frequency of approximately 784 Hz.

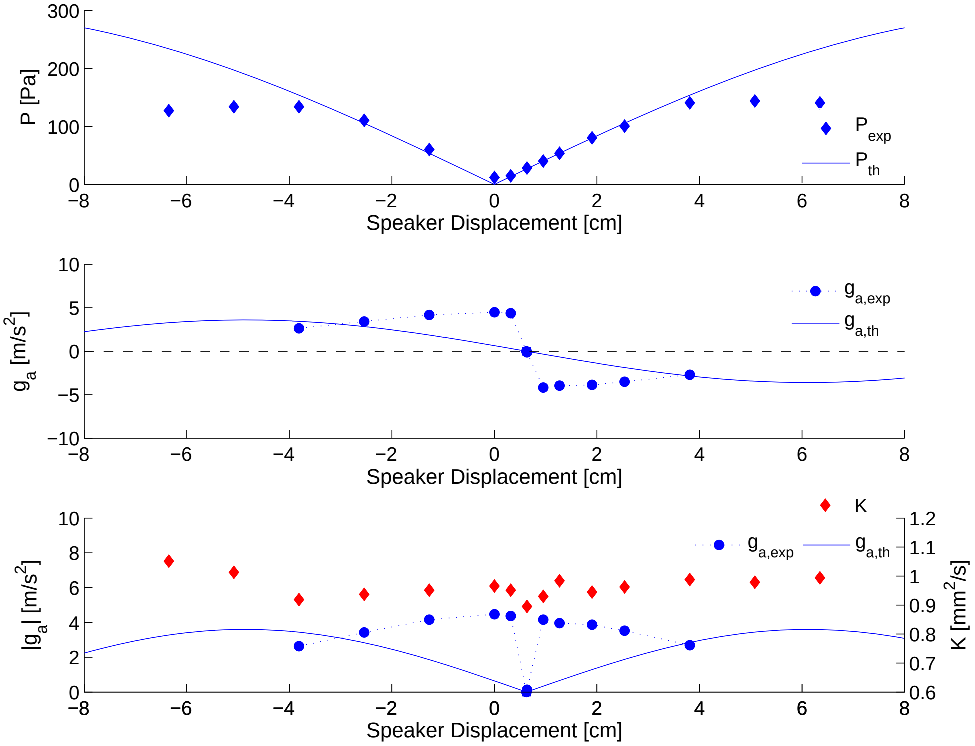

Figure 3.12: Pressure perturbations, estimated theoretical and actual acoustic accelerations g_a, and average burning rate constant K as a function of the displacement of the speakers with respect to the original position (0 cm) for the JP-8/FT blend droplet burning in the vicinity of a pressure node at a frequency of approximately 784 Hz.

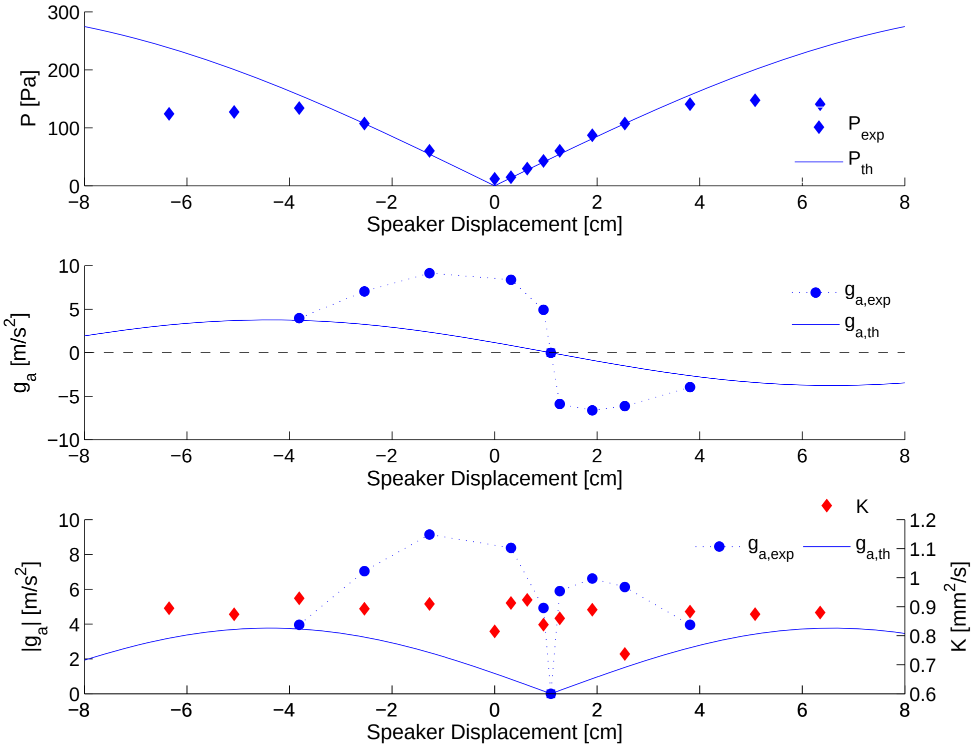

Figure 3.13: Pressure perturbations, estimated theoretical and actual acoustic accelerations g_a, and average burning rate constant K as a function of the displacement of the speakers with respect to the original position (0 cm) for the FT droplet burning in the vicinity of a pressure node at a frequency of approximately 784 Hz.

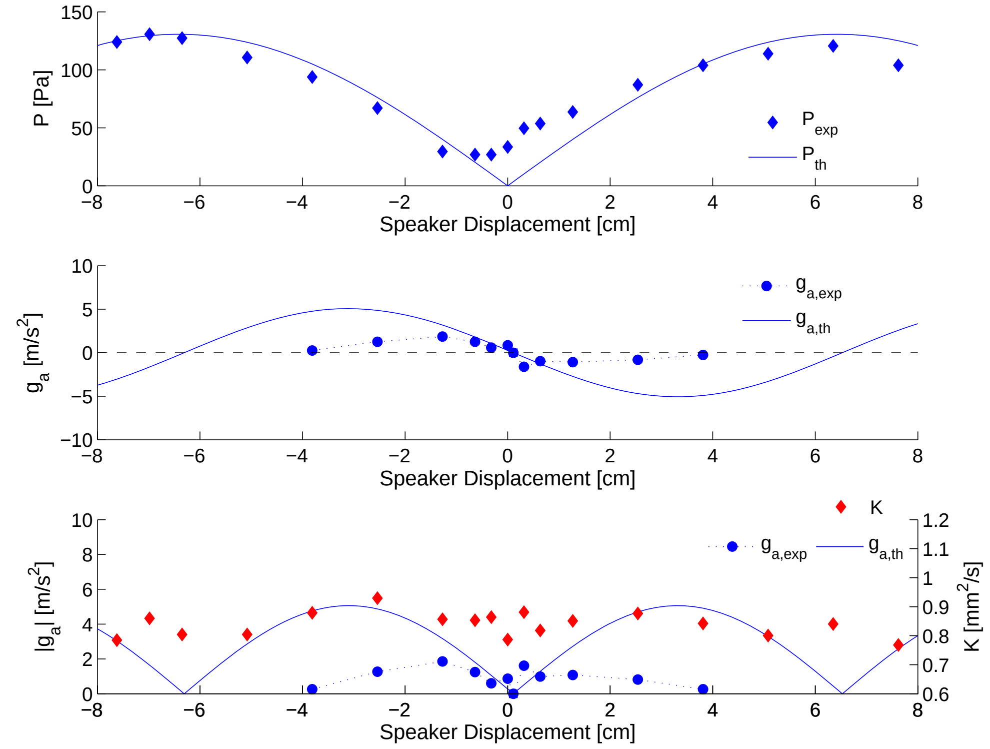

Figure 3.14: Pressure perturbations, estimated theoretical and actual acoustic accelerations g_a, and average burning rate constant K as a function of the displacement of the speakers with respect to the original position (0 cm) for the ethanol droplet burning in the vicinity of a pressure node at a frequency of approximately 1340 Hz.

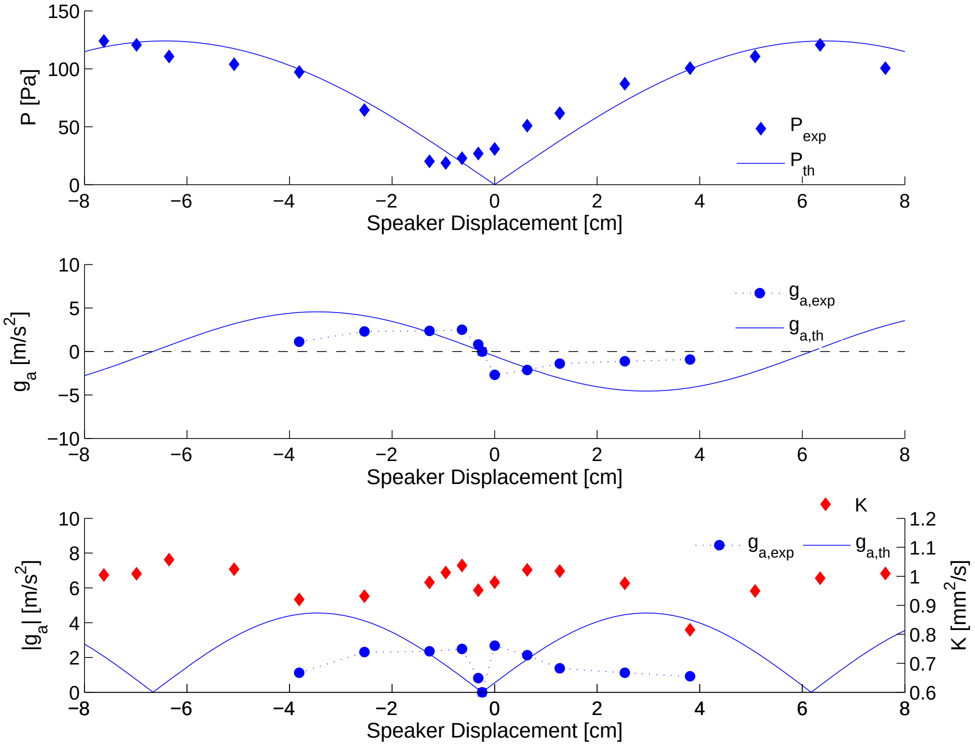

Figure 3.15: Pressure perturbations, estimated theoretical and actual acoustic accelerations g_a, and average burning rate constant K as a function of the displacement of the speakers with respect to the original position (0 cm) for the JP-8 droplet burning in the vicinity of a pressure node at a frequency of approximately 1340 Hz.

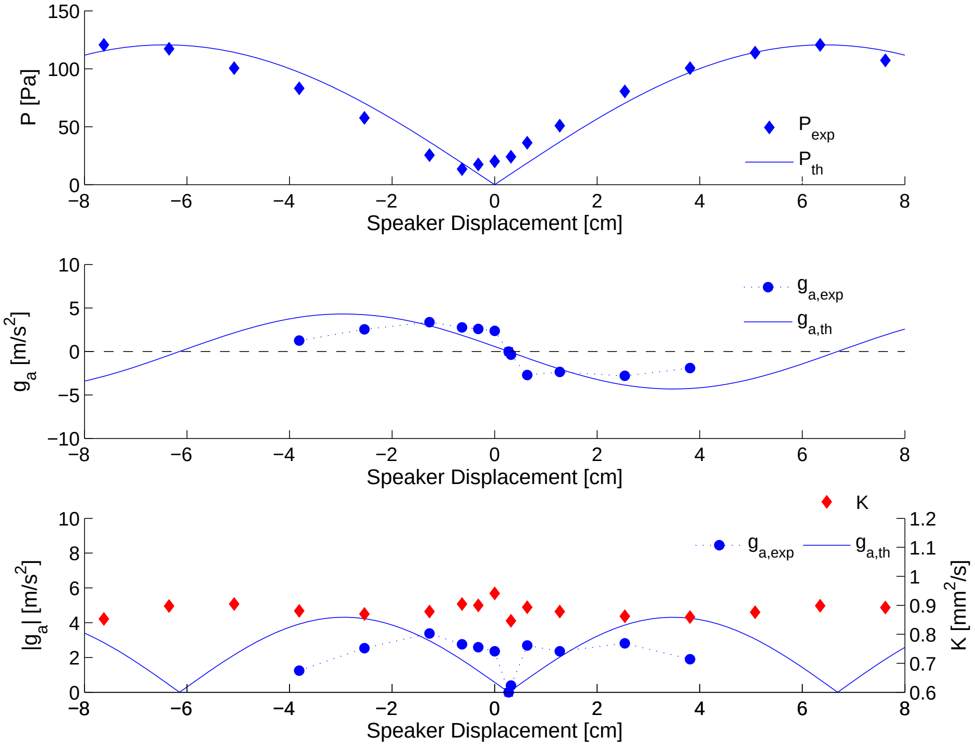

Figure 3.16: Pressure perturbations, estimated theoretical and actual acoustic accelerations g_a, and average burning rate constant K as a function of the displacement of the speakers with respect to the original position (0 cm) for the FT droplet burning in the vicinity of a pressure node at a frequency of approximately 1340 Hz.

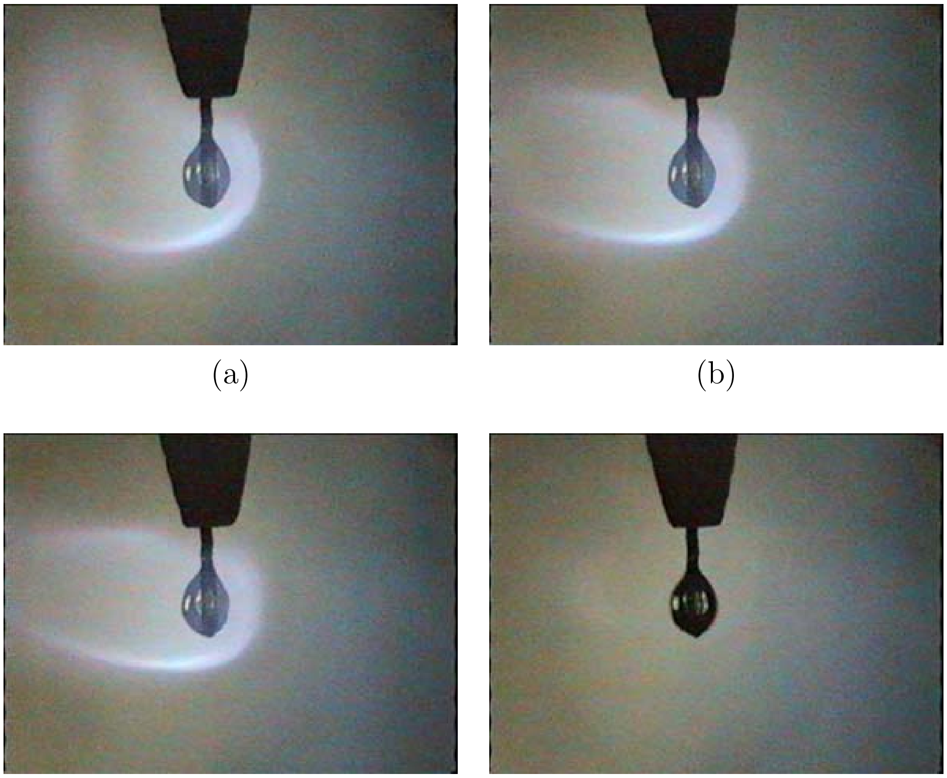

(a) (b)

(c) (d)

Figure 3.17: A sequence of images showing the extinction process of the flame surrounding an ethanol fuel droplet. The time span between the consequetive images was approximately 33 ms. The sound pressure level was 142.3 dB, and the estimated strain rate at extinction for this case was 260 $s^{-}1$.

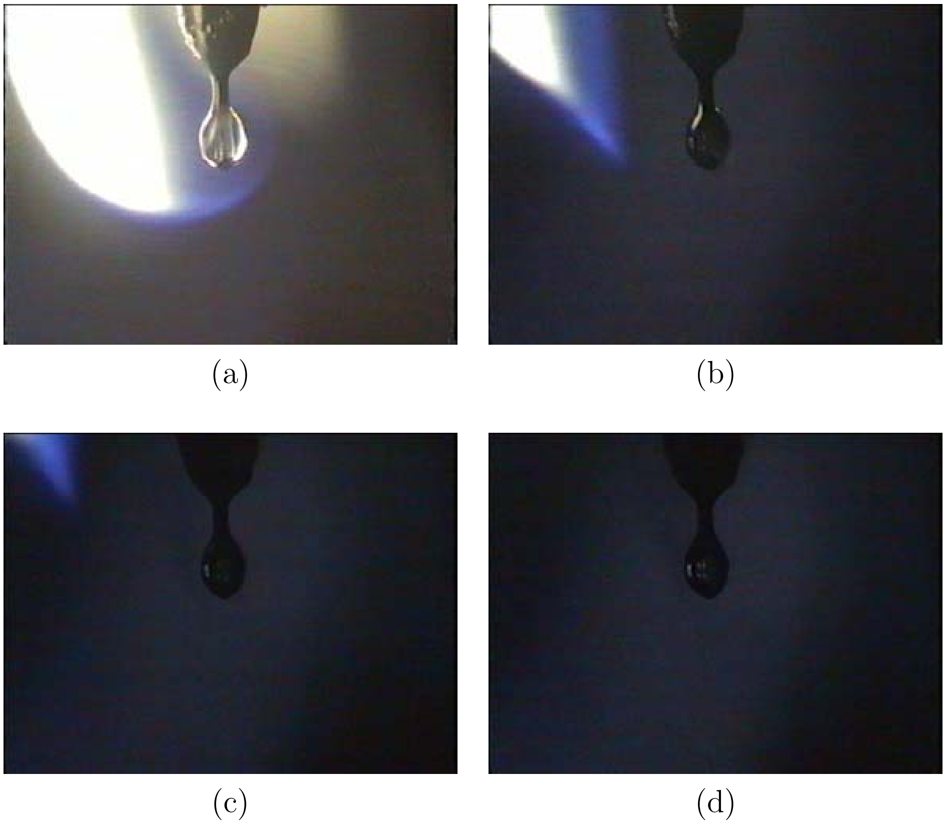

(a) (b)

(c) (d)

Figure 3.18: A sequence of images showing the extinction process of the flame surrounding a JP-8 fuel droplet. The time span between the consequetive images was approximately 33 ms. The sound pressure level was 140.8 dB, and the estimated strain rate at extinction for this case was 230 $s^{-}1$.

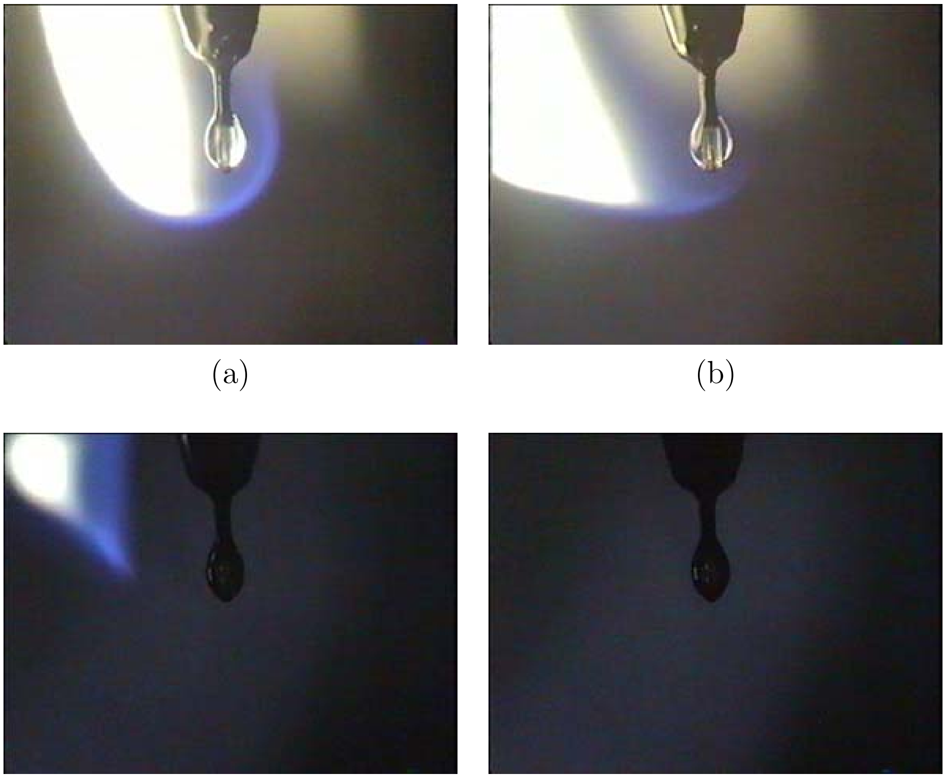

(a) (b)

(c) (d)

Figure 3.19: A sequence of images showing the extinction process of the flame surrounding a JP-8/FT fuel blend droplet. The time span between the consequetive images was approximately 33 ms. The sound pressure level was 141.8 dB, and the estimated strain rate at extinction for this case was 350 s^-1.

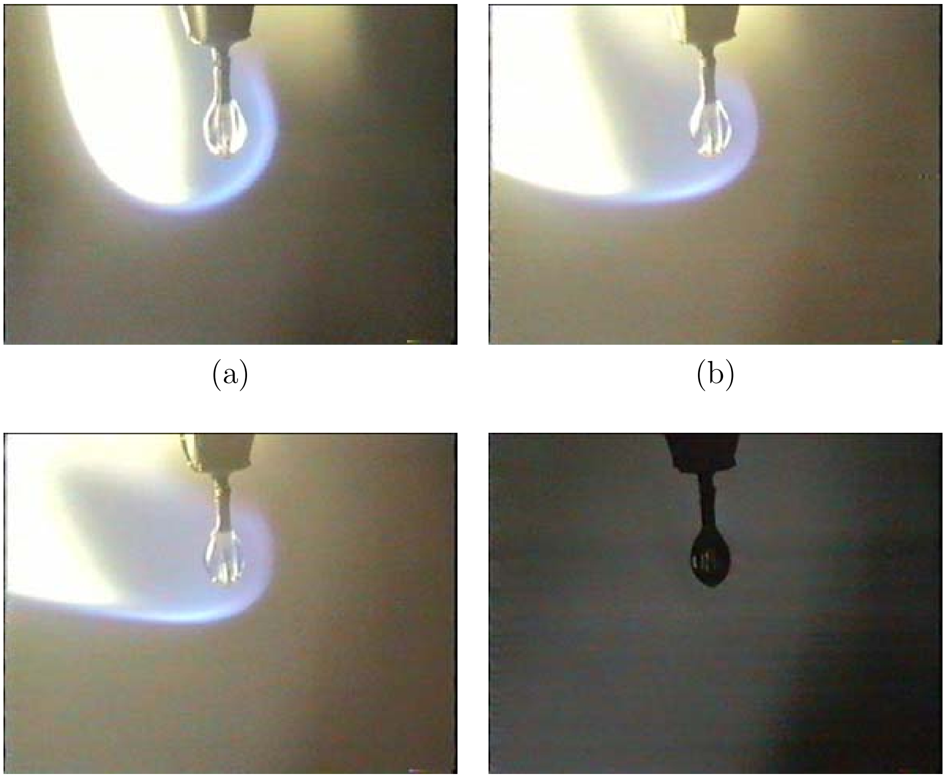

(a) (b)

(c) (d)

Figure 3.20: A sequence of images showing the extinction process of the flame surrounding an FT fuel droplet. The time span between the consequetive images was approximately 33 ms. The sound pressure level was 141.6 dB, and the estimated strain rate at extinction for this case was 360 $s^{-}1$.

CHAPTER 4

Experimental Set-Up and Methodology

The experiments in the non-reactive shear-coaxial study were conducted in the cryogenic supercritical flow facility (EC-4) at the Air Force Research Laboratory located at Edwards Air Force Base, CA. This facility was primarily designed to study non-reactive flows under different pressure (at or well above standard atmosphere) and temperature (at or well below room temperature) conditions. Accordingly, it is equipped with a high-pressure supply line of ambient temperature N_2, which was used as both the pressurizing and test fluid. In addition, liquid nitrogen (LN_2) was used as the chilling fluid for achieving the desired test fluid temperature. A detailed set of standard operating procedures (SOP) for using this facility are given in Appendix B.

In the following subsections, a brief description of the major components of the high pressure chamber and flow facility will be given followed by the main test articles, which are the shear-coaxial injectors. An overview of the acoustics generation and image visualization techniques are then discussed. A detailed discussion of the analysis method of the acquired high-speed image data are presented. Finally, the inherent experimental errors, and their propagation to the resulting uncertainties in the reported measured quantities are discussed.

4.1 High Pressure Chamber and Flow Facility

A schematic of the experimental facility is shown in Figure 4.1. The main pressure chamber, which is made of 304 stainless steel, was designed to operate at pressures up to 13.8 MPa (136 atm). It had four optical access ports on its lateral faces, two of which were used for installing the acoustic waveguides. The remaining two ports on opposite faces (not shown in Figure 4.1) measure 12 cm in diameter and were closed with Sapphire windows. It had additional holes and ports on the top and bottom faces for providing access to chamber pressurization and vent lines, test fluid inlets, and different instrumentation cables.

The chamber was mainly pressurized with ambient temperature N_2 tapped off from a high-pressure supply line. A pressure regulator reduced the incoming high-pressure gas, which was then flown to the chamber via a metering valve as shown in the chamber pressurization line in the piping and instrumentation diagram in Figure A.1 in Appendix A. A controlled rate of pressure build-up was then attained by adjusting the coarse and fine thread metering valves placed on the chamber vent line. This resulted in a continuous purging of the chamber. A ball valve placed on a bypass vent line remained closed during normal operating conditions, and was fully opened to completely vent the system.

Although flowing an ambient temperature high-pressure N_2 was the primary means of pressurizing the chamber, the inner and outer jet flows issued from the injector also contribute to pressurizing the chamber. Similar to the chamber pressurization flow, the inner jet flow was tapped off from the high-pressure supply line, and reduced to a calibrated inlet pressure of a Porter mass flow meter (a 200 slpm model 123-DKASVDAA). A fine thread metering valve placed downstream of the mass flow meter was used to adjust to the desired testing mass flow rate. Temperature conditioning of the inner jet was achieved using a simple heat exchanger whereby the warm inner jet flew through a 1/8 inch coiled 316 stainless steel tube placed in a 1/2 inch tube flowing LN_2. The plumbing was arranged so that either a coflow or counterflow arrangement was possible. Due to the desired low inner jet temperatures, and its enhanced heat transfer characteristics, the counterflow arrangement was used in all of the present experiments.

The outer jet flow set-up was identical to that of the inner jet with only minor differences. Since some of the test cases required relatively large outer jet mass flow rates, a 500 slpm mass flow meter of the same Porter model was used. In addition, both a coarse and fine thread metering valves were used. A two-step chill-down of the outer jet using a coflow (HE-0208 in Figure A.1) followed by a counterflow (HE-0209) concentric tube heat exchanger was possible. The former utilized LN_2 that was already used to chill-down the inner jet flow, and was used for prechilling the outer jet flow before passing on to the main (counterflow) heat exchanger. The prechiller was used only for test cases that required enhanced cooling of the outer jet flow.

As mentioned above, LN_2 stored in a 2,850 L supply tank was used to chill-down the inner and outer jet flows to the desired testing temperatures. The ullage pressure of the tank was maintained at a constant pressure of about 410 ± 30 kPa. For a constant inner and outer jet mass flow rates, the heat transfer was controlled by adjusting the LN_2 flow rate using needle valves placed downstream of the heat exchangers on the LN_2 exhaust line.

4.2 Shear-Coaxial Injectors

The shear-coaxial injector consisted of concentric straight tubes, where the inner jet was flown through the center tube while the outer jet was flown through the annulus. All injector parts were made of 316 stainless steel. A schematic of a section view of the entire injector assembly is shown in Figure 4.2.

The inner jet was introduced through the top inlet hole of the assembly, and enters a small plenum, which served as a settling chamber for the inner jet flow. An Omega EMQSS-020E, Type E, unshielded, 0.5 mm sheath diameter thermocouple inside the plenum measured the injector inlet temperature. A Kulite XCE-093-50D differential pressure transducer placed at the plenum wall provided measurements of any flow disturbances in the upstream section of the injector. The inner jet fluid then exited the injector down through a 7.6 cm straight tube connected to the plenum.

The outer jet was introduced into a settling chamber through two ports located on the side of the assembly. A Kulite CCQ-093-750A absolute pressure transducer and a similar thermocouple as for the the inner jet were also used for the outer jet. The outer jet fluid was then led down a funnel section to a 4.3 cm long straight tube, which constituted the outer jet injector. Since the inner jet tube passed through the entire outer jet injector section of the assembly, it created an annular tube configuration. Hence, heat transfer between the inner (core) jet and outer (annular) jet took place from the outer jet plenum to the injector exit.

As discussed in the Introduction, two parameters were varied for the two types of injectors considered in this study: the ratio of the inner jet tube thickness to the inner jet tube I.D., and the outer jet to inner jet cross-sectional area ratio. Figure 4.3 shows a schematic, and Table 4.2 below gives a summary of the dimensions of the injector exit. The injector with the large area ratio (LAR) and thin inner tube post was labeled ‘LAR-thin’ while the injector with the small area ratio (SAR) and thick post was labeled ‘SAR-thick’.

In order to ensure that a fully-developed turbulent flow emerged at the injector exit, the inner and outer jet Re were determined based on the typical entrance length estimation for turbulent flows as given by $X_E/D = 4.4Re^{1/6}$ [**?**]. The LAR-thin injector had an X_E/D of 109 for the inner jet, and 29 for the outer jet, where D for the outer

Table 4.1: Injector exit dimensions (mm)

Injector	D_1	D_2	D_3	D_4	t/D_1	A_o/A_i
LAR-thin	0.70	0.89	2.44	3.94	0.13	10.6
SAR-thick	1.47	3.96	4.70	6.35	0.84	2.90

jet is the hydraulic diameter of the annulus. The SAR-thin had an X_E/D of 52 and 62 for the inner and outer jets, respectively.

4.3 Inner Chamber: Acoustic Waveguide and Characterization

The inner chamber consisted of an acoustic waveguide attached to each side of a rectangular test section as shown in Figure 4.1. In order to provide optical access for backlighting and camera view, the front and back walls of the test section was made of 1.3 cm thick acrylic pieces. Three Kulite XCQ-093-50D differential pressure transducers were placed flush with the inside face of the back acrylic wall on the far side of the camera. One pressure transducer was placed at the same transverse location as the injector while the other two were located equidistant on either side of the center. A solid piece of stainless steel plate covered the bottom of the test section with an exhaust hole in the middle, while a perforated place with a hole for inserting the injector tube covered the top of the test section. The size of the perforations were much smaller than the wavelengths of the acoustic waves generated during testing, and provided a means for maintaining pressure equilibrium between the inner and main sections of the pressure chamber.

The acoustic waveguide was contoured so as to provide a smooth transition from the circular cross-section of the acoustic sources to the rectangular cross-section of the test section. These acoustic sources, known as piezo-sirens, were custom-designed and built by Hersh Acoustical Engineering, Inc. They can generate sound pressure levels exceeding 180 dB near their design operating frequency of 3 kHz. Since the experiments were conducted at elevated chamber pressures, as high as 36 atmospheres, these piezo-sirens provided the ideal means for generating acoustic waves in the high density medium. Pictures of one of the two piezo-siren elements and acoustic waveguides are shown in Figures 4.4a and 4.4b.

A 2-channel Fluke 292 waveform generator supplied continuous sine wave signals, which were amplified via Trek PZD2000A high-voltage amplifiers, to each piezo-siren. The waveform generators output signals were locked in frequency. However, their phase difference was varied in order to create a pressure antinode (PAN) and pressure node (PN) conditions at the injector location as measured by the center pressure transducer.

4.4 Measurement of Physical Properties

The physical parameters of the coaxial jet flow, namely J, were determined based on the injector exit flow properties. The jet exit temperatures were measured using an Omega EMQSS-010E, Type E, unshielded, 0.25 mm sheath diameter thermocouple mounted on a pair of linear positioners, and placed within a distance D_1 downstream of the injector exit plane. Two linear positioning stages ANPx51 manufactured by Attocube Systems AG provided a 3 mm back-and-forth, and a 6 mm transverse range of motions with a resolution on the order of microns. This enabled the measurement of the jet exit temperature profile, from which the inner jet and outer jet core temperatures were extracted. With knowledge of two state properties, the exit T and P, all other thermophysical properties of the jet were evaluated using NIST REFPROP [61] tables.

All of the instrumentation (pressure tranducer, thermocouple, and mass flow meter) data recordings were sychronized with the image frame recordings. Pacific Instruments PI 6013, 6017, 6030 and 6030HF data acquisition boards with the PI 660 Acquistion and Control Software were used for all data acquisition and recording tasks.

4.5 Jet Visualization

The primary means of studying the coaxial jet flow dynamics was provided by back-lit high speed images. A variable power Newport model 66986 that ran a 300 W Xe lamp, and emitted a collimated beam in the near ultraviolet spectrum, was used as the back-light source. Differences in the refractive index of the jets and the surrounding medium provided the necessary distinction between the fluids of interest. The denser inner jet, due to its low temperature, appeared as a dark column of fluid as viewed by the high-speed camera on the opposide side of the light source. The less dense outer jet was also in many cases distinguishable from the relatively warmer, and hence, even less dense ambient N_2 in the chamber. Examples of such back-lit images of the coaxial jet stream are shown in Figure 4.5 for a subcritical and nearcritical flow using the LAR-thin injector.

Phantom v7.1 and v710 high-speed cameras were used to capture the fast dynamical processes inherent to an unforced coaxial jet flow as well as those present during a high frequency acoustic forcing. Image framing rates of 25 kHz were used in order to avoid aliasing of up to the fourth harmonic of the forcing frequency. An external trigger was used to start recording the image frames, which were sychronized to the Kulite dynamic pressure transducer recordings at the sample rate of 25 kHz using an IRIG-B timecode.

4.6 Measurement of Dark-Core Length

The measurements reported as the "dark-core length" in this document refer to the axial length of the dark-core. Accordingly, the goal was to identify the longest contour line that outlined the dark-core structure attached to the injector body. In order to do this, first each image with an 8-bit depth grayscale was converted to a binary image using the *im2bw* subroutine after obtaining a thresholding constant derived from the *graythresh* subroutine, both of which are found in the MATLAB® image processing toolbox. The thresholding was done based on Otsu's method [62]. Then, the dark regions in the binary image whose contour lines where connected to that of the injector body, also a dark region, were identified. This ensured that the dark structures considered were part of the unbroken portion of the inner jet starting from the injector exit. Finally, the countour line with the maximum continuous length represented the boundary of the dark-core that was sought for. Figure 4.6 shows the major steps involved in identifying the dark-core contour line. An automated routine repeated the above steps for 1000 image frames.

The dark-core length was computed by measuring the distance in pixels from the bottom of the injector to the largest row pixel on the dark-core contour line. The injector body width (the outer injector's outer diameter, D_4) in pixels was used as a scaling factor for converting the dark-core length in pixels to millimeters. The standard deviation of the mean for the sample of 1000 images was also computed.

4.7 Proper Orthogonal Decomposition of Pixel Intensity Data Array

Proper orthogonal decomposition (POD), also known as Principal Component Analysis (PCA), has proven to be a powerful means for extracting relevant qualitative and quantitative information from an otherwise complicated and noise-ridden measurement data. Berkooz *et al.* [63] and Chatterjee [64] give an in-depth discussion on the fundamentals of POD. Arienti and Soteriou [65] show its application to high-speed image analysis, where a pixel intensity data matrix, $\mathbf{A}$, for a set of images is represented as

$$\mathbf{A} = \sum_{k=1}^{N} a_k(t)\phi_k(x) \tag{4.1}$$

where a_k are vectors of temporal amplitude coefficients, ϕ_k are vectors of proper orthogonal modes, k is the mode number, and N is the number of modes.

In a similar manner, in the present study, POD was used to extract the most dominant and periodic coherent flow structures in the recorded high-speed image frames. However, in order to implement this method, the pixel intensities, which are the measured parameters used to identify the flow structures, had to be arranged into a single aggregate data array for all image frames. This was achieved by first forming a row vector consisting of all pixel intensity values of each image frame (of resolution n rows by m columns) in order of increasing columns, followed by increasing rows as depicted in Figure 4.7a. Then, all such row vectors were combined for a sequence of N image frames, resulting in a matrix $\mathbf{A}$ consisting of N rows by $M(= n \times m)$ columns of intensity values as shown in Figure 4.7b. Thus, $\mathbf{A}$ is an array of N sets of M pixel intensities in a single frame.

Furthermore, as the goal was to identify periodic coherent structures, the intensity fluctuations need only be considered. Thus, the temporal mean of each pixel intensity was subtracted resulting in a matrix of intensity fluctuations $\tilde{\mathbf{A}}$. That is,

$$\tilde{\mathbf{A}}_{ij} = \mathbf{A}_{ij} - \frac{1}{N}\sum_{i} \mathbf{A}_{ij} \tag{4.2}$$

where $i = 1...N$, $j = 1...M$. Figure 4.8a shows a single image frame, and Figure 4.8b shows the corresponding averaged image for $N = 10^3$ frames.

Typically, $\tilde{\mathbf{A}}$ is a rectangular matrix where $N < M$. A singular value decomposition (SVD) can be readily computed for a non-square matrix as opposed to eigenvalue decomposition, which can only be applied to a square matrix. The geometric interpretation of SVD as well as its relation to eigenvalue decomposition is discussed in Chatterjee [?]. The SVD of $\tilde{\mathbf{A}}$, represented as

$$\tilde{\mathbf{A}} = \mathbf{U}\mathbf{S}\mathbf{V}^T, \tag{4.3}$$

was computed in MATLAB® resulting in an $N \times N$ orthogonal matrix $\mathbf{U}$, an $N \times M$ diagonal matrix of singular values $\mathbf{S}$, and an $M \times M$ orthogonal matrix $\mathbf{V}$. However, since $N << M$, only the first N diagonal elements of $\mathbf{S}$ and the first N columns of $\mathbf{V}$ are non-zero. Accordingly, it was computationally more efficient to reduce $\mathbf{S}$ and $\mathbf{V}$ to an $N \times N$ and $M \times N$ matrices, respectively.

By convention, since the singular values are arranaged in descending order of magnitude, the columns of $\mathbf{U}$ and $\mathbf{V}$, which represent an orthonormal bases set of the column and row space of $\tilde{\mathbf{A}}$, respectively, were arranged in a corresponding manner. Furthermore, each column of $\mathbf{Q} = \mathbf{US}$, equivalent to $a_k(t)$ in Equation 4.1, is a vector of time-dependent amplitude coefficients, while the columns of $\mathbf{V}$ are the proper orthogonal modes. The first column of $\mathbf{Q}$ may thus be interpreted as containing the temporal characteristic of the coherent flow structure of the first (most) dominant mode, and the first column of $\mathbf{V}$ as containing the spatial distribution of the first mode, and so on, for subsequent columns. Figure 4.9 shows a plot of the singular values for all $N = 10^3$ modes of a baseline flow.

The spatial distrubution of mode-1, corresponding to the mode with the maximum singular value in Figure 4.9, was constructed from the first column of $\mathbf{V}$ as shown in Figure 4.10a; this is called the proper orthogonal mode (POM) image. As stated earlier, because only the fluctuation in intensity levels were considered, the background fluid and the relatively uniform portion of the inner jet flow were subtracted out, and thus, were depicted by a gray region to indicate a mean level in a gray-scaled image. Lobes of dark and light regions indicate locations where fluid (emanating from the dense inner jet flow) was present and absent, respectively. Moreover, at a given downstream location, the presence of identical adjacent lobe regions indicates the formation of symmetric structures about the inner jet, while a dark region next to a light one indicates asymmetry. The spatial distributions of subsequent modes could be constructed similarly from the remaining columns of **V**.

The frequency content of these coherent lobe structures were obtained from the power spectral density (PSD) plots of each column of **Q**. Figure 4.10b shows one such plot for mode-1 obtained from the first column of **Q**. It represents how the magnitude of the intensity fluctuation is distributed with frequency. A peak in the spectrum denotes a recurring flow structure that originates from the inner jet flow with the associated peak frequency. Similarly, the POM image and PSD plot for mode-2 are shown in Figures 4.10a and 4.10b, respectively.

The product of a column vector in **Q** with a corresponding row vector in $\mathbf{V}^T$ gave the time progression of the spatial distribution represented by a single mode, such as in Figure 4.10a for mode-1. Figure 4.11a shows a time sequence of frames of images represented by mode-1. This sequence reveals that the dynamics captured by mode-1 merely represent a standing wave type of progression in time of the flow structures. However, it can easily be shown in 1-D waves that the superposition of two standing waves $\psi_1 = B\cos(kx)e^{i\omega t}$ and $\psi_2 = B\cos(kx-\phi)e^{i(\omega t-\phi)}$ with similar amplitude and frequency, and a spatial and temporal phase difference $\phi = \pm 90^o$ will be a traveling wave. That is,

$$\begin{aligned} \psi &= \psi_1 + \psi_2 \\ &= B\left(\cos(kx) - i\sin(kx)\right)e^{i\omega t} \\ &= Be^{i(kx-\omega t)} \end{aligned} \tag{4.4}$$

Arienti and Soteriou [65] define conjugate mode pairs as any two modes whose cross-power spectra magnitude peaks near a phase of $\pm 90^o$, such as the one shown in Figure

4.12 for mode-1 and mode-2, and are represented by similar lobe patterns. The cross-power spectral density of a conjugate mode pair with temporal amplitude coefficients, a_k and b_k was computed as

$$\text{CPSD} = \sum_{s=0}^{N-1} \text{corr}(a_k, b_k) e^{-i\omega s} \tag{4.5}$$

where $\text{corr}(a_k, b_k)$ represents the cross-correlation of a_k and b_k. Therefore, the superposition of the two modes resulted in a lobe pattern that convected downstream as time progressed. Figure 4.11b shows a time sequence of frames for the superposition of mode-1 and mode-2. It is distinguished from Figure 4.11a in that the coherent flow structures are convected downstream with each time step.

4.8 Measurement Uncertainty

As do all measured quantities, the measurement results reported in this document have an inherent uncertainty in them. These uncertainties arise both from the systematic or bias error associated with the measurment devices or the repeatability of individual measurements commonly knows as precision errors. It is important to realize the limitation of a measurement on how accurately it represents the true value, and even more importantly, to keep track of how that measurement uncertainty propagates to other parameters that are defined by the measured quantities. Thus, error propagation was performed on the measured physical parameters with significant sources of error in order to determine the appropriate degree of accuracy with which to report other dependent physical quantities.

These dependent quantities mainly pertain to the calculated jet exit velocities, velocity ratios, and momentum flux ratios, which depend on the measured mass flow rates, exit area, and density, which, in turn, depends on the measured exit temperature and static pressure. The precision errors in all of the high frequency data samples acquired during the mass flow rate, temperature and pressure measurements were significantly smaller than the bias errors of the measurement devices. Hence, only bias error propagation was considered.

The jet exit velocities were determined using the relation

$$U_k = \frac{\dot{m}_k}{\rho_k A_k}, \tag{4.6}$$

where $k \equiv$ i, o for the inner and outer jet flows, respectively. Following the standard rule of error propagation for a function of several variables [66], the uncertainty in the calculated jet velocities was determined as

$$\delta U_k = U_k \sqrt{\left(\frac{\delta \dot{m}_k}{\dot{m}_k}\right)^2 + \left(\frac{\delta \rho_k}{\rho_k}\right)^2 + \left(\frac{\delta A_k}{A_k}\right)^2} \tag{4.7}$$

Similarly, the uncertainty in the momentum flux, $M_k \equiv \frac{\dot{m}_k{}^2}{\rho_k A_k}$, was

$$\delta M_k = M_k \sqrt{4\left(\frac{\delta \dot{m}_k}{\dot{m}_k}\right)^2 + \left(\frac{\delta \rho_k}{\rho_k}\right)^2 + \left(\frac{\delta A_k}{A_k}\right)^2} \tag{4.8}$$

Vendor calibration reports provided the measurement uncertainties for the mass flow meters and the pressure transducer. The Porter mass flow meters had an accuracy of ±1.0% full scale, and the Stellar absolute pressure transducer was accurate to within ±0.02% full scale. Accordingly, the uncertainties in the measured mass flow rates were ±36 mg/s and ±97 mg/s for the inner and outer jets, respectively, while that for the chamber pressure was ±0.004 MPa. The uncertainty in the thermocouple measurements determined based on a calibration using an RTD [58, 46] were ±1 K.

As stated previously, the exit jet densities were evaluated, based on the measured exit temperatures and chamber pressure, using NIST REFPROP [61] tables. According to [67], as long as the error from a particular source is significantly smaller than all other sources of error, it is ignored. Since density has a much weaker dependence on pressure than on temperature, the uncertainty in density due to pressure variation was ignored. Thus, for the purpose of measurement error analysis in this study, $\rho(p, T) \approx \rho(T)$.

Finally, the uncertainties in the momentum flux ratio and velocity ratio were determined as

$$\delta J = J\sqrt{\left(\frac{\delta M_o}{M_o}\right)^2 + \left(\frac{\delta M_i}{M_i}\right)^2} \tag{4.9}$$

and

$$\delta R = R\sqrt{\left(\frac{\delta U_o}{U_o}\right)^2 + \left(\frac{\delta U_i}{U_i}\right)^2}, \tag{4.10}$$

respectively.

The precision uncertainty in the L/D_1 values reported was as the standard deviation, σ, for a total of 1000 measurements. That is, one standard deviation represented uncertainty in the L/D_1 measurement from a single image. It should be noted that for such a large sample size, the uncertainties in the mean, given by the standard deviation of the mean ($\sigma_{mean} = \sigma/\sqrt{1000}$), of the measured dark-core lengths were negligible.

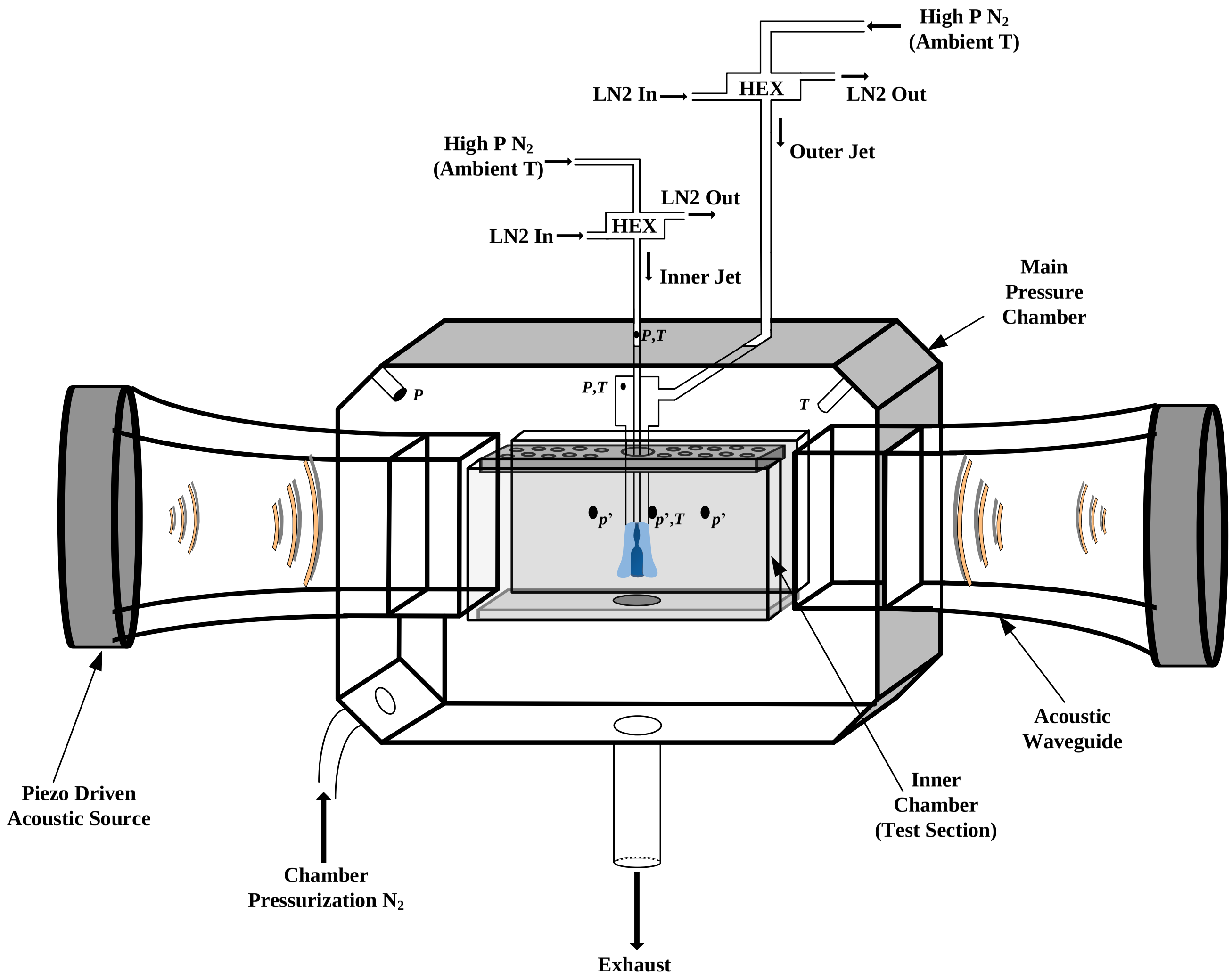
High P N$_2$
(Ambient T)
LN2 In
HEX
LN2 Out
Outer Jet
High P N$_2$
(Ambient T)
LN2 Out
LN2 In
HEX
Inner Jet
Main
Pressure
Chamber
P,T
P,T
P
T
p'
p',T
p'
Piezo Driven
Acoustic Source
Chamber
Pressurization N$_2$
Exhaust
Inner
Chamber
(Test Section)
Acoustic
Waveguide

Figure 4.1: A schematic of the chamber and peripheral lines.

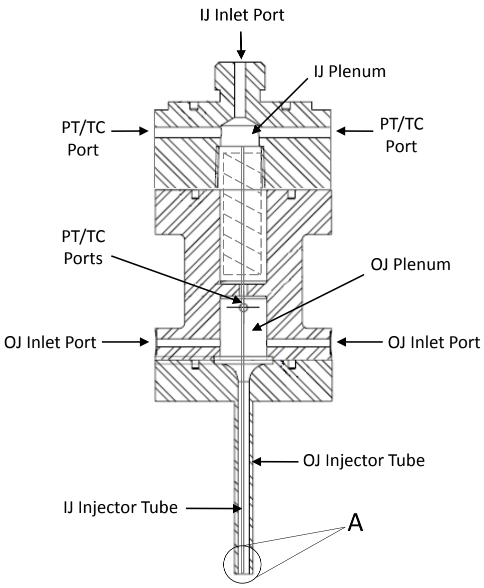
IJ Inlet Port
IJ Plenum
PT/TC Port
PT/TC Port
PT/TC Ports
OJ Plenum
OJ Inlet Port
OJ Inlet Port
OJ Injector Tube
IJ Injector Tube
A

Figure 4.2: A schematic of the shear-coaxial injector assembly (expanded view of **A**: See Figure 4.3).

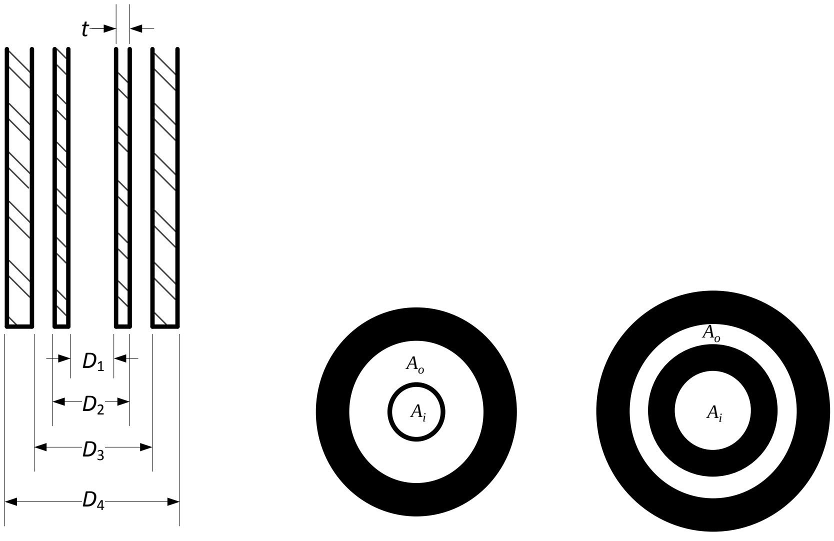
t
D1
D2
D3
D4
Ao
Ai
Ao
Ai

(a) Expanded view of **A** (b) LAR-thin (c) SAR-thin

Figure 4.3: A schematic of the shear-coaxial injector exit.

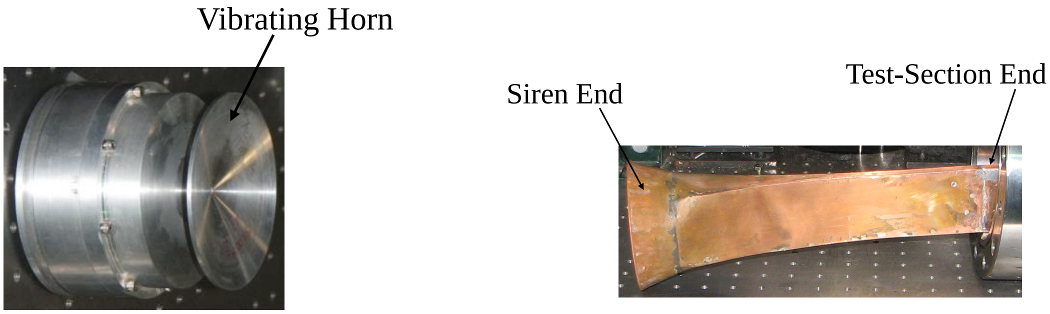

(a) Piezo-siren (b) Acoustic waveguide

Figure 4.4: Pictures of the acoustic elements. Acoustic waves generated by the piezosiren enter the end of the waveguide of circular cross-section and propagate down to the test-section of rectangular cross-section .

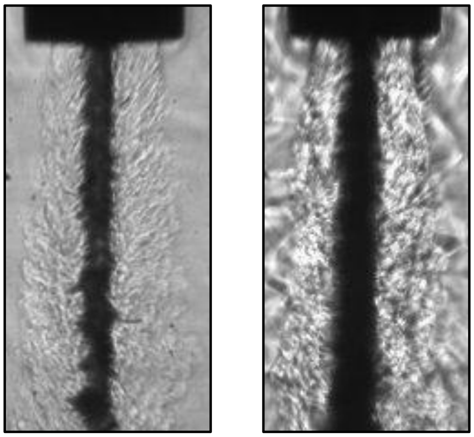

(a) (b)

Figure 4.5: Back-lit images of baseline LAR-thin injector flows at $J = 0.1$ where the chamber pressure, and the chamber, outer jet and inner jet temperatures were: (a) 1.5 MPa, 243 K, 198 K, 107 K, and (b) 3.57 MPa, 252 K, 195 K, 114 K, respectively.

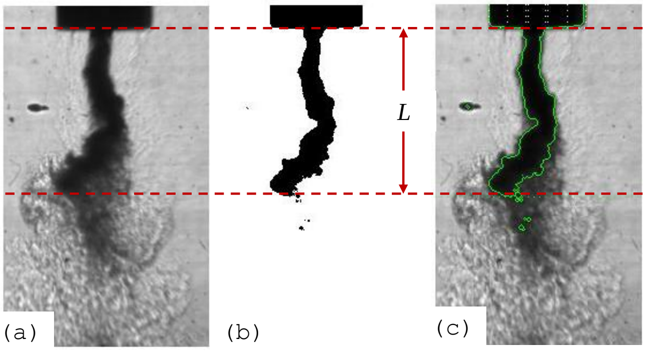

Figure 4.6: Measurement of dark-core length: (a) original image (b) black and white image after thresholding (c) Contour used to define the dark-core length (L).

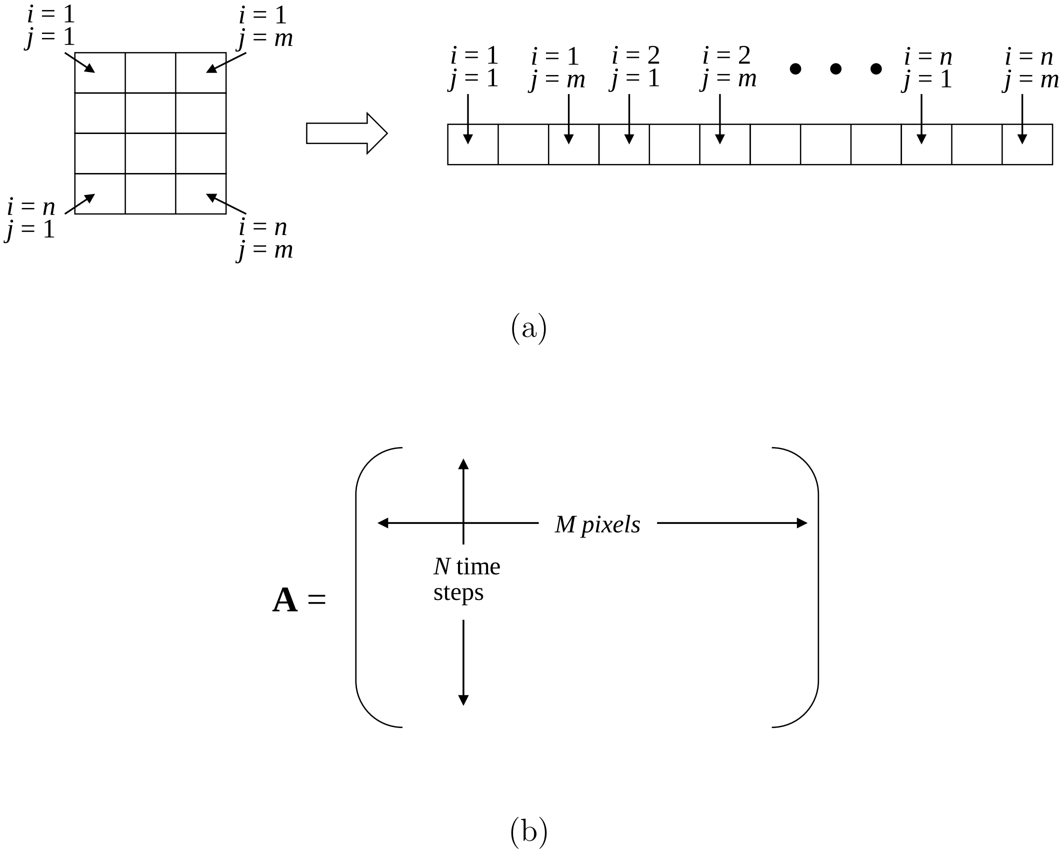
i = 1
j = 1
i = 1
j = m
i = n
j = 1
i = n
j = m
i = 1
j = 1
i = 1
j = m
i = 2
j = 1
i = 2
j = m
• • •
i = n
j = 1
i = n
j = m
(a)
A =
M pixels
N time steps
(b)

Figure 4.7: Illustration of (a) how pixel intensity values from a single image are arranged into a row vector; (b) the construction of $\mathbf{A}$, data matrix of pixel intensities.

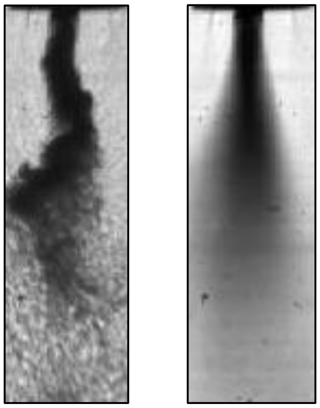

(a) (b)

Figure 4.8: PN forced ($f_F = 3.12$ kHz) LAR-thin injector flow at $P_r = 0.44$, $J = 5.2$: (a) a snapshot image captured at 25 kHz; (b) a time-averaged image from 1000 consecutive images.

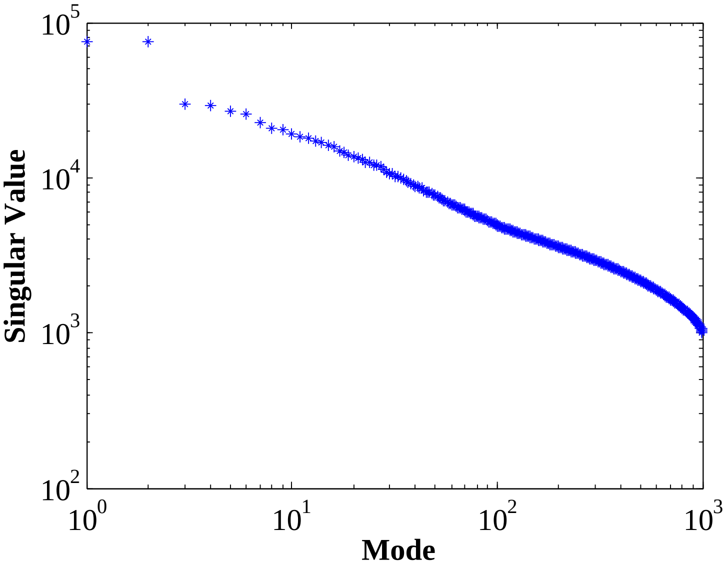

Figure 4.9: Singular values for PN forced ($f_F = 3.12$ kHz) LAR-thin injector flow at $P_r = 0.44$, $J = 5.2$.

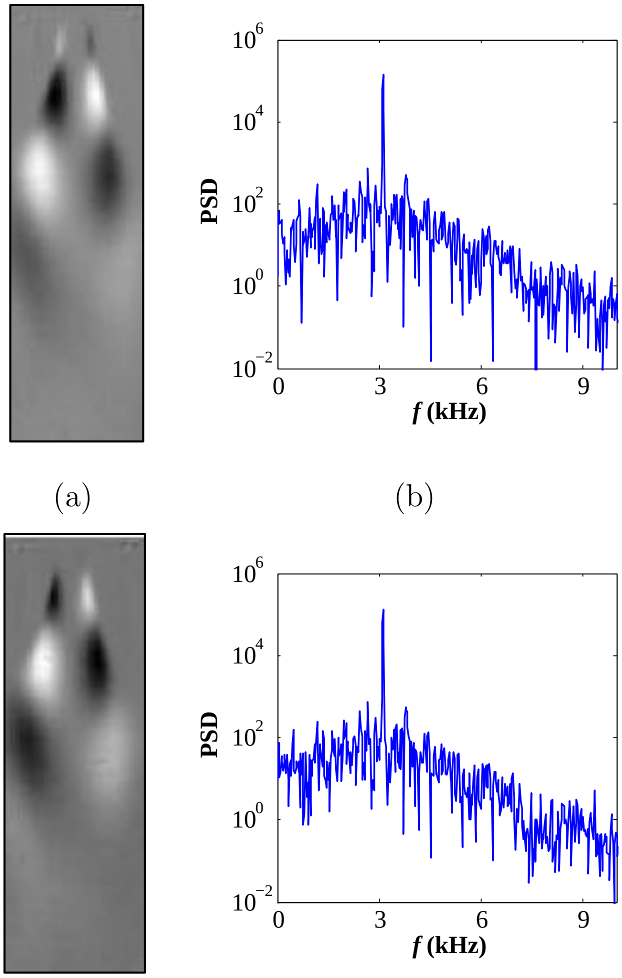

(a) (b)

(c) (d)

Figure 4.10: Proper orthogonal mode (POM) image and power spectral density (PSD) of the temporal amplitude coefficients for PN forced ($f_F = 3.12$ kHz) LAR-thin injector flow at $P_r = 0.44$, $J = 5.2$: mode-1 (a) POM, (b) PSD; mode-2 (c) POM (d) PSD.

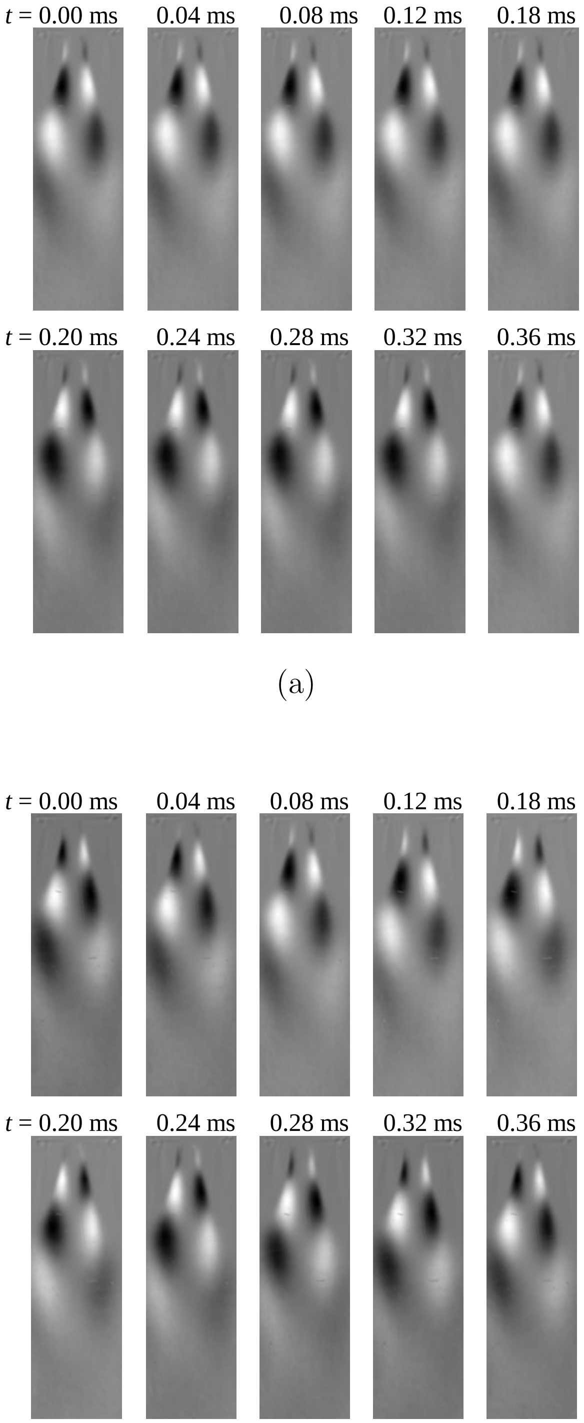

(a)

(b)

Figure 4.11: A time sequence of POM images for PN forced ($f_F = 3.12$ kHz) LAR-thin injector flow at $P_r = 0.44$, $J = 5.2$: (a) mode-1 only, (b) superposition of mode-1 and mode-2.

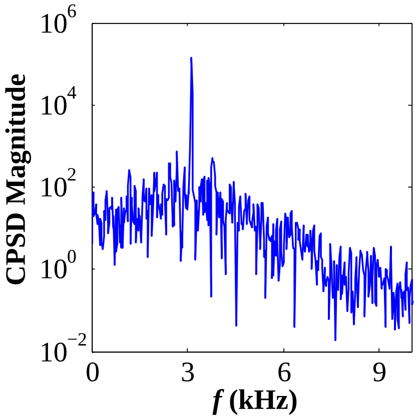

(a)

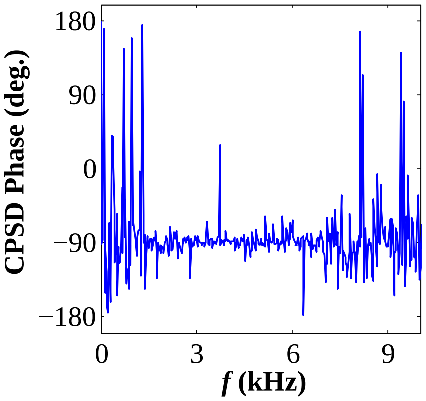

(b)

Figure 4.12: Cross-power spectral density (CPSD) of mode-1 and mode-2 for PN forced ($f_F = 3.12$ kHz) LAR-thin injector flow at $P_r = 0.44$, $J = 5.2$: (a) magnitude, (b) phase.

CHAPTER 5

Shear-Coaxial Jets: Results and Discussion

The experiments done under subcritical (reduced pressure, $P_r = 0.44$) pressure conditions were such that the inner jet was in the liquid phase, while the outer jet was in the gas phase at temperatures well above the saturation temperature of N_2. Under transcritical (reduced pressure, $P_r = 1.05$) conditions, the inner jet temperatures were below the critical temperature, while that of the outer jet were well above the critical temperature, thereby resulting in a supercritical outer fluid. A summary of all the flow conditions and parameters is given in Tables C.1 and C.2 in the Appendix. As previously noted, for coaxial jets of different densities, the outer to inner jet momentum flux ratio, J, is one of the governing parameters of coaxial jet mixing. In the present work, for a set of test conditions in a particular pressure regime, the outer-to-inner jet density ratio ($S = \rho_o/\rho_i$) was held approximately constant while R was varied. Thus, the variation in J in these studies resulted mainly due the variation in R.

Although the goal was to maintain constant inner jet flow conditions, small changes were necessary to achieve subcooled or subcritical inner jet exit temperatures at higher J values. This was due to the enhancement in heat transfer between the coaxial jet while flowing down the concentric injector tubes. This was especially challenging with the LAR-thin inner jet flow because the ratio of outer to inner jet volume per unit tube length was considerably larger for this injector. Thus, the LAR-thin injector inner jet temperature was much more sensitive to the outer jet flow rate. Since a liquid inner jet was desired at the exit, maintaining a low exit inner jet temperature required lowering the outer jet mass flowrate. This can be explained by considering a simple energy balance, assuming small changes in the specific heat constants, between the coflowing jets inside the injector as follows:

$$\text{Injector} : T_{i,\text{exit}} = T_{i,\text{inlet}} + \frac{(\dot{m}c_p\Delta T)_o}{(\dot{m}c_p)_i}. \tag{5.1}$$

As Equation 5.1 shows, lowering the outer jet mass flowrate enabled to reduce the heat gained by the inner jet. However, in order to achieve the desired high J, the inner jet mass flowrate also had to be reduced. In addition, a reduction in the inner jet mass flowrate also assisted in lowering the injector inlet temperature of the inner jet. This may be deduced from Equation 5.2, which shows a similar simple energy balance between the inner jet fluid and the coolant LN_2 flowing the the heat exchanger:

$$\text{Heat Exchanger} : T_{i,\text{exit}} = T_{i,\text{inlet}} + \frac{(\dot{m}c_p\Delta T)_{\text{LN}_2}}{(\dot{m}c_p)_i}. \tag{5.2}$$

5.1 Shear-Coaxial Jets without Acoustic Forcing

5.1.1 Qualitative Characteristics of Baseline Flows

As mentioned previously, the high-speed images were obtained at framing rates that exceeded three times the highest frequency of the dominant baseline flow structures. Although the overall flow dynamics cannot be captured in a single snapshot image, this section will give a brief account of the general observable behavior of the coaxial jets for the two injector configurations with varying J at the different chamber pressure regimes. Since the back-lit images only revealed the dense inner jet flow, the discussion will be limited to the dark-core flow region and the identifiable flow structures on its periphery. It is to be noted that the inner jet tube for the LAR-thin injector was not perfectly flush, but stuck out by about $0.2D_1$. This allowed for direct visual confirmation that the inner jet injector tube was not oscillating due to turbulent flow disturbances in the outer jet.

Figure 5.1 shows the baseline LAR-thin injector flows of various momentum flux ratios at $P_r = 0.44$. At $J = 0.1$, the presense of the very low momentum outer jet flow had minimal impact on the development of the liquid inner jet flow. The low aerodynamic Weber number ([68] $\mathrm{We}_o \equiv \rho_o(U_o - U_i)^2 * D_1/\sigma \approx 21$) for this low J flow enabled the inner jet to maintain coherence for over $20D_1$ downstream of the exit, which is about where the field of view in the image ends. Although small periodic surface wrinkles started forming about $10D_1$ downstream of the exit, they were not large enough to disrupt the continuity of the jet. As the outer jet flow rate was increased resulting in $J = 0.5$, the dark-core region of the inner jet flow still stayed intact for over $20D_1$. However, surface instabilities were enhanced and occurred earlier than the lower J case. As J increased to higher than one, the dark-core region could no longer remain intact within the field of view, and broke up into fine droplet spray. The presence of a larger shear force at the jets' interface also aided in the formation of a fine mist of droplets on the periphery of the inner jet flow. Enhanced entrainment of the inner jet flow into the outer flow was evident in the increased spread of the inner jet. Higher J values aided in the break-up and dispersion of the inner jet and rapid mixing with outer jet at closer distances to the injector exit. Accordingly the dark-core length became shorter with increasing J. However, a much more gradual decrease in the dark-core region was seen over the range of higher momentum flux ratios, $J = 11 - 20$, than at the lower ones.

As Figure 5.2 shows, similar trends in the dark-core lengths were seen at $P_r = 1.05$ with increasing J. The dark-core again remained intact for the entire length of the image for the two lowest J flows ($J = 0.1, 0.5$). However, both flows showed increased spread as evident in the wider inner flow relative to the corresponding flows at $Pr = 0.44$. Despite being below the critical temperature at the exit, the lack of discrete structures and droplets emanating from the inner jet was due to the diminishing cohesive surface tension force as the critical point was approached, and its absence in the supercritical fluid regime. Since the temperature of the inner jet at the interface was supercritical, hence a supercritical fluid, the periphery of the inner jet did not form a well defined boundary like a liquid would. For $J = 1.9 - 12$, further decrease in the dark-core region was observed as J increased. The dark-core regions were also shorter compared to the flows with similar J values at $P_r = 0.44$.

Figure 5.3 shows the baseline SAR-thick injector flows at $P_r = 0.44$ and for J values similar to those of the LAR-thin flows. At $J = 0.1$, just as with the LAR-thin flow, the inner jet stayed intact and undisturbed along the entire field of view of about $13D_1$ in length. In contrast to the LAR-thin injector flow, the thick inner injector post created a unique flow field, whereby for this low J case, the low momentum outer jet fluid formed an axisymmetric recirculation zone just below the thick post and surrounding the inner jet flow. The sense of rotation of the recirculating flow was such that a local counterflow condition existed at the interface of the inner jet and the recirculation zone. At $J = 0.5$, there was a significant presence of surface irregularities that formed ligaments just a few D_1 downstream of the exit, and subsequently broke down and dispersed into droplets. Yet, the dark-core region still remained intact for the entire field of view. The recirculation zone also consisted of the outer jet fluid with small traces of droplets that came off the surface of the inner flow.

When the momentum flux ratio was increased to $J = 2.1$, higher entrainment by the outer flow caused most of the recirculation zone to be filled with the lower momentum inner jet fluid. The presence of the dense, dark fluid in the recirculation zone created a perception of "necking" in the dark-core flow. Further downstream, the dark-core could no longer maintain its coherence and was fully dispersed into droplets. By $J = 5.7$, the recirculation zone was completely filled with the inner jet fluid. The remaining inner jet fluid underwent increased dispersion resulting in a shorter dark-core. Together with the recirculation flow, the inner jet started forming a conical dark-core region. The shape of the conical dark-core region became well defined by $J = 10$, and the dark-core length was significantly reduced. Increasing to $J = 15$ and $J = 21$ showed relatively small decreases in the dark-core length.

Figure 5.4 shows the corresponding baseline SAR-thick injector flows at $P_r = 1.05$. At $J = 0.1$, the inner jet showed greater spread than its counterpart at the lower chamber pressure. It, nevertheless, maintain a long, intact dark-core region. The slightly darker fluid in the recirculation zone was evidence that the denser inner jet fluid was also present. An even more diffused inner jet flow at $J = 0.5$ resulted in a shorter dark-core region compared to the $P_r = 0.44$. At $J = 2.1$, the recirculation zone was fully filled with inner jet fluid, and a similar "necking" in the dark-core region was observed. Further increase in J resulted in shorter conical dark-core regions. Beyond $J = 9.2$, relatively small changes in the dark-core lengths were observed with increasing J. Moreover, the recirculation zone grew until and stayed constant beyond $J = 9.2$.

5.1.2 Baseline Dark-Core Length Measurements

The high-speed images showed that the back-lit coaxial jets created a silhouette of the relatively high density inner jet that formed a dark-core flow region in the images. As noted earlier, the axial length of the intact dark-core region was used to gauge the extent of mixing between the outer and inner jets. In an analogous manner, the length of an inner velocity potential core has been used to mark the extent of the inner shear-layer growth in coaxial jets. Thus, a dark-core length and a potential-core length may be considered as two different physical parameters that describe different aspects of flow processes pertinent to mixing of coaxial jets.

The baseline flow dark-core lengths, L_B were measured, normalized by D_1 and plotted versus J for the LAR-thin and SAR-thick injectors as shown in Figures 5.5 and 5.6, respectively. The dark-core lengths for the two lowest J flows ($J = 0.1$ and $J = 0.5$) were omitted since their dark-core region exceeded the field of view. Also included in these plots are the measurement uncertainties in single measurements of L_B/D_1, and the uncertainties in the reported J values. The rather large uncertainties in the higher J values, especially for the LAR-thin injector flows, were due to the large relative uncertainties in the inner jet mass flowrates in Equation 4.8. This was because lower inner jet mass flowrates were used in order to attain the desired flow temperatures as already discussed at the beginning of this chapter. On the other hand, the uncertainties in the L_B/D_1 for both injectors showed statistically significant decrease for lower J values, and relatively small differences for higher ones.

Figure 5.7 shows a power-law curve-fit of the form $c_1 J^{c_2}$, where c_1 and c_2 are constants, through each data set of L_B/D_1 for each injector at $P_r = 0.44$ and $P_r = 1.05$. It can be seen that at $P_r = 1.05$, the variation of L_B/D_1 with J was similar for both injectors, and was also in agreement with that obtained by Davis [58] and Rodriguez [46] using a different injector configuration, for which they reported $c_2 \approx 0.5$. In terms of the labeling convention used for the present work's injectors, Davis used a LAR-thick injector and Rodriguez used both a LAR-thick and SAR-thin injector. On the other hand, at $P_r = 0.44$, although both the LAR-thin and SAR-thick injectors again had comparable variation of L_B/D_1 with J, they did not agree well with the $c_2 \approx 0.2$ reported by Davis and Rodriguez. It was also shown that for a given J, the SAR-thick injector flows had consistently lower L_B/D_1 under both pressure regimes, and that for each injector and a given J, the L_B/D_1 at $P_r = 1.05$ was lower than that at $P_r = 0.44$. In general, it may be deduced that for a specific J baseline flow, the SAR-thick injector at elevated pressures had the most enhanced mixing.

A revision of the L_B/D_1 data that Rodriguez [46] and Leyva *et al.* [45] obtained using a LAR-thick injector, and Rodriguez [46] and Graham *et al.* [69] obtained using a SAR-thin injector were compared with the L_B/D_1 data from the LAR-thin and SAR-thin as shown in Figures 5.8 and 5.9 at $P_r = 0.44$ and $P_r = 1.05$, respectively. The dimensions for these injectors are given in Table 1.2. Unlike the flushed outer and inner injector tube exits used in the present study and those by Leyva *et al.*, Rodriguez, and Graham *et al.* introduced a $0.5D_1$ recess in the inner injector tube. However, at $P_r = 0.44$, there was negligible differences in L_B/D_1 between the flushed and recessed configurations of the SAR-thin injector. Moreover, for low J flows, the SAR-thick and SAR-thin injectors showed comparable L_B/D_1, which were significantly lower than that of the LAR-thin and LAR-thick injectors. This was in agreement with observations by Champagne and Wygnanski [31] and Gladnick *et al.* [38] that the potential core length is longer for larger area ratio. The large difference in L_B/D_1 between the LAR-thin and LAR-thick injectors may be attributed to the presence of the recirculation zone behind the thick inner tube post of the LAR-thick injector that entrained a significant portion of th inner jet fluid for $J \approx 2$ and higher. For large J, the data for all injectors appeared to asymptote to the same L_B/D_1. However, due to experimental limitations, large enough J were not attainable to verify this trend.

At $P_r = 1.44$, challenges with conditioning the inner jet temperatures resulted in a wide range of inner jet exit temperatures for a given J using the different injectors. In order to mitigate the impact of the resulting large differences in the inner jet exit densities on the measured L_B/D_1, each measured L_B/D_1 was scaled by the ratio of a chosen reference inner jet density (at $T_i = 109$ K) to the actual inner jet density:

$$\left(\frac{L_B}{D_1}\right)_{\text{adjusted}} = \frac{L_B}{D_1}\frac{\rho|_{T=109K}}{\rho}. \tag{5.3}$$

As Figure 5.9 shows, for the low J flows, again the SAR-thick injector had the lowest L_B/D_1. The agreement between the SAR-thin injector's flushed and recessed data at

$P_r = 0.44$ was not upheld at the elevated pressures. The flushed cases had consistently higher L_B/D_1. On the overall, L_B/D_1 showed less separation for a given J compared with those at $P_r = 0.44$. They also appeared to approach an asymptotic L_B/D_1 at large enough J.

The wide variation in the measured L_B/D_1 of the different injectors, especially for lower J flows, was an evidence that J is not the only governing parameter, but also the injector geometry, namely t/D_1 and A_o/A_i. To estimate the dependence of L_B/D_1 on J and these geometric parameters, a functional dependence of the following form was assumed:

$$\left(\frac{L_B}{D_1}\right) = c_1 J^{c_2} \left(\frac{t}{D_1}\right)^{c_3} \left(\frac{A_o}{A_i}\right)^{c_4}. \tag{5.4}$$

All of the L_B/D_1 at each P_r was used in a non-linear regression analysis used to estimate the constants $c_1 - c_4$, whose converged values are listed in Table 5.1.2. The results of the regression are given in Figures 5.10 and 5.11 for $P_r = 0.44$ and $P_r = 1.05$, respectively, in which L_B/D_1 was plotted versus G (the right-hand-side of Equation 5.4). The regression constants revealed that L_B/D_1 increased with A_o/A_i, as expected, while it decreased with J and t/D_1 at both pressure regimes. They also revealed a stronger dependence on A_o/A_i at $P_r = 0.44$ than at $P_r = 1.05$. The reason as to why this was the case is yet to be determined.

Table 5.1: Values of the constants in Equation 5.4 obtained from non-linear regression of the L_B/D_1 data.

P_r	c_1	c_2	c_3	c_4
0.44	9	-0.34	-0.15	0.30
1.05	11	-0.43	-0.12	0.15

5.1.3 Characterization of Dominant Behavior of Baseline Flow Structures

Application of POD on the pixel intensity fluctuations in the high speed images, revealed spatial and temporal characteristics of the dominant periodic flow structures present in the coaxial jet flow. Figures 5.12a-g show snapshot images of the LAR-thin injector flow at $Pr = 0.44$ along with time-averaged images of 1,000 consecutive images acquired at 25,000 frames per second, images of the proper orthogonal mode (POM) of the conjugate modes, and the corresponding cross-power spectral density (CPSD) magnitude plots. The images shown span a distance of about $20D_1$ downstream of the injector exit plane. For $J = 0.1$, the average image shows a relatively undisturbed dark-core flow for over $20D_1$. In contrast to the snapshot image, the average image was characterized by the absence of any discrete flow structures emanating from the dark-core at the outer-inner jet interface.

As described in Section **??**, the POM image represented fluctuations in intensities with dark and light shades, which indicated a local periodic presence and absence, respectively, of dense fluid structures. Regions which showed no change in intensity over a span of 1,000 image frames, such as near the axis of the inner jet flow and the outer jet flow, were depicted in gray as a means to represent the DC component or the reference mean on an 8-bit grayscale. Accordingly, the majority of the field of view in the POM image of Figure 5.12a shows the absence of any significant dynamic dense fluid structures except in the inner shear-layer region far downstream of the injector exit.

Also shown in Figure 5.12a is the CPSD magnitude of the conjugate mode pair corresponding to the POM image. The low frequency peak in the spectrum indicated the temporal periodicity of the dark and light lobes in the POM images around that frequency. It has been shown that the superposition of a conjugate pair represents downstream propagating flow structures in time, per the discussion in Section **??**. Therefore, the information conveyed in the POM image and the CPSD magnitude spectrum was that the $J = 0.1$ flow had spatially and temporally periodic dominant flow structures as shown in the dark and light lobes, and spectral peaks, respectively. The staggered or antisymmetric arrangement of the lobes in the POM image suggests that the flow structures were propagating as a helical disturbance. This may be a strong claim to make based on a planar view of an axisymmetric flow. However, in the absence of external disturbances that can impose a preferred direction of flow oscillation, it may be argued that the only manner of propagation for the periodic antisymmetric structures must be in the form of a helical disturbance. Hence, viewing the jet from two perpendicular lines of sight should reveal indistinguishable features for a baseline coaxial jet, as Davis [58] previously showed for some flow conditions .

Figure 5.12b shows the same set of images and spectral plot for the $J = 0.5$ case. Compared to that for $J = 0.1$, the average image showed a noticeable spread with increasing downstream distance. The dominant periodic structures in the POM image were also comparably larger and started forming a few diameters upstream of those for $J = 0.1$. Their antisymmetric arrangement again was an indication of the propagation of helical disturbances. The low frequency peak in the CPSD magnitude spectrum was the characteristic frequency associated with these structures. It was broader and shifted slightly to a higher frequency.

As the momentum flux ratio increased to $J = 2.1$, the average image in Figure 5.12c shows that the inner jet spread also continued to increase. The dominant flow structures were antisymmetric as the two lower J cases, but their inception moved farther upstream. Their CPSD magnitude spectral peak was relatively broader and situated at a higher frequency. Figures 5.12d,e for $J = 5.2, 11$ also show similar trends seen with increasing J.

For reasons described at the beginning of this chapter, the jet flowrates were lower for $J = 14$ than for $J = 11$. As Figure 5.12f shows, the inception point of the antisymmetric structures was relatively unchanged. However, the broad peak in the magnitude spectrum shifted back to lower frequencies. Thus, the peak frequency in the CPSD magnitude spectrum, which is the characteristic frequency of the dominant flow structures identified, was cleary also dependent on the magnitude of the outer jet flowrate and not only on J. The next higher J case shown in Figure 5.12g for the same inner jet flowrate, but increased outer jet flowrate, confirmed the increasing trend of the peak frequency with increasing outer flowrate.

Figures 5.13a-e show similar snapshot, average and POM images along with the CPSD magnitude for the LAR-thin injector flows at $Pr = 1.05$. At this elevated transcritical pressure, the outer to inner jet density ratio, S, was larger by almost three times that of the subcritical pressure cases. This difference may have brought about a difference in the development of the shear-layer disturbances under the two pressure conditions. For the low momentum flux ratio of $J = 0.5$, however, no significant differences were discernable between the two pressure regimes. The inner jet spread depicted in the average image in Figure 5.13a was comparable to that of the $Pr = 0.44$. In addition, the onset of antisymmetric structures, and the CPSD magnitude spectrum were also comparable. For the $J = 0.5$ flow at $Pr = 1.05$, however, the peak frequency was slightly lower perhaps partly due to the lower outer jet flowrate.

As the momentum flux ratio increased, the onset of the dominant antisymmetric structures moved farther upstream as the dark-core length was reduced. However, compared to that of the $Pr = 0.44$ cases, the onset of these antisymmetric structures was relatively closer to the end of the dark-core as shown in Figures 5.12b-e. In other words, helical disturbances had slightly delayed start under the higher chamber pressure conditions, where S was larger. These disturbances appeared to penetrate deeper towards the jet axis and also appeared to have shorter wavelength compared to those of comparable J at $P_r = 1.05$. On the other hand, in a manner that was observed at $Pr = 0.44$, the peaks in the magnitude spectra shifted to higher frequencies with increasing J due to increasing outer jet flowrates.

Similarly, Figures 5.14a-g show snapshot images of the SAR-thick injector flow at $Pr = 0.44$ along with a time-averaged image of 500 consecutive images acquired at 25,000 frames per second, POM images of the conjugate modes, and the corresponding CPSD magnitude plots. The images shown span a distance of about $8D_1$ downstream of the injector exit plane. For $J = 0.1$, the average image in Figures 5.14a shows a relatively undisturbed dark-core flow for over $8D_1$. However, the POM image shows weak but symmetric flow disturbances propagating along the inner jet surface. Based on the same argument used to suggest that antisymmetric structures represented helical disturbances in baseline flows due to the absence of directional bias, it may be argued that the symmetric flow structures represented axisymmetric disturbances. A possible cause for the axisymmetric disturbances to dominate over the helical disturbances may have been the presence of the axisymmetric, recirculating low momentum outer jet flow just below the inner post and surrounding a region of about $1D_1$ just downstream of the inner jet exit. The peak in the CPSD magnitude associated with these disturbances was at a low frequency, similar to the LAR-thin injector flow with the same J and P_r.

For $J = 0.5$, the average image in Figure 5.14b shows a sudden spread in the dark-core at the location where the recirculation zone ends. Due to entrainment of the outer jet by the inner jet at low J, once it exited the injector, the outer flow was forced to converge towards the jets' axis while tracing the outer edge of the recirculation zone. It, thus, impinged on the inner jet at an angle, and the reattached outer jet flowed parallel to the inner jet. Thus, this impinging flow may have been the cause for the sudden spread at the reattachment point visible in the average image. The POM image does not clearly identify whether symmetric or antisymmetric disturbances exist. The peak frequency in the magnitude spectrum still stayed at lower frequencies.

As J increased, the snapshot and average images show the recirculation zone filled with the dense inner jet fluid. This implied that the higher momentum outer jet fluid entrained more of the inner jet fluid, while the reverse happened for low J flows. The apparent "necking" in the dark-core flows profile that was described earlier, and is clearly visible in the average images, also became less severe with increasing J as less of the outer jet was pulled towards the center. For $J = 2.1$, the POM image in Figure 5.14c shows distinct antisymmetric structures denoting the presence of helical disturbances, and the CPSD magnitude shows a low frequency peak. The higher momentum flux ratio cases, $J = 5.7 - 21$, in Figure 5.14d-g also show antisymmetric structures. However, unlike the LAR-thin flows, the peaks in the mangitude spectra stayed at low frequencies.

At $P_r = 1.05$, the average images in Figures 5.15a,b for $J = 0.1$ and $J = 0.5$ show that the recirculation zone was filled with dark fluid, unlike their counterparts at $P_r = 0.44$, implying relatively more inner jet fluid was entrained into the recirculation zone. The POM images not so well-defined antisymmetric structures with low characteristic frequencies denoted by the low frequency peaks in the magnitude spectra. As J increased, antisymmetric structures became the dominant form of disturbances as the POM images in Figures 5.15c-g show. Similar to the SAR-thick flows at $P_r = 0.44$, the peaks in the magnitude spectra stayed at low frequencies.

Clearly, one of the main differences between the two injectors' baseline flows was the spectral nature of the dominant periodic antisymmetric structures with increasing J. The LAR-thin injector flows had structures with peak frequencies that became broader and moved to higher frequencies as J increased. Unlike a single jet with a coflowing ambient fluid, the coaxial jet configuration in this study had finite area ratio due to the finite diameter outer jet. Nevertheless, the behavior of the instability peak frequencies agreed with analogous analytical results of Michalke and Hermann [48] that with increasing coflow velocity, the region of unstable frequencies becomes broader and that the peak of the spatial growth rates shift to higher frequencies. On the contrary, as the CPSD magnitude spectra for the SAR injector flows show, the peak frequencies were unaffected by increasing J. This contradiction with the LAR-thin flow behavior may be explained by how soon the inner and outer jets attained a single jet behavior, thereby rendering the effect of coflow nonexistent.

Another notable outcome from the spectra was that the peak frequencies for the LAR-thin injector flows were not only dependent on R or J, but on the magnitude of the outer jet flowrate while the peaks for the SAR-thick injector flows were relatively insensitive to the changing outer jet flowrates. Note that at constant density and a fixed injector exit area, the effects of varying the jet mass flowrates may be regarded as equivalent to the effects of varying jet velocities. In order to investigate this, downstream convection velocities, U_s, of the dominant periodic structures depicted in the POM images were estimated based on the relation $U_s = \lambda f_s$, where λ is the wavelength measured from the images, and f_s is the characteristic frequency. The frequency, f_s, was obtained from the frequency that corresponded to the maximum CPSD magnitude that was closest to a CPSD phase of $\pm 90^o$ as illustrated in Figure 4.12. The estimated U_s along with exit velocity of the inner jet, outer jet, and their mean are shown in Figures 5.16 and 5.17 for the two injectors at $P_r = 0.44$ and $P_r = 1.05$, respectively. For uniform density coaxial jets, the inner shear layer convection velocity may be approximated by the mean velocity. On the other hand, for variable density jets, as it is the case in this study, the shear-layer velocity velocity is less than the mean velocity when the high-velocity jet is less dense [41]. The estimated values of U_s for both the LAR and SAR injector flows depict this. However, U_s for the LAR-thin injector flow appeared to closely depend on the magnitude of U_o more than those for SAR-thick injector flow did. This may be an indication that in the LAR-thin geometry, the outer jet governed the dynamics of the inner shear layer structures. However, further investigation will need to be done to generalize this outcome.

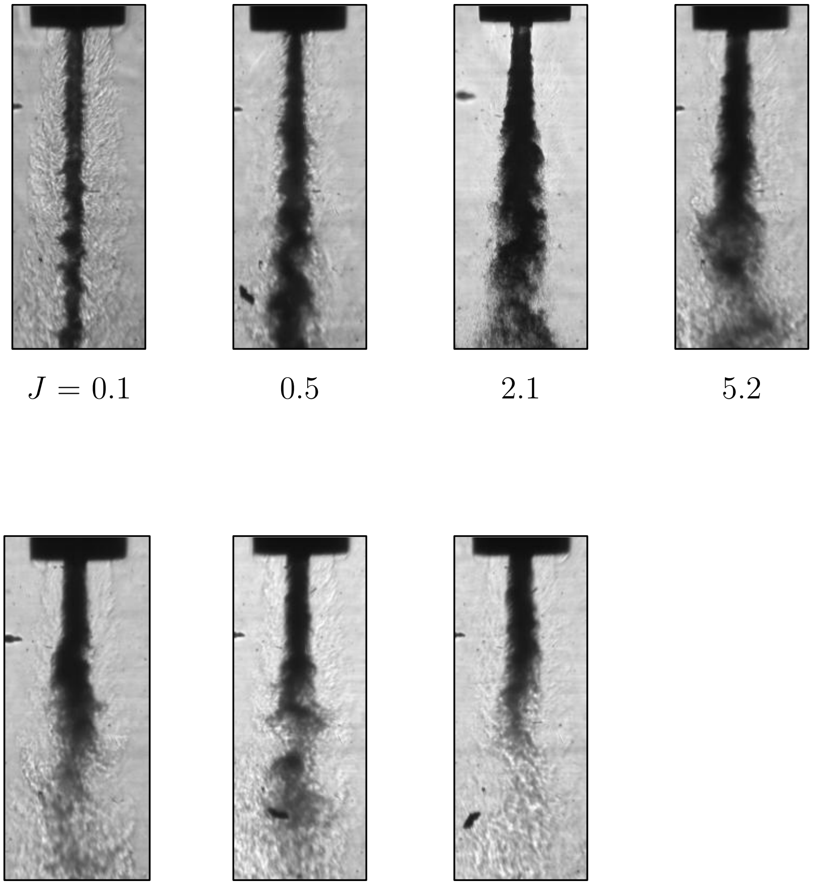

$J = 0.1$ 0.5 2.1 5.2

$J = 11$ 14 20

Figure 5.1: Back-lit images of the LAR-thin injector baseline flow at $P_r = 0.44$ and varying J. The image framing rate was 25 kHz. At subcritical chamber pressure, the inner jet was in liquid state while the outer jet was in gaseous state. Table C.1 gives a summary of the flow conditions.

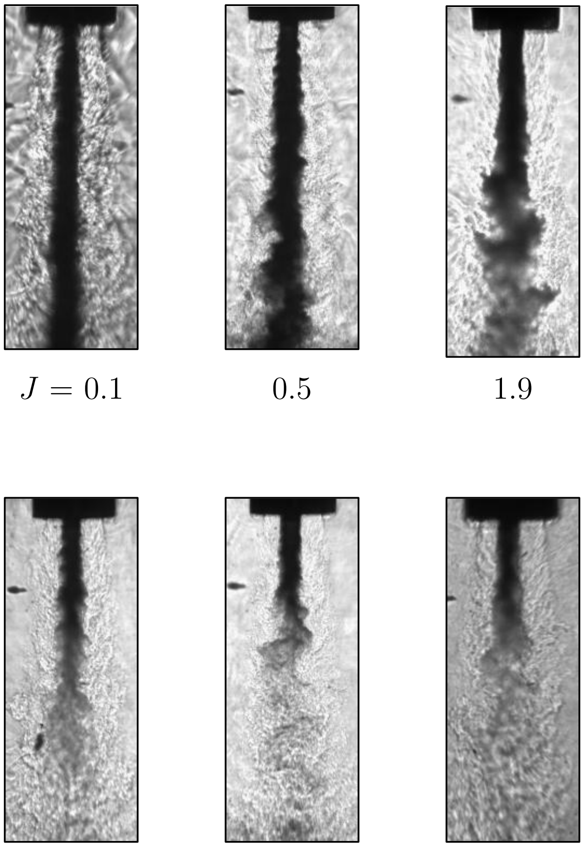

$J = 0.1$ 0.5 1.9

$J = 5.0$ 8.5 12

Figure 5.2: Back-lit images of the LAR-thin injector baseline flow at $P_r = 1.05$ and varying J. The image framing rate was 25 kHz. At nearcrtical chamber pressure, the inner jet was in liquid state while the outer jet was supercritical. Table C.1 gives a summary of the flow conditions.

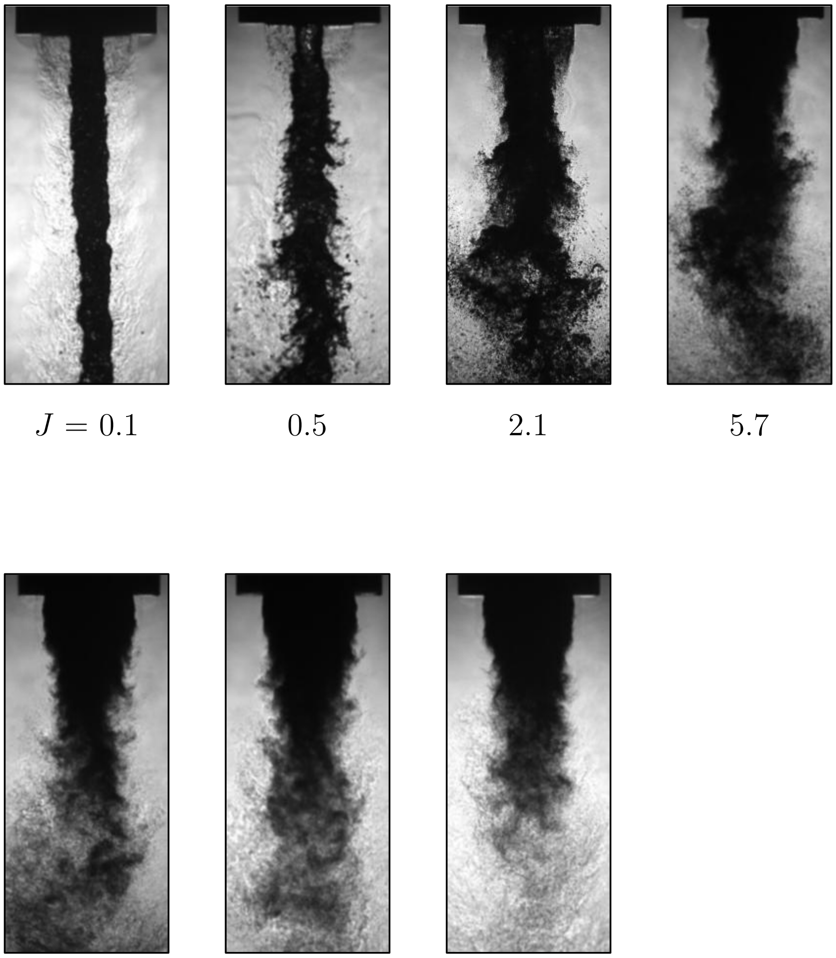

$J = 0.1$ 0.5 2.1 5.7

$J = 10$ 15 21

Figure 5.3: Back-lit images of the SAR-thick injector baseline flow at $P_r = 0.44$ and varying J. The image framing rate was 25 kHz. At subcritical chamber pressure, the inner jet was in liquid state while the outer jet was in gaseous state. Table C.2 gives a summary of the flow conditions.

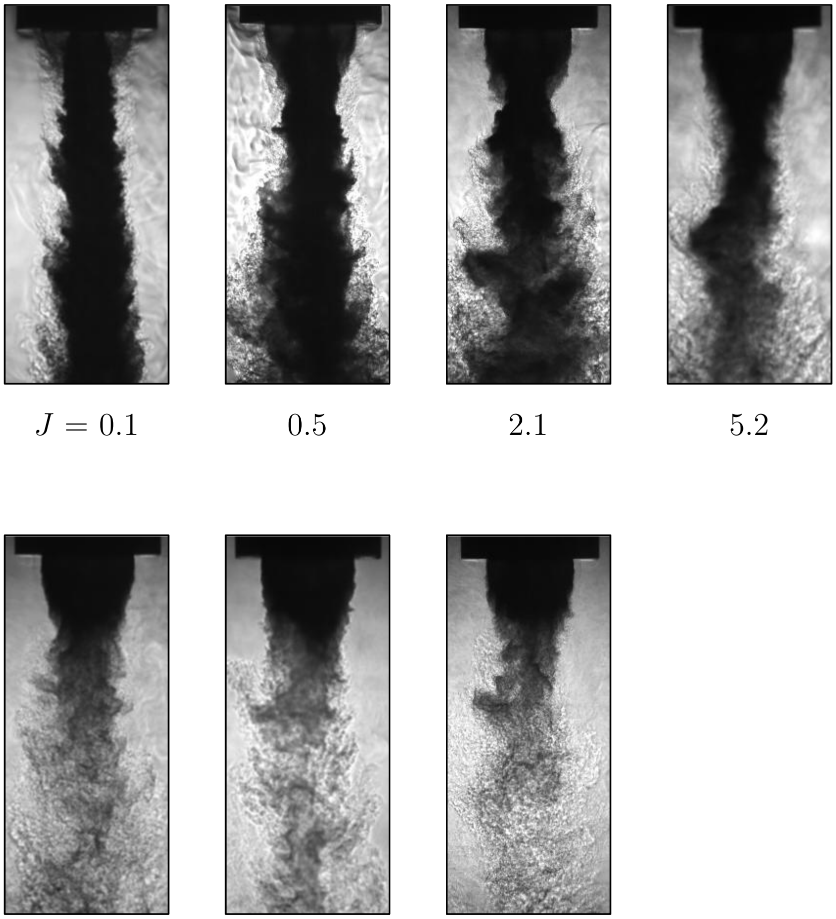

$J = 0.1$ 0.5 2.1 5.2

$J = 9.2$ 14 21

Figure 5.4: Back-lit images of the SAR-thick injector baseline flow at $P_r = 1.05$ and varying J. The image framing rate was 25 kHz. At nearcrtical chamber pressure, the inner jet was in liquid state while the outer jet was supercritical. Table C.2 gives a summary of the flow conditions.

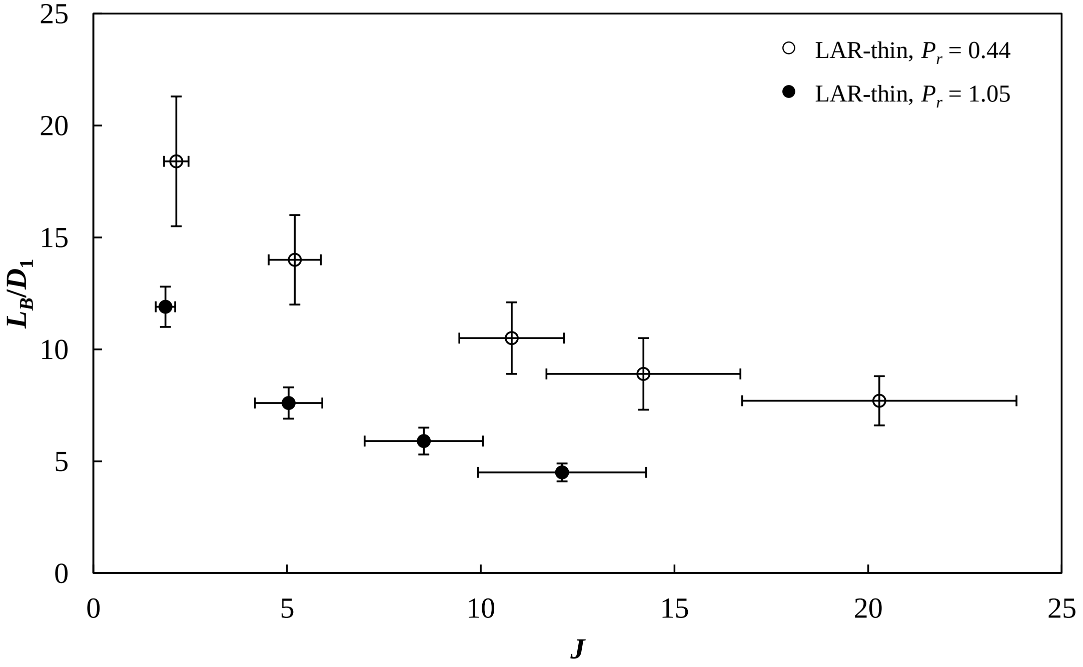

Figure 5.5: Measurements of the LAR-thin injector baseline flows dark-core lengths, L_B normalized by the inside diameter of the inner injector, D_1. The vertical error bars represent the uncertainty in a single measurement to within 2σ of the mean for 1000 measurements. The horizontal error bars represent the bias errors in the measurement of J. The large errors at higher J values were mainly due to the large relative uncertainties $(\delta\dot{m}_i/\dot{m}_i)$ in the low inner jet flowrate measurements.

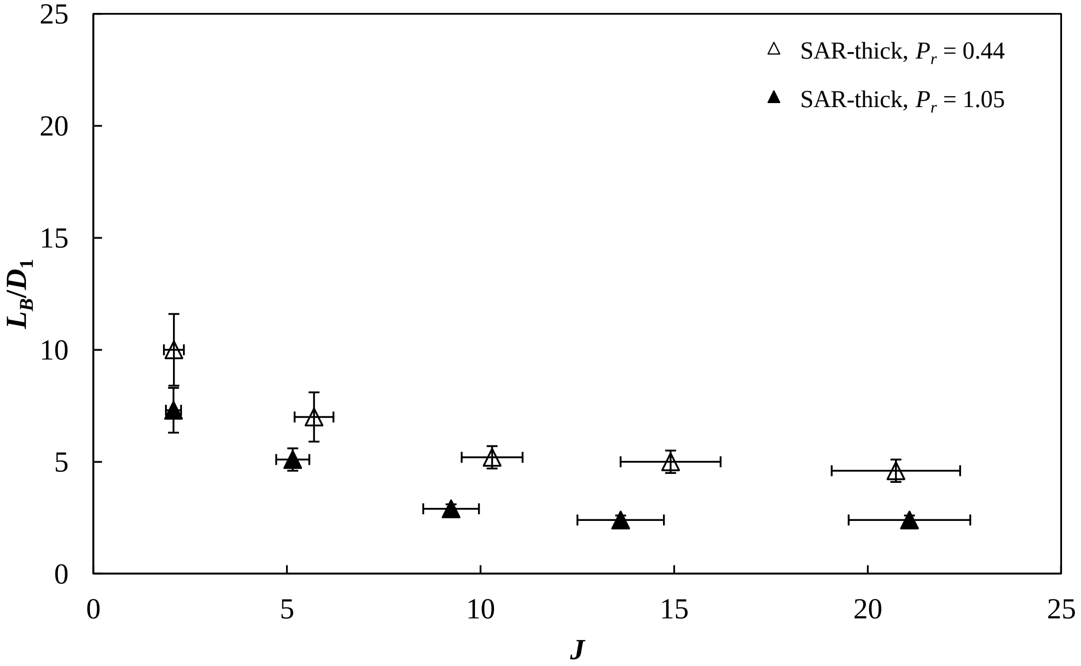

Figure 5.6: Measurements of the SAR-thick injector baseline flows dark-core lengths, L_B normalized by the inside diameter of the inner injector, D_1. The vertical error bars represent the uncertainty in a single measurement to within 2σ of the mean for 1000 measurements. The horizontal error bars represent the bias errors in the measurement of J.

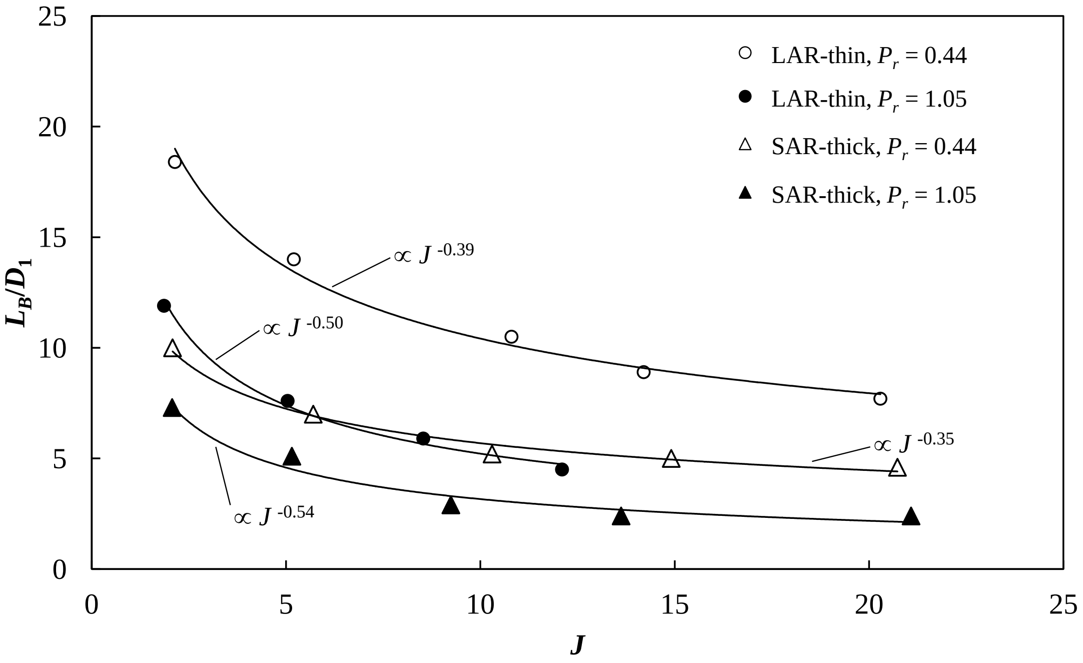

Figure 5.7: A power-law curve-fit to the L_B/D_1 data plotted in Figures 5.6 and 5.5. The variation of L_B/D_1 with J was similar for both injector flows in the same pressure regime. In addition, the SAR-thick injector L_B/D_1 were consistently lower than the LAR-thin injector, and those at $P_r = 1.05$ were lower than at $P_r = 0.44$.

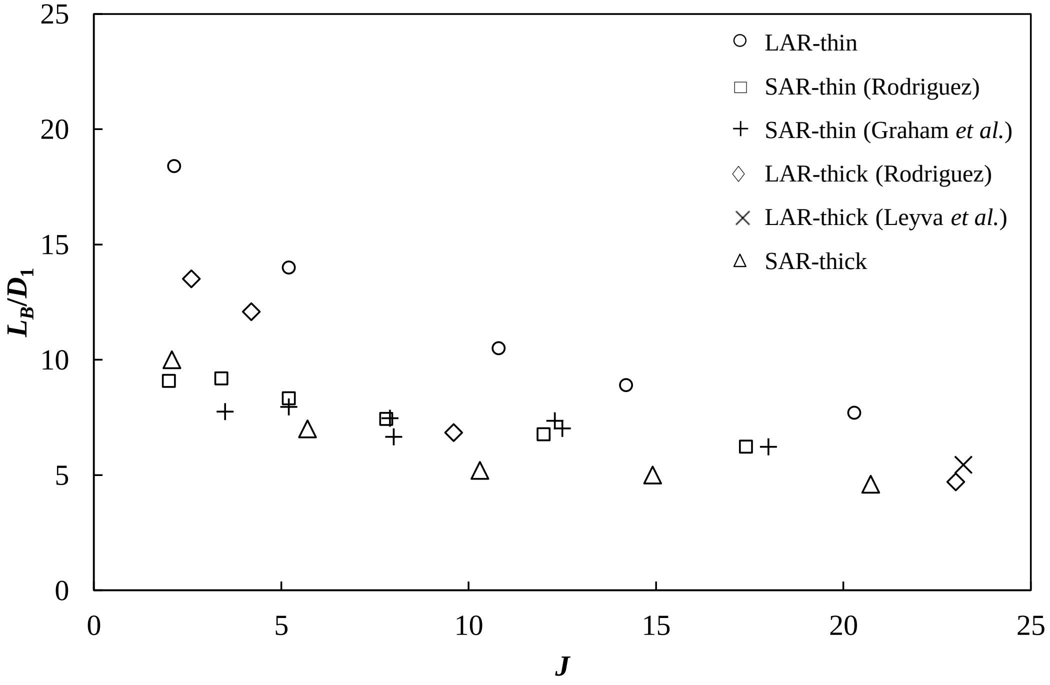

Figure 5.8: Measured L_B/D_1 at $P_r = 0.44$ using different injector configurations including those used by Rodriguez [46], Graham *et al.* [69], and Leyva *et al.* [45]. The dimensions of the LAR-thick and SAR-thin injectors are given in Table 1.2.

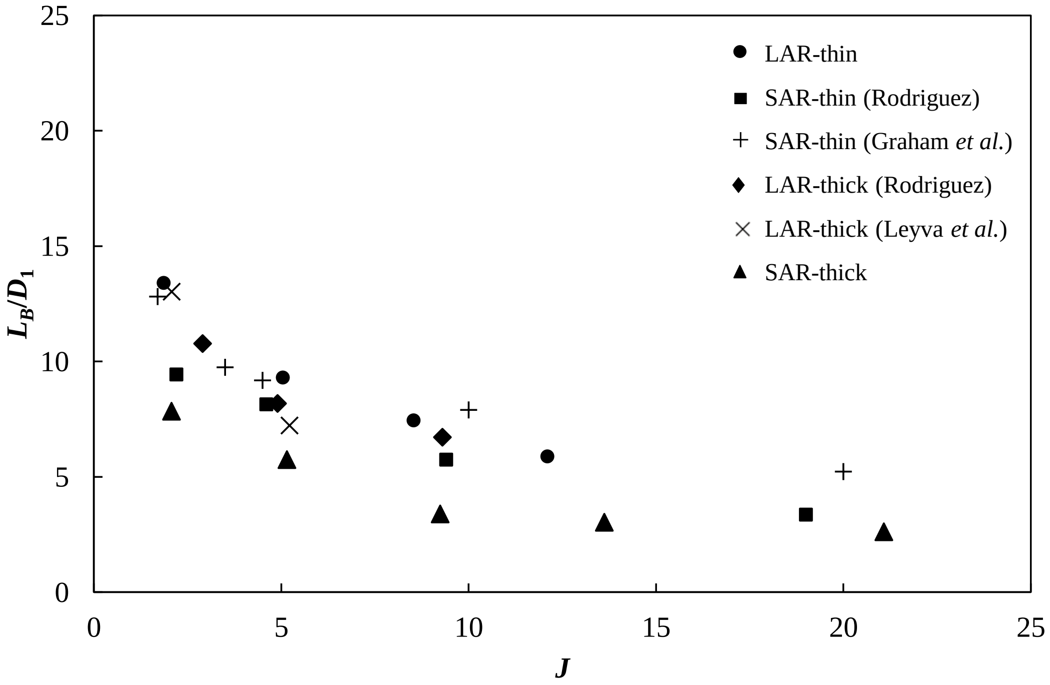

Figure 5.9: Measured L_B/D_1 at $P_r = 1.05$ using different injector configurations including those used by Rodriguez [46], Graham *et al.* [69], and Leyva *et al.* [45]. The dimensions of the LAR-thick and SAR-thin injectors are given in Table 1.2.

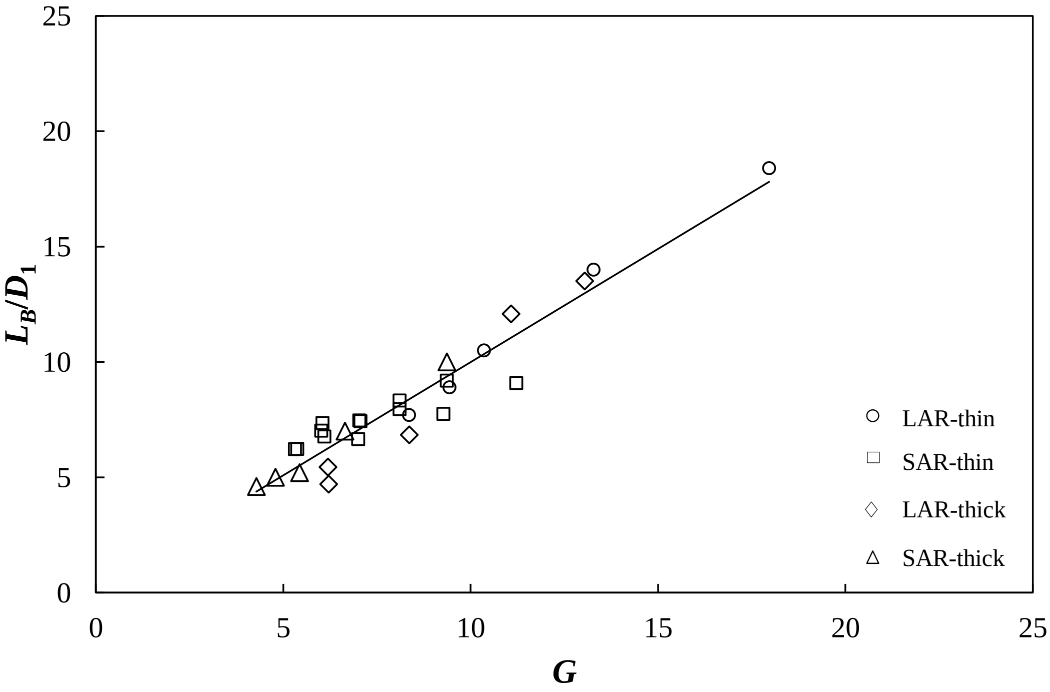

Figure 5.10: Measured L_B/D_1 for the different injectors at $P_r = 0.44$ plotted versus $G = c_1 J^{c_2}(t/D_1)^{c_3}(A_o/A_i)^{c_4}$, where the constants were obtained using non-linear regression, and whose values are listed in Table 5.1.2. The nearly linear line with a unit slope indicated that L_B/D_1 may be predicted with knowledge of the flow J and the injector geometry.

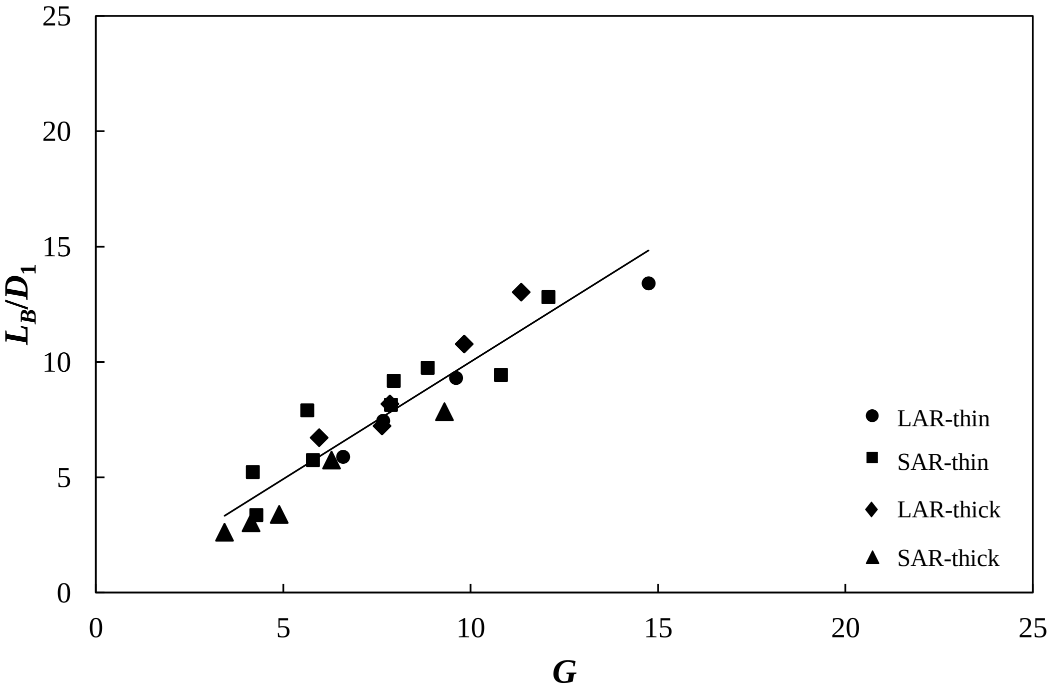

Figure 5.11: Measured L_B/D_1 for the different injectors at $P_r = 1.05$ plotted versus $G = c_1 J^{c_2}(t/D_1)^{c_3}(A_o/A_i)^{c_4}$, where the constants were obtained using non-linear regression, and whose values are listed in Table 5.1.2. The nearly linear line with a unit slope indicated that L_B/D_1 may be predicted with knowledge of the flow J and the injector geometry.

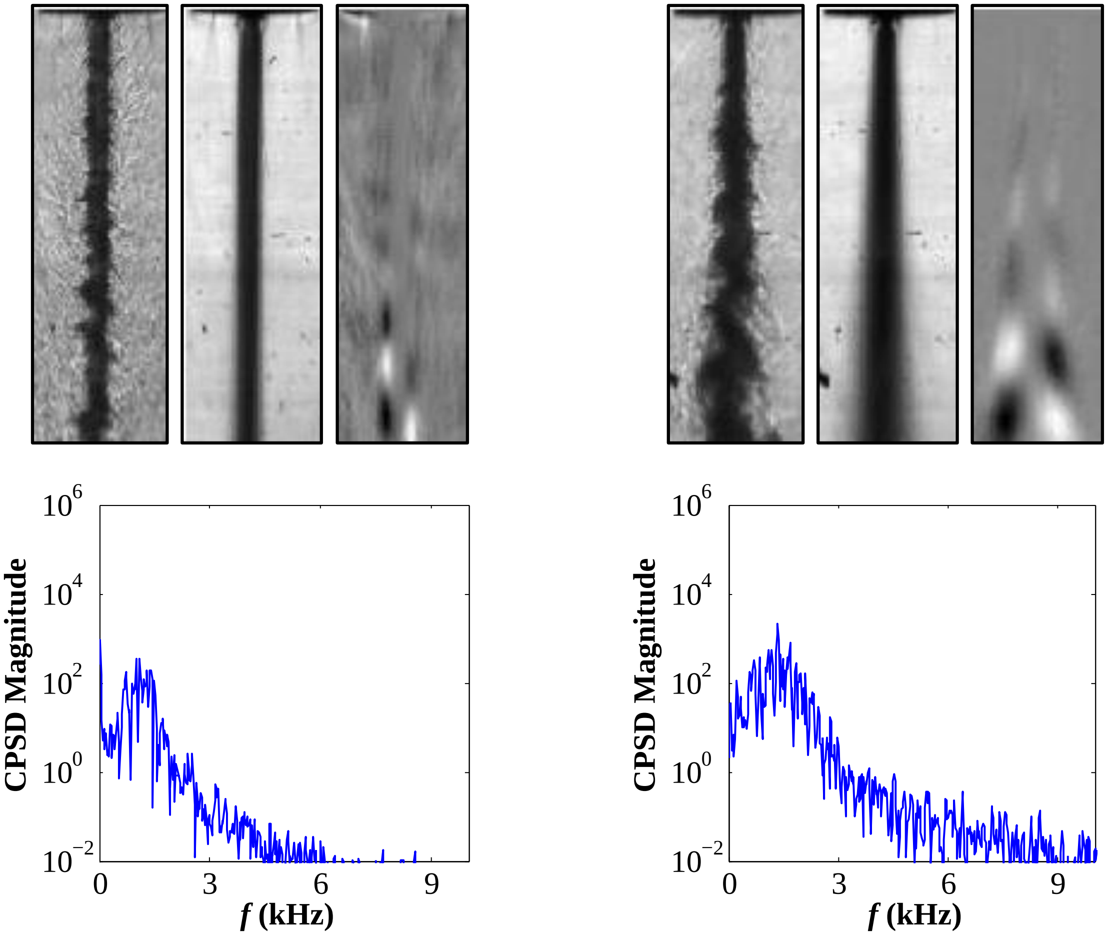

(a) $J = 0.1$

(b) $J = 0.5$

Figure 5.12: See caption on page 118.

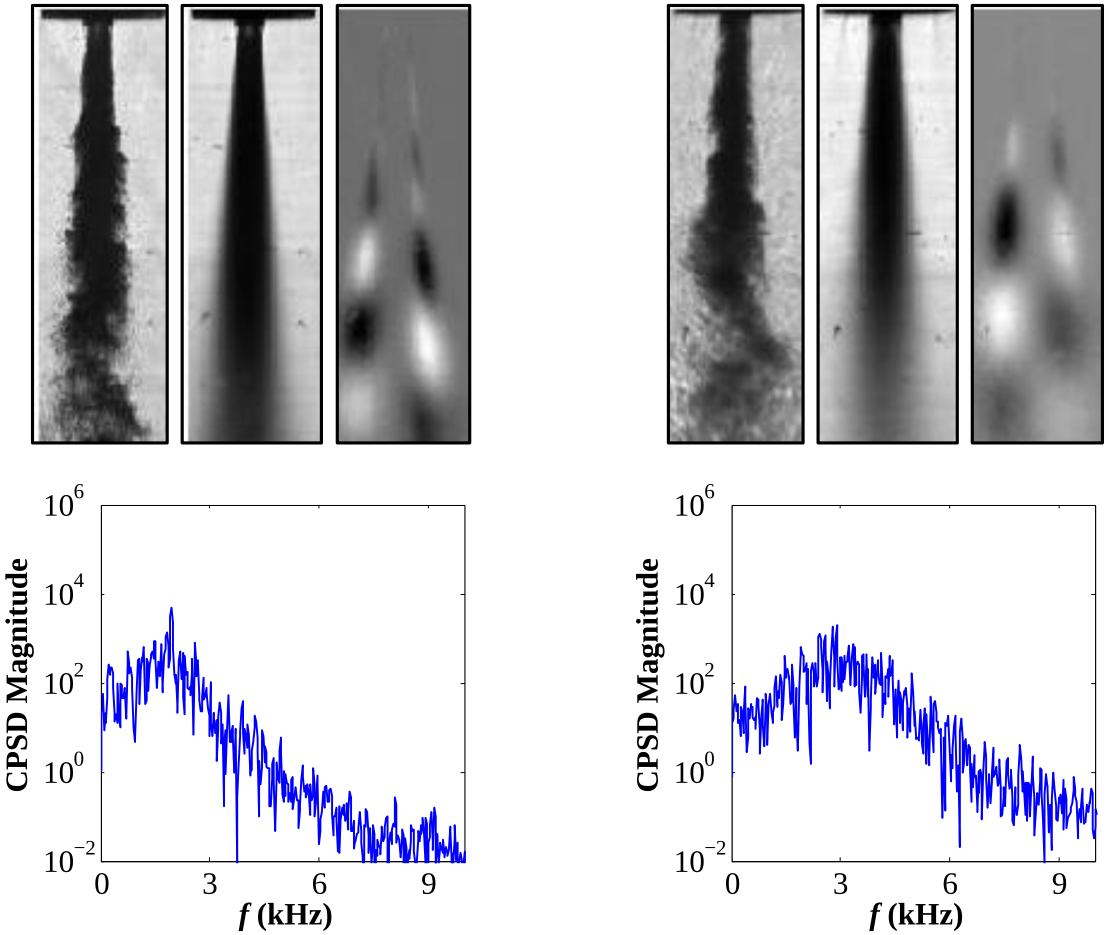

(c) $J = 2.1$

(d) $J = 5.2$

Figure 5.12: See caption on page 118.

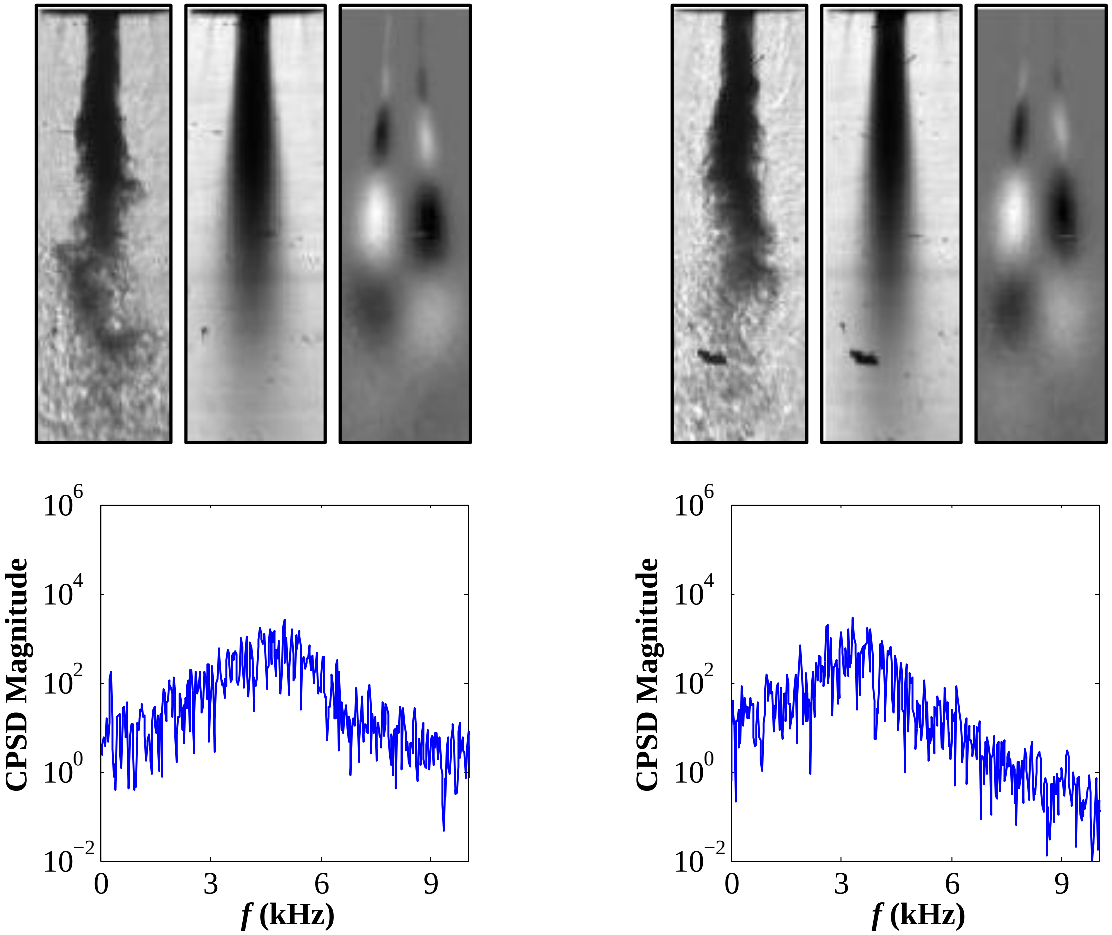

(e) $J = 11$

(f) $J = 14$

Figure 5.12: See caption on page 118.

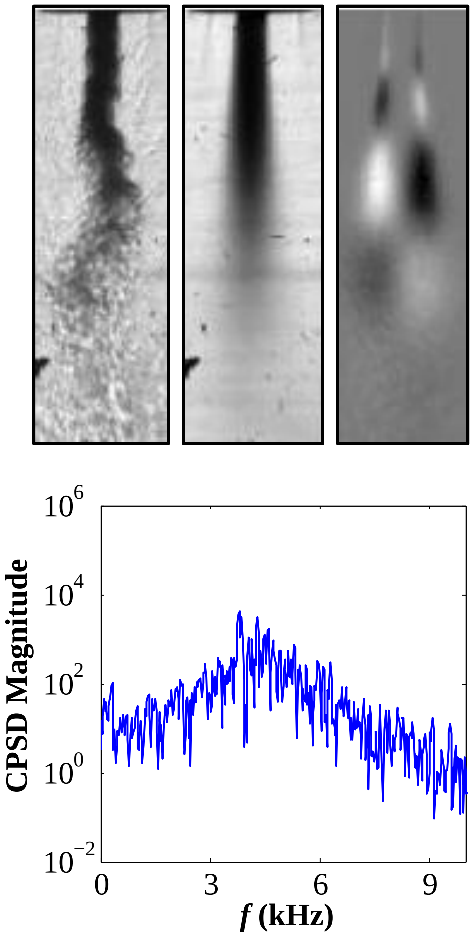

(g) $J = 20$

Figure 5.12: A back-lit image of the LAR-thin injector baseline flow at $P_r = 0.44$ similar to those in Figure 5.1, a time-averaged image and an image of the superposed conjugate proper orthogonal modes (POMs) are shown for each J. The averaged image consisted of 1000 frames sampled at 25 kHz. The corresponding plots are the cross-power spectral density (CPSD) magnitude of the time-dependent amplitude cofficients of the conjugate modes. The peaks in the spectra are the characteristic frequencies of the periodic flow structures identified in the POM images.

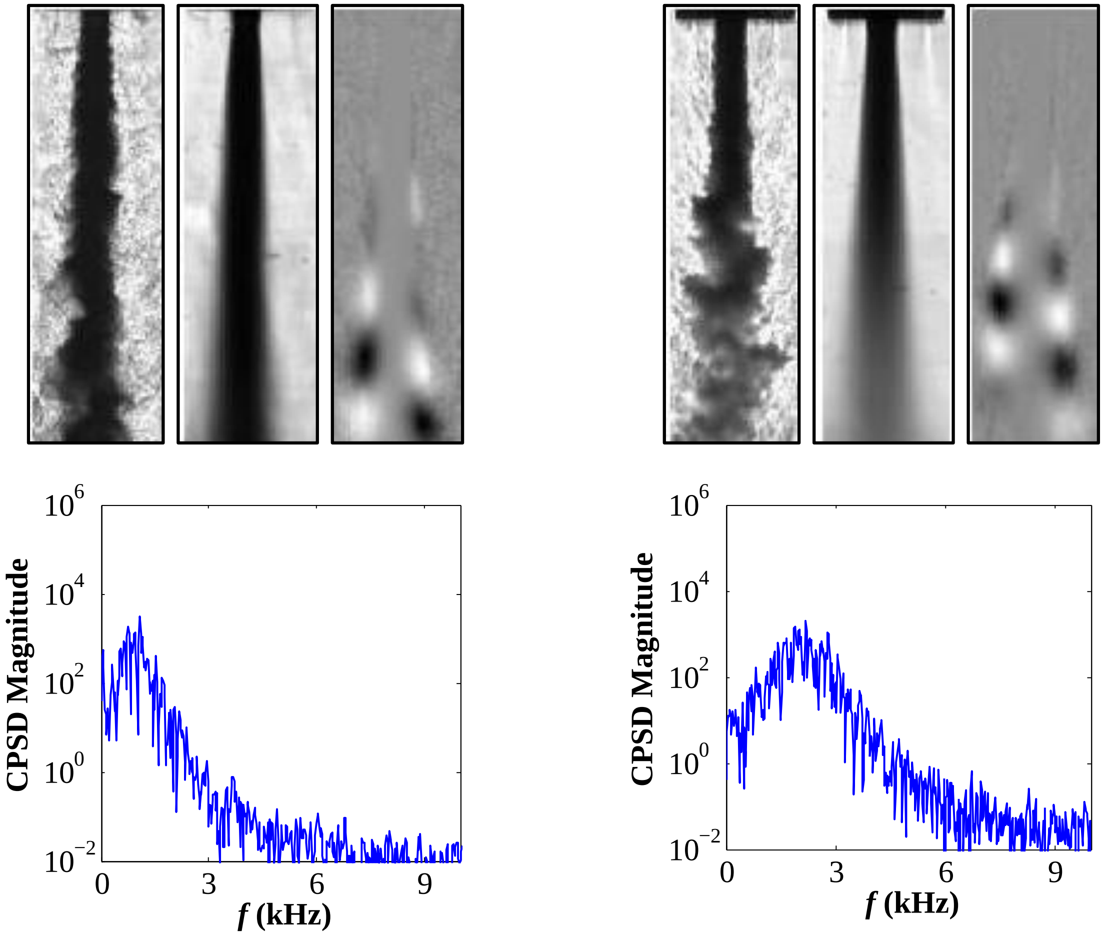

(a) $J = 0.5$

(b) $J = 1.9$

Figure 5.13: See caption on page 121.

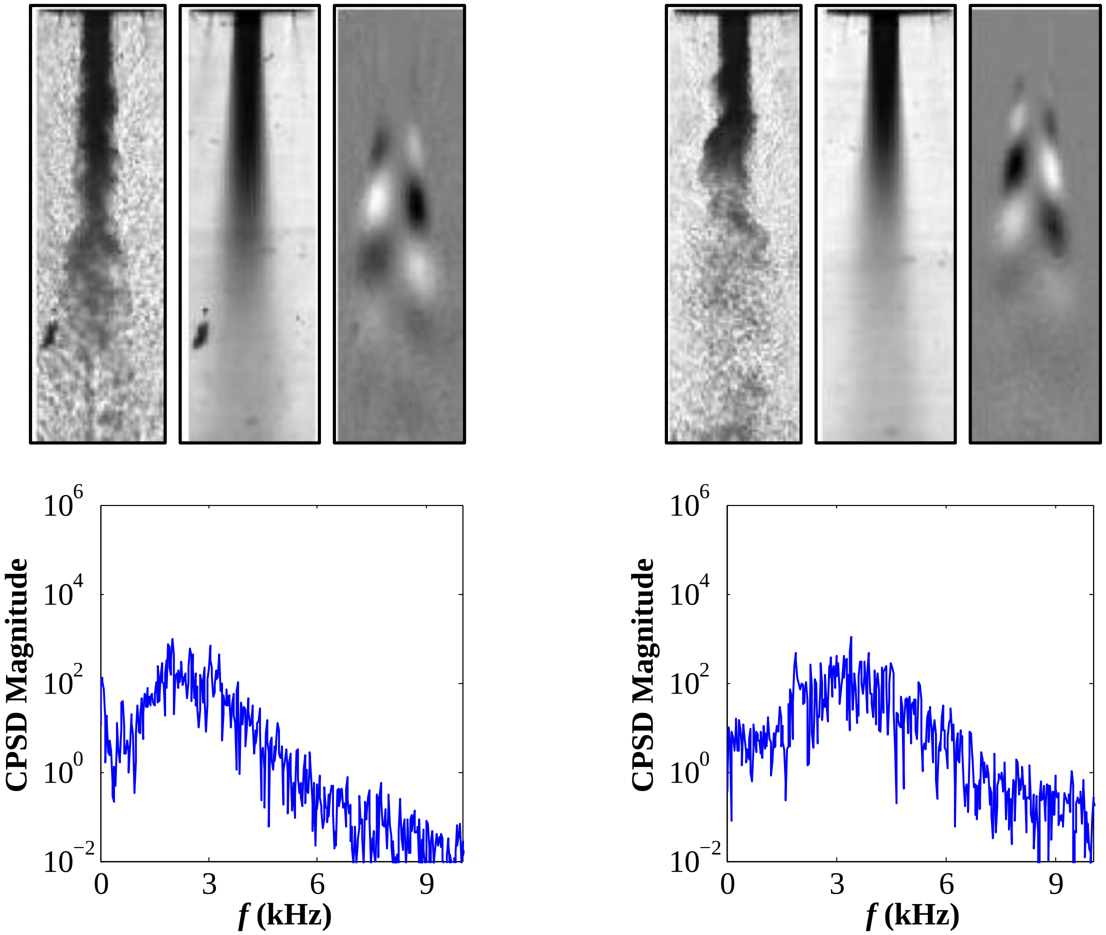

(c) $J = 5.0$

(d) $J = 8\text{-}5$

Figure 5.13: See caption on page 121.

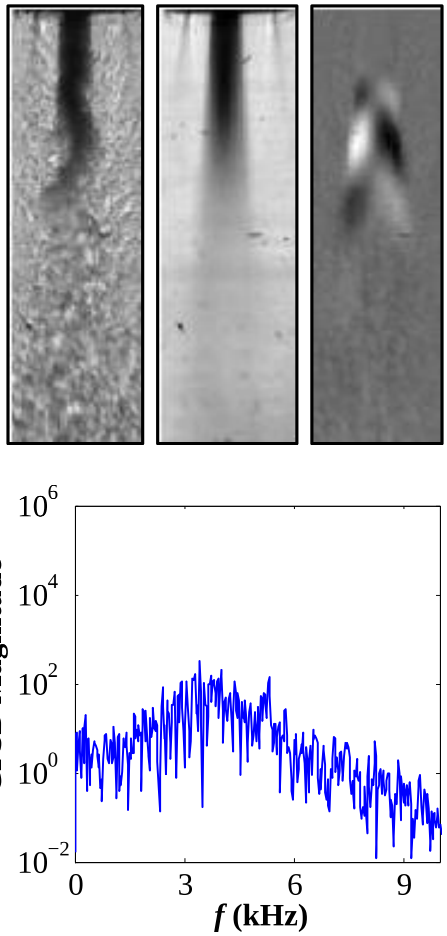

(e) $J = 12$

Figure 5.13: A back-lit image of the LAR-thin injector baseline flow at $P_r = 1.05$ similar to those in Figure 5.2, a time-averaged image and an image of the superposed conjugate proper orthogonal modes (POMs) are shown for each J. The averaged image consisted of 1000 frames sampled at 25 kHz. The corresponding plots are the cross-power spectral density (CPSD) magnitude of the time-dependent amplitude cofficients of the conjugate modes. The peaks in the spectra are the characteristic frequencies of the periodic flow structures identified in the POM images.

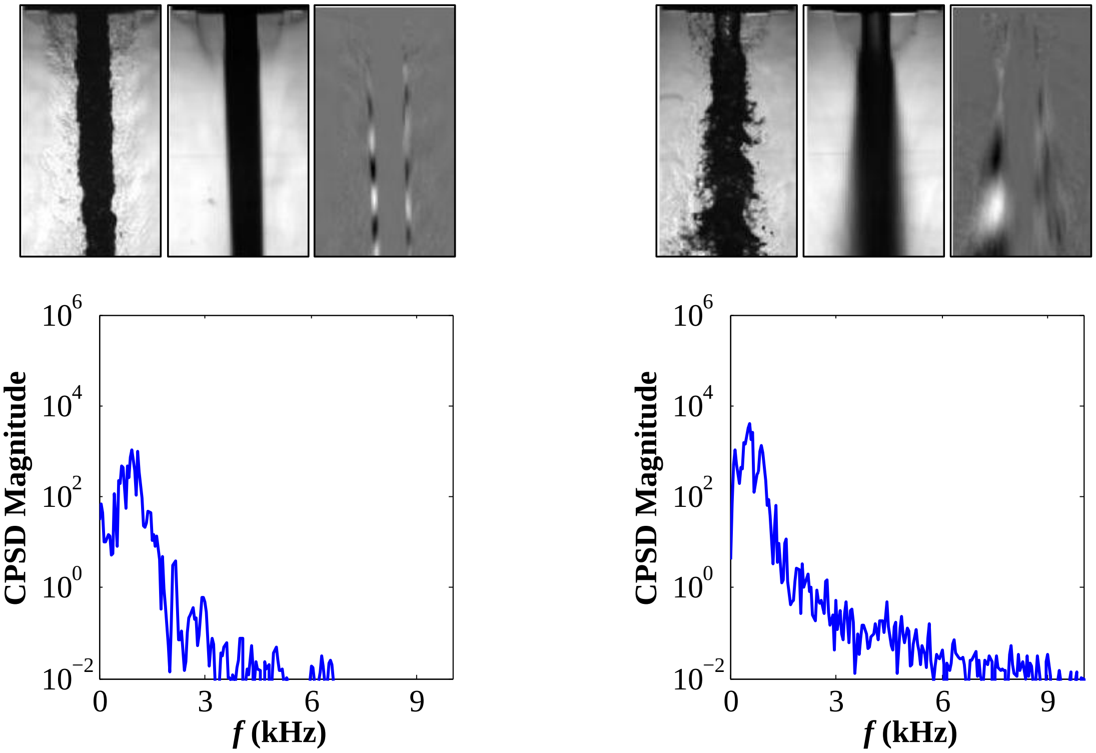

(a) $J = 0.1$ (b) $J = 0.5$

Figure 5.14: See caption on page 125.

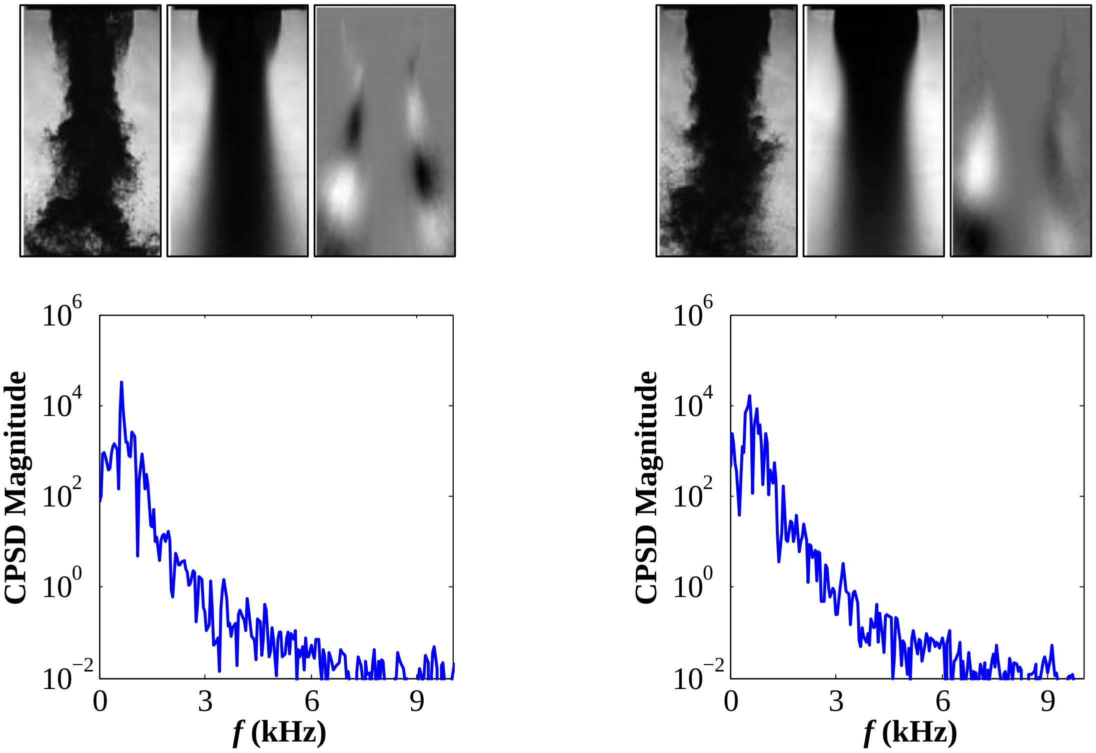

(c) $J = 2.1$

(d) $J = 5.7$

Figure 5.14: See caption on page 125.

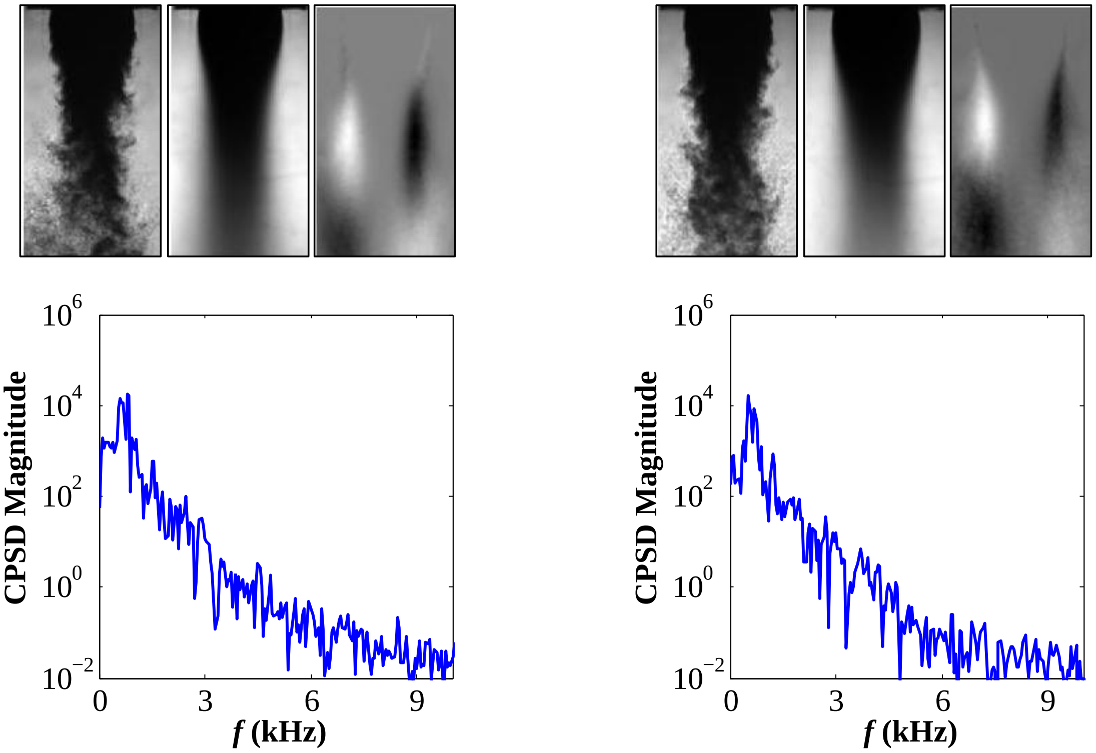

(e) $J = 10$

(f) $J = 15$

Figure 5.14: See caption on page 125.

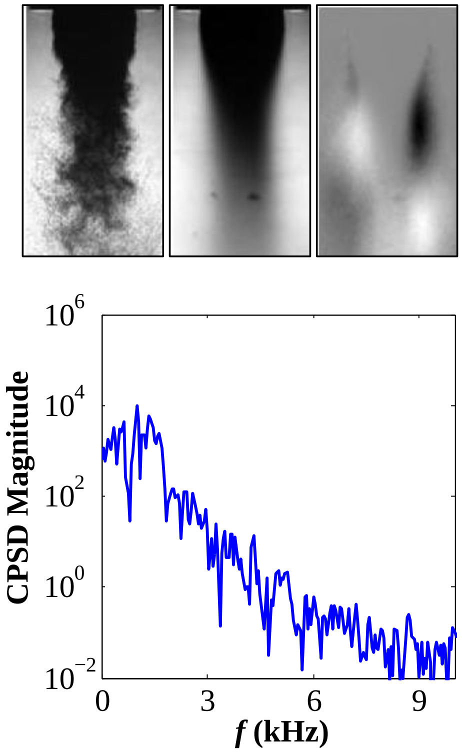

(g) $J = 21$

Figure 5.14: A back-lit image of the SAR-thick injector baseline flow at $P_r = 0.44$ similar to those in Figure 5.3, a time-averaged image and an image of the superposed conjugate proper orthogonal modes (POMs) are shown for each J. The averaged image consisted of 500 frames sampled at 25 kHz. The corresponding plots are the cross-power spectral density (CPSD) magnitude of the time-dependent amplitude cofficients of the conjugate modes. The peaks in the spectra are the characteristic frequencies of the periodic flow structures identified in the POM images.

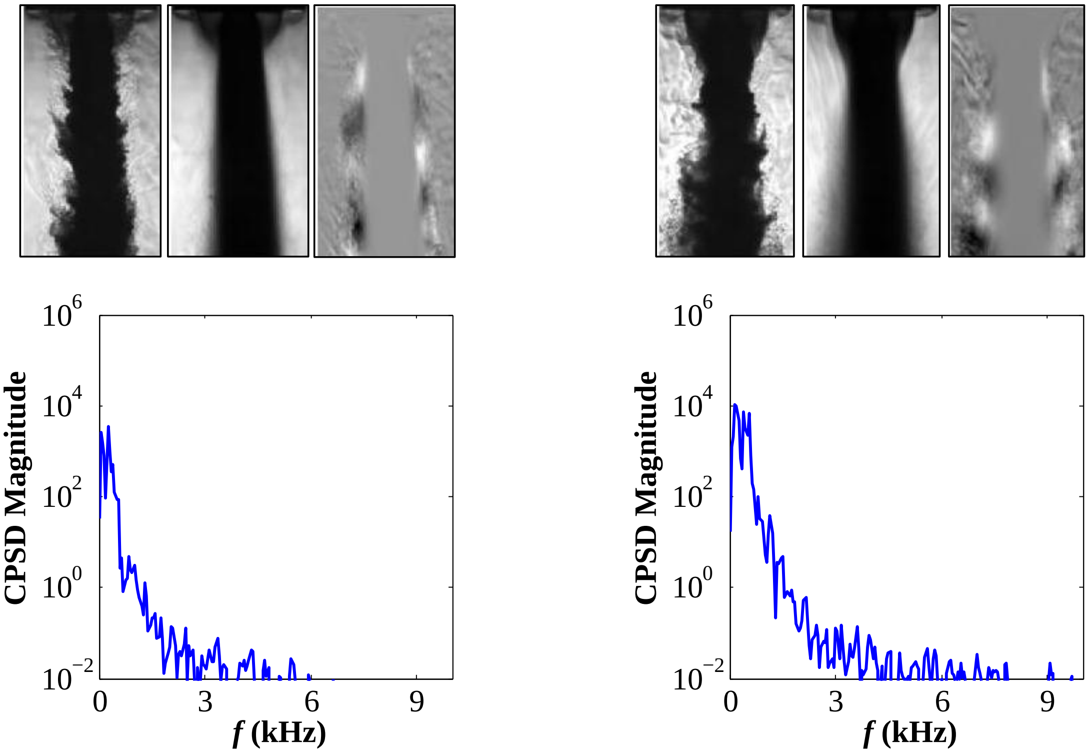

(a) $J = 0.1$ (b) $J = 0.5$

Figure 5.15: See caption on page 129.

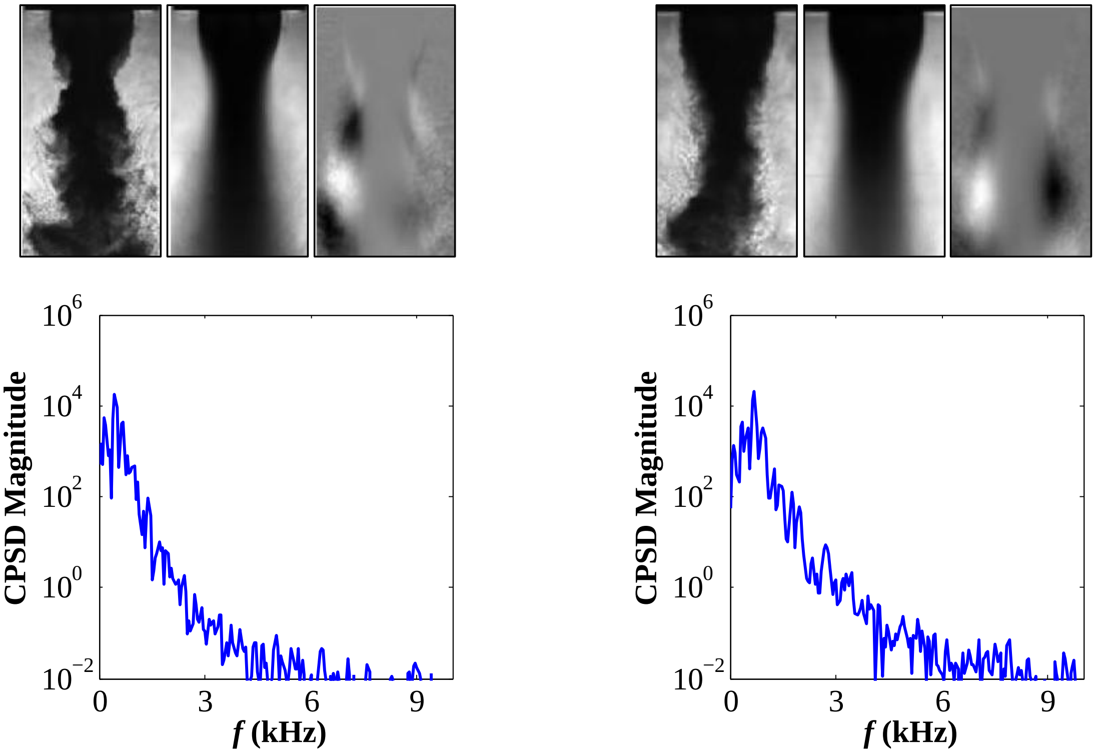

(c) $J = 2.1$

(d) $J = 5.2$

Figure 5.15: See caption on page 129.

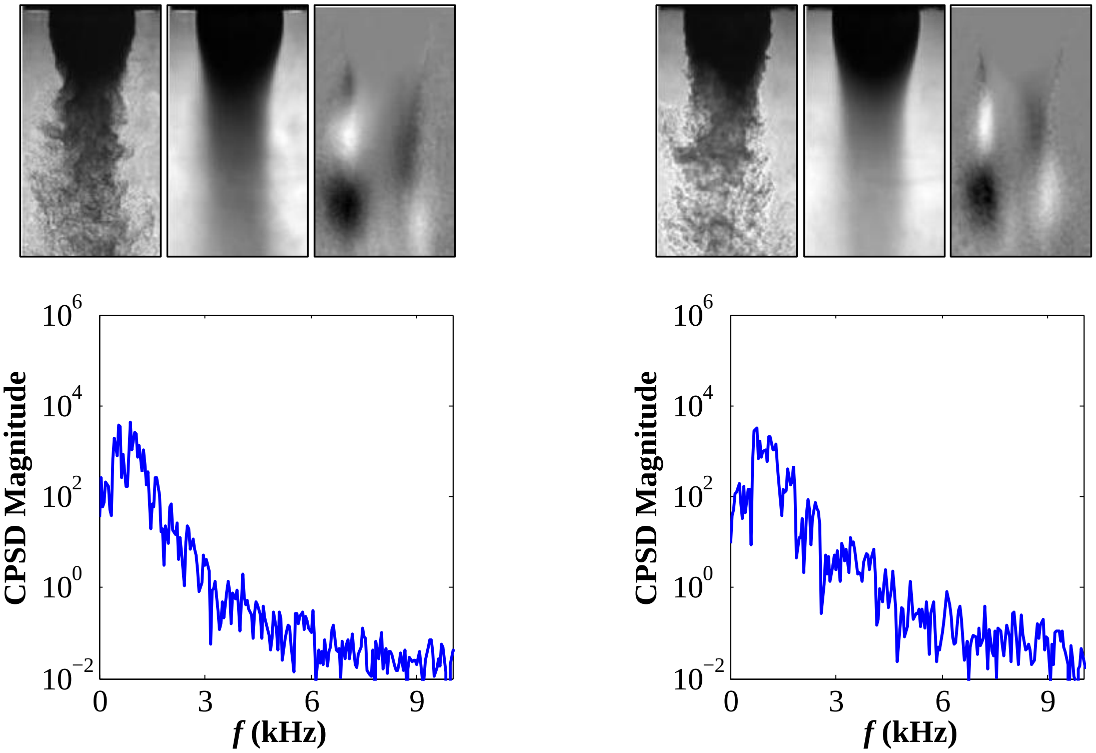

(e) $J = 9.2$

(f) $J = 14$

Figure 5.15: See caption on page 129.

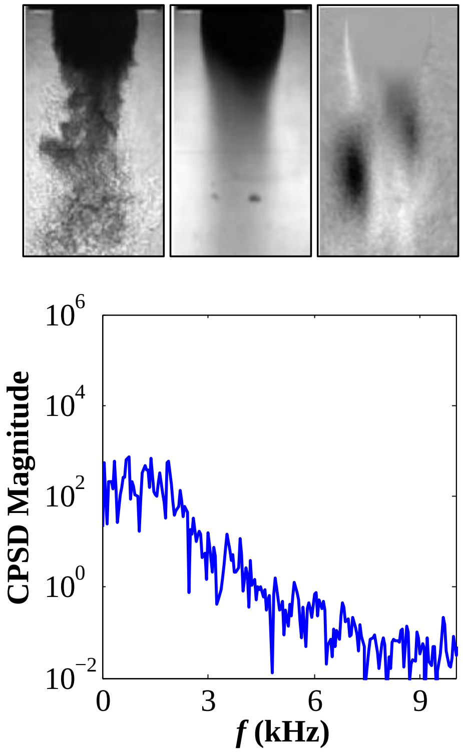

(g) $J = 21$

Figure 5.15: A back-lit image of the SAR-thick injector baseline flow at $P_r = 1.05$ similar to those in Figure 5.4, a time-averaged image and an image of the superposed conjugate proper orthogonal modes (POMs) are shown for each J. The averaged image consisted of 500 frames sampled at 25 kHz. The corresponding plots are the cross-power spectral density (CPSD) magnitude of the time-dependent amplitude cofficients of the conjugate modes. The peaks in the spectra are the characteristic frequencies of the periodic flow structures identified in the POM images.

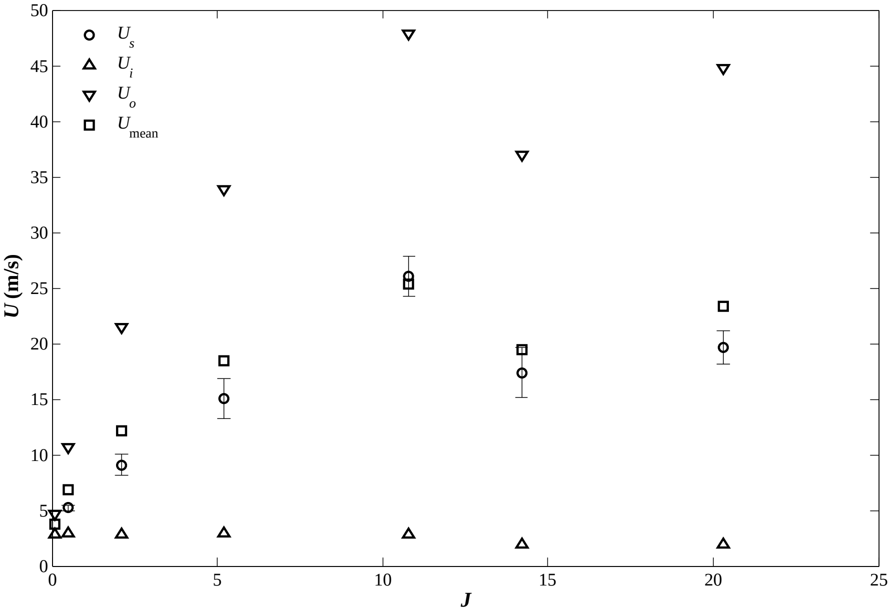

(a) LAR-thin

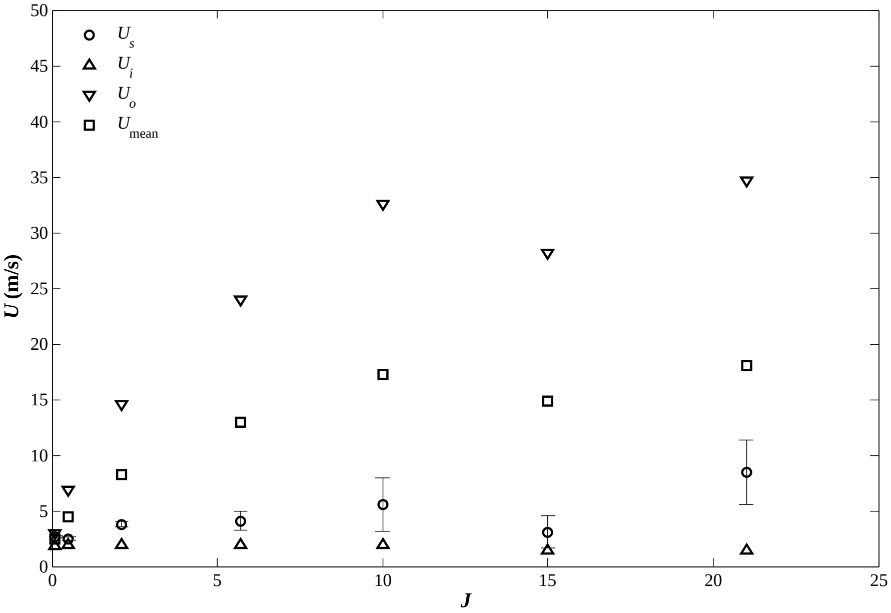

(b) SAR-thick

Figure 5.16: Plots of the outer jet exit velocities, U_o, inner jet exit velocities, U_i, their corresponding mean velocities, U_{mean}, and the estimated convection velocities of the dominant flow structures, U_s for the LAR-thin and SAR-thick injector flows at $P_r = 0.44$. It can be seen that the LAR-thin injector outer jet flow had more influence on the inner shear layer flow than did the SAR-thick outer jet flow.

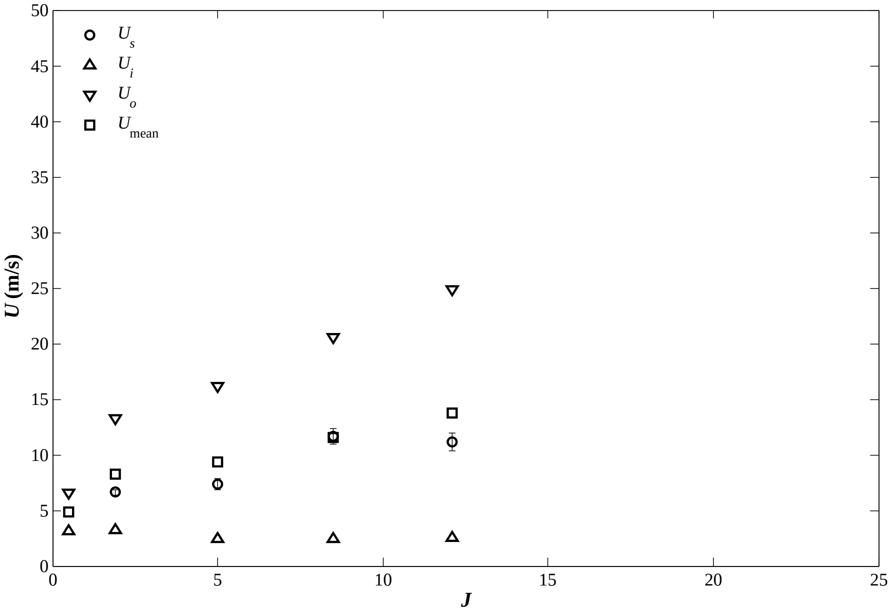

(a) LAR-thin

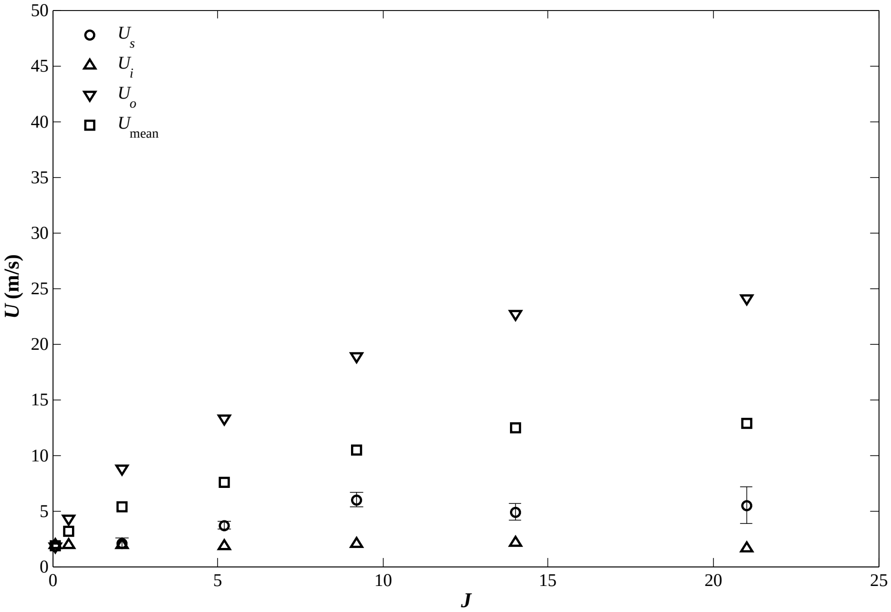

(b) SAR-thick

Figure 5.17: Plots of the outer jet exit velocities, U_o, inner jet exit velocities, U_i, their corresponding mean velocities, U_{mean}, and the estimated convection velocities of the dominant flow structures, U_s for the LAR-thin and SAR-thick injector flows at $P_r = 1.05$. Again, it is clear that the LAR-thin injector outer jet flow had more influence on the inner shear layer flow than did the SAR-thick outer jet flow.

5.2 Transverse Acoustic Forcing of Shear-Coaxial Jets

As described in Section 4.3, two types of transverse acoustic forcing conditions were investigated: a pressure antinode (PAN) and a pressure node (PN) at the coaxial jet location. A PAN condition created a region of locally maximum pressure fluctuation in the vicinity of the coaxial jets so that the velocity fluctuation was minimum or non-existent in the ideal case. As pressure is a scalar physical quantity, a PAN can essentially be regarded as a condition that created a symmetric pressure fluctuation about the jet center plane that was normal to the transverse direction of propagation of the acoustic waves. On the other hand, a PN condition created a region of locally maximum velocity fluctuation, or a locally minimum pressure fluctuation, where the fluid in this viscinity was displaced in the transverse direction, perpendicular to the jet axis and the line of sight of the jet.

The maximum peak-to-peak pressure perturbation, p'_{pk-pk}, amplitude attained in the present experiments were well below 5% of the mean chamber pressure, P_c, where 5% is considered to be the threshold for the onset of rough combustion (Sutton [70]). On average, slightly higher p'_{pk-pk}/P_c were attainable at $P_r = 0.44$ than at $P_r = 1.05$ because of the higher chamber fluid density in the latter. Most PAN forcing conditions had $p'_{pk-pk}/P_c = 1.00\% - 1.50\%$ at $P_r = 0.44$, and $p'_{pk-pk}/P_c = 0.70\% - 1.20\%$ at $P_r = 1.05$. Ideally, PN forcing conditions should not have produced pressure perturbations larger that what was measured under baseline flow conditions, which was $p'_{pk-pk}/P_c \leq 0.02\%$. However, a lot of factors prevent the complete cancelation of the pressure waves at the coaxial jet location including imperfect match between the individual traveling waves, the presence of access holes and flow obstructions such as the injector tube, which can produce additional reflected running waves. Thus, most PN forcing conditions had $p'_{pk-pk}/P_c = 0.05\% - 0.30\%$ although there were a few cases that registered higher amplitude pressure perturbations.

The forcing frequencies applied for all forcing conditions, except one anomalous case forced at 3.41 kHz, were in the 3.00 - 3.12 kHz range since the frequency response of the piezosirens were maximum in that frequency range. For both injectors, these forcing frequencies were within 5-10% of the fundamental resonance frequency of the outer jet injector tube. In actual combustion chambers, these kilohertz range frequencies constitute what are known as screeching or screaming instabilities, which are associated with the most destructive type of combustion instability.

5.2.1 Qualitative Characteristics of Acoustically Forced Flows

The impact of the PAN and PN forcing on the mixing characteristics and on the natural development of flow instabilities was found to depend on flow parameters, namely the momentum flux ratio, as well as the injector geometry. Figures 5.18a-g show snapshot images of the LAR-thin injector flows at $P_r = 0.44$ under the PAN and PN forcing conditions. The corresponding baseline flow images are also shown for reference. For $J = 0.1$, Figure 5.18a shows that the PAN forcing produced uniformly spaced bulges on either side of the planar view of the inner jet. Unlike baseline flow conditions, since transverse forcing introduced a bias to the flow in the vicinity of the coaxial jet, it would no longer be valid to generalize the observed behavior in the planar view to an axisymmetric flow behavior. Thus, the most that can be deduced from the observable response of the $J = 0.1$ jet is that the PAN forcing produced periodic disturbances of the flow that were symmetric about a plane perpendicular to the transverse direction and passing through the jet center. In planar jet configurations, such a symmetric disturbances in the shear-layer vortex sheets is commonly known as a varicose mode of disturbance (Yu and Monkewitz [71]). The resulting waves of instability were evenly spaced closer to the exit, but merged and formed disorderly structures farther downstream. The dark-core length was also notably shorter than that of the baseline flow. In contrast, the PN forcing condition imposed periodic transverse displacements of the inner shear layer, resulting in a sinuous mode of disturbance that became more prominent with increasing downstream distance.

The $J = 0.5$ LAR-thin injector flows in Figure 5.18b showed similar responses to the PAN and PN forcing conditions as $J = 0.1$. The evenly spaced and growing surface waves on the inner jet formed during the PAN forcing could be seen until the end of the dark-core region. The PN forcing also produced a prominent sinuous disturbance of the inner jet. Both forcing conditions promoted the disintegration of the inner jet, thereby, leading to enhanced mixing of the outer and inner jets.

For $J = 2.1$, although the presence of a varicose mode of disturbance during the PAN forcing was discernable in the image, the growth of the resulting symmetric structures was relatively subdued. Yet, the PN forcing still imposed a significant sinuous disturbance on the inner jet. With increasing J, the effect of acoustic forcing gradually subsided. For $J = 5.2$, varicose disturbances were barely visible during the PAN forcing while sinuous disturbance during the PN forcing was still present. For the higher momentum flux ratio flows, $J = 11 - 20$ shown in Figures 5.18e-g, the flows under the PAN forcing were virtually similar to the corresponding baseline flows. Meanwhile, although the sinuous disturbances of the inner jet were considerably reduced compared to the lower J flows, their presence was still evident in the images. It is worth noting that while the undulations in the inner jet began close to the injector exit for low J, it was merely limited to the end of the dark-core at higher J values.

Figures 5.19a-f show a similar set of images of the LAR-thin injector flows at $P_r = 1.05$. The PN forcing cases were only obtained for the $J = 0.5$ and $J = 5.0$ flows. Similar to the observations at $P_r = 0.44$, the PAN forcing conditions imposed strong varicose disturbances on the inner shear layer that subsided with increasing J. The periodic disturbance structures formed during PAN forcing of the $J = 0.1$ shown in Figure 5.19a were not distinctly visible. The absence of such discrete flow structures may be due to the negligible surface tension at $P_r = 1.05$.

For $J = 0.5$ and $J = 1.9$, the familiar symmetric structures were clearly visible during the PAN forcing as shown in Figures 5.19b and 5.19c, respectively. As the momentum flux ratio increased to $J = 5.0$ and higher, the inner shear layer became progressively less vulnerable to the varicose mode of disturbance during the PAN forcing. The PN forcing condition for $J = 0.5$ showed very small sinuous disturbances while that for $J = 5.0$ showed stronger undulations. This may be since the latter case had a better defined PN condition whose p'_{pk-pk}/P_c was closer to zero.

In general, under both chamber pressure conditions, the dynamics of the inner jet of the LAR-thin flow configuration became less and less sensitive to acoustic forcing with increasing J values. This was especially true with PAN forcing. To elaborate on the mechanism and to illustrate how the effect of a PAN forcing on the dynamics of the inner jet depended on J, a sequence of 15 images at 40 μs intervals are shown in Figures 5.20 and 5.21 for the $J = 0.5$ and $J = 14$ flows, respectively, at $P_r = 0.44$. The raw images were enhanced to create some contrast between the outer jet and the ambient fluid. Figures 5.22 and 5.23 show a time series plot of the normalized local pressure perturbation amplitudes at the instant that each corresponding image frame was recorded during the PAN acoustic forcings at 3.14 kHz and 3.11 kHz, respectively. Thus, the sets of images represent a period of about one and a half acoustic cycles.

Based on the pressure perturbation amplitudes in Figure 5.22, for example, images 2-5 and 10-13 in Figure 5.20 show the compression cycles while images 6-9 show the expansion cycle. At the onset of each compression cycle, a large vortex structure was formed in the outer shear layer. As it was being convected downstream, it grew and entrained fluid from the inner shear layer along with part of the inner jet. Thus, inner shear-layer vortices were formed at the same frequency as did the outer shear-layer vortices, which were in turn, formed at the acoustic forcing frequency. However, for the higher J flow shown in Figure 5.21, where the outer jet velocities were considerably larger, the outer shear-layer vortex convection time scales became much smaller than their formation and growth time scales. Accordingly, for higher J flows under comparable PAN forcing conditions, the interaction between the outer shear-layer vortices and the inner shear layer could no longer be initiated and sustained near the jet exit, therefore, leaving the inner jets relatively undisturbed for longer distances downstream with increasing J. In addition to the increased convection speed, the large outer to inner jet area ratio also played a role in delaying the interaction between the outer and inner shear layers because it dictated the size that the outer shear-layer vortices had to grow to before being able to interact with the inner shear layer.

Similar snapshot images of the acoustically forced SAR-thick injector flows at $P_r = 0.44$ and $P_r = 1.05$ are shown in Figures 5.24a-g and Figures 5.25a-g, respectively. Despite showing response to acoustic forcing to some extent for all J values, coherent and periodic flow structures were only formed at higher J. For the $J = 0.1$ and $J = 0.5$ flows, vortical structures were only observed in the recirculation zone, while no organized flow structures developed in the inner shear layer and the inner jet. This was in contradiction with the response seen with the LAR-thin injector flows, which exhibited strong response at lower J in the form of periodic structures due to varicose or sinuous disturbances, and gradually subdued response with increasing J.

For the lowest J SAR-thick injector flow at $P_r = 0.44$ shown in Figure 5.24a, PAN forcing resulted in the formation of random ligament structures on the surface of the inner jet that grew with increasing downstream distance. The portion of the inner jet closer to the recirculation zone appeared relatively undisturbed. One possible reason for this may be because the fluid in the recirculation zone shielded the inner jet from being overcome by the outer shear-layer vortices. In the case of PN forcing, again the portion of the inner jet closer to the recirculation zone was relatively undisturbed, while farther downstream, it formed a dispersion of fine droplets.

The PAN forcing of the $J = 0.5$ flow in Figure 5.24b caused the outer shear-layer vortices to entrain fluid in the recirculation zone, but was unable to form coherent structures on the inner jet surface. However, increased spread was observed in the initial region of the inner jet, and also resulted in break-up and scattering of the ligament structures into fine droplets. On the other hand, PN forcing was less dispersive with no apparent sinuous disturbance in the inner jet.

As discussed previously, for $J = 0.1$ and $J = 0.5$, the sense of rotation of the fluid inside the recirculation zone was such that a counterflow existed at the inner jet boundary. When the momentum flux ratio increased to $J = 2.1$, the fluid inside the recirculation zone mainly consisted of the lower momentum inner jet fluid, and the sense of rotation was such that a counterflow existed at the inside boundary of the outer jet. Thus, for $J = 2.1$ and higher, the outer shear-layer vortices had the same sense of rotation as the fluid in the recirculation zone, unlike for lower J flows. One would then expect that coupling between these flow regions during varicose disturbances due to the PAN forcing may induce symmetric flow structures on the inner jet surface. However, as Figure 5.24c shows, besides imparting a merely irregular and dispersive flow pattern, the PAN forcing did not result in a periodic, varicose type of disturbance pattern on the inner jet. The PN forcing did not form any coherent sinuous motion of the jet as well.

Interestingly, as Figures 5.24d-g show, the next higher and subsequent J values exhibited the expected symmetric flow disturbances during the PAN forcing. They appeared to start just beyond the end of the recirculation zone, rolled-up and entrained the inner jet fluid further downstream. In addition, for the higher J flows, the dark-core region of the inner jet was too stubby to manifest any appreciable sinuous disturbance during the PN forcing.

At $Pr = 1.05$, acoustic forcing of the low momentum flux ratio flows, $J = 0.1$ and $J = 0.5$, in Figures 5.25a and 5.25b also exhibited weak response. This may be partly attributed to the relatively low forcing amplitudes that were achieved for those conditions. Although during the PAN forcing the outer shear layer dynamics dominated the flow in the recirculation zone, it had minimal impact on the inner jet, which appeared to be reasonably comparable to the corresponding baseline cases. The flow also had subdued response to the PN forcing.

As J increased and the sense of rotation in the recirculation zone reversed, the effect of the PAN forcing became more and more prominent. For $J = 2.1$ shown in Figure 5.25c, the PAN forcing induced what appeared to be organized, periodic structures forming along the inner jet. Its effect became increasingly pronounced for $J = 5.2 - 21$, where the symmetric outer shear-layer vortex roll-ups dominated the inner jet flow dynamics. The growing impact of the PN forcing was also seen for this range of J values, with alternate vortex roll-ups instead of symmetric ones.

5.2.2 Acoustically Forced Dark-Core Length Measurements

The dark-core lengths of the acoustically forced flows were measured and normalized by their corresponding baseline flows as shown in Figures 5.26 and 5.27 for the PAN and PN forcing conditions, respectively. Since the $J = 0.1$ and $J = 0.5$ flows had dark-core regions exceeded the borders of the image, they were excluded from these plots. The normalized PAN forcing dark-core lengths, L_{PAN}/L_B and PN forcing dark-core lengths, L_{PN}/L_B, gave a measure of the effect of each forcing condition relative to the baseline flow.

As Figures 5.26 shows, the overall trend in L_{PAN}/L_B for the LAR-thin injector flows was that it approached one with increasing J. This implied that the PAN forcing condition had less impact on the dark-core lengths at higher J. However, the effect of the PAN forcing seemed to have depended on the outer jet flowrate as well as J. This may be seen in the reduction of L_{PAN}/L_B at $P_r = 0.44$, as the momentum flux ratio increased from $J = 11$ to $J = 14$ while the outer and inner jet flowrates were reduced (Table C.1). When the momentum flux ratio was raised to $J = 21$ with further increase in the outer jet flow rate while holding the inner jet flowrate constant, the L_{PAN}/L_B also increased. This again underlined the role that the outer jet flowrate played in diminishing the impact of the PAN forcing. At $P_r = 1.05$, a similar monotonic increase in L_{PAN}/L_B with J can be seen. Furthermore, for a given J and comparable forcing conditions, L_{PAN}/L_B at $P_r = 1.05$ were lower than those at $P_r = 0.44$ as can be seen for $J \approx 2, 5$.

On the other hand, the effect of the PAN forcing on the SAR-thick injector flows was seen at higher J values. At $P_r = 0.44$, the dark-core lengths stayed relatively unchanged from that of the baseline until $J = 11$, beyond which it decreased with J. It showed a similar trend at $P_r = 1.05$ except that the dark-core region got longer at $J = 9.2$ and $J = 14$ before decreasing to below that of the baseline at $J = 21$. Thus, for the SAR-thick injector flows, the outer jet flow in the recirculation zone at low J played a major role in dampening the disturbances due to the PAN forcing.

The response to the PN forcing of the LAR-thin injector flows at $P_r = 0.44$ was similar to the PAN forcing as shown in Figure 5.27. The dark-core lengths approached that of the baseline with increasing J decreased as the jet flowrates were reduced. Unlike the PAN forcing cases, the SAR-thick injector flows showed relatively low L_{PN}/L_B that monotonically increased towards one as J increased, with an exception of the $J = 2.1$ flow at $P_r = 1.05$. Thus, these results showed that the flow in the recirculation zone was not as effective in diminishing the effect of the PN forcing condition on the SAR-thick flows.

5.2.3 Characterization of Dominant Dynamic Flow Structures

Application of POD on the high speed images of the acoustically forced flows was used to further draw contrast between the flow response to the PAN and PN forcing conditions, and the corresonding baseline conditions for the two injector configurations. Similar to the analysis results presented for the baseline flow in Section 5.1.3, time-averaged images, POM images of the conjugate modes, and the corresponding CPSD magnitude plots were used to reveal and describe the key differences. For ease of comparison, the baseline spectra are included in the CPSD magnitude plots and are shown with dotted lines.

Figures 5.28a and 5.28b show the results for the LAR-thin injector $J = 0.1$ flow during the PAN and PN forcing conditions, respectively, at $P_r = 0.44$. Unlike the baseline flow, the average image for the PAN forcing showed a more diffuse dark-core flow. In addition, as was already observed in the snapshot images, the POM images identified adjacent dark lobes, which started forming immediately downstream of the injector exit, indicating the presence of symmetric flow structures due to the varicose mode of disturbance. The dominant sharp peak in the magnitude spectrum denoted the characteristic frequency of these symmetric structures, and it was identical to the acoustic forcing frequency. The baseline flow spectral characteristic, shown in dotted line, was clearly absent in the forced flow spectrum. That is, the dominant inner shear-layer flow dynamics was completely altered during PAN forcing. In the case of the PN forcing condition, antisymmetric structures shown in the POM image indicated the presence of sinusoid disturbances as opposed to the helical disturbances in baseline flows, since the PN forcing imposed a bias in the transverse direction. The corresponding magnitude spectrum again had a sharp peak frequency identical to the acoustic forcing frequency, and it can be seen that the low frequency peak of the baseline flow was also removed from this spectrum.

The next two higher momentum flux ratio flows, $J = 0.5$ and $J = 2.1$, also exhibited similar responses to the PAN and PN forcing conditions. The POM images in Figures 5.29a and 5.30a showed the formation of symmetric structures due to the PAN forcing condition. As discussed earlier, with increasing J, the outer shear-layer vortices attained larger convection speed due to the increasing outer jet mass flowrate. Since the observed symmetric structures were a direct outcome of the interaction of the outer shear-layer vortices with the inner shear layer, this increased convection speed was apparent in the stretching of the dark and light lobes in the POM images. The magnitude spectra also had dominant sharp peaks at the forcing frequency without any significant remnant of the baseline spectral characteristic. For the PN forcing conditions in Figures 5.29b and 5.30b, the sinusoidal disturbances were depicted with antisymmetric structures in the POM images. The apparent stretch in the dark lobes with increasing J again showed the corresponding increases in the disturbance propagation speed. The sharp dominant peaks at the forcing frequencies also indicated strong response to the PN forcing.

When the momentum flux ratio further increased to $J = 5.2$, the identified dominant structures during the PAN forcing condition were mainly antisymmetric as shown in Figure 5.31a. Although it cannot be deduced without further evidence that these antisymmetric structures represented helical disturbances as in baseline flow conditons, it can nevertheless be argued that unlike the PN forcing condition, which set-up a velocity antinode at the jet location, PAN forcing did not induce a net motion in the transverse direction. Thus, these antisymmetric structures may very well have represented helical disturbances. Moreover, despite still having a dominant peak at the forcing frequency in the magnitude spectrum, the $J = 5.2$ flow retained some of the baseline flow spectral behavior, in contrast to the lower J flows. The PN forcing condition, on the other hand, continued imposing strong sinuoidal disturbances as shown in the POM image in Figure 5.31b. As with the PAN forcing condition, the magnitude spectrum had a dominant peak at the forcing frequency but also retained the baseline spectral characteristic.

At the higher momentum flux ratios, $J = 11$, 14, and 20, the diminishing impact of the PAN forcing became more evident in the baseline flow types of antisymmetric structures, and even more importantly, in their spectral behavior as shown in Figures 5.32a, 5.33a, and 5.34a, respectively. The magnitude spectra still clearly show a peak at the forcing frequency. However, the broad characteristic peaks in the baseline spectra were retained, and were also relatively significant in amplitude. The PN forcing conditions in Figures 5.32b, 5.33b, and 5.34b also exhibited this retentive behavior although they still had a relatively strong peak at the forcing frequency.

At $P_r = 1.05$, the LAR-thin injector flows during the PAN forcing condition also showed the trend where a gradual shift occurred from flows with symmetric structures and spectral characteristic dominated by the forcing frequency to those with antisymmetric structures and spectra that also retained the baseline flow characteristic with increasing J. Accordingly, the lower momentum flux ratio flows, $J = 0.5$ and $J = 1.9$, formed symmetric structures in response to PAN forcing as shown in Figures 5.35a and 5.36. Their magnitude spectra also showed single dominant peaks at frequencies identical to the forcing frequencies, and none of their baseline spectral characteristics were retained. As the momentum flux ratio increased to $J = 5.0$, only antisymmetric structures were sustained as shown in Figure 5.37a. However, its spectral characteristic was still distinct from that of the baseline. For the higher momentum flux ratio flows, $J = 8.5$ and $J = 12$, although their spectra still had dominant peaks at the forcing frequency, the baseline spectral characteristics were also retained as shown in Figures 5.38 and 5.39. The PN forcing conditions for only the $J = 0.5$ in Figure 5.35b and $J = 5.0$ in Figure 5.37b were obtained. It can be seen that both flow conditions exhibited the expected sinusoid disturbances and dominant peaks at the forcing frequencies.

As discussed earlier, one of the distinguishing features of the SAR-thick injector flows was the presence of a flow recirculation zone. This created a delay in the interaction between the inner jet and the outer shear layer. Moreover, it was observed that for low momentum flux ratio flows, such as $J = 0.1$ and $J = 0.5$, the recirculation zone was filled with the outer jet fluid that had an opposite sense of rotation from the outer shear-layer vortices during the PAN forcing. Thus, this prevented the outer shear-layer vortices to dominate the dynamics of the inner shear layer. In light of this, for the $J = 0.1$ flow during the PAN forcing at $P_r = 0.44$, the POM image exhibited antisymmetric structures with low characteristic frequency as shown in Figure 5.40. The resulting behavior of the dominant flow structures was indeed different from the corresponding baseline case shown in Figure 5.14a. However, unlike the LAR-thin flows, there was no response at the forcing frequency.

The $J = 0.5$ and $J = 2.1$ flows also exhibited similar behavior during PAN forcing as shown in Figures 5.41 and 5.42a, respectively. Based on the snapshot images as well as the POM images, the dominant flow disturbance structures during the PAN forcing were clearly distinct from their baseline counterparts. However, as their magnitude spectra show, none of these flow structures had characteristic frequencies identical to the forcing frequencies. This again shows that the low J, SAR-thick injector inner jet flow dynamics was insensitive to the PAN acoustic forcing. Moreover, as Figure 5.42b shows, the $J = 2.1$ flow during the PN forcing also showed a similar spectral behavior. The PN forcing cases for the $J = 0.1$ and $J = 0.5$ were not reported because conjugate modes could not be identified.

When the momentum flux ratio increased to $J = 5.7$, symmetric disturbance structures appeared downstream of the recirculation zone as shown in the POM images for the PAN forcing condition in Figure 5.43a. A dominant peak at the forcing frequency was identified in the magnitude spectrum. A dominant peak was also identified in the spectrum during the PN forcing condition as shown in Figure 5.43b. Its corresponding POM image shows initially antisymmetric structures due to the sinusoid disturbances, but appeared symmetric further downstream.

The POM images in Figures 5.44a, 5.45a, and 5.46a, for the $J = 10$, $J = 15$, and $J = 21$ flows, respectively, also showed similar symmetric structures during the PAN forcing condition. Their magnitude spectra had dominant peaks at the forcing frequency as well, thus providing further evidence that the SAR-thick flows were more responsive to the PAN forcing at higher J. A unique feature of the $J = 21$ flow was that initially symmetric structures gradually became antisymmetric further downstream perhaps due to the dominant nature of helical instabilities at such a high J. Meanwhile, the POM images in Figures 5.44b, 5.45b, and 5.46b for these high J flows showed the expected antisymmetric structures due to the periodic transverse displacements during the PN forcing condition. The spectra also show distinct peaks at the forcing frequencies.

Likewise at $P_r = 1.05$, the low J flows showed subdued response to the PAN forcing while the higher J flows formed symmetric structures with characteristic frequencies identical to the forcing frequencies. Accordingly, the POM images and magnitude spectra in Figures 5.47, 5.48a, and 5.49a for the $J = 0.1$, $J = 0.5$, and $J = 2.1$ flows, respectively, showed neither the symmetric structures nor dominant peak frequencies at the forcing frequency. On the contrary, the $J = 5.2$ and higher flows exhibited the familiar symmetric structures with strong responses at the forcing frequencies. Similarly, the higher J flows also showed stronger response to the PN forcing condition as evident in the antisymmetric structures seen in the POM images, and the dominant peaks at the forcing frequencies in the magnitude spectra shown in Figures 5.50b, 5.51b, 5.52b, and 5.53b.

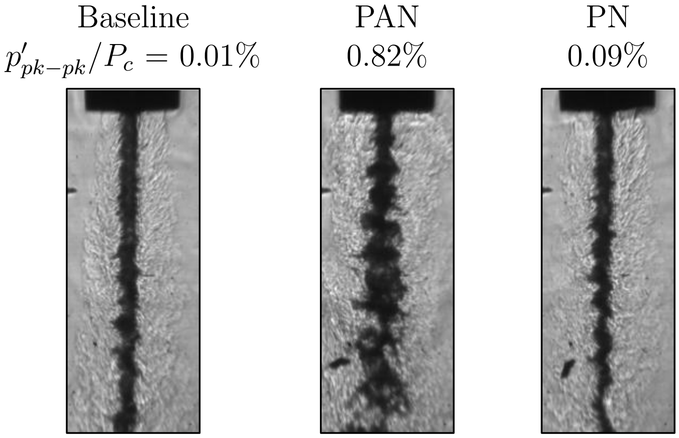

Baseline $p'_{pk-pk}/P_c = 0.01\%$ | PAN 0.82% | PN 0.09%

(a) $J = 0.1$, $f_F = 3.13$ kHz

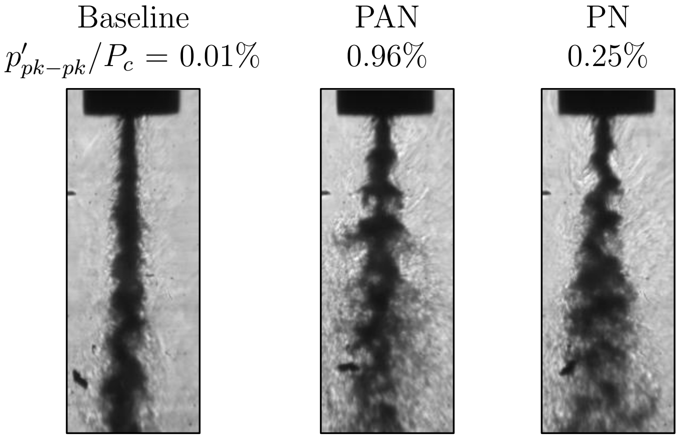

Baseline $p'_{pk-pk}/P_c = 0.01\%$ | PAN 0.96% | PN 0.25%

(b) $J = 0.5$, $f_F = 3.14$ kHz

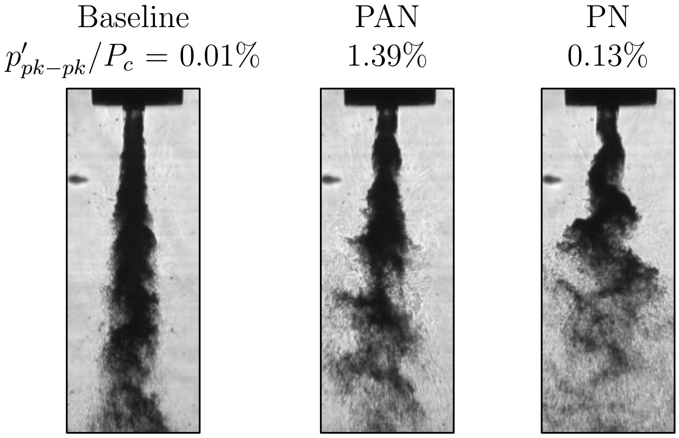

Baseline $p'_{pk-pk}/P_c = 0.01\%$ | PAN 1.39% | PN 0.13%

(c) $J = 2.1$, $f_F = 3.12$ kHz

Figure 5.18: See caption on page 147.

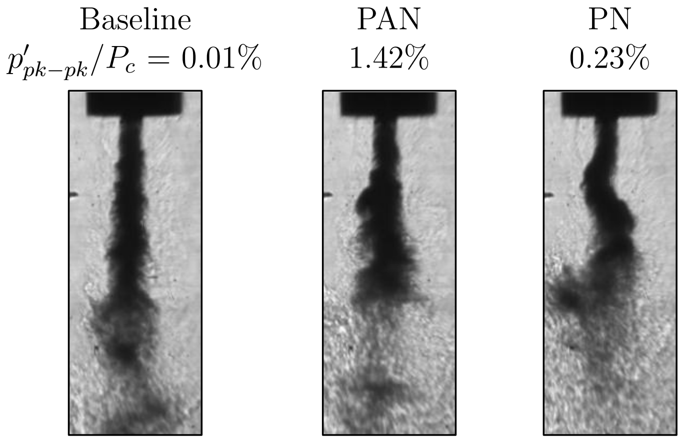
Baseline $p'_{pk-pk}/P_c = 0.01\%$ PAN 1.42% PN 0.23%

(d) $J = 5.2$, $f_F = 3.12$ kHz

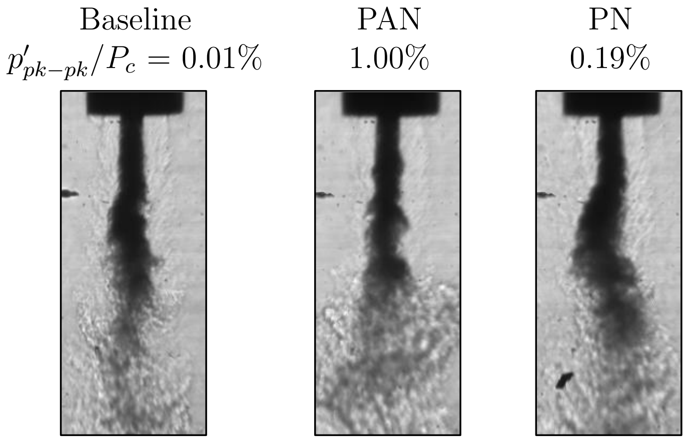
Baseline $p'_{pk-pk}/P_c = 0.01\%$ PAN 1.00% PN 0.19%

(e) $J = 11$, $f_F = 3.10$ kHz

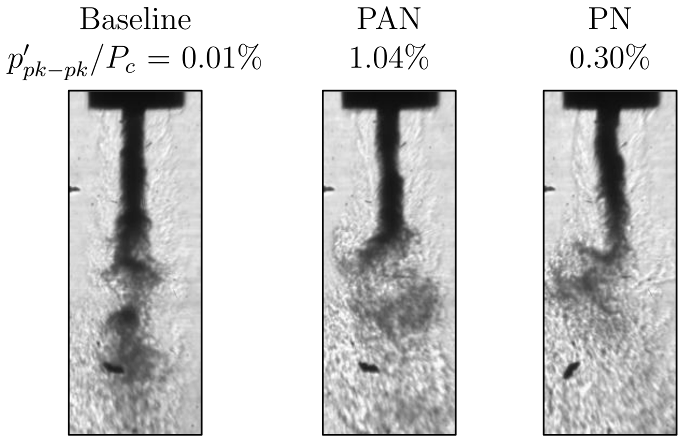
Baseline $p'_{pk-pk}/P_c = 0.01\%$ PAN 1.04% PN 0.30%

(f) $J = 14$, $f_F = 3.11$ kHz

Figure 5.18: See caption on page 147.

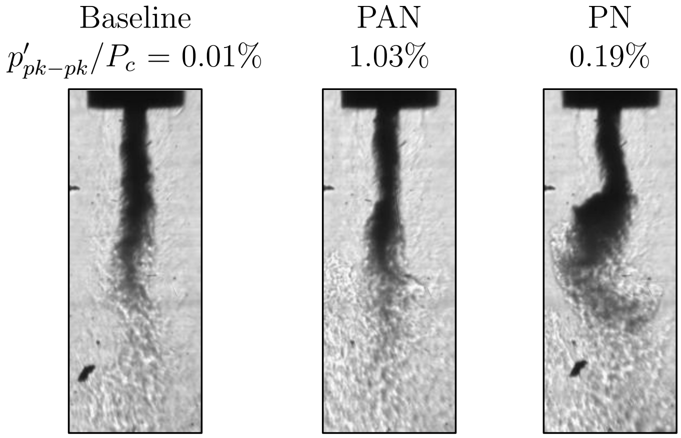
Baseline
$p'_{pk-pk}/P_c = 0.01\%$
PAN
1.03%
PN
0.19%

(g) $J = 20$, $f_F = 3.11$ kHz

Figure 5.18: Back-lit images of the LAR-thin injector PAN flow at $P_r = 0.44$ and varying J. The image framing rate was 25 kHz. Table C.3 gives a summary of the acoustic forcing frequencies and amplitudes.

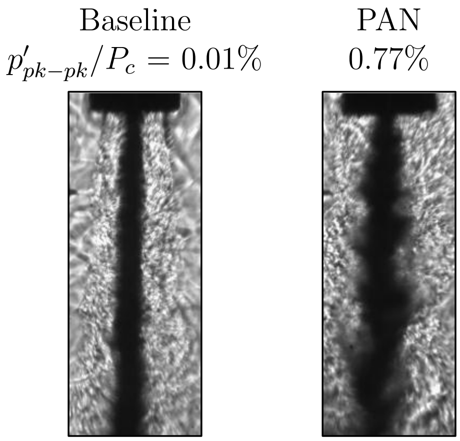
Baseline
$p'_{pk-pk}/P_c = 0.01\%$
PAN
0.77%

(a) $J = 0.1$, $f_F = 3.16$ kHz

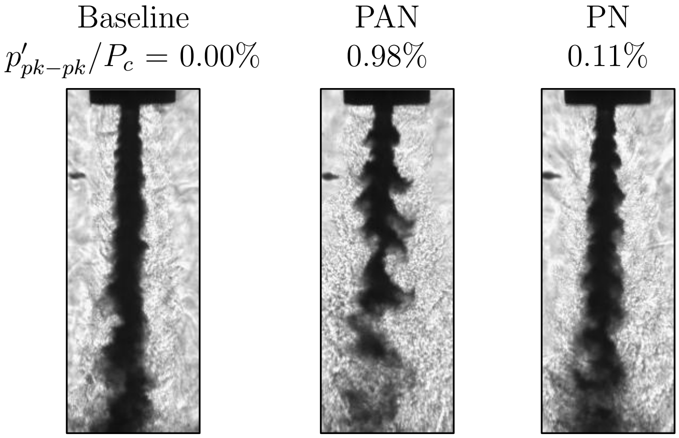
Baseline
$p'_{pk-pk}/P_c = 0.00\%$
PAN
0.98%
PN
0.11%

(b) $J = 0.5$, $f_F = 3.10$ kHz

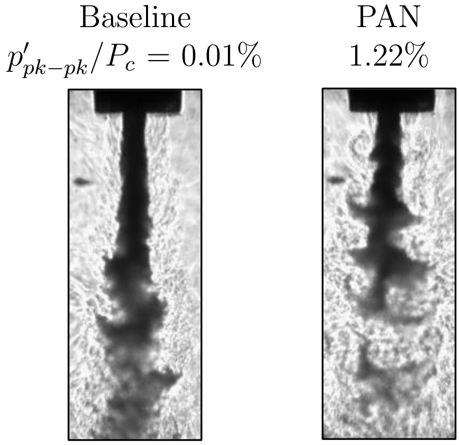
Baseline
$p'_{pk-pk}/P_c = 0.01\%$
PAN
1.22%

(c) $J = 1.9$, $f_F = 3.10$ kHz

Figure 5.19: See caption on page 149.

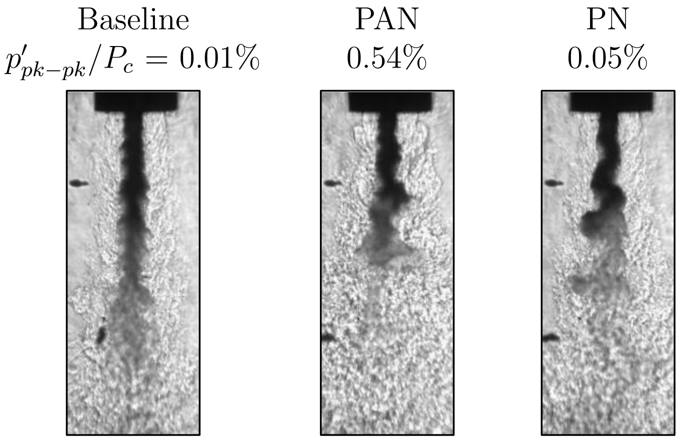
Baseline $p'_{pk-pk}/P_c = 0.01\%$ | PAN 0.54% | PN 0.05%

(d) $J = 5.0$, $f_F = 3.41$ kHz

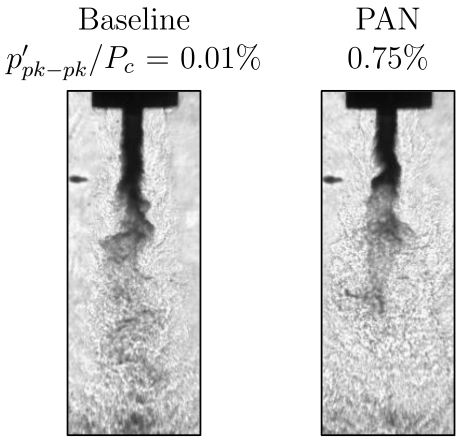
Baseline $p'_{pk-pk}/P_c = 0.01\%$ | PAN 0.75%

(e) $J = 8.5$, $f_F = 3.10$ kHz

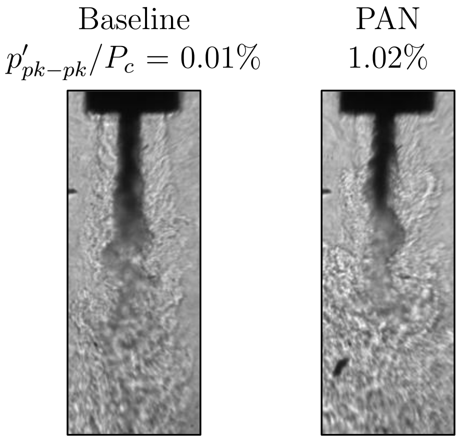
Baseline $p'_{pk-pk}/P_c = 0.01\%$ | PAN 1.02%

(f) $J = 12$, $f_F = 3.10$ kHz

Figure 5.19: Back-lit images of the LAR-thin injector PAN flow at $P_r = 1.05$ and varying J. The image framing rate was 25 kHz. Table C.3 gives a summary of the acoustic forcing frequencies and amplitudes.

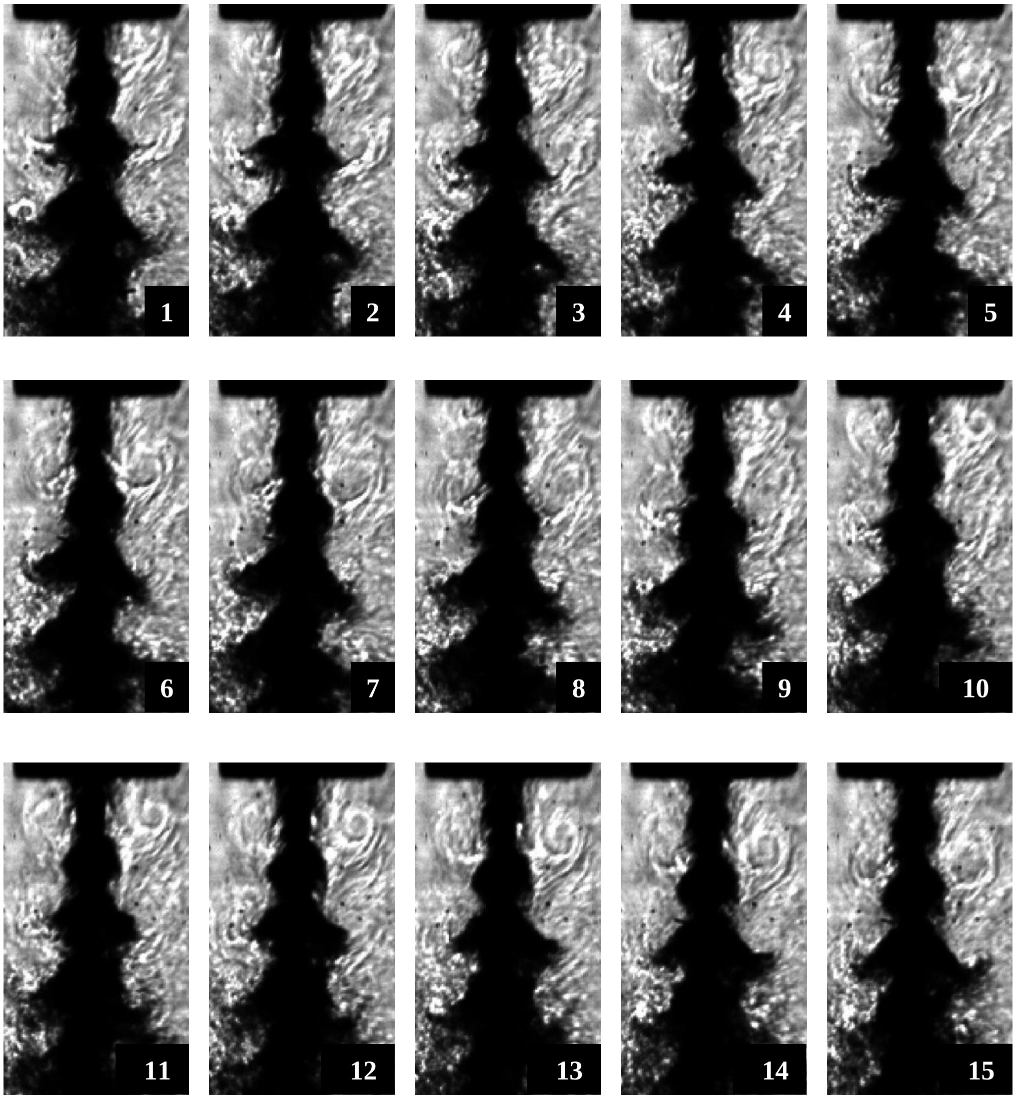

Figure 5.20: A time-sequence of images during PAN forcing ($f_F = 3.14$ kHz) of the $J = 0.5$ LAR-thin injector flow at $P_r = 0.44$. The images were captured at 40 μs intervals, and show formation of the outer shear layer vortices, which grow and dominate the inner shear layer and inner jet flow dynamics.

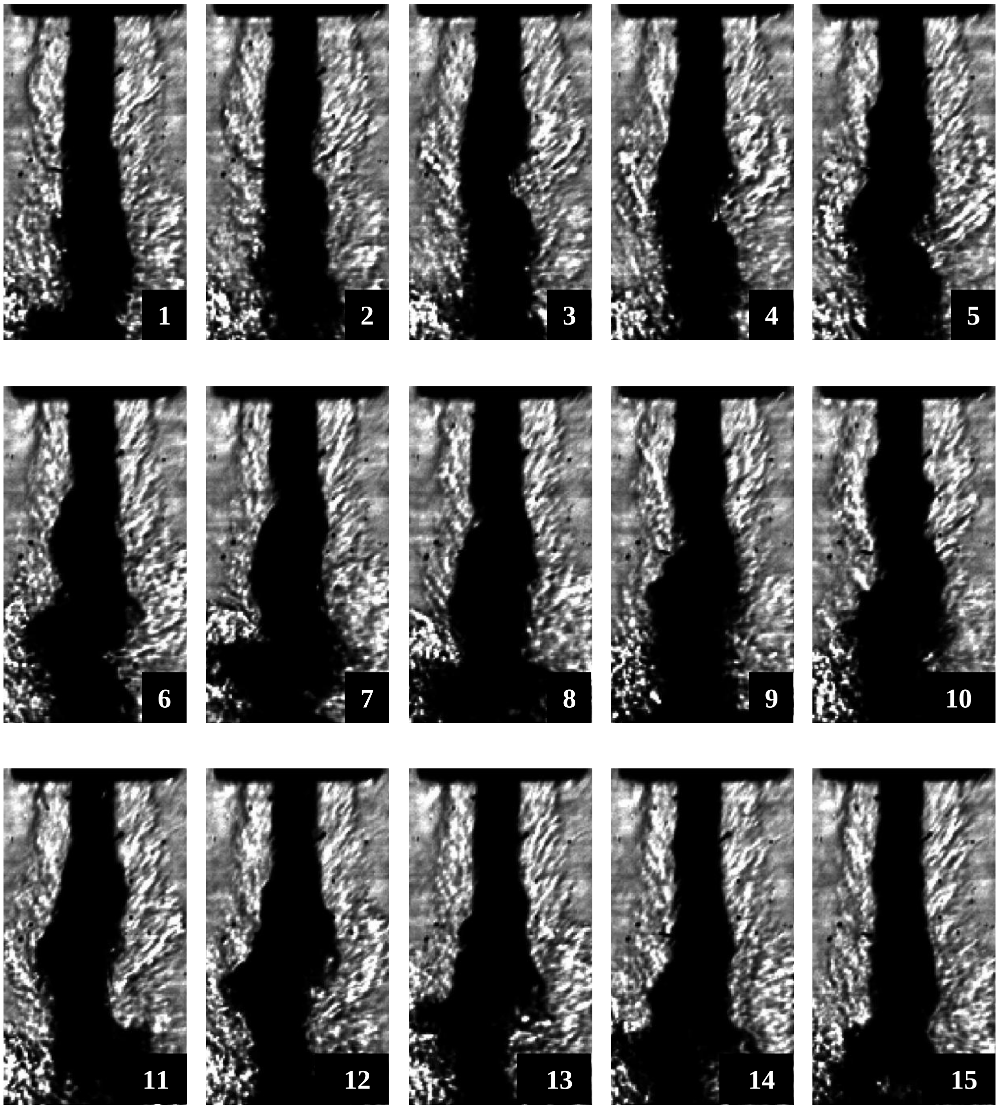

Figure 5.21: A time-sequence of images during PAN forcing ($f_F = 3.11$ kHz) of the $J = 14$ LAR-thin injector flow at $P_r = 0.44$. The images were captured at 40 μs intervals. Unlike the $J = 0.5$ flow in Figure 5.20, the large convection speed of the shear layer vortices prevented their interaction with the inner shear layer.

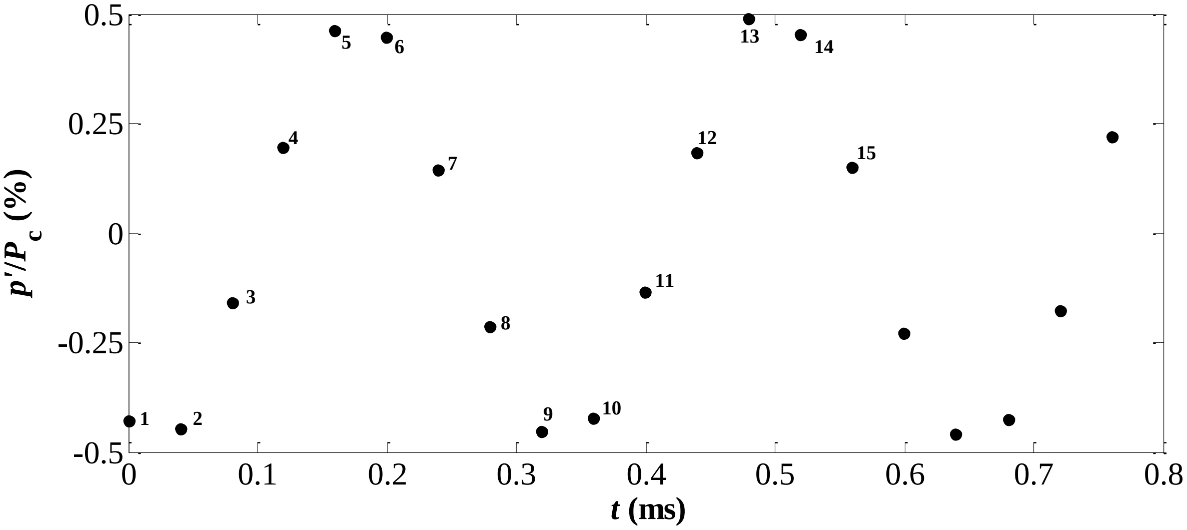

Figure 5.22: Synchronized acoustic pressure perturbation measurements during PAN forcing (f_F = 3.14 kHz) of the J = 0.5 LAR-thin injector flow at P_r = 0.44. The numbers next to the data points refer to the amplitudes measured corresponding to the image numbers in Figure 5.20.

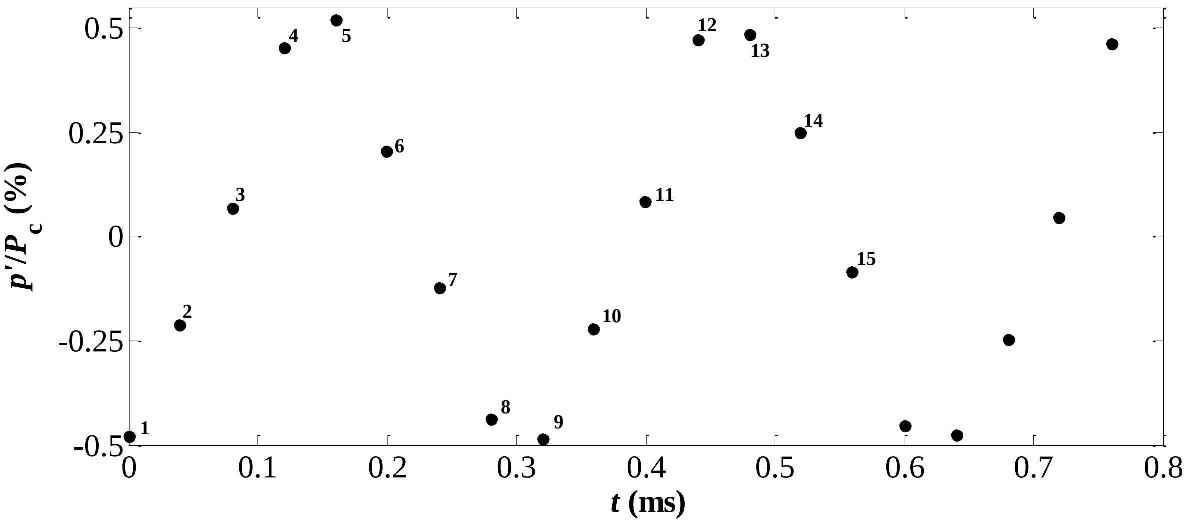

Figure 5.23: Synchronized acoustic pressure perturbation measurements during PAN forcing (f_F = 3.11 kHz) of the J = 14 LAR-thin injector flow at P_r = 0.44. The numbers next to the data points refer to the amplitudes measured corresponding to the image numbers in Figure 5.21.

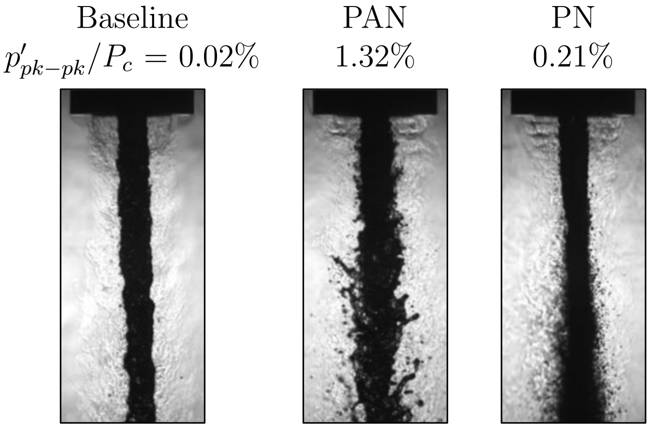
Baseline
PAN
PN
$p'_{pk-pk}/P_c = 0.02\%$
1.32%
0.21%

(a) $J = 0.1$, $f_F = 3.10$ kHz

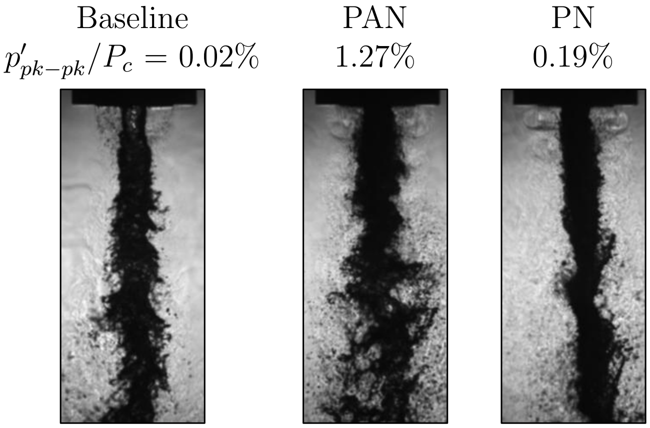
Baseline
PAN
PN
$p'_{pk-pk}/P_c = 0.02\%$
1.27%
0.19%

(b) $J = 0.5$, $f_F = 3.04$ kHz

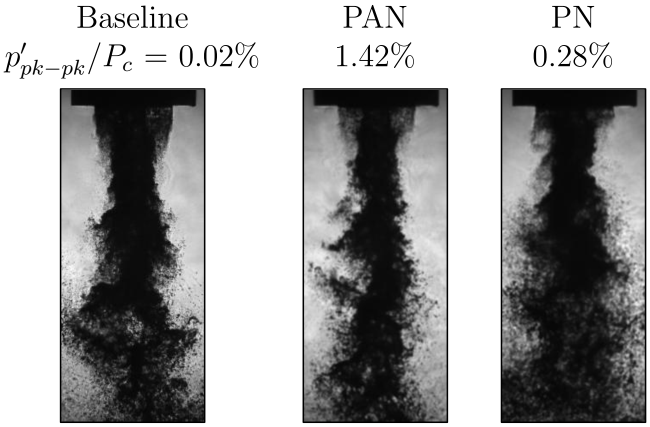
Baseline
PAN
PN
$p'_{pk-pk}/P_c = 0.02\%$
1.42%
0.28%

(c) $J = 2.1$, $f_F = 3.07$ kHz

Figure 5.24: See caption on page 155.

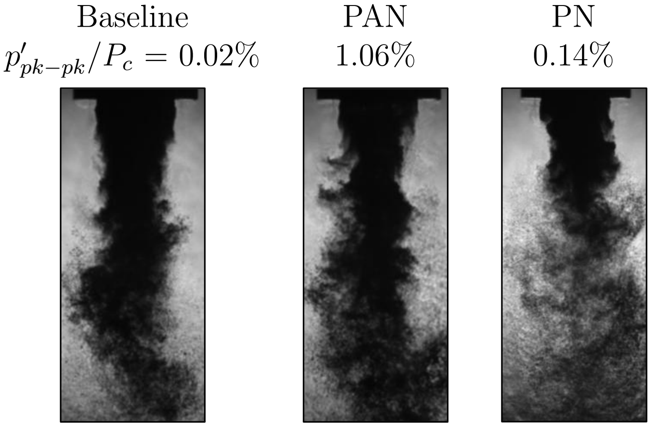
Baseline
$p'_{pk-pk}/P_c = 0.02\%$
PAN
1.06%
PN
0.14%

(d) $J = 5.7$, $f_F = 3.11$ kHz

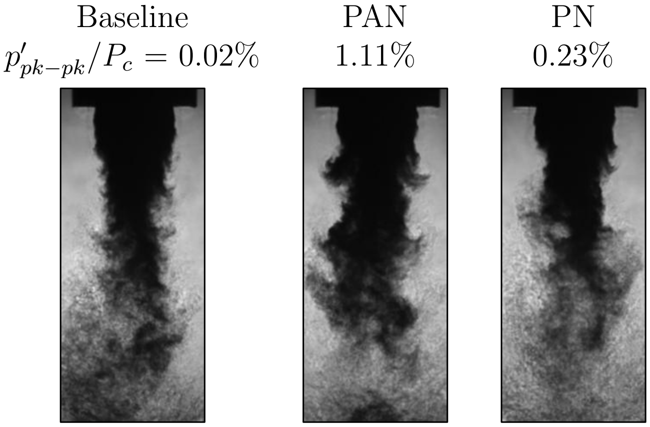
Baseline
$p'_{pk-pk}/P_c = 0.02\%$
PAN
1.11%
PN
0.23%

(e) $J = 10$, $f_F = 3.11$ kHz

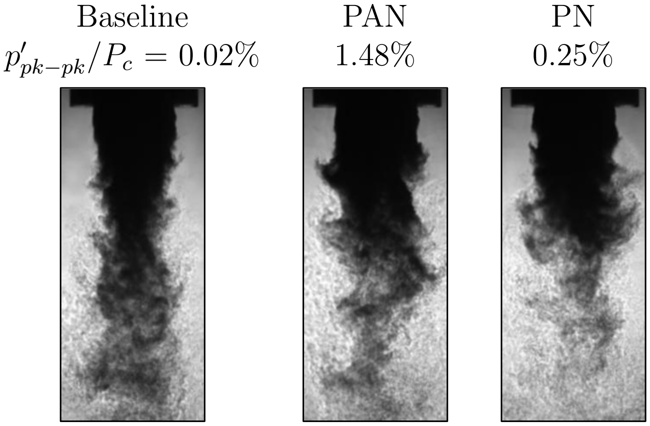
Baseline
$p'_{pk-pk}/P_c = 0.02\%$
PAN
1.48%
PN
0.25%

(f) $J = 15$, $f_F = 3.04$ kHz

Figure 5.24: See caption on page 155.

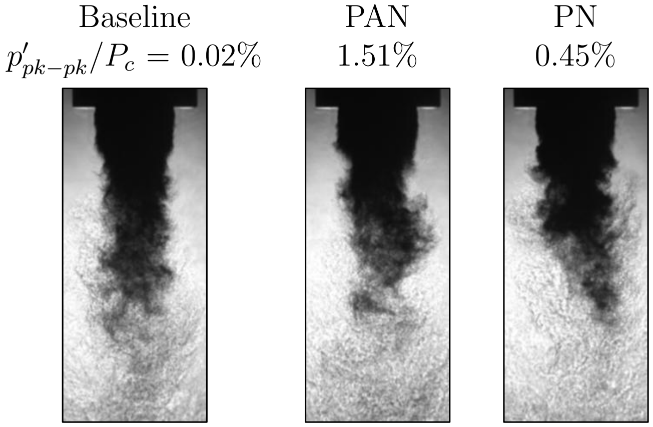
Baseline
$p'_{pk-pk}/P_c = 0.02\%$
PAN
1.51%
PN
0.45%

(g) $J = 21$, $f_F = 3.11$ kHz

Figure 5.24: Back-lit images of the SAR-thick injector PAN flow at $P_r = 0.44$ and varying J. The image framing rate was 25 kHz. Table C.4 gives a summary of the acoustic forcing frequencies and amplitudes.

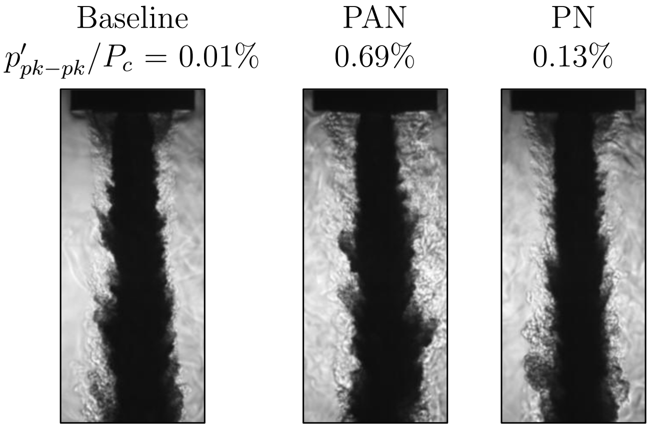
Baseline
$p'_{pk-pk}/P_c = 0.01\%$
PAN
0.69%
PN
0.13%

(a) $J = 0.1$, $f_F = 3.12$ kHz

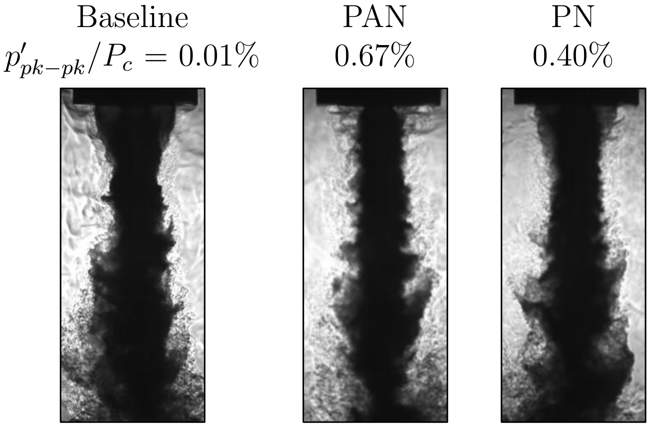
Baseline
$p'_{pk-pk}/P_c = 0.01\%$
PAN
0.67%
PN
0.40%

(b) $J = 0.5$, $f_F = 3.00$ kHz

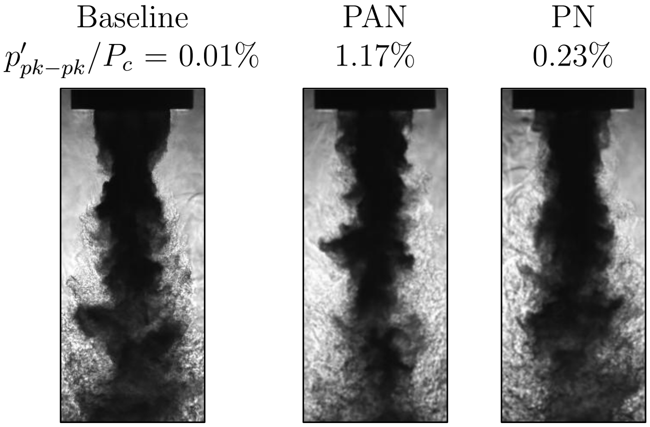
Baseline
$p'_{pk-pk}/P_c = 0.01\%$
PAN
1.17%
PN
0.23%

(c) $J = 2.1$, $f_F = 3.04$ kHz

Figure 5.25: See caption on page 158.

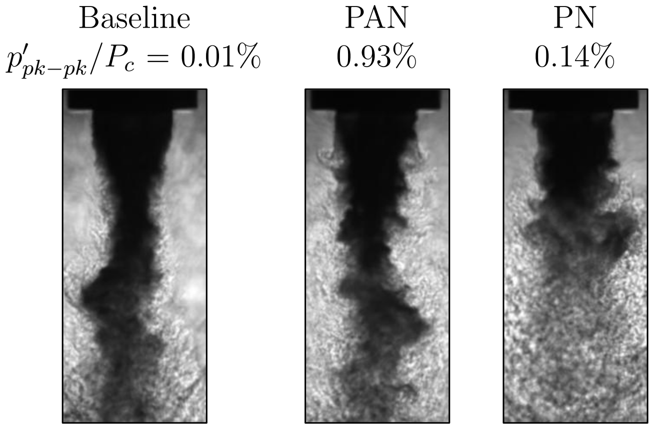
Baseline
$p'_{pk-pk}/P_c = 0.01\%$
PAN
0.93%
PN
0.14%

(d) $J = 5.2$, $f_F = 3.08$ kHz

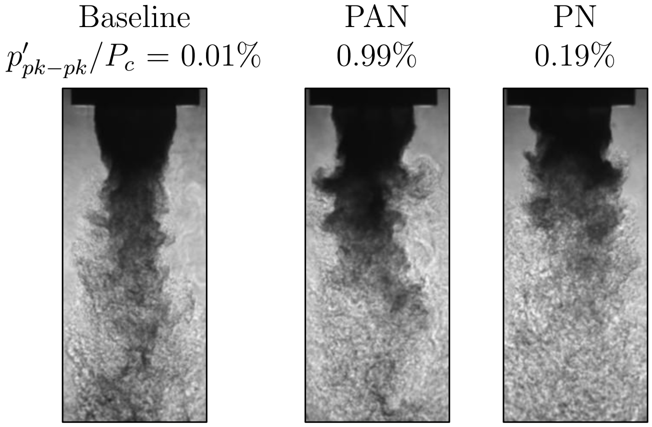
Baseline
$p'_{pk-pk}/P_c = 0.01\%$
PAN
0.99%
PN
0.19%

(e) $J = 9.2$, $f_F = 3.11$ kHz

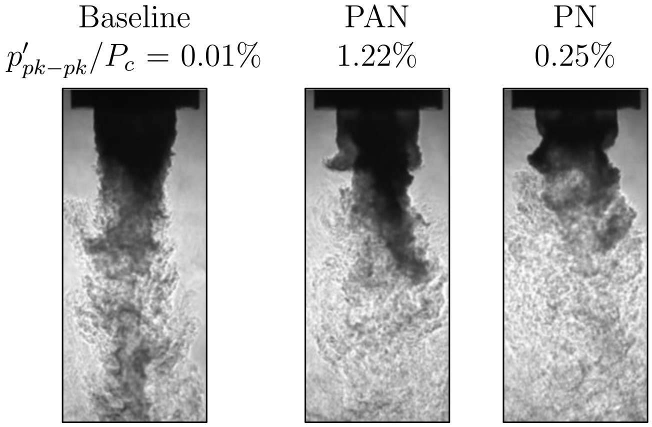
Baseline
$p'_{pk-pk}/P_c = 0.01\%$
PAN
1.22%
PN
0.25%

(f) $J = 14$, $f_F = 3.04$ kHz

Figure 5.25: See caption on page 158.

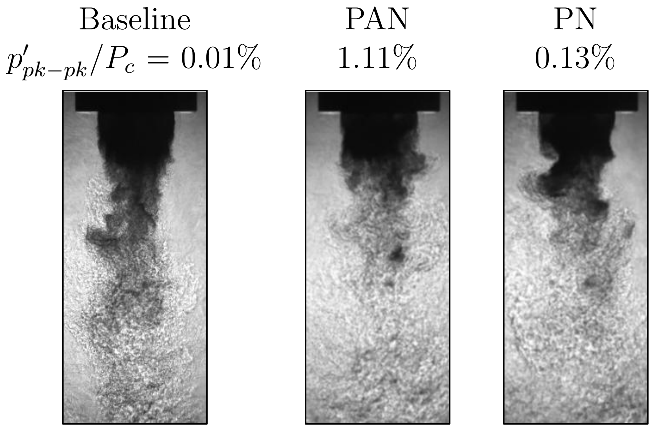

(g) $J = 21$, $f_F = 3.12$ kHz

Figure 5.25: Back-lit images of the LAR-thin injector PAN flow at $P_r = 1.05$ and varying J. The image framing rate was 25 kHz. Table C.4 gives a summary of the acoustic forcing frequencies and amplitudes.

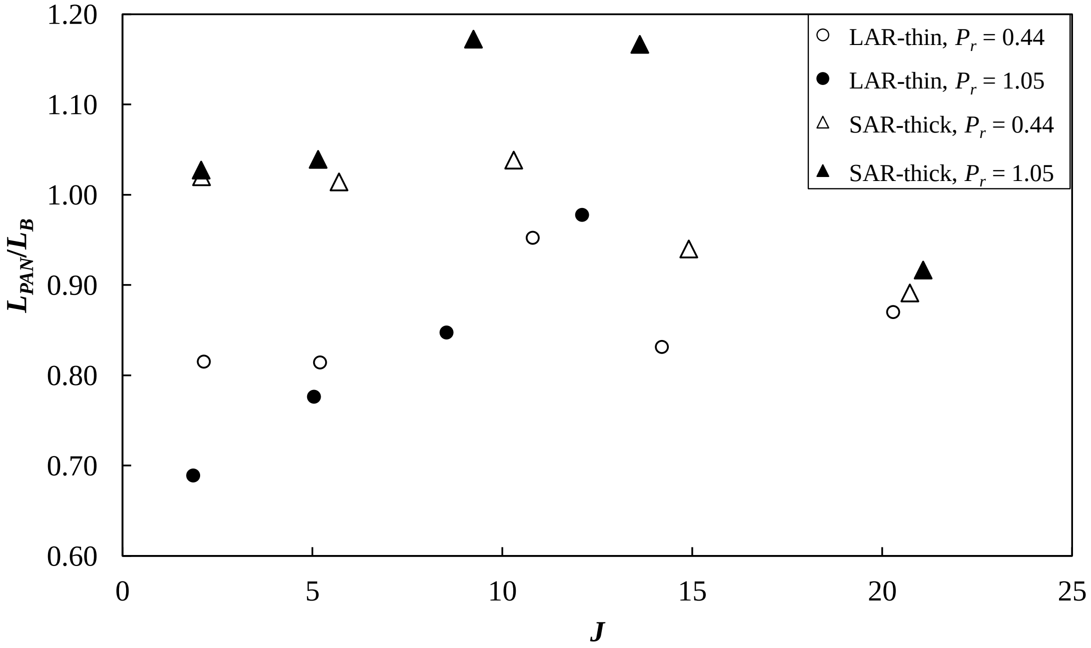

Figure 5.26: Measurements of the PAN forced flow dark-core length, L_PAN normalized by the corresponding baseline flow dark-core length, L_B.

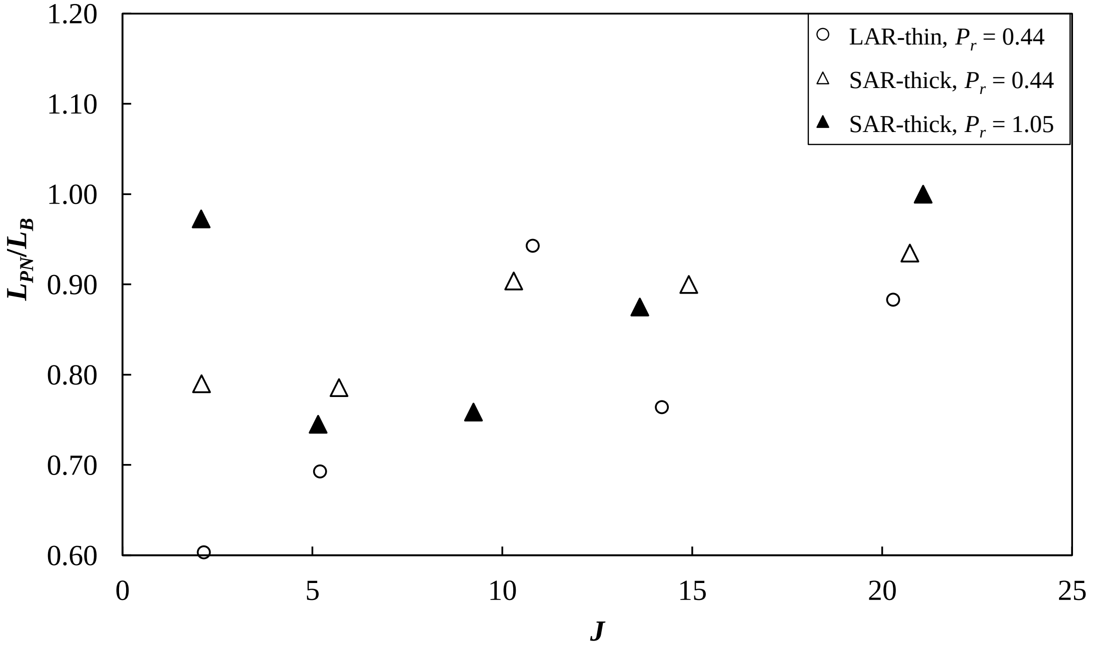

Figure 5.27: Measurements of the PN forced flow dark-core length, L_PN normalized by the corresponding baseline flow dark-core length, L_B.

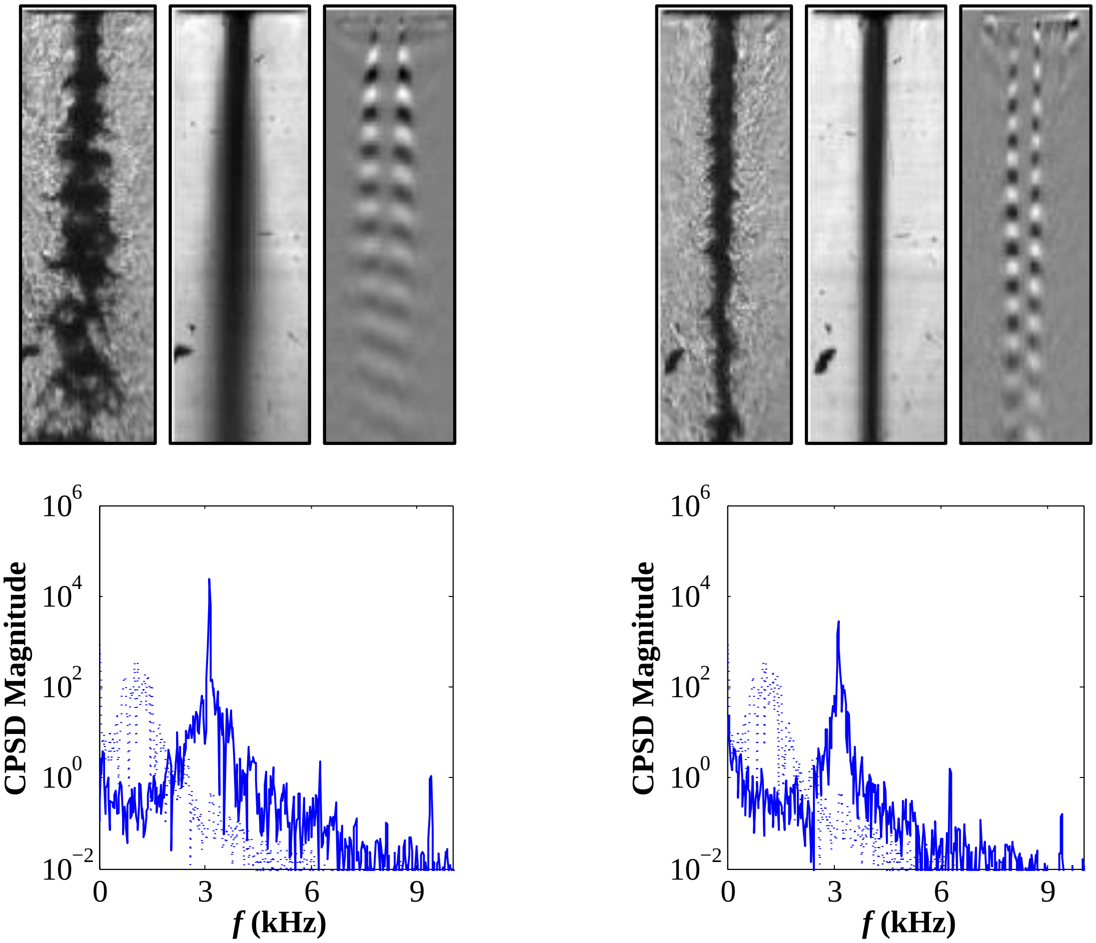

(a) $J = 0.1$, PAN

(b) $J = 0.1$, PN

Figure 5.28: A back-lit image of the LAR-thin injector forced ($f_F = 3.13$ kHz) flows at $P_r = 0.44$ similar to that in Figure 5.18, a time-averaged image and an image of the superposed conjugate proper orthogonal modes (POMs). The averaged image consisted of 1000 frames sampled at 25 kHz. The corresponding plots are the cross-power spectral density (CPSD) magnitude of the time-dependent amplitude cofficients of the conjugate modes. The peak characteristic frequencies of the periodic flow structures were identical to f_F. For the purpose of comparison, the baseline spectra are shown in dots. Under both the PAN and PN forcing conditions, the forced spectra were completely different from that of the baseline. (.........Baseline, ———Forced)

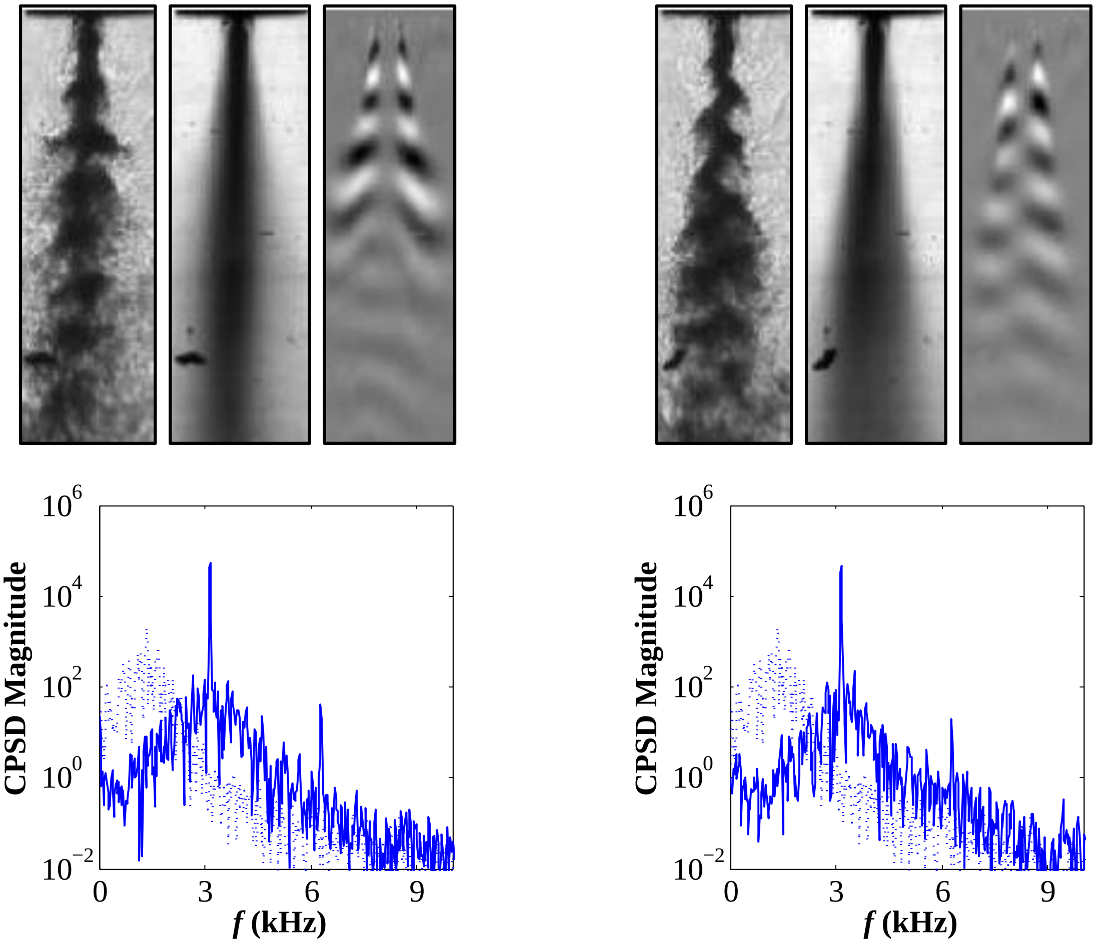

(a) $J = 0.5$, PAN

(b) $J = 0.5$, PN

Figure 5.29: A back-lit image of the LAR-thin injector forced ($f_F = 3.14$ kHz) flows at $P_r = 0.44$ similar to that in Figure 5.18, a time-averaged image and an image of the superposed conjugate proper orthogonal modes (POMs). The averaged image consisted of 1000 frames sampled at 25 kHz. The corresponding plots are the cross-power spectral density (CPSD) magnitude of the time-dependent amplitude cofficients of the conjugate modes. The peak characteristic frequencies of the periodic flow structures were identical to f_F. For the purpose of comparison, the baseline spectra are shown in dots. Under both the PAN and PN forcing conditions, the forced spectra were completely different from that of the baseline. (.........Baseline, ———Forced)

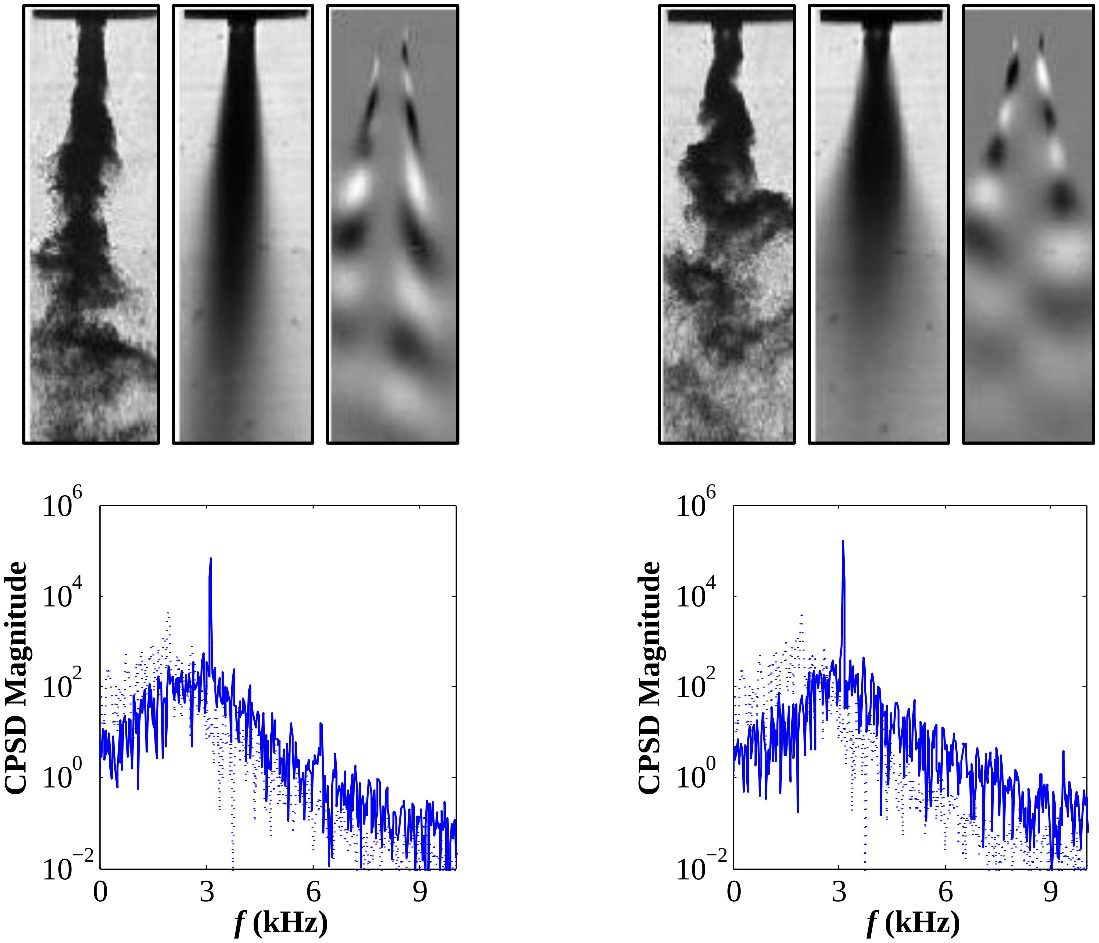

(a) $J = 2.1$, PAN

(b) $J = 2.1$, PN

Figure 5.30: A back-lit image of the LAR-thin injector forced ($f_F = 3.12$ kHz) flows at $P_r = 0.44$ similar to that in Figure 5.18, a time-averaged image and an image of the superposed conjugate proper orthogonal modes (POMs). The averaged image consisted of 1000 frames sampled at 25 kHz. The corresponding plots are the cross-power spectral density (CPSD) magnitude of the time-dependent amplitude cofficients of the conjugate modes. The peak characteristic frequencies of the periodic flow structures were identical to f_F. For the purpose of comparison, the baseline spectra are shown in dots. Under both the PAN and PN forcing conditions, the forced spectra were still different from that of the baseline. (.........Baseline, ———Forced)

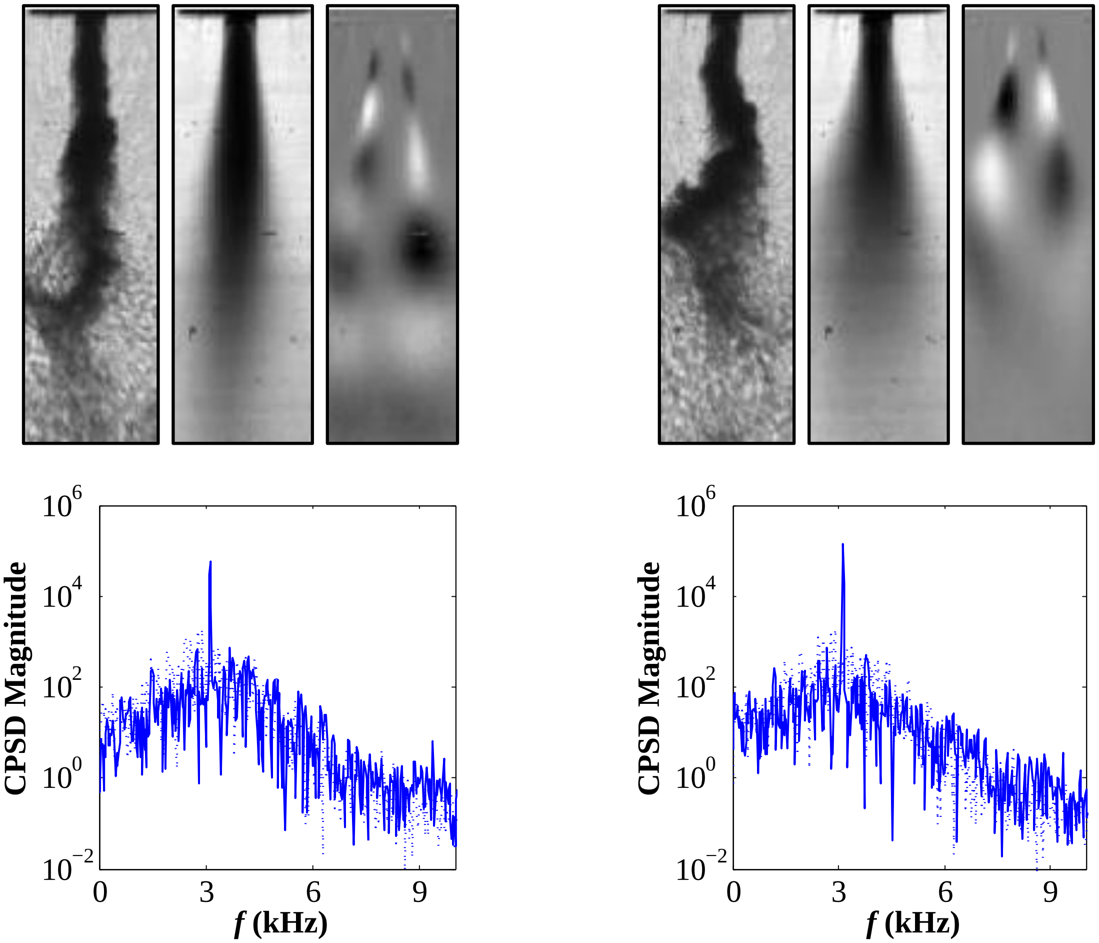

(a) $J = 5.2$, PAN

(b) $J = 5.2$, PN

Figure 5.31: A back-lit image of the LAR-thin injector forced ($f_F = 3.12$ kHz) flows at $P_r = 0.44$ similar to that in Figure 5.18, a time-averaged image and an image of the superposed conjugate proper orthogonal modes (POMs). The averaged image consisted of 1000 frames sampled at 25 kHz. The corresponding plots are the cross-power spectral density (CPSD) magnitude of the time-dependent amplitude cofficients of the conjugate modes. The peak characteristic frequencies of the periodic flow structures were identical to f_F. For the purpose of comparison, the baseline spectra are shown in dots. (.........Baseline, ———Forced)

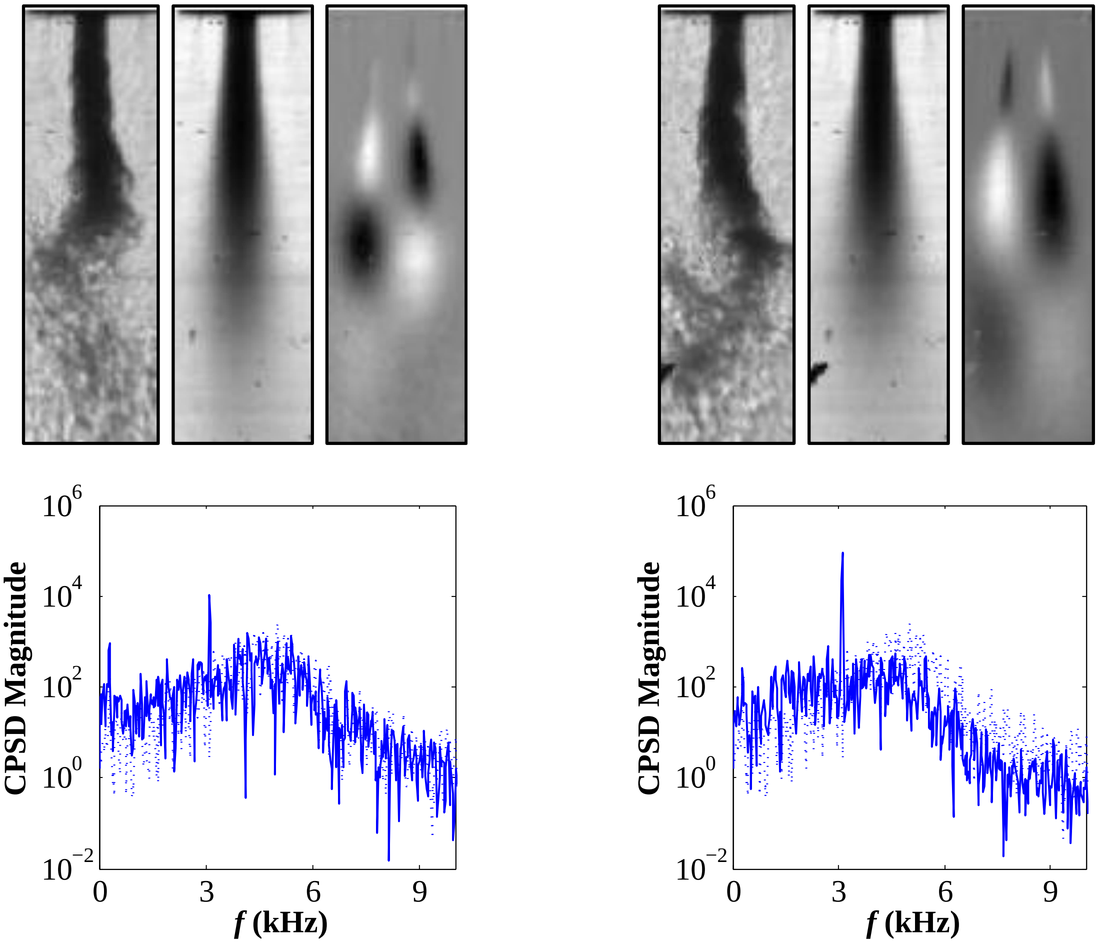

(a) $J = 11$, PAN

(b) $J = 11$, PN

Figure 5.32: A back-lit image of the LAR-thin injector forced ($f_F = 3.10$ kHz) flows at $P_r = 0.44$ similar to that in Figure 5.18, a time-averaged image and an image of the superposed conjugate proper orthogonal modes (POMs). The averaged image consisted of 1000 frames sampled at 25 kHz. The corresponding plots are the cross-power spectral density (CPSD) magnitude of the time-dependent amplitude cofficients of the conjugate modes. The peak characteristic frequencies of the periodic flow structures were identical to f_F. For the purpose of comparison, the baseline spectra are shown in dots. Under the PAN forcing condition, the forced spectrum retained the baseline spectrum. (.........Baseline, ———Forced)

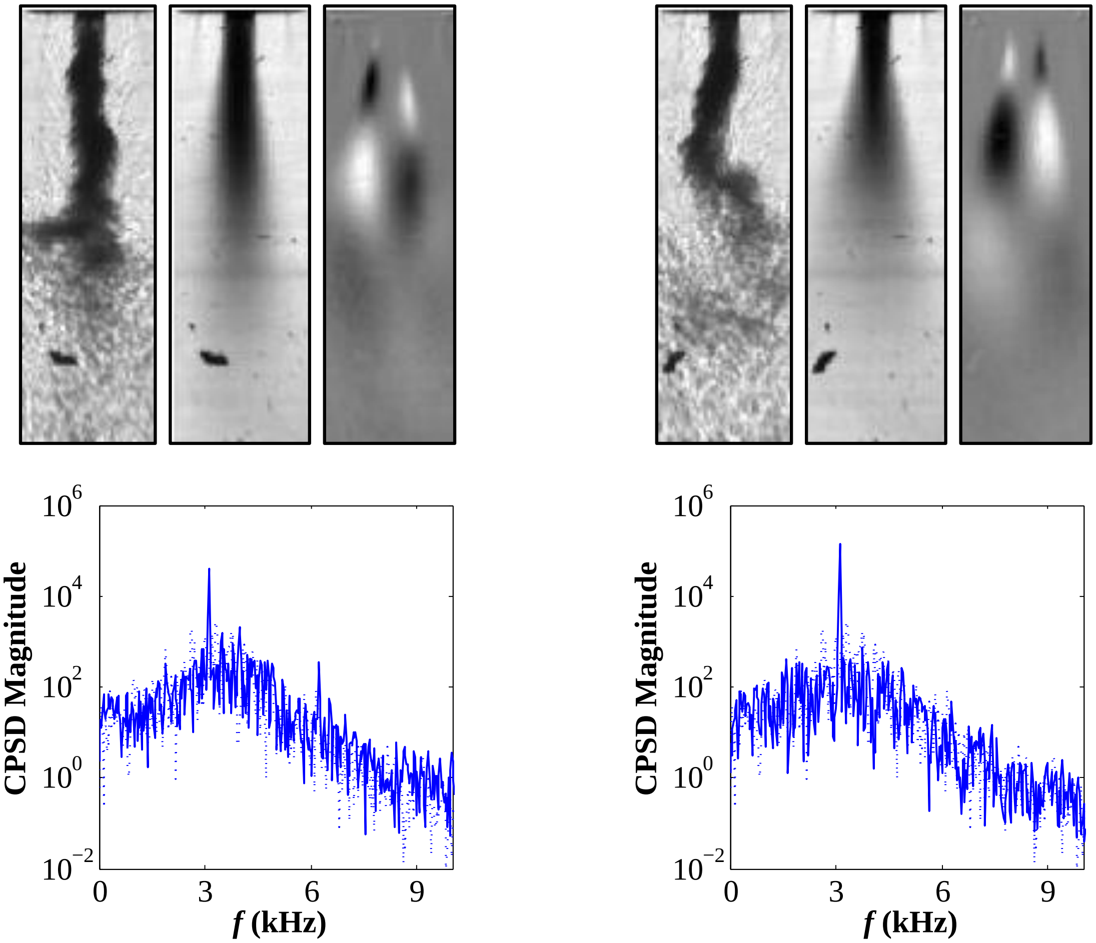

(a) $J = 14$, PAN

(b) $J = 14$, PN

Figure 5.33: A back-lit image of the LAR-thin injector forced ($f_F = 3.11$ kHz) flows at $P_r = 0.44$ similar to that in Figure 5.18, a time-averaged image and an image of the superposed conjugate proper orthogonal modes (POMs). The averaged image consisted of 1000 frames sampled at 25 kHz. The corresponding plots are the cross-power spectral density (CPSD) magnitude of the time-dependent amplitude cofficients of the conjugate modes. The peak characteristic frequencies of the periodic flow structures were identical to f_F. For the purpose of comparison, the baseline spectra are shown in dots. Under the PAN forcing condition, the forced spectrum retained the baseline spectrum. (.........Baseline, ———Forced)

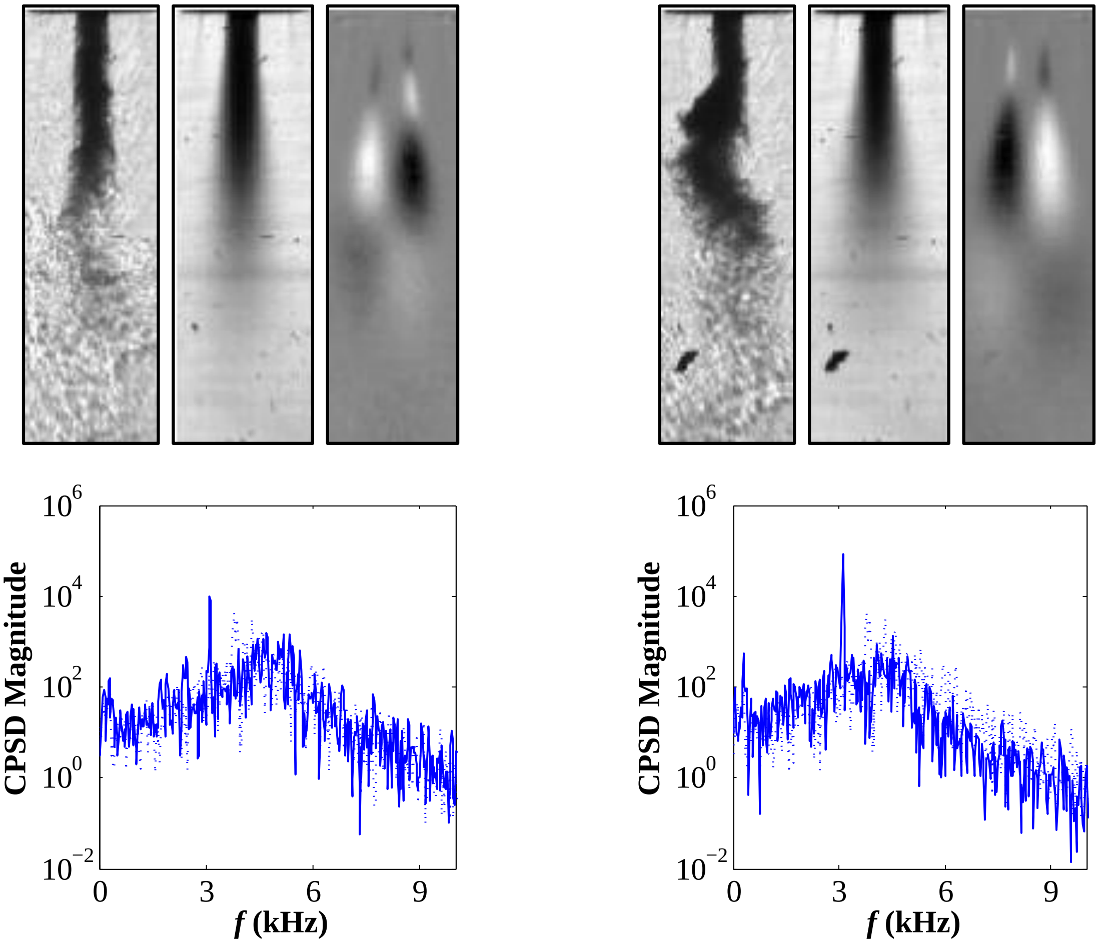

(a) $J = 20$, PAN

(b) $J = 20$, PN

Figure 5.34: A back-lit image of the LAR-thin injector forced ($f_F = 3.11$ kHz) flows at $P_r = 0.44$ similar to that in Figure 5.18, a time-averaged image and an image of the superposed conjugate proper orthogonal modes (POMs). The averaged image consisted of 1000 frames sampled at 25 kHz. The corresponding plots are the cross-power spectral density (CPSD) magnitude of the time-dependent amplitude cofficients of the conjugate modes. The peak characteristic frequencies of the periodic flow structures were identical to f_F. For the purpose of comparison, the baseline spectra are shown in dots. Under the PAN forcing condition, the forced spectrum retained the baseline spectrum. (.........Baseline, ———Forced)

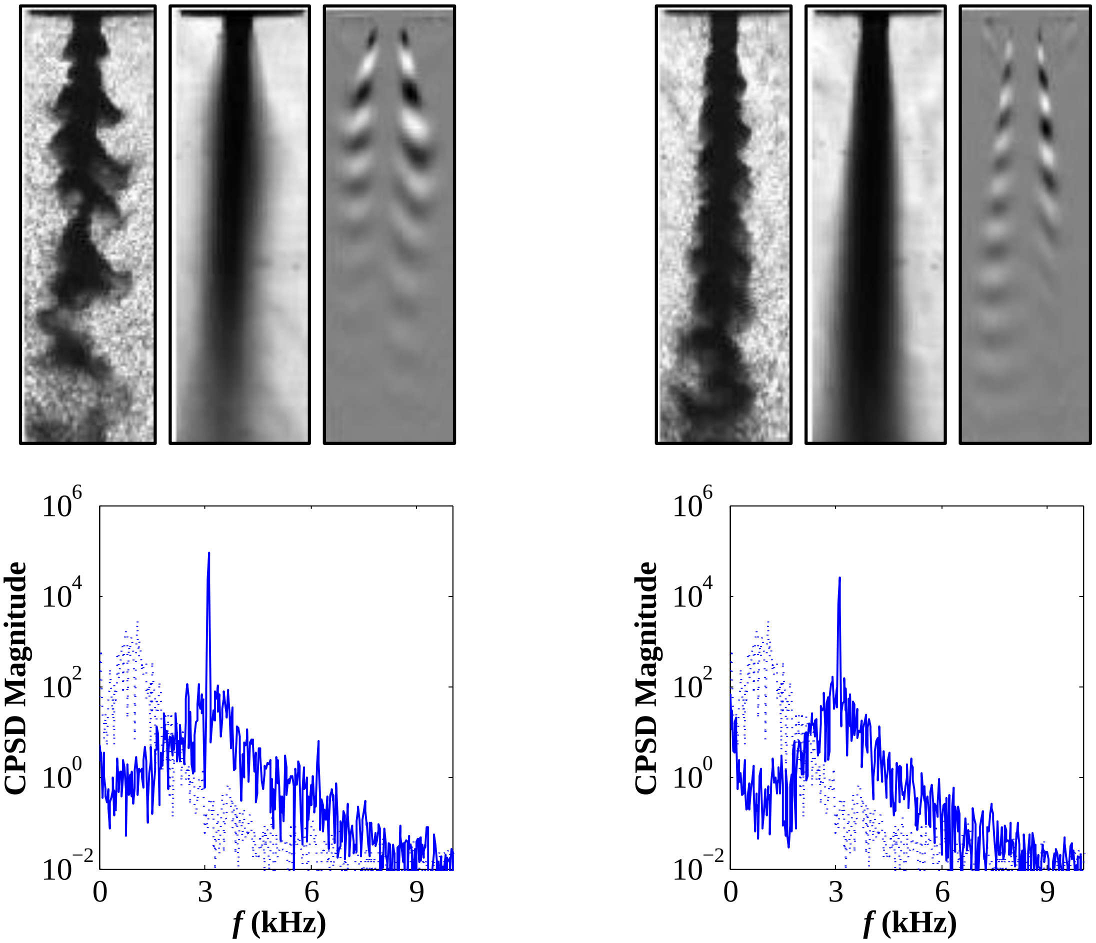

(a) $J = 0.5$, PAN

(b) $J = 0.5$, PN

Figure 5.35: A back-lit image of the LAR-thin injector forced ($f_F = 3.10$ kHz) flows at $P_r = 1.05$ similar to that in Figure 5.19, a time-averaged image and an image of the superposed conjugate proper orthogonal modes (POMs). The averaged image consisted of 1000 frames sampled at 25 kHz. The corresponding plots are the cross-power spectral density (CPSD) magnitude of the time-dependent amplitude cofficients of the conjugate modes. The peak characteristic frequencies of the periodic flow structures were identical to f_F. For the purpose of comparison, the baseline spectra are shown in dots. Under both the PAN and PN forcing conditions, the forced spectra were completely different from that of the baseline. (.........Baseline, ———Forced)

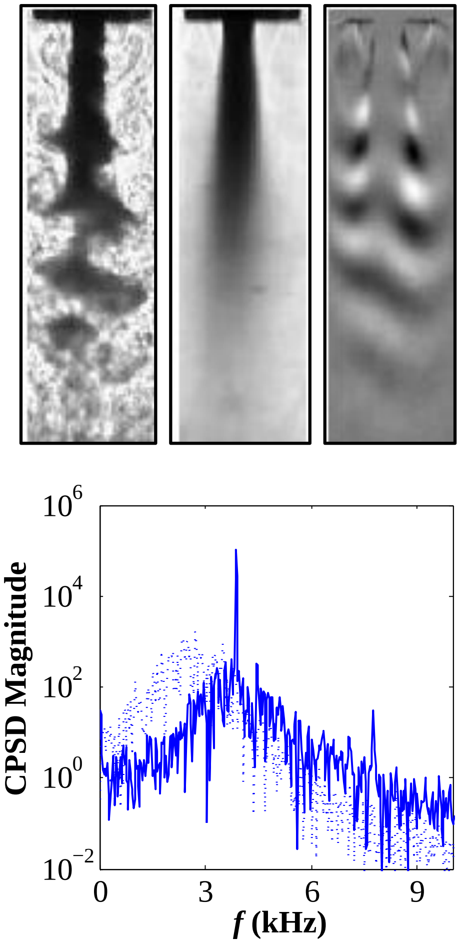

$J = 1.9$, PAN

Figure 5.36: A back-lit image of the LAR-thin injector forced ($f_F = 3.10$ kHz) flows at $P_r = 1.05$ similar to that in Figure 5.19, a time-averaged image and an image of the superposed conjugate proper orthogonal modes (POMs). The averaged image consisted of 1000 frames sampled at 25 kHz. The corresponding plots are the cross-power spectral density (CPSD) magnitude of the time-dependent amplitude cofficients of the conjugate modes. The peak characteristic frequencies of the periodic flow structures were identical to f_F. For the purpose of comparison, the baseline spectra are shown in dots. Under the PAN forcing condition, the forced spectrum was completely different from that of the baseline. (.........Baseline, ———Forced)

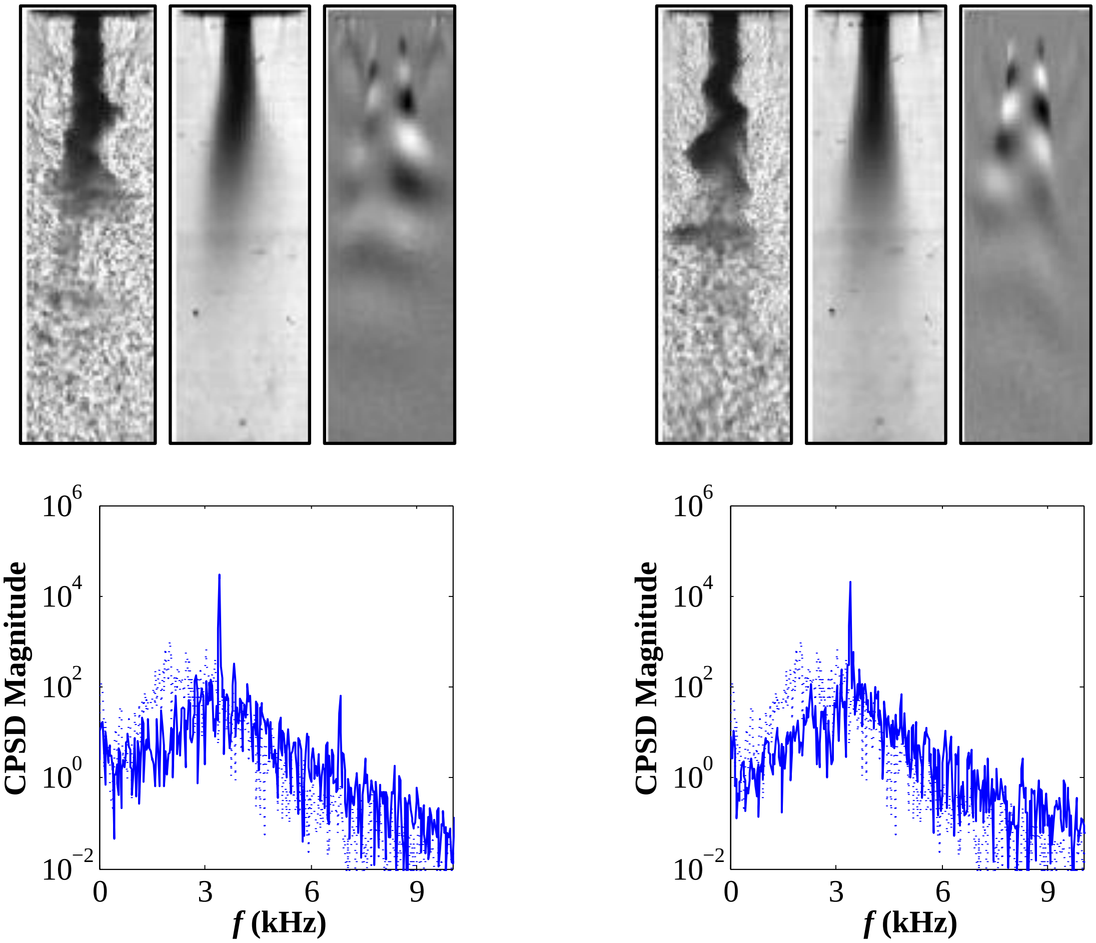

(a) $J = 5.0$, PAN

(b) $J = 5.0$, PN

Figure 5.37: A back-lit image of the LAR-thin injector forced ($f_F = 3.41$ kHz) flows at $P_r = 1.05$ similar to that in Figure 5.19, a time-averaged image and an image of the superposed conjugate proper orthogonal modes (POMs). The averaged image consisted of 1000 frames sampled at 25 kHz. The corresponding plots are the cross-power spectral density (CPSD) magnitude of the time-dependent amplitude cofficients of the conjugate modes. The peak characteristic frequencies of the periodic flow structures were identical to f_F. For the purpose of comparison, the baseline spectra are shown in dots. Under both the PAN and PN forcing conditions, the forced spectra were completely different from that of the baseline. (.........Baseline, ———Forced)

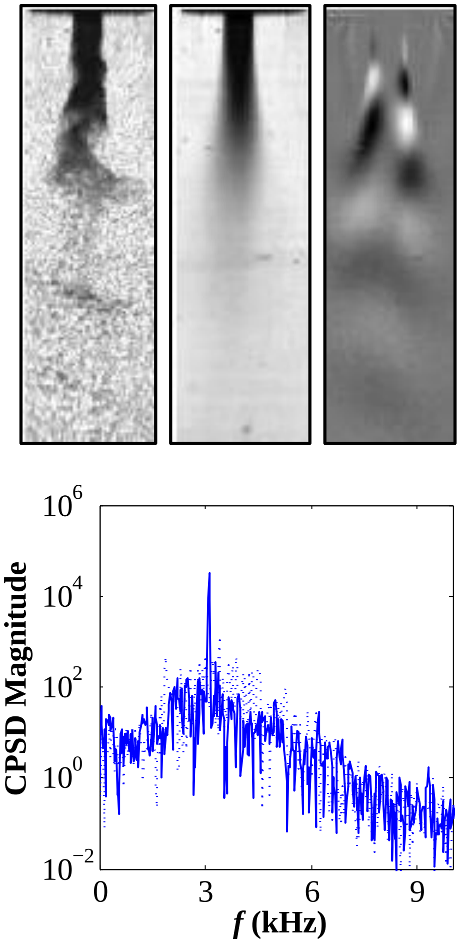

$J = 8.5$, PAN

Figure 5.38: A back-lit image of the LAR-thin injector forced ($f_F = 3.10$ kHz) flows at $P_r = 1.05$ similar to that in Figure 5.19, a time-averaged image and an image of the superposed conjugate proper orthogonal modes (POMs). The averaged image consisted of 1000 frames sampled at 25 kHz. The corresponding plots are the cross-power spectral density (CPSD) magnitude of the time-dependent amplitude cofficients of the conjugate modes. The peak characteristic frequencies of the periodic flow structures were identical to f_F. For the purpose of comparison, the baseline spectra are shown in dots. Under the PAN forcing condition, the forced spectrum retained the baseline spectrum. (.........Baseline, ———Forced)

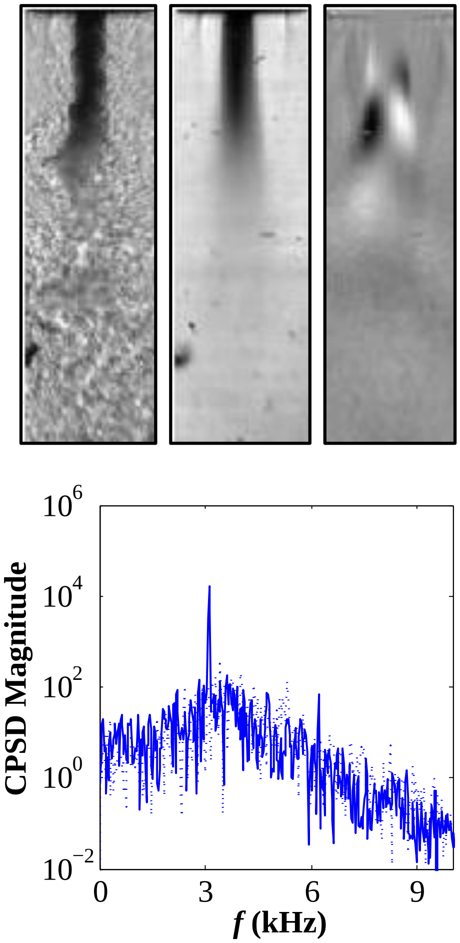

$J = 12$, PAN

Figure 5.39: A back-lit image of the LAR-thin injector forced ($f_F = 3.10$ kHz) flows at $P_r = 1.05$ similar to that in Figure 5.19, a time-averaged image and an image of the superposed conjugate proper orthogonal modes (POMs). The averaged image consisted of 1000 frames sampled at 25 kHz. The corresponding plots are the cross-power spectral density (CPSD) magnitude of the time-dependent amplitude cofficients of the conjugate modes. The peak characteristic frequencies of the periodic flow structures were identical to f_F. For the purpose of comparison, the baseline spectra are shown in dots. Under the PAN forcing condition, the forced spectrum retained the baseline spectrum. (.........Baseline, ———Forced)

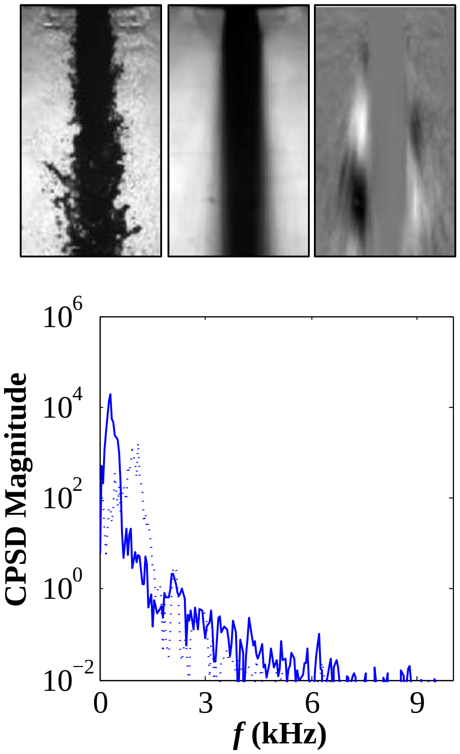

$J = 0.1$, PAN

Figure 5.40: A back-lit image of the SAR-thick injector forced ($f_F = 3.10$ kHz) flows at $P_r = 0.44$ shown in Figure 5.24, a time-averaged image and an image of the superposed conjugate proper orthogonal modes (POMs). The averaged image consisted of 500 frames sampled at 25 kHz. The corresponding plots are the cross-power spectral density (CPSD) magnitude of the time-dependent amplitude cofficients of the conjugate modes. The low frequency peak associated with the periodic flow structures was not identical to f_F. For the purpose of comparison, the baseline spectra are shown with dots. (.........Baseline, ———Forced)

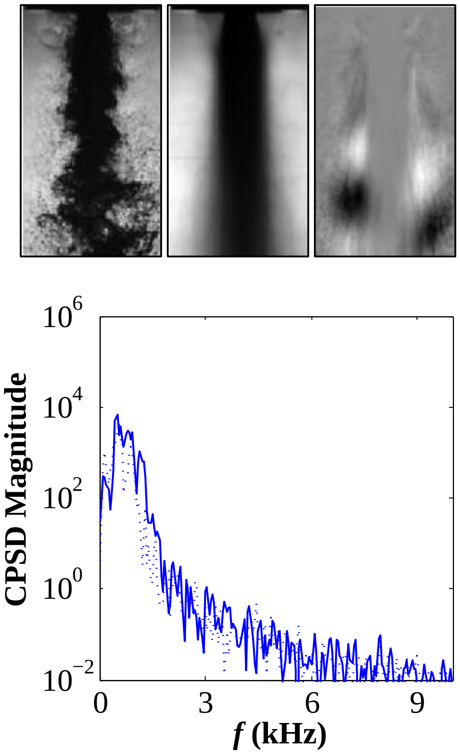

J = 0.5, PAN

Figure 5.41: A back-lit image of the SAR-thick injector forced (f_F = 3.04 kHz) flows at P_r = 0.44 shown in Figure 5.24, a time-averaged image and an image of the superposed conjugate proper orthogonal modes (POMs). The averaged image consisted of 500 frames sampled at 25 kHz. The corresponding plots are the cross-power spectral density (CPSD) magnitude of the time-dependent amplitude cofficients of the conjugate modes. The low frequency peak associated with the periodic flow structures was not identical to f_F. For the purpose of comparison, the baseline spectra are shown with dots. (.........Baseline, ———Forced)

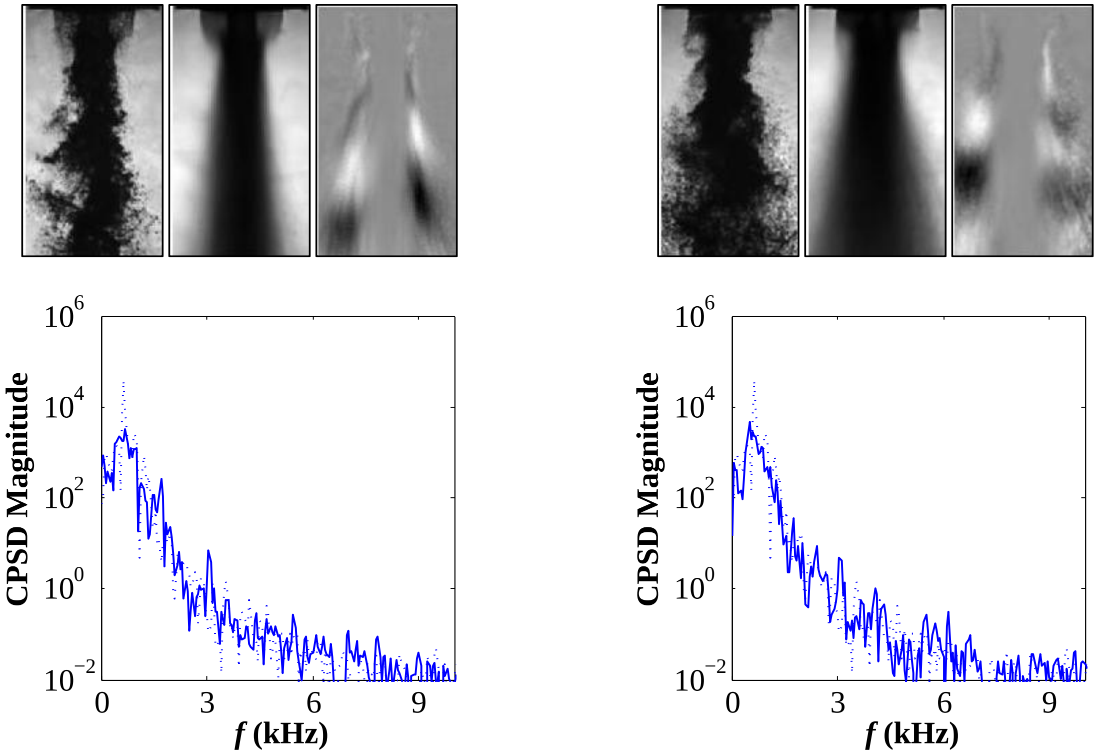

(a) $J = 2.1$, PAN

(b) $J = 2.1$, PN

Figure 5.42: A back-lit image of the SAR-thick injector forced ($f_F = 3.07$ kHz) flows at $P_r = 0.44$ shown in Figure 5.24, a time-averaged image and an image of the superposed conjugate proper orthogonal modes (POMs). The averaged image consisted of 500 frames sampled at 25 kHz. The corresponding plots are the cross-power spectral density (CPSD) magnitude of the time-dependent amplitude cofficients of the conjugate modes. The low frequency peaks associated with the periodic flow structures was not identical to f_F. For the purpose of comparison, the baseline spectra are shown with dots. (.........Baseline, ———Forced)

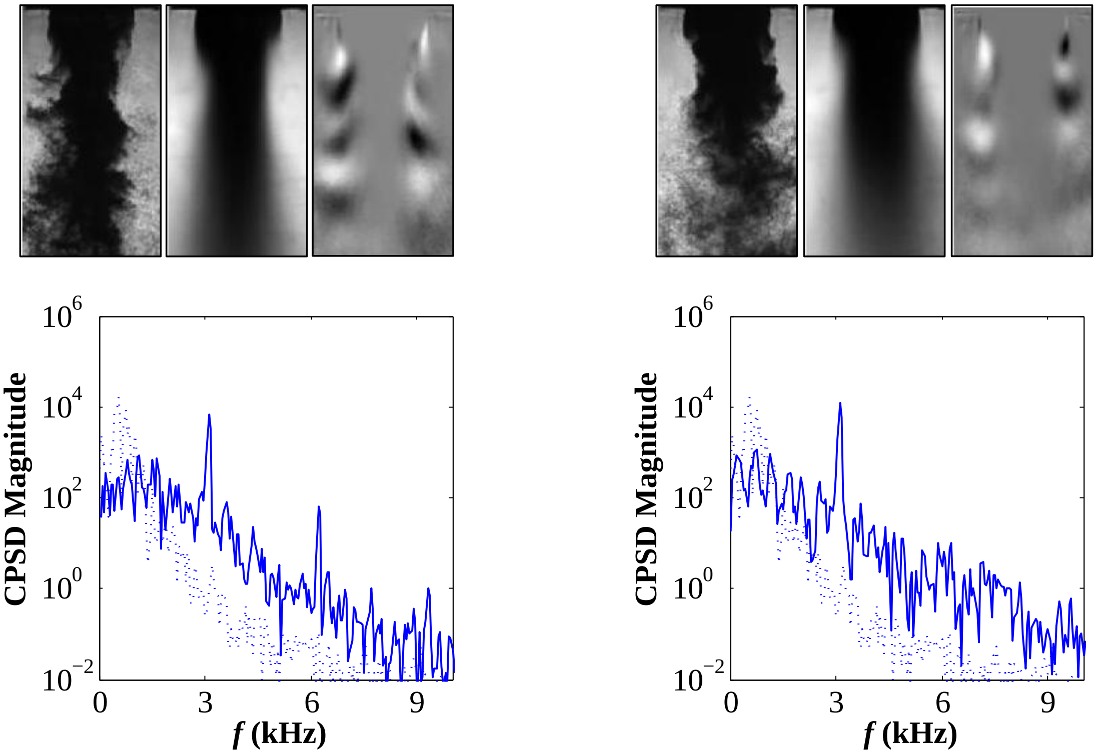

(a) $J = 5.7$, PAN

(b) $J = 5.7$, PN

Figure 5.43: A back-lit image of the SAR-thick injector forced ($f_F = 3.11$ kHz) flows at $P_r = 0.44$ shown in Figure 5.24, a time-averaged image and an image of the superposed conjugate proper orthogonal modes (POMs). The averaged image consisted of 500 frames sampled at 25 kHz. The corresponding plots are the cross-power spectral density (CPSD) magnitude of the time-dependent amplitude cofficients of the conjugate modes. The peak frequencies of the periodic flow structures were identical to f_F. For the purpose of comparison, the baseline spectra are shown with dots. (.........Baseline, ———Forced)

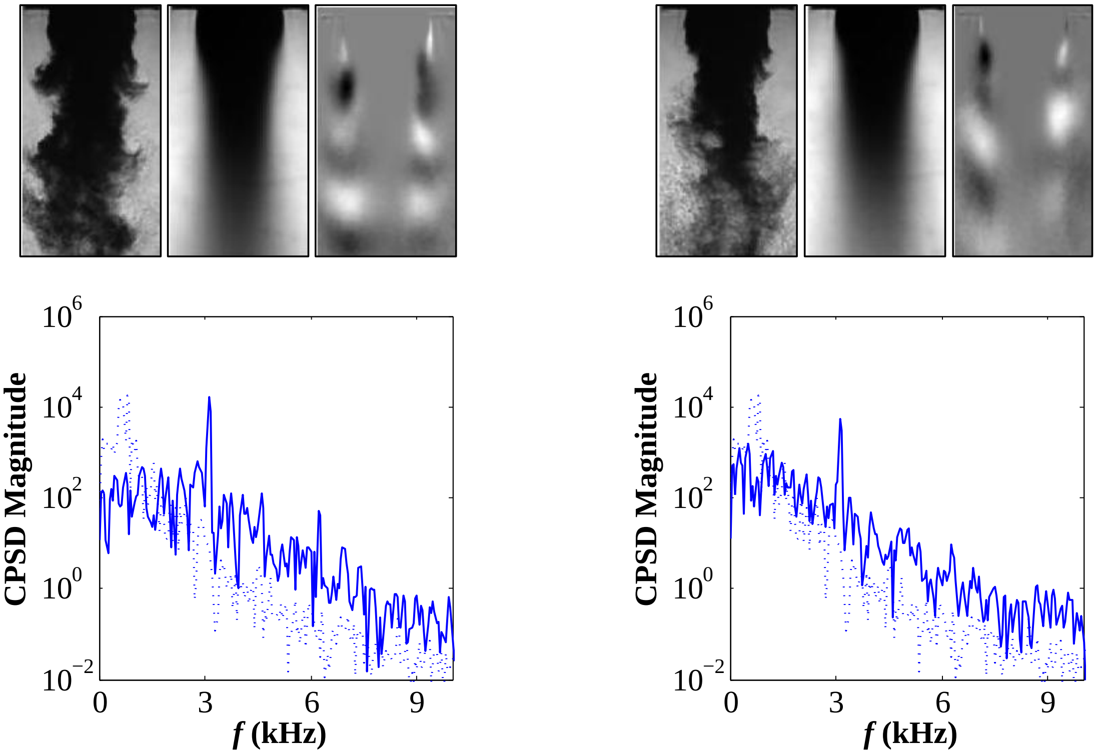

(a) $J = 10$, PAN

(b) $J = 10$, PN

Figure 5.44: A back-lit image of the SAR-thick injector forced ($f_F = 3.11$ kHz) flows at $P_r = 0.44$ shown in Figure 5.24, a time-averaged image and an image of the superposed conjugate proper orthogonal modes (POMs). The averaged image consisted of 500 frames sampled at 25 kHz. The corresponding plots are the cross-power spectral density (CPSD) magnitude of the time-dependent amplitude cofficients of the conjugate modes. The peak frequencies of the periodic flow structures were identical to f_F. For the purpose of comparison, the baseline spectra are shown with dots. (.........Baseline, ———Forced)

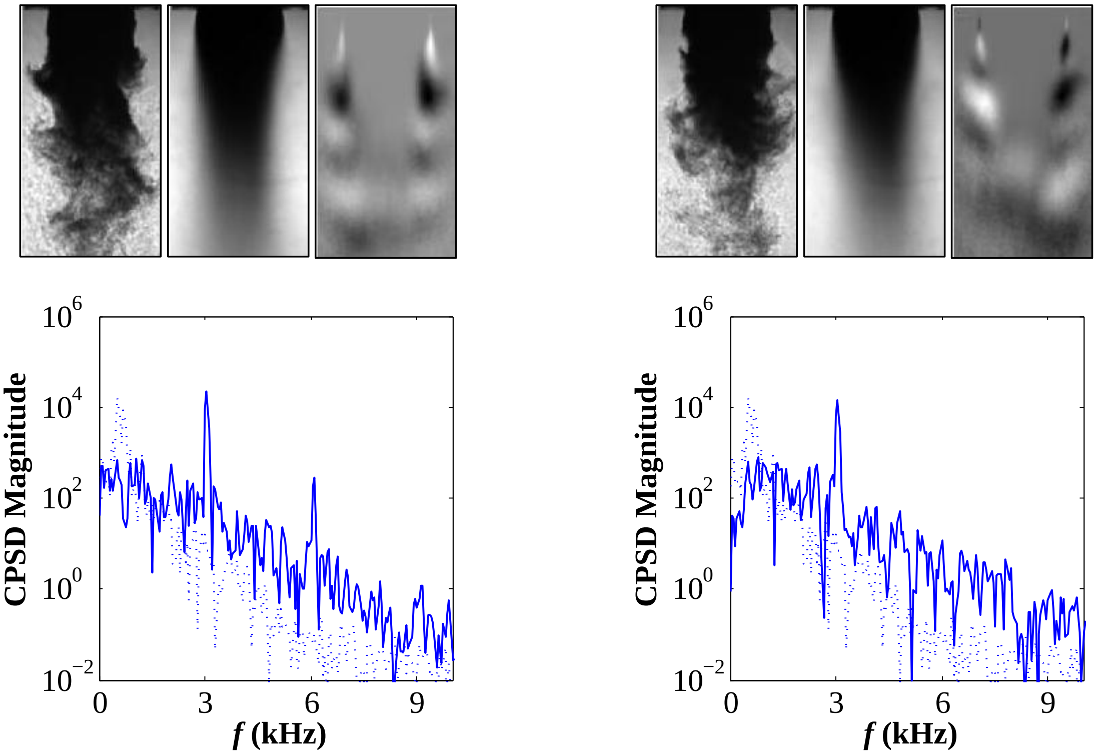

(a) $J = 15$, PAN

(b) $J = 15$, PN

Figure 5.45: A back-lit image of the SAR-thick injector forced ($f_F = 3.04$ kHz) flows at $P_r = 0.44$ shown in Figure 5.24, a time-averaged image and an image of the superposed conjugate proper orthogonal modes (POMs). The averaged image consisted of 500 frames sampled at 25 kHz. The corresponding plots are the cross-power spectral density (CPSD) magnitude of the time-dependent amplitude cofficients of the conjugate modes. The peak frequencies of the periodic flow structures were identical to f_F. For the purpose of comparison, the baseline spectra are shown with dots. (.........Baseline, ———Forced)

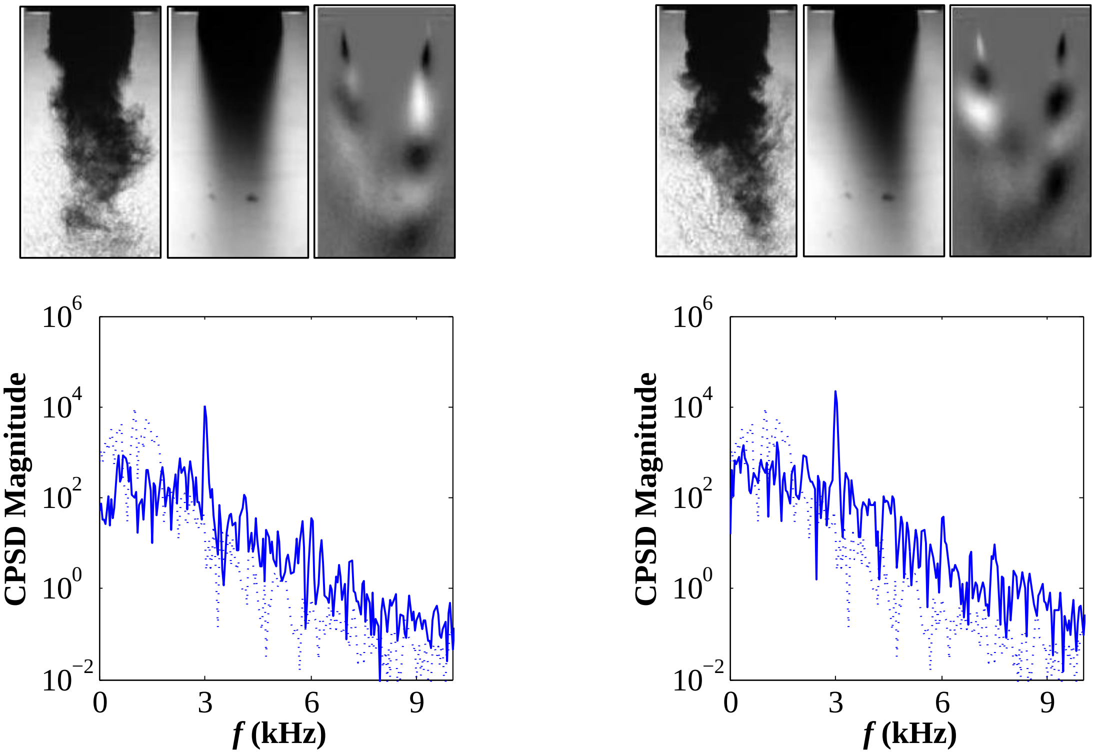

(a) $J = 21$, PAN (b) $J = 21$, PN

Figure 5.46: A back-lit image of the SAR-thick injector forced ($f_F = 3.11$ kHz) flows at $P_r = 0.44$ shown in Figure 5.24, a time-averaged image and an image of the superposed conjugate proper orthogonal modes (POMs). The averaged image consisted of 500 frames sampled at 25 kHz. The corresponding plots are the cross-power spectral density (CPSD) magnitude of the time-dependent amplitude cofficients of the conjugate modes. The peak frequencies of the periodic flow structures were identical to f_F. For the purpose of comparison, the baseline spectra are shown with dots. (.........Baseline, ———Forced)

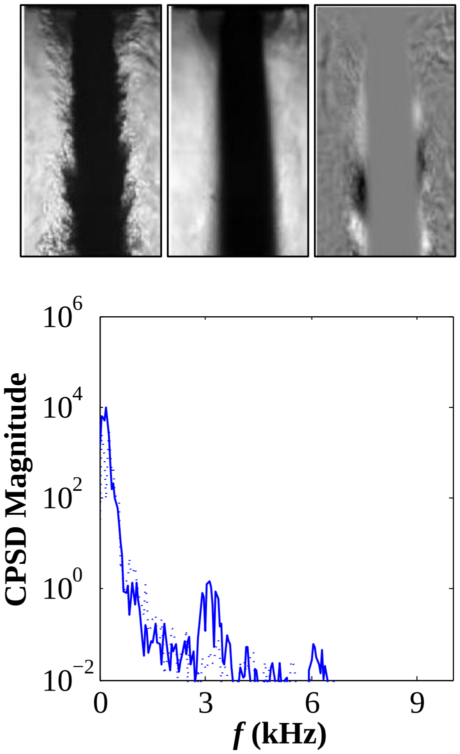

$J = 0.1$, PAN

Figure 5.47: A back-lit image of the SAR-thick injector forced ($f_F = 3.12$ kHz) flows at $P_r = 1.05$ shown in Figure 5.25, a time-averaged image and an image of the superposed conjugate proper orthogonal modes (POMs). The averaged image consisted of 500 frames sampled at 25 kHz. The corresponding plots are the cross-power spectral density (CPSD) magnitude of the time-dependent amplitude cofficients of the conjugate modes. The low frequency peak associated with the periodic flow structures was not identical to f_F. For the purpose of comparison, the baseline spectra are shown with dots. (.........Baseline, ———Forced)

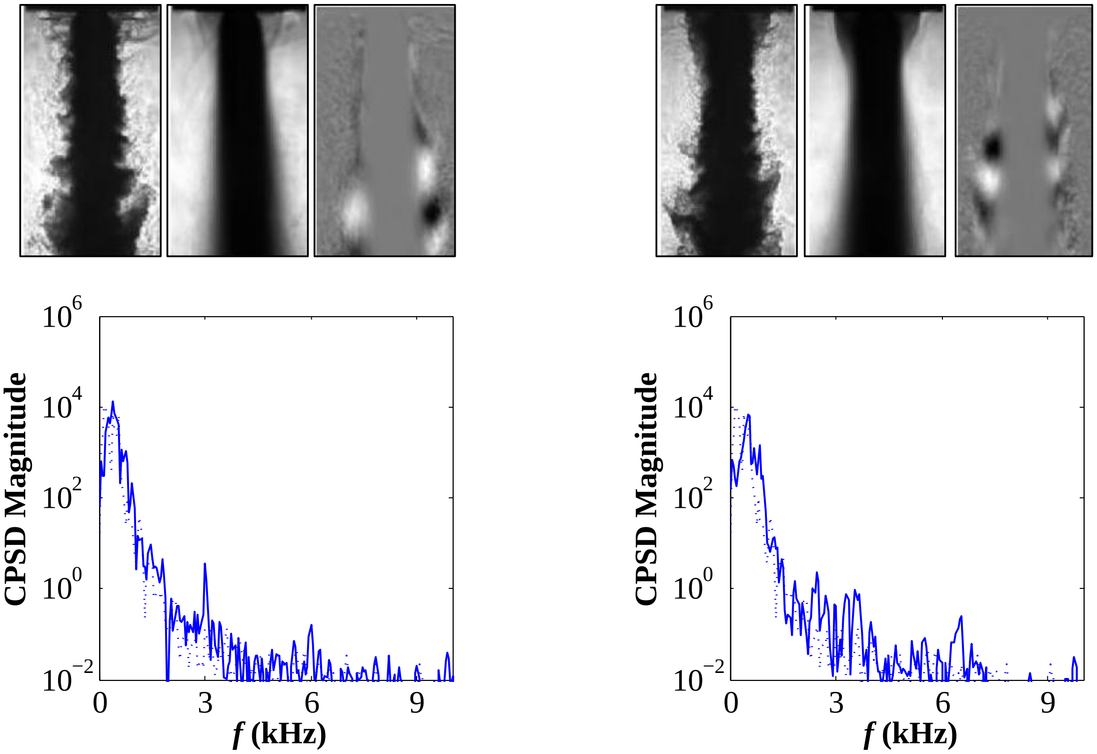

(a) $J = 0.5$, PAN

(b) $J = 0.5$, PN

Figure 5.48: A back-lit image of the SAR-thick injector forced ($f_F = 3.00$ kHz) flows at $P_r = 1.05$ shown in Figure 5.25, a time-averaged image and an image of the superposed conjugate proper orthogonal modes (POMs). The averaged image consisted of 500 frames sampled at 25 kHz. The corresponding plots are the cross-power spectral density (CPSD) magnitude of the time-dependent amplitude cofficients of the conjugate modes. The low frequency peaks associated with the periodic flow structures were not identical to f_F. For the purpose of comparison, the baseline spectra are shown with dots. (.........Baseline, ———Forced)

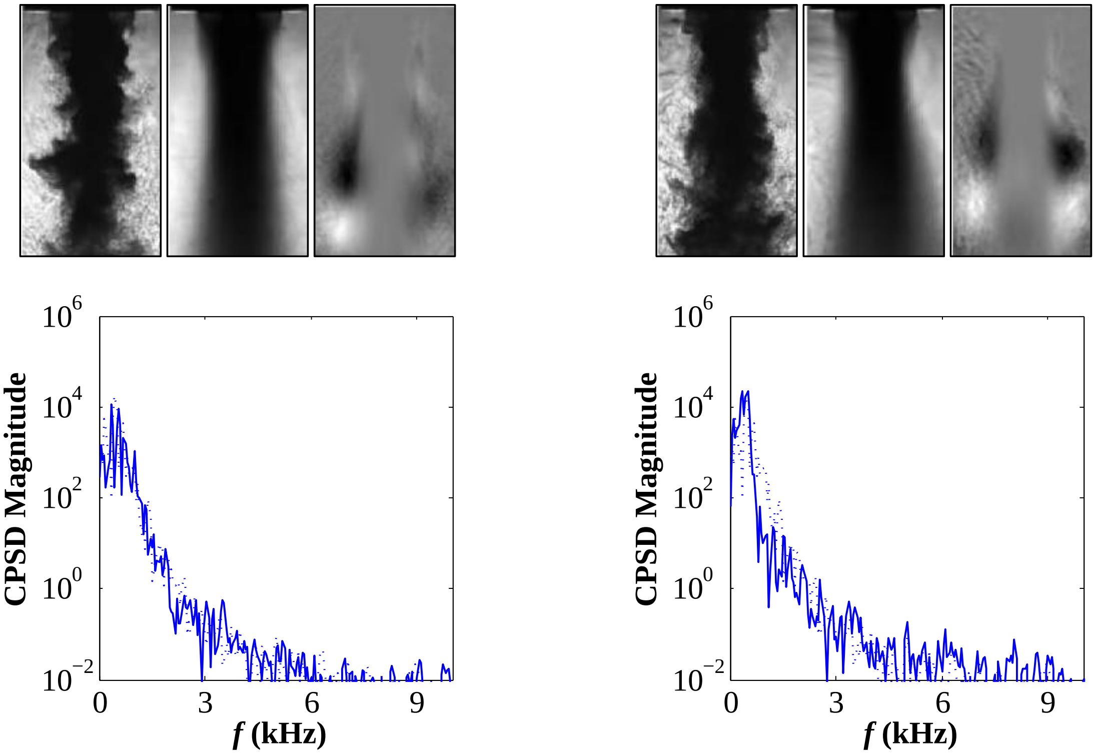

(a) $J = 2.1$, PAN

(b) $J = 2.1$, PN

Figure 5.49: A back-lit image of the SAR-thick injector forced ($f_F = 3.04$ kHz) flows at $P_r = 1.05$ shown in Figure 5.25, a time-averaged image and an image of the superposed conjugate proper orthogonal modes (POMs). The averaged image consisted of 500 frames sampled at 25 kHz. The corresponding plots are the cross-power spectral density (CPSD) magnitude of the time-dependent amplitude cofficients of the conjugate modes. The low frequency peaks associated with the periodic flow structures were not identical to f_F. For the purpose of comparison, the baseline spectra are shown with dots. (.........Baseline, ———Forced)

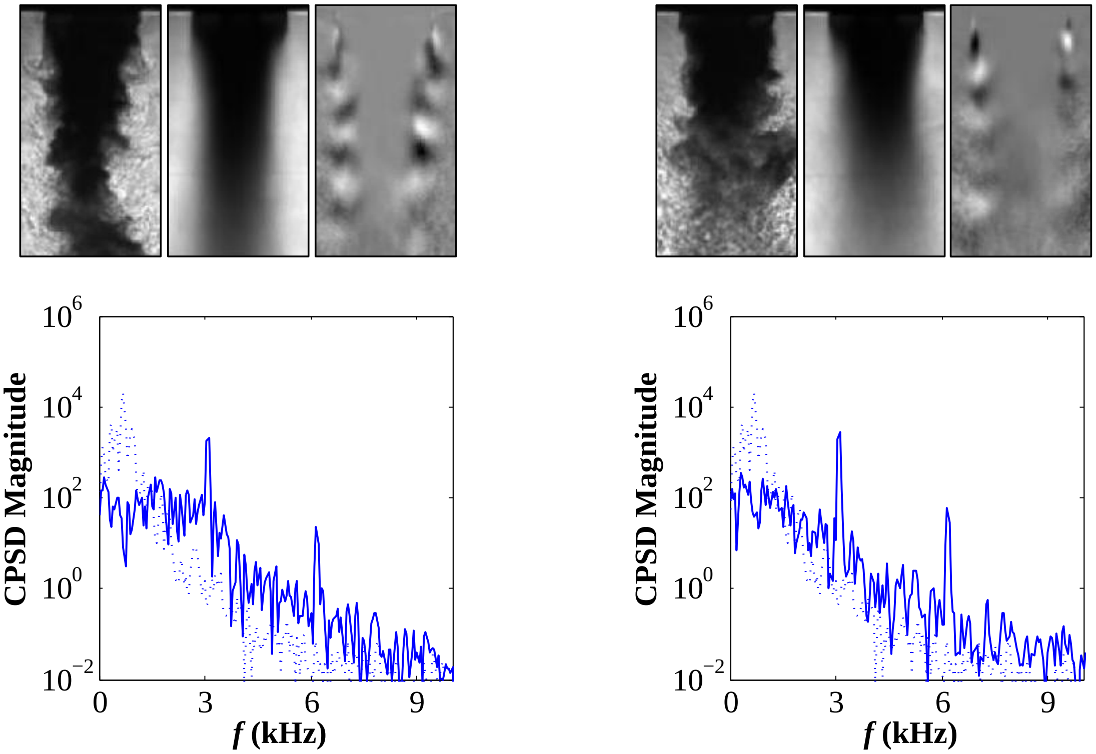

(a) $J = 5.2$, PAN

(b) $J = 5.2$, PN

Figure 5.50: A back-lit image of the SAR-thick injector forced ($f_F = 3.08$ kHz) flows at $P_r = 1.05$ shown in Figure 5.25, a time-averaged image and an image of the superposed conjugate proper orthogonal modes (POMs). The averaged image consisted of 500 frames sampled at 25 kHz. The corresponding plots are the cross-power spectral density (CPSD) magnitude of the time-dependent amplitude cofficients of the conjugate modes. The peak frequencies of the periodic flow structures were identical to f_F. For the purpose of comparison, the baseline spectra are shown with dots. (.........Baseline, ———Forced)

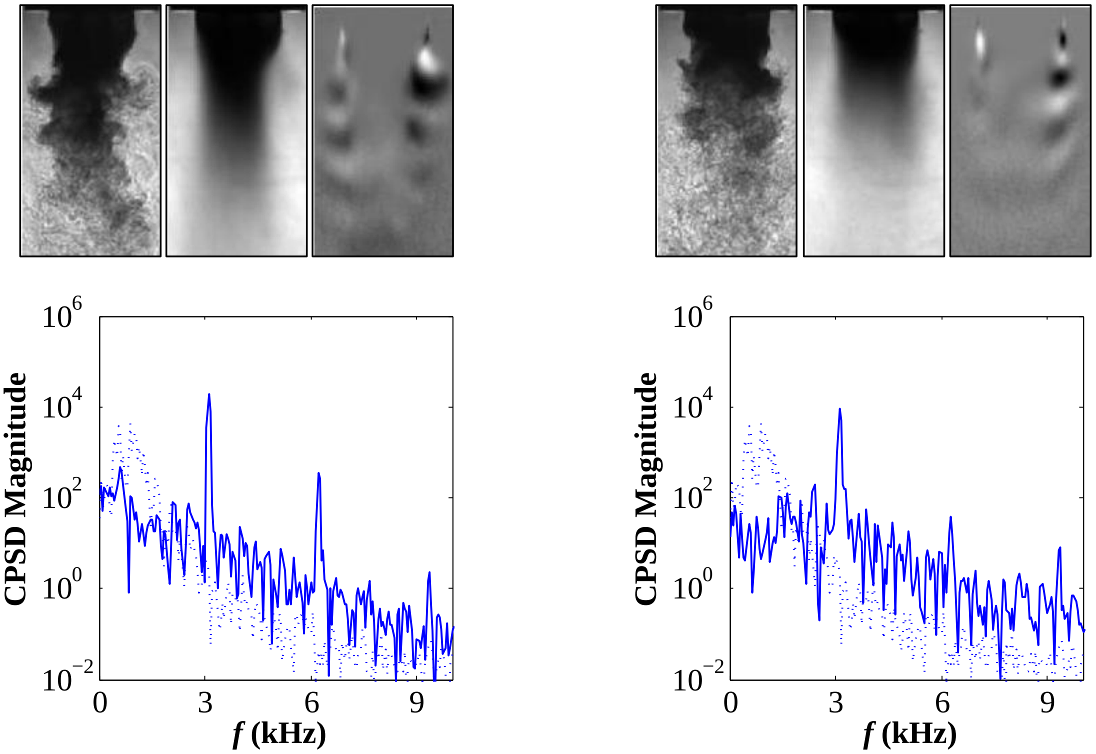

(a) $J = 9.2$, PAN

(b) $J = 9.2$, PN

Figure 5.51: A back-lit image of the SAR-thick injector forced ($f_F = 3.11$ kHz) flows at $P_r = 1.05$ shown in Figure 5.25, a time-averaged image and an image of the superposed conjugate proper orthogonal modes (POMs). The averaged image consisted of 500 frames sampled at 25 kHz. The corresponding plots are the cross-power spectral density (CPSD) magnitude of the time-dependent amplitude cofficients of the conjugate modes. The peak frequencies of the periodic flow structures were identical to f_F. For the purpose of comparison, the baseline spectra are shown with dots. (.........Baseline, ———Forced)

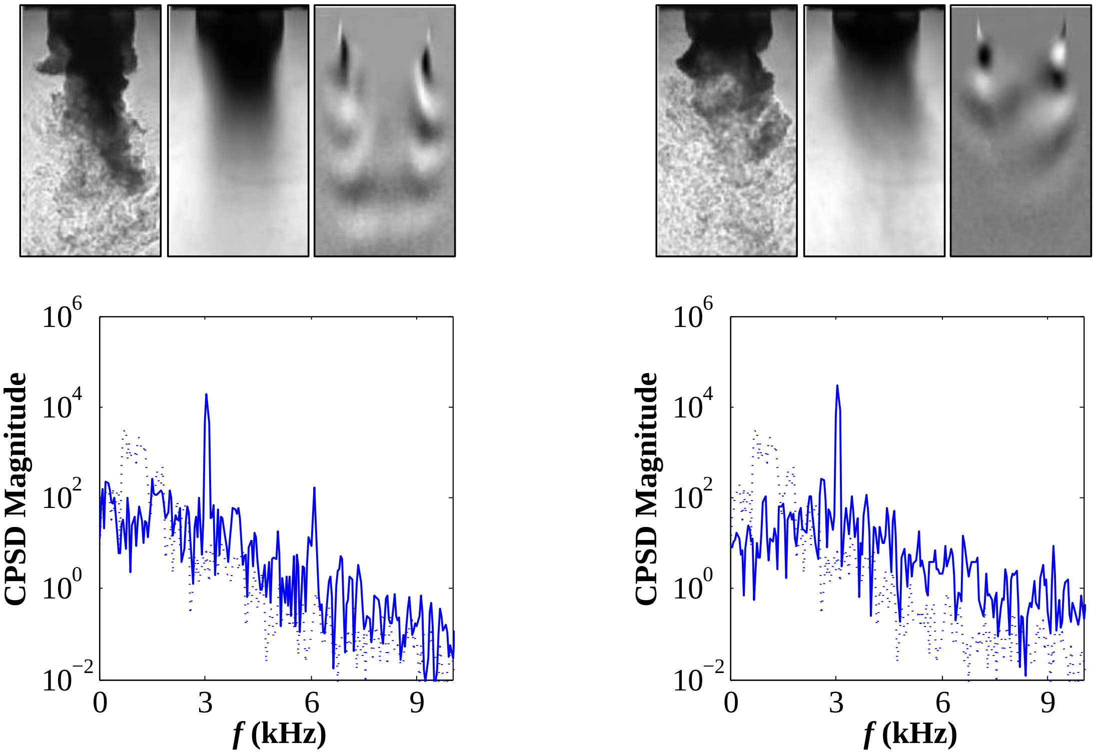

(a) J = 14, PAN

(b) J = 14, PN

Figure 5.52: A back-lit image of the SAR-thick injector forced (f_F = 3.05 kHz) flows at P_r = 1.05 shown in Figure 5.25, a time-averaged image and an image of the superposed conjugate proper orthogonal modes (POMs). The averaged image consisted of 500 frames sampled at 25 kHz. The corresponding plots are the cross-power spectral density (CPSD) magnitude of the time-dependent amplitude cofficients of the conjugate modes. The peak frequencies of the periodic flow structures were identical to f_F. For the purpose of comparison, the baseline spectra are shown with dots. (.........Baseline, ———Forced)

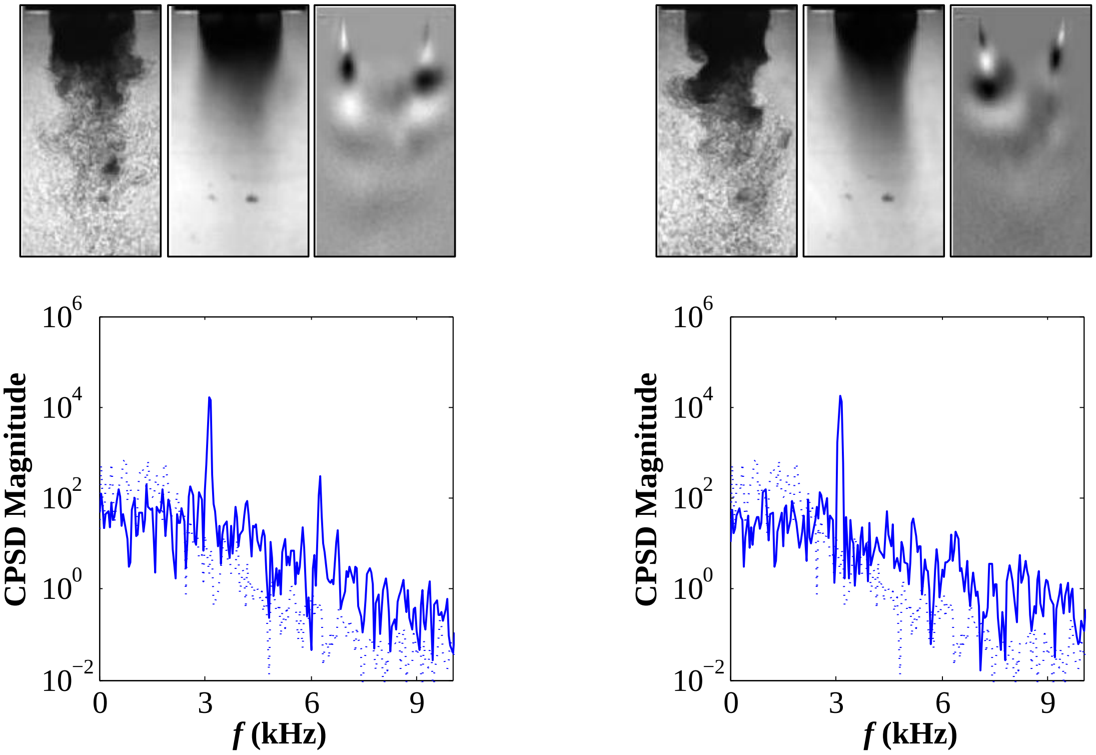

(a) $J = 21$, PAN

(b) $J = 21$, PN

Figure 5.53: A back-lit image of the SAR-thick injector forced ($f_F = 3.12$ kHz) flows at $P_r = 1.05$ shown in Figure 5.25, a time-averaged image and an image of the superposed conjugate proper orthogonal modes (POMs). The averaged image consisted of 500 frames sampled at 25 kHz. The corresponding plots are the cross-power spectral density (CPSD) magnitude of the time-dependent amplitude cofficients of the conjugate modes. The peak frequencies of the periodic flow structures were identical to f_F. For the purpose of comparison, the baseline spectra are shown with dots. (.........Baseline, ———Forced)

CHAPTER 6

Summary, Conclusions and Recommendations for Future Work

6.1 Droplet Combustion

The single fuel droplet experiments allowed for the exploration of alternative fuel combustion characteristics in the presence of acoustic perturbations. These included changes that can occur in the mean burning rates associated with a single burning fuel droplet, and flame extinction limits for a range of acoustic excitation conditions . The flame deflections observed at moderate acoustic intensities were qualitatively in accordance with the predictions of the acoustic radiation force theory. The directions of the theoretical and measured acoustic accelerations were consistent with each other. However, the magnitudes of the measured acoustic accelerations were larger and steeper in the vicinity of the pressure node than predicted by theory. This was contrary to the expected profile, where a maximum acceleration was expected to occur at approximately $\lambda/8$ away from the pressure node. The variation in magnitude of the burning rate constants, despite not being significantly larger than the measurement uncertainties, showed a closer correspondence to the variation in magnitude of the measured acoustic accelerations than the theoretical acoustic accelerations.

Conducting the experiments in normal gravity resulted in natural convection being a significant factor in the magnitude of the burning rate constants at moderate levels of acoustic forcing, thereby diminishing the impact of the acoustic radiation force. At very high amplitudes of forcing, however, the nearly horizontal deflected flames indicated that g_a exceeded gravitational acceleration by a significant degree.

Based on preliminary extinction strain rate results obtained thus far, there was no significant difference between the alcohols and the hydrocarbon fuels. The current method of evaluating strain rates involved estimating an equivalent bulk flow velocity due to the strong acoustic acceleration and gravitation accleration. Since the acoustic acceleration was measured based on the degree of flame deflection, and the flame orientation was nearly horizontal at the instant before extinction, the estimated bulk flow velocity was thus very sensitive to measured angles of flame deflection. As little as two to three degrees of uncertainity in the measured flame deflection angle brought about changes in the estimated strain rates of more than $40s^{-1}$. A more refined method of estimating the extinction strain rates for the flames of the different fuels must be sought.

6.2 Non-Reactive Shear-Coaxial Jets

The high pressure, cryogenic shear-coaxial jets experiment provided a means to break down the complex phenomena associated with combustion instabilities, and focus on the non-reactive flow processes that contribute to their growth and sustenance. Chamber pressures below (reduced pressure, $P_r = 0.44$) and just above the critical pressure ($P_r = 1.05$) of nitrogen, and cryogenic jet temperatures allowed for the exploration of different injection phases of the nitrogen test fluid: a liquid inner jet with a cold, gaseous outer jet, and a transcritical inner jet with a supercritical outer jet. A range of momentum flux ratios, $J = 0.1 - 21$, were achieved by holding the inner jet flowrate constant and varying the outer jet flowrate. Two injector configurations that had different outer to inner jet exit area ratio, A_o/A_i, and inner injector post thickness to inner injector inside diamter ratio, t/D_1. Accordingly, one injector had a large A_o/A_i (LAR) with a small t/D_1 (thin) while the other had a small A_o/A_i (SAR) with a large t/D_1 (thick). Dark-core lengths based on the silhouette of the dense inner jet fluid were measured for different J flows at $P_r = 0.44$ and $P_r = 1.05$, with and without transverse acoustic forcing, which created either a pressure antinode (PAN) or a pressure node (PN) condition at the coaxial jet location. A proper orthogonal decomposition of the high-speed image data pixel intensities was used to identify the spatial and temporal characteristics of dominant flow structures.

Under baseline or no acoustic forcing condition, dark-core length L_B to inner jet diameter D_1 ratio, L_B/D_1, of the LAR-thin and SAR-thick injector flows at both P_r showed a decreasing trend with increasing J. This decreasing trend also had a steeper gradient for lower J than for higher J values. A power-law curve-fit to the L_B/D_1 variation with J revealed a slightly stronger dependence on J at $P_r = 1.05$, where the LAR-thin injector flow L_B/D_1 varied as $J^{-0.50}$ and that of the SAR-thick injector flow as $J^{-0.54}$, while at $P_r = 0.44$, L_B/D_1 varied as $J^{-0.39}$ and as $J^{-0.35}$ for the LAR-thin and

SAR thick injector flows, respectively. For comparable J values, flows at $P_r = 0.44$ had larger L_B/D_1 than those at $P_r = 1.05$. Furthermore, for comparable J values and the same P_r, the SAR-thick injector flows had smaller L_B/D_1 than the LAR-thin injector flows.

The baseline dark-core length measurments for the LAR-thin and SAR-thick injectors were also compared with two other alternate injector exit configurations from previous works in the present experimental facility using a SAR-thin and a LAR-thick injector. Unlike the current work, most of the results obtained using the SAR-thin and LAR-thick injectors had the inner jet injector recessed by $0.5D_1$. However, a similar set of experiments done with and without recess using the SAR-thin injector showed no statistically significant differences in their dark-core lengths. A comparison of L_B/D_1 for the four different injectors showed a large spread for low J flows, where it was the largest for the LAR-thin injector flows, and the smallest for the SAR-thick and SAR-thin injector flows. For low J flows, the LAR-thick L_B/D_1 were less than the LAR-thin, and greater than both SAR injectors. At high J values, all but the LAR-thin had L_B/D_1 that approached the same value. For J values beyond highest reported in these studies, the trend in the LAR-thin L_B/D_1 also appeared to asymptote to the same value as the others. In general, it was found that L_B/D_1 increased with increasing A_o/A_i while it decreased with increasing J and t/D_1. Thus, the extent of mixing may be controlled by altering these flow and geometric parameters.

In the presence of transverse acoustic excitation, the PAN and PN forcing conditions produced a trend in the LAR-thin injector flow dark-core lengths, L_F, that were different from those of the SAR-thick injector flows. The ratio of the forced to baseline dark-core lengths, L_F/L_B, for the PAN forced LAR-thin injector flows, in general, monotonically increased towards unity with increasing J at both P_r. This implied that the overall mixing characteristics resembled progressively more of the baseline with increasing J.

However, lower flowrates resulted in decreased L_F/L_B despite increased J. Thus, the magnitude of the flowrates also influenced the response to external disturbances. Similar behavior in L_F/L_B was also observed during the PN forcing condition. In contrast, the L_F/L_B for the PAN forced SAR-thick injector deviated from one for higher J ($J \geq 10$) flows only. This attested to the impact of the delayed interaction between the inner and outer jets due to the presence of the recirculating outer jet fluid for lower J flows. However, it was more susceptible to the PN forcing, and became less so with increasing J.

The spatial and temporal characteristics of the dominant flow disturbance structures were identified using proper orthogonal decompostion (POD) of the high-speed image pixel intensities. The LAR-thin injector baseline flows at both P_r and all J were characterized by antisymmetric periodic flow structures that indicated the presence of helical disturbances in the inner shear layer. The associated peak frequencies of these structures became broader and shifted to higher frequencies with increasing J and increasing outer jet flowrate. [...] On the other hand, the SAR-thick injector showed well-defined antisymmetric flow structures for $J \geq 2$. However, the peak frequencies in the magnitude spectra remained at low frequencies despite increasing J or increasing outer jet flowrate. Unlike the LAR-thin injector, the region immediately downstream of the thick inner jet post formed a flow recirculation zone, which delayed the formation of the inner shear layer. This delayed interaction between the inner and outer jets in addition to the SAR-thick injector's thin annulus outer jet may have been the cause for this limited influence on the spectral characteristics of the inner shear layer disturbances.

The PAN forcing condition had a greater impact on the low J ($J < 5$) LAR-thin injector flows at both P_r. As a result of this forcing condition, periodic and symmetric flow disturbance structures that resembled varicose disturbances, formed in the inner shear layer region. The corresponding magnitude of the cross-power spectra of conjugate modes of the POD also showed dominant peaks at the forcing frequency. These strong responses at the forcing frequecies subsided for higher J flows, resulting in the formation of antisymmetric flow structures similar to the ones identified in the baseline flows. The magnitude spectra for these higher J flows also retained the baseline spectral characteristics further indicating a transition to reduced susceptibility to external pressure disturbances. Such variation with J in the degree of sensitivity was not observed for the PN forcing condition, which imposed sinuous disturbances in the form of tranverse velocity fluctuations. The magnitude spectra, nevertheless, did retain aspects of the baseline spectral behavior at higher J.

The low J ($J < 2$) SAR-thick injector flow response to the PAN forcing conditions at both P_r was unlike the LAR-thin injector flows. Although direct observation of the high-speed images confirmed the formation of vortical structures in the recirculation zone, as a result of interaction with the outer shear-layer vortices, there were no symmetric or antisymmetric periodic flow disturbances in the inner shear layer. The absence of dominant peaks at the forcing frequency in the magnitude spectra confirmed this observation. For $J > 5$, the PAN forcing produced symmetric structures below the recirculation zone with associated peaks in the spectra at the forcing frequencies. The low J flows also showed no appreciable response to the PN forcing until about $J > 5$, beyond which antisymmetric structures were formed due to sinuous disturbances.

For a given geometry, the nature of the flow response to an external disturbance depending on the flow condition, namely J, may be used to characterize the state of stability of the flow. Literature [72, 73, 74] on flow stability characterize convectively unstable flows as noise amplifiers; that is, they are prone to external flow disturbances such as acoustic disturbances as used in this study. Their spectral characteristics are such that when exposed to external forcing, their natural instabilities are completely removed and replaced by instabilities whose frequency match those of the forcing frequency [75].

Absolutely unstable flows, on the other hand, are characterized as naturally self-excited flows that do not respond well to external disturbances. Their spectra preserve the natural instabilities with or without a coexisting frequency content associated with the forcing frequency. These and the flow responses observed may be used to argue that the LAR-thin injector flows can be characterized as convectively unstable for low J flows, and transition into absolutely unstable flows with increasing J values, while the SAR-thick injector flows depicted the behavior of convectively unstable flows at the higher J values. However, this characterization deserves further exploration in future studies.

APPENDIX A

Shear-Coaxial Jets Experimental Facility: Piping and Instrumentation Diagram

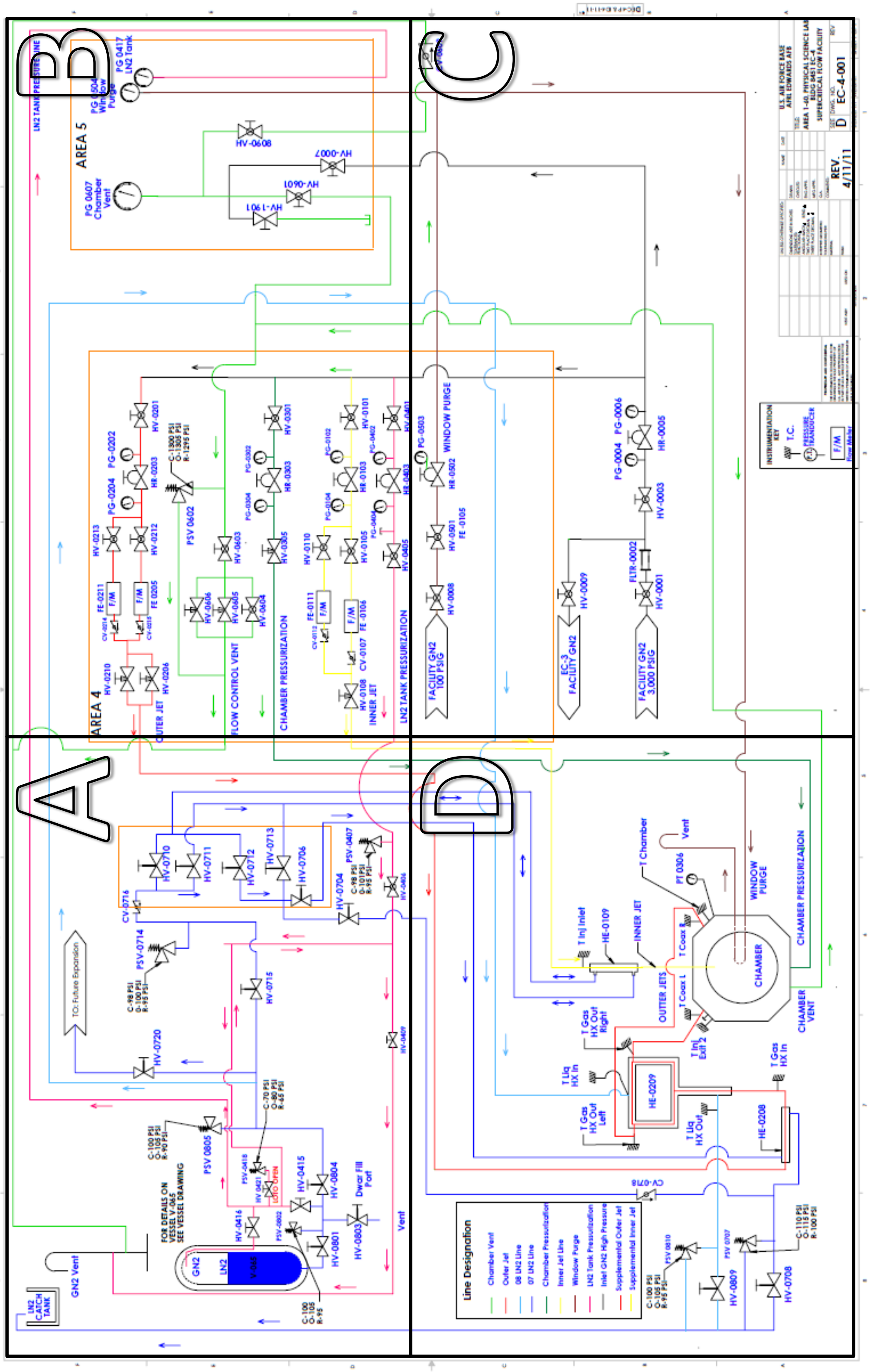
A
B
C
D
AREA 4
AREA 5
LN2 TANK PRESSURE LINE
PG 0607 Chamber Vent
PG 0417 LN2 Tank
HV-0608
HV-0007
HV-0601
HV-1901
OUTER JET
FLOW CONTROL VENT
CHAMBER PRESSURIZATION
INNER JET
LN2 TANK PRESSURIZATION
WINDOW PURGE
FACILITY GN2 100 PSIG
EC-3 FACILITY GN2
FACILITY GN2 3,000 PSIG
PSV 0602
HV-0201
HV-0301
HV-0101
HV-0001
HV-0009
HV-0008
HR-0005
HR-0003
FLTR-0002
TO: Future Expansion
HV-0720
PSV-0714
CV-0716
HV-0710
HV-0711
HV-0712
HV-0713
HV-0706
HV-0704
PSV-0407
HV-0715
PSV 0805
FOR DETAILS ON VESSEL V-06.5 SEE VESSEL DRAWING
GN2
LN2
GN2 Vent
LN2 CATCH TANK
HV-0416
HV-0415
HV-0804
HV-0801
HV-0803
Dwar Fill Port
Vent
Line Designation
Chamber Vent
Outer Jet
08 LN2 Line
07 LN2 Line
Chamber Pressurization
Inner Jet Line
Window Purge
LN2 Tank Pressurization
Inlet GN2 High Pressure
Supplemental Outer Jet
Supplemental Inner Jet
HV-0809
HV-0708
PSV 0810
PSV 0707
CV-0718
HE-0208
HE-0209
T Liq HX In
T Gas HX In
T Gas HX Out Left
T Gas HX Out Right
T Liq HX Out
T Inj Inlet
HE-0109
INNER JET
OUTTER JETS
T Chamber
PT 0306
Vent
WINDOW PURGE
CHAMBER
CHAMBER VENT
CHAMBER PRESSURIZATION
INSTRUMENTATION KEY
T.C.
PRESSURE TRANSDUCER
F/M Flow Meter
U.S. AIR FORCE BASE
AFRL EDWARDS AFB
SUPERCRITICAL FLOW FACILITY
EC-4-001
REV. 4/11/11

Figure A.1: Experimental facility piping and instrumentation diagram.

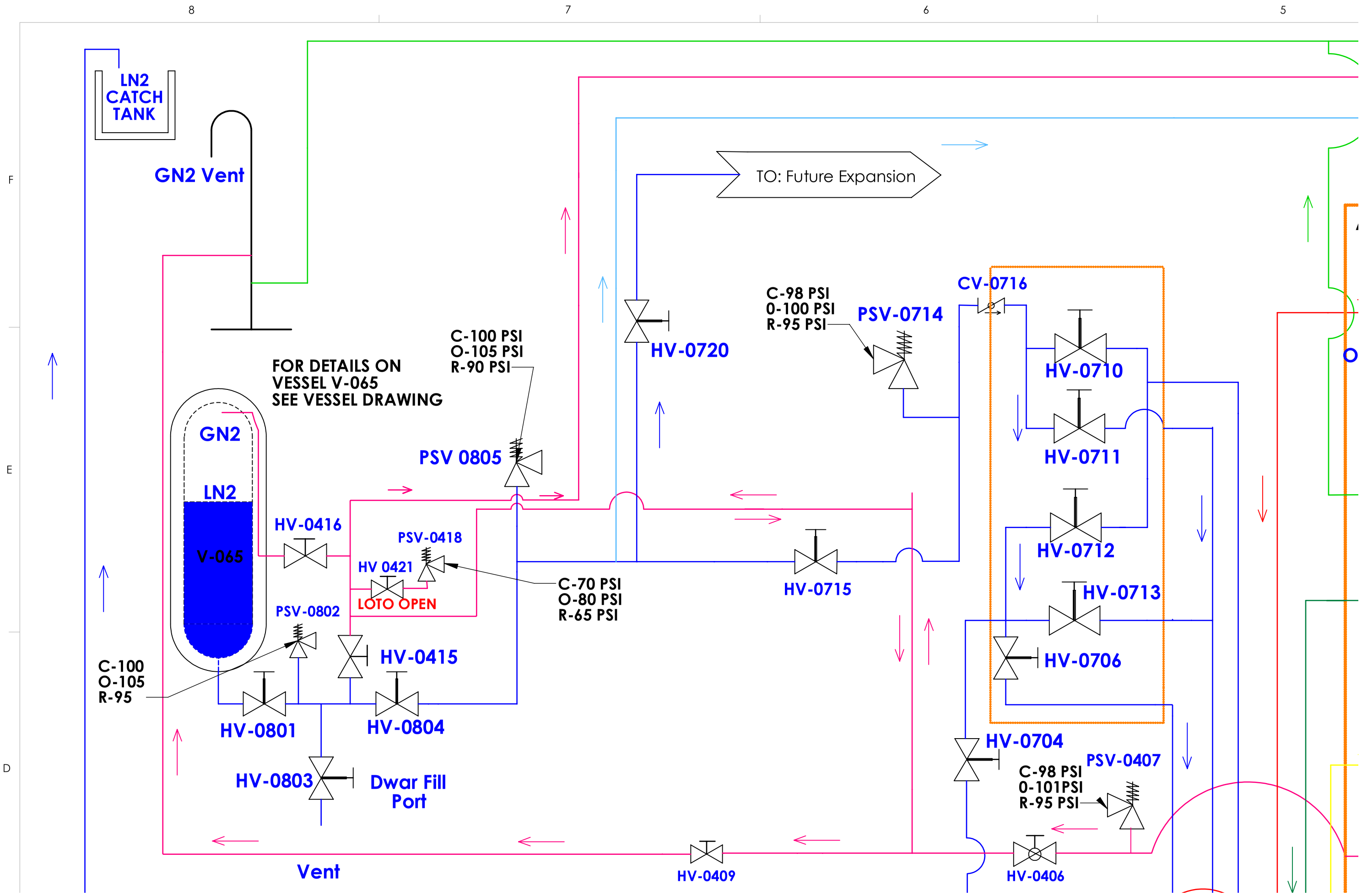
8
7
6
5
F
E
D
LN2
CATCH
TANK
GN2 Vent
TO: Future Expansion
CV-0716
C-98 PSI
0-100 PSI
R-95 PSI
PSV-0714
HV-0720
HV-0710
HV-0711
HV-0712
HV-0713
HV-0706
HV-0704
PSV-0407
C-98 PSI
0-101PSI
R-95 PSI
HV-0406
C-100 PSI
O-105 PSI
R-90 PSI
FOR DETAILS ON
VESSEL V-065
SEE VESSEL DRAWING
GN2
LN2
V-065
PSV 0805
HV-0416
PSV-0418
HV 0421
LOTO OPEN
C-70 PSI
O-80 PSI
R-65 PSI
HV-0715
PSV-0802
HV-0415
C-100
O-105
R-95
HV-0801
HV-0804
HV-0803
Dwar Fill
Port
Vent
HV-0409

Figure A.2: Expanded view of section A in Figure A.1.

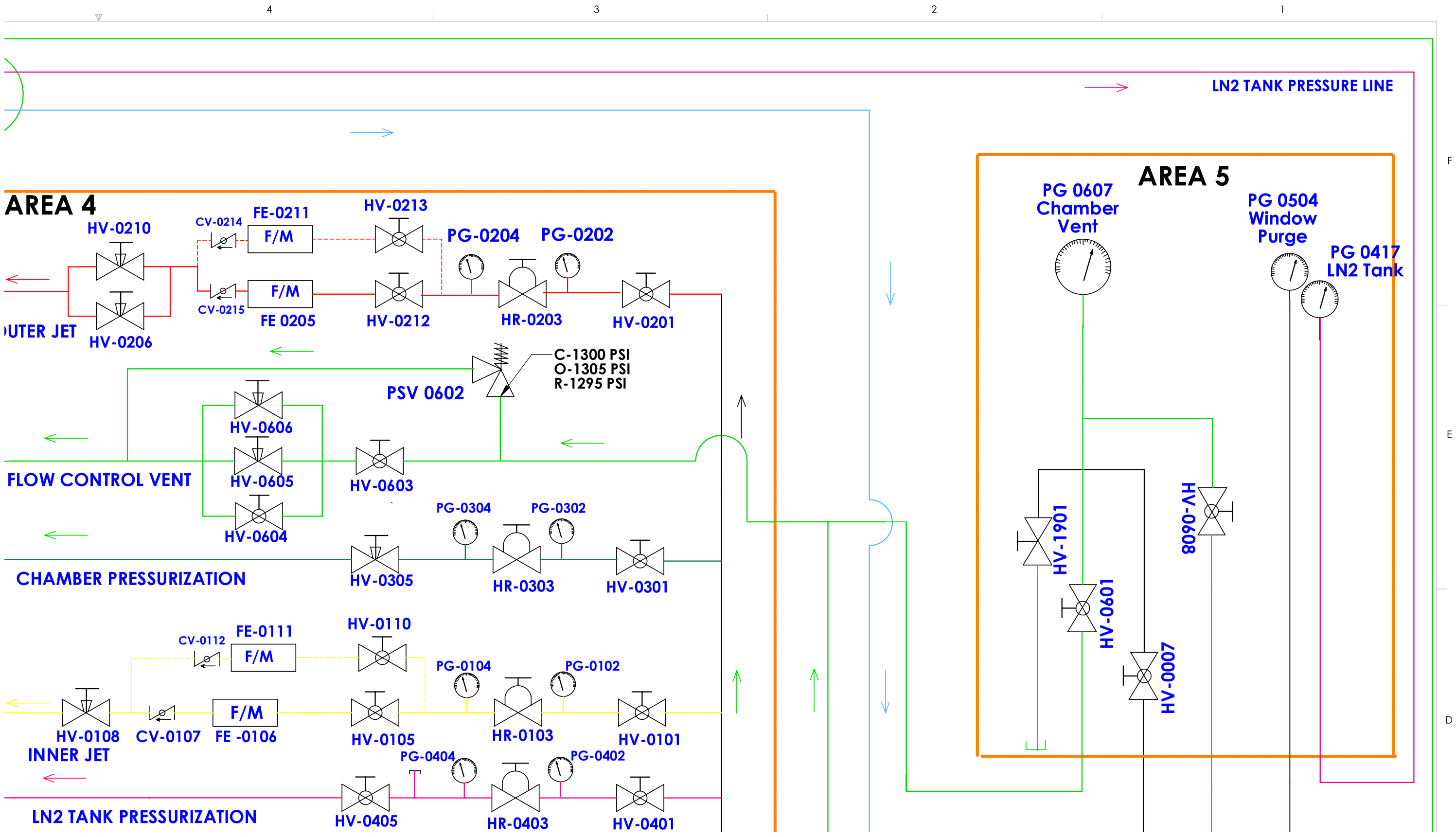
4
3
2
1
F
E
D
LN2 TANK PRESSURE LINE
AREA 4
HV-0210
CV-0214
FE-0211
F/M
HV-0213
PG-0204
PG-0202
F/M
CV-0215
FE 0205
HV-0212
HR-0203
HV-0201
UTER JET
HV-0206
C-1300 PSI
O-1305 PSI
R-1295 PSI
PSV 0602
HV-0606
HV-0605
HV-0604
HV-0603
FLOW CONTROL VENT
PG-0304
PG-0302
HV-0305
HR-0303
HV-0301
CHAMBER PRESSURIZATION
CV-0112
FE-0111
F/M
HV-0110
PG-0104
PG-0102
F/M
HV-0108
INNER JET
CV-0107
FE -0106
HV-0105
HR-0103
HV-0101
PG-0404
PG-0402
HV-0405
HR-0403
HV-0401
LN2 TANK PRESSURIZATION
AREA 5
PG 0607
Chamber
Vent
PG 0504
Window
Purge
PG 0417
LN2 Tank
HV-1901
HV-0601
HV-0608
HV-0007

Figure A.3: Expanded view of section B in Figure A.1.

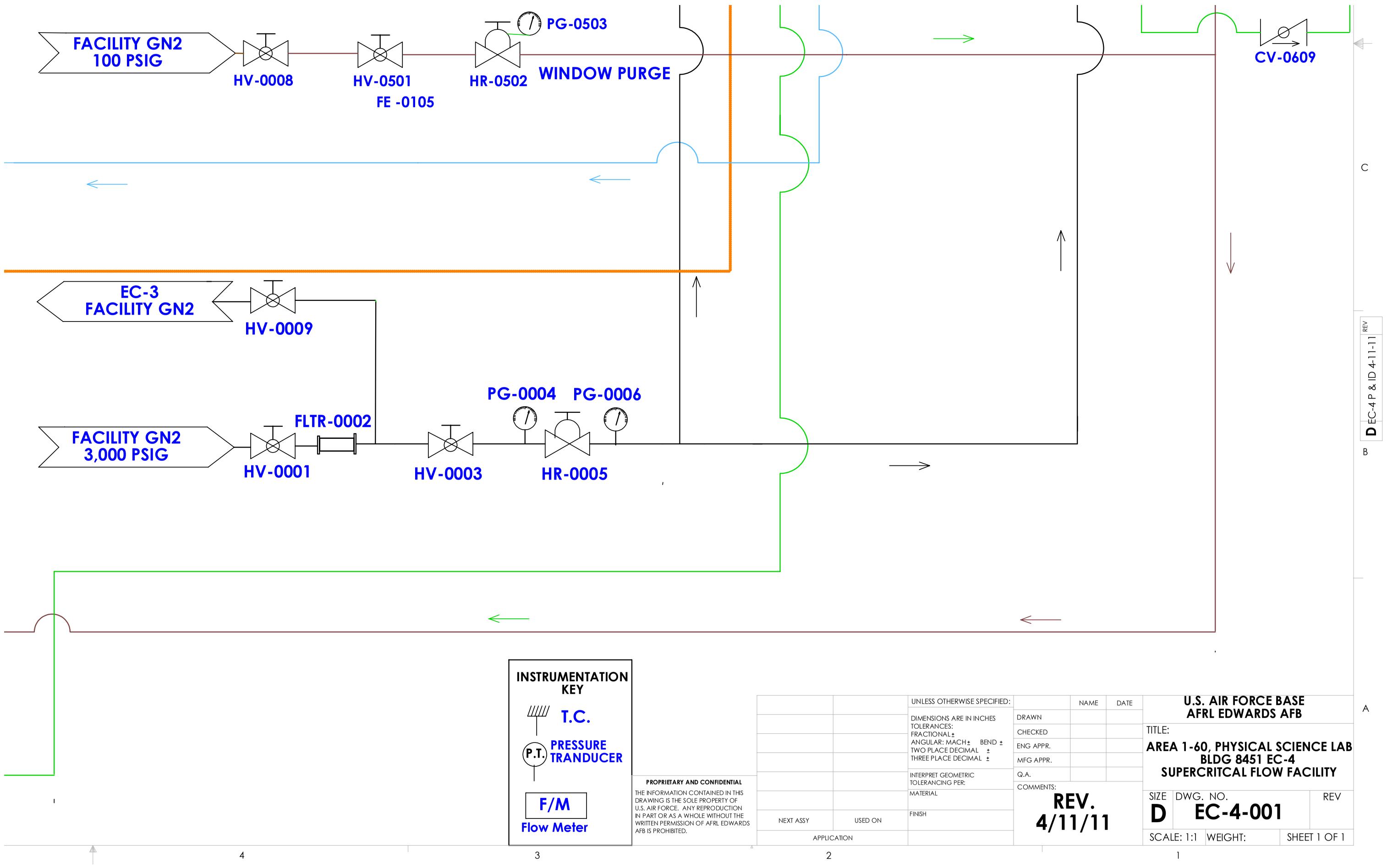
FACILITY GN2
100 PSIG
HV-0008
HV-0501
FE -0105
HR-0502
PG-0503
WINDOW PURGE
CV-0609
EC-3
FACILITY GN2
HV-0009
FACILITY GN2
3,000 PSIG
HV-0001
FLTR-0002
HV-0003
PG-0004
PG-0006
HR-0005
INSTRUMENTATION KEY
T.C.
P.T.
PRESSURE TRANDUCER
F/M
Flow Meter
PROPRIETARY AND CONFIDENTIAL
THE INFORMATION CONTAINED IN THIS DRAWING IS THE SOLE PROPERTY OF U.S. AIR FORCE. ANY REPRODUCTION IN PART OR AS A WHOLE WITHOUT THE WRITTEN PERMISSION OF AFRL EDWARDS AFB IS PROHIBITED.
NEXT ASSY
USED ON
APPLICATION
UNLESS OTHERWISE SPECIFIED:
DIMENSIONS ARE IN INCHES
TOLERANCES:
FRACTIONAL ±
ANGULAR: MACH ± BEND ±
TWO PLACE DECIMAL ±
THREE PLACE DECIMAL ±
INTERPRET GEOMETRIC TOLERANCING PER:
MATERIAL
FINISH
NAME
DATE
DRAWN
CHECKED
ENG APPR.
MFG APPR.
Q.A.
COMMENTS:
REV.
4/11/11
U.S. AIR FORCE BASE
AFRL EDWARDS AFB
TITLE:
AREA 1-60, PHYSICAL SCIENCE LAB
BLDG 8451 EC-4
SUPERCRITCAL FLOW FACILITY
SIZE
D
DWG. NO.
EC-4-001
REV
SCALE: 1:1
WEIGHT:
SHEET 1 OF 1
D EC-4 P & ID 4-11-11
REV
A
B
C
1
2
3
4

Figure A.4: Expanded view of section C in Figure A.1.

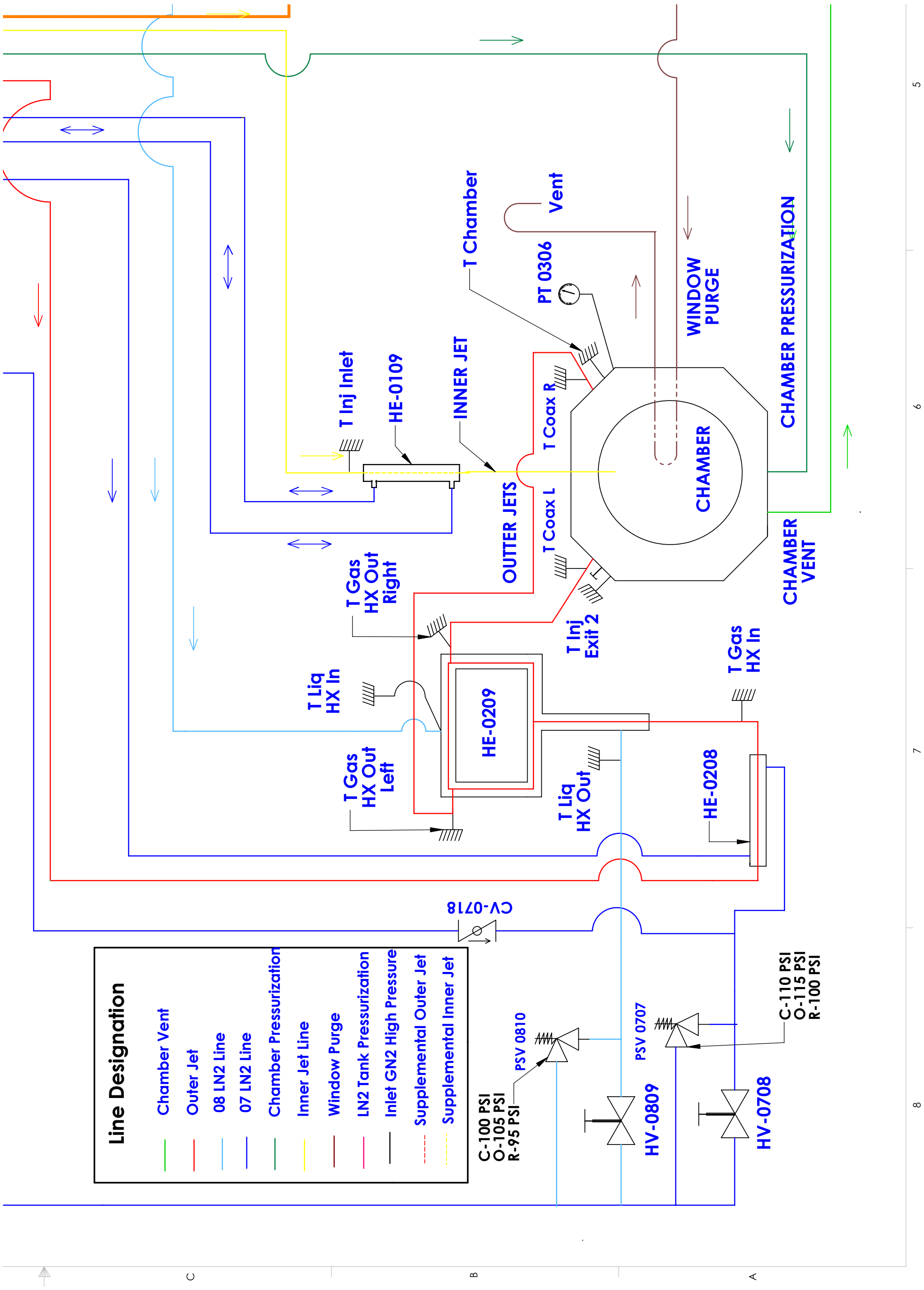

Line Designation
Chamber Vent
Outer Jet
08 LN2 Line
07 LN2 Line
Chamber Pressurization
Inner Jet Line
Window Purge
LN2 Tank Pressurization
Inlet GN2 High Pressure
Supplemental Outer Jet
Supplemental Inner Jet
T Inj Inlet
HE-0109
INNER JET
T Chamber
Vent
PT 0306
WINDOW PURGE
CHAMBER PRESSURIZATION
T Coax R
T Coax L
OUTTER JETS
CHAMBER
CHAMBER VENT
T Gas HX Out Right
T Inj Exit 2
T Liq HX In
HE-0209
T Gas HX In
T Gas HX Out Left
T Liq HX Out
HE-0208
CV-0718
PSV 0810
PSV 0707
C-100 PSI
O-105 PSI
R-95 PSI
C-110 PSI
O-115 PSI
R-100 PSI
HV-0809
HV-0708
5
6
7
8
C
B
A

Figure A.5: Expanded view of section D in Figure A.1.

APPENDIX B

Shear-Coaxial Jets Experiment:
Standard Operating Procedures

FLUID SUBSYSTEM NUMBER DESIGNATION

The first digit of the number indicates the fluid in the line, where 0 designates nitrogen fluid. The second digit, ranging from 0 – 8 listed in the Table below, indicates the fluid subsystem based upon its function. The last two digits indicate the component number.

Fluid Subsystem Number Designation.

Subsystem Number	Function
0	High Pressure Facility GN2
1	N_2 to Feed Inner Injector
2	N_2 to Feed Outer Injector
3	N_2 to Pressurize the Chamber
4	N_2 for Pressurization of LN2 Systems
5	Low Pressure GN2 for Window Purge
6	GN2 Vent
7	LN2 from Dewar
8	LN2 from External Tank

ALL TEST TEAM MEMBERS are responsible for the safe performance of the test, and must have read and understood all portions of the test procedure. Any Test Team Member can declare an emergency or unsafe condition.

____1. ABBREVATIONS AND ACRYONMS

EC - Experimental Cell
ER - Engineering Request
FE - Flow Element
GN2 - Gaseous Nitrogen
HE - Heat Exchanger
HR - Hand Regulator
HV - Hand Valve
LN2 - Liquid Nitrogen
PC - Pressure Chamber
PG - Pressure Gauge
PPE - Personal Protective Equipment
SCF - Supercritical Facility
SOCC - Site Operations Control Center

____2. PRETEST PREPARATIONS

____2.1. DON Test PPE: Lab coat or coveralls, safety goggles, safety shoes, and ear muffs (noise protection as required)

____2.2. Turn ON and Verify portable oxygen sensors are operational and calibrated

____2.3. Turn ON or Verify ON EC-4 Air Handler ventilation system.

____2.4. Turn OFF Air Handler.

____2.5. UNLOCK EC-4 outside door

____2.6. NOTE any potential hazards in and outside EC-4

____2.7. Verify GREEN, AMBER, and RED lights are functional and return to GREEN

____2.8. Turn on the Attocube power supply

____2.9. If Acoustic Testing Verify Gain or Turn Gain on Amplifier to the ZERO position

____2.10. If Acoustic Testing, Turn ON Amplifier to allow warm up as per ER______________________

____2.11. If Acoustic Testing, POST "HEARING PROTECTION REQUIRED" signs on the outside of the doors to EC-4, Room 19, foam door and adjacent hallway

____2.12. Turn on Data Acquisition System and System Electronics

____2.13. Position "Restricted Area" signs at the exit doors to horseshoe in rooms 39, 41, and adjacent to room 19 near the LN2 catch tank

____2.14. Position "DO NOT ENTER" signs outside of the room 19 and EC-4 doors

____2.15. Place chain in front of entrance to horseshoe

____3. **INITIAL SETUP**

____3.1. OPEN / Verify OPEN HV-0001 (EC-3, EC-4 Primary Facility Isolation Valve) - Area 3

____3.2. CLOSE / Verify CLOSED HV-0003 (EC-4 Secondary Facility Isolation Valve) - Area 3

____3.3. CLOSE / Verify CLOSED HV-0008 (EC-4 Low Pressure Facility Isolation Valve) - Area 3

____3.4. CLOSE / Verify CLOSED HV-0009 (EC-3 Secondary Facility Isolation Valve) - Area 3

____3.5. CLOSE / Verify CLOSED HV-0406 (Tank GN2 Pressurization Isolation Valve) - Area 2

____3.6. CLOSE / Verify CLOSED HV-0409 (LN2 Tank Pressurization Vent Isolation Valve) - Area 2

____3.7. OPEN / Verify OPEN HV-0715 (Direct LN2 Supply Valve) - Area 2

____3.8. Close/ Verify Closed HV-0720 (Future LN2 Expansion) – Area 2

____3.9. OPEN / Verify OPEN HV-0704 (Heat Exchanger LN2 Bypass Valve) – Area 3

____3.10. CLOSE / Verify CLOSED HV-0706 (Heat Exchanger Flow Valve) – Area 3

____3.11. CLOSE / Verify CLOSED HV-0801 (LN2 Tank Isolation Valve) – Area1

____3.12. OPEN / Verify OPEN HV-0803 (LN2 Vent Isolation Valve) – Area1

____3.13. CLOSE / Verify CLOSED HV-0804 (LN2 Tank Secondary Isolation Valve) – Area 1

____3.14. CLOSE / Verify CLOSED HV-0415 (Vacuum Jacketed Line Purge Valve) – Area 1

NOTE: In case the LN2 line needs to be broken, moisture could get in. This valve permits purging of the line after it is reconnected

____**3.15.** CLOSE / Verify CLOSED HV-0416 (Tank GN2 Pressurization Valve) – Area 1

____**3.16.** CLOSE / Verify CLOSED HV-1901 (He System Isolation Valve) - Area 5

____**3.17.** CLOSE / Verify CLOSED HV-0601 (PC Vent PG Isolation Valve) - Area 5

____**3.18.** OPEN / Verify OPEN HV-0608 (Gauge Vent Valve) - Area 5

____**3.19.** CLOSE / Verify CLOSED HV-0007 (Upstream Regulator Pressure Valve) - Area 5

____**3.20.** OPEN / Verify OPEN HV-0603 (Chamber Pressure Build Valve) - Area 4

____**3.21.** OPEN / Verify OPEN HV-0604 (Primary Chamber Pressure Vent Valve) - Area 4

____**3.22.** CLOSE / Verify CLOSED HV-0605 (Secondary Chamber Pressure Vent Valve) - Area 4

____**3.23.** CLOSE / Verify CLOSED HV-0606 (Tertiary Chamber Pressure Vent Valve) - Area 4

____**3.24.** CLOSE / Verify CLOSED HV-0708 (Heat Exchanger LN2 Throttle Vent Valve) – ceiling between Area 4 & Area 5

____**3.25.** CLOSE / Verify CLOSED HV-0809 (Outer Heat Exchanger LN2 Throttle Vent Valve) – ceiling between Area 4 & Area 5

____**3.26.** CLOSE / Verify CLOSED HV-0710 (Primary Co-Flow Valve) – Area 4

____**3.27.** OPEN / Verify OPEN HV-0711 (Primary Counter Flow Valve) – Area 4

____**3.28.** OPEN / Verify OPEN HV-0712 (Secondary Counter Flow Valve) – Area 4

____**3.29.** CLOSE / Verify CLOSED HV-0713 (Secondary Co-Flow Valve) – Area 4

____**3.30.** Verify PG-0607 (Chamber Pressure Gauge) reads 0 psig– Area 5

____**3.31.** Verify PG-0004 (EC-4 System Inlet Pressure Gauge) reads 0 psig – Area 5

____**3.32.** DECREASE FULLY / Verify FULLY DECREASED HR-0005 (EC-4 Facility Pressure Regulator) – Area 5

____**3.33.** Verify PG-0006 (EC-4 System Outlet Pressure Gauge) reads 0 psig – Area 5

____**3.34.** CLOSE / Verify CLOSED HV-0101 (Inner Jet GN2 Isolation Valve) – Area 4

____**3.35.** Verify PG-0102 (Inner Jet GN2 System Inlet Pressure Gauge) reads 0 psig – Area 4

____**3.36.** DECREASE FULLY / Verify FULLY DECREASED HR-0103 (Inner Jet GN2 Pressure Regulator) – Area 4

____**3.37.** Verify PG-0104 (Inner Jet GN2 Regulated Pressure Gauge) reads 0 psig – Area 4

____**3.38.** CLOSE / Verify CLOSED HV-0105 (Inner Jet Low Flow Isolation Valve) – Area 4

____**3.39.** CLOSE / Verify CLOSED HV-0110 (Inner Jet High Flow Isolation Valve) – Area 4

____**3.40.** CLOSE / Verify CLOSED HV-0108 (Inner Jet GN2 Throttle Valve) – Area 4

____**3.41.** CLOSE / Verify CLOSED HV-0201 (Outer Jet GN2 Isolation Valve) – Area 4

____**3.42.** Verify PG-0202 (Outer Jet GN2 System Inlet Pressure Gauge) reads 0 psig – Area 4

____**3.43.** DECREASE FULLY / Verify FULLY DECREASED HR-0203 (Outer Jet GN2 Pressure Regulator) – Area 4

____**3.44.** Verify PG-0204 (Outer Jet GN2 Regulated Pressure Gauge) reads 0 psig – Area 4

____**3.45.** CLOSE / Verify CLOSED HV-0212 (Outer Jet High Flow Isolation Valve) – Area 4

____**3.46.** CLOSE / Verify CLOSED HV-0213 (Outer Jet Low Flow Isolation Valve) – Area 4

____**3.47.** CLOSE / Verify CLOSED HV-0206 (fine Outer Jet GN2 Throttle Valve) – Area 4

____**3.48.** CLOSE/ Verify CLOSED HV-0210 (coarse Outer Jet GN2 Throttle valve) – Area 4

____**3.49.** CLOSE / Verify CLOSED HV-0301 (Chamber Pressurization Isolation Valve) – Area 4

____**3.50.** Verify PG-0302 (Chamber Pressurization System Inlet Pressure Gauge) reads 0 psig – Area 4

____**3.51.** DECREASE FULLY / Verify FULLY DECREASED HR-0303 (Chamber Pressurization Regulator) – Area 4

____**3.52.** Verify PG-0304 (Chamber Pressure Regulated Pressure Gauge) reads 0 psig – Area 4

____**3.53.** CLOSE / Verify CLOSED HV-0305 (Chamber Pressurization Throttle Valve) – Area 4

____**3.54.** CLOSE / Verify CLOSED HV-0401 (LN2 Tank Pressurization Isolation Valve) – Area 4

____**3.55.** Verify PG-0402 (LN2 Tank GN2 System Inlet Pressure Gauge) reads 0 psig – Area 4

____**3.56.** DECREASE FULLY / Verify FULLY DECREASED HR-0403 (LN2 Tank GN2 Pressure Regulator) – Area 4

____**3.57.** Verify PG-0404 (LN2 Tank Pressurization Pressure Gauge) reads 0 psig – Area 4

____**3.58.** CLOSE / Verify CLOSED HV-0405 (LN2 Supply Tank Isolation Valve) – Area 4

____**3.59.** CLOSE / Verify CLOSED HV-0501 (Window Purge Isolation Valve) – Area 4

____**3.60.** Verify PG-0504 (Window Purge Pressure Gauge) reads 0 psig – Area 5

____**3.61.** DECREASE FULLY / Verify FULLY DECREASED HR-0502 (Window Purge Pressure Regulator) – Area 4

____**3.62.** Verify PG-0417 (LN2 Tank Pressure Gauge) reads 0 psig – Area 5
If not:
A – OPEN HV-0409 – Area 2
B – CLOSE HV-0409 – Area 2

____**4.** **WINDOW PURGE**

____**4.1.** Notify SOCC via hotline (or 5-5632) in EC-1, EC-2 or EC-3 control room that EC-4 is going into a RED condition for SCF testing

____**4.2.** Verify all personnel are wearing Test PPE

____**4.3.** Change EC-4 light to RED

____**4.4.** Record Time ___________________

____**4.5.** Verify window purge apparatus is in satisfactory condition

____**4.6.** OPEN HV-0008 (EC-4 Low Pressure Facility Isolation Valve) – Area 3

____**4.7.** OPEN HV-0501 (Window Purge Isolation Valve) – Area 4

CAUTION: Do NOT Increase HR-0502 so that PG-0504 reads greater than 5 psig as it will damage PG-0504

____**4.8.** INCREASE HR-0502 (Window Purge Pressure Regulator) until PG-0504 (Window Purge Pressure Gauge) reads 1.5 psig +/- 0.5 psig – Area 4

____**4.9.** Permit window purge to continue according to ER_______________________

____5. **FACILITY GN2 SETUP**

____5.1. *Slowly* OPEN HV-0003 (EC-4 Facility Isolation Valve) – Area 3

____5.2. Verify PG-0004 (EC-4 System Inlet Pressure Gauge) reads a pressure greater than 2000 psig – Area 4 ______________

____5.3. OPEN HV-0007 (Upstream Regulator Pressure Valve) – Area 5

____5.4. CLOSE HV-0608 (Gauge Vent Valve) – Area 5

____5.5. INCREASE HR-0005 (EC-4 Facility Pressure Regulator) until PG-0607 (Chamber Pressure Gauge) reads 2000 psig +/- 50 psig – Area 5

____

NOTE: Open and quickly close HV-0608 to check if PG-0607 actually reads 2000 psig

____5.6. CLOSE HV-0007 (Upstream Regulator Pressure Valve) – Area 5

____5.7. *Slowly* OPEN HV-0608 (Gauge Vent Valve) – Area 5

____5.8. Verify PG-0607 (Chamber Pressure Gauge) reads 0 psig – Area 5

____5.9. OPEN HV-0601 (PC Vent PG Isolation Valve) – Area 5

____5.10. CLOSE HV-0608 (Gauge Vent Valve) – Area 5

____5.11. Verify PG-0607 (Chamber Pressure Gauge) reads 0 psig – Area 5

____5.12. Turn ON Air Handler, *per ER or as necessary*

____6. **CHAMBER PURGE**

____6.1. Record Time ____________________

____6.2. Record zero values for Pressure Transducer (Agilent Ch. 103), Inner Jet Mass Flow Meter (Agilent Ch. 104) and Outer Jet Mass Flow Meter (Agilent Ch. 102).

____6.3. *Slowly* OPEN HV-0301 (Chamber Pressurization Isolation Valve) – Area 4

____6.4. Verify PG-0302 (Chamber Pressurization System Inlet Pressure Gauge) reads 2000 psig +/- 150 psig – Area 4 _______________

____6.5. INCREASE HR-0303 (Chamber Pressure GN2 Pressure Regulator) until PG-0304 (Chamber Pressure Regulated Pressure Gauge) reads ______ psig +0/-100 psig as per ER – Area 4

____6.6. OPEN HV-0305 (Chamber Pressurization Throttle Valve) as per ER____________ – Area 4

NOTE: Perform next 3 steps in quick succession

____6.7. CLOSE HV-0603 (Chamber Pressure Build Valve) – Area 4

____6.8. Verify PG-0607 (Chamber Pressure Gauge) indicates that chamber pressure is increasing to indicate purge is flowing. – Area 5

____6.9. OPEN HV-0603 (Chamber Pressure Build Valve) – Area 4

____6.10 Go to Chamber Pressurization Section if taking ambient T measurements with no flows

____7. **INNER JET PURGE**

____7.1. *Slowly* OPEN HV-0101 (Inner Jet GN2 Isolation Valve) – Area 4

____7.2. Verify PG-0102 (Inner Jet GN2 System Inlet Pressure Gauge) reads 2000 psig +/- 150 psig – Area 4 __________________

____**7.3.** OPEN HV-0105 (Inner Jet Low Flow Isolation Valve) for use with FE-0106 (flow rates up to 50 SLPM)
or HV-0110 (Inner Jet High Flow Isolation Valve) for use with FE-0111 (flow rates up to 200 SLPM) as per ER _________

____**7.4.** INCREASE HR-0103 (Inner Jet GN2 Pressure Regulator) until PG-0104 (Inner Jet GN2 Regulated Pressure Gauge) reads ________ psig +0/-100 psig as per ER – Area 4

____**7.5.** OPEN HV-0108 (Inner Jet GN2 Throttle Valve) as per ER___________ – Area 4

NOTE: Check chamber pressure periodically Ch. 103 in Agilent (at least every 500 mg/s)

____**7.6.** Verify FE-0106 (Inner Jet GN2 Flow Meter) indicates purge is flowing

NOTE: Ch. 104 in Agilent

____8. OUTER JET PURGE

____**8.1.** *Slowly* OPEN HV-0201 (Outer Jet GN2 Isolation Valve) – Area 4

____**8.2.** Verify PG-0202 (Outer Jet GN2 System Inlet Pressure Gauge) reads 2000 psig +/- 150 psig – Area 4 ___________

____**8.3.** Open HV-0212 (Outer Jet High Flow Isolation Valve) for use with FE-0205 (flow rates up to 500 SLPM)
or HV-0213 (Outer Jet High Flow Isolation Valve) for use with FE-0211 (lower flow rates) as per ER _________

____**8.4.** INCREASE HR-0203 (Outer Jet GN2 Pressure Regulator) until PG-0204 (Outer Jet GN2 Regulated Pressure Gauge) reads ______ psig +0/-100 psig as per ER – Area 4

NOTE: 1100 psig is the high limit for PG-0204. The calibration curve available does not go beyond this pressure.

____**8.5.** OPEN HV-0206 (Outer Jet GN2 Throttle Valve) as per ER___________ – Area 4

NOTE: Check chamber pressure periodically Ch. 103 in Agilent (at least every 500 mg/s)

____**8.6.** Verify FE-0205 (Outer Jet GN2 Flow Meter) indicates purge is flowing

NOTE: Ch. 102 in Agilent

____**9.** **CHAMBER PRESSURIZATION**

____**9.1.** OPEN HV-0605 (Secondary Chamber Pressure Vent Valve) 2 turns – Area 4

____**9.2.** OPEN HV-0606 (Tertiary Chamber Pressure Vent Valve) 8 turns – Area 4

____**9.3.** CLOSE HV-0604 (Primary Chamber Pressure Vent Valve) – Area 4

____**9.4.** ADJUST HV-0605 (Secondary Chamber Pressure Vent Valve) and HV-0606 (Tertiary Chamber Pressure Vent Valve) until PG-0607 (Chamber Pressure Gauge) reads INITIAL CHAMBER PRESSURE as per ER____________ – Area 4

____**9.5.** Wait for required time to elapse from step 13.1 as per ER____________

____**9.6.** IF taking measurements at room temperature

A - Take measurements

B - Reduce chamber pressure after measurements

C - Return to “Inner Jet Purge” section

____**10.** **SYSTEM CHILL DOWN**

____**10.1.** Verify Red Crew has donned Cryogenic PPE as outlined in Step 5.2

____**10.2.** CLOSE HV-0803 (LN2 Vent Isolation Valve) – Area 1

____**10.3.** OPEN HV-0801 (LN2 Tank Isolation Valve) – Area 1

____**10.4.** OPEN HV-0804 (LN2 Tank Secondary Isolation Valve) – Area 1

____**10.5.** OPEN HV-0416 (pressurize tank with GN2) – Area 1

____**10.6.** Remove Cryogenic PPE and don Test PPE as listed in Step 5.2

____**10.7.** *Slowly* OPEN HV-0401 (LN2 Tank Pressurization Isolation Valve) – Area 4

____**10.8.** Verify PG-0402 (LN2 Tank GN2 System Inlet Pressure Gauge) reads 2000 psig +/-150 psig – Area 4 ____________________

____**10.9.** Increase HR-0403 (LN2 Tank GN2 Pressure Regulator) until PG-0404 (Dewar and Tank Pressurization Pressure Gauge) reads as per ER – Area 4 _________________

____**10.10.** OPEN HV-0405 (LN2 Supply Tank Isolation Valve) – Area 4

____**10.11.** OPEN HV-0406 (LN2 Tank GN2 Pressurization Isolation Valve) – Area 2

____**10.12.** Record Time __________________

____**10.13.** OPEN HV-0809 (Outer Heat Exchanger LN2 Throttle Vent Valve) as per ER____________ ceiling between Area 4 & 5

NOTE: Rotate valve ¼ of a turn and wait 10 minutes

____**10.14.** OPEN HV-0708 (Heat Exchanger LN2 Throttle Vent Valve) as per ER____________ ceiling between Area 4 & 5

NOTE: Rotate valve ¼ of a turn and wait 10 minutes

____**10.15.** Wait Required time for chill down as per ER____________

____11. TESTING

____11.1. If acoustic testing, follow the procedure for setting up the acoustic drivers

____11.2. Verify all personnel are wearing ear muffs if acoustic testing

____11.3. Adjust HR-0103 (Inner Jet GN2 Pressure Regulator) to maintain desired flow rates

NOTE: Ch. 104 in Agilent

____11.4. Adjust HR-0203 (Outer Jet GN2 Pressure Regulator) to maintain desired flow rates

NOTE: Ch. 102 in Agilent

____11.5. Adjust HV-0606 (Tertiary Chamber Pressure Vent Valve) and HV-0605 (Secondary Chamber Pressure Vent Valve) to maintain desired chamber pressure

NOTE: Ch. 103 in Agilent

____11.6. Direct red crew leader to operate system as per test needs

____11.7. OPERATE System as directed by test conductor

____12. **SHUT DOWN**

____12.1. CLOSE HV-0003 (EC-4 Secondary Facility Isolation Valve) – Area 2

____12.2. CLOSE HV-0008 (EC-4 Low Pressure Facility Isolation Valve) – Area 2

____12.3. Turn OFF/ Verify OFF air handler

____12.4. DON Cryogenic PPE

____12.5. CLOSE HV-0801 (LN2 Tank Isolation Valve) – Area 1

____12.6. CLOSE HV-0416 (Tank GN2 Pressurization Isolation Valve) – Area 1

____12.7. REMOVE Cryogenic PPE

____12.8. OPEN HV-0409 (LN2 Tank Pressurization Vent Isolation Valve) – Area 2

____12.9. Wait for PG-0004 (EC-4 System Inlet Pressure Gauge) to read 0 psig – Area 5

____12.10. Fully DECREASE HR-0005 (EC-4 Facility Pressure Regulator) – Area 5

____12.11. Verify PG-0006 (EC-4 System Regulated Pressure Gauge) reads 0 psig – Area 5

____12.12. Verify PG-0102 (Inner Jet GN2 System Inlet Pressure Gauge) reads 0 psig – Area 4

____12.13. CLOSE HV-0101 (Inner Jet GN2 Isolation Valve) – Area 4

____12.14. Fully DECREASE HR-0103 (Inner Jet GN2 Pressure Regulator) – Area 4

____12.15. Verify PG-0104 (Inner Jet GN2 Regulated Pressure Gauge) reads 0 psig – Area 4

____12.16. CLOSE HV-0105 (Inner Jet Low Flow Isolation Valve) – Area 4

____12.17. CLOSE HV-0110 (Inner Jet High Flow Isolation Valve) – Area 4

____12.18. CLOSE HV-0108 (Inner Jet GN2 Throttle Valve) – Area 4

____**12.19.** Verify PG-0202 (Outer Jet GN2 System Inlet Pressure Gauge) reads 0 psig -– Area 4

____**12.20.** CLOSE HV-0201 (Outer Jet GN2 Isolation Valve) – Area 4

____**12.21.** Fully DECREASE HR-0203 (Outer Jet GN2 Pressure Regulator) – Area 4

____**12.22.** Verify PG-0204 (Outer Jet GN2 Regulated Pressure Gauge) reads 0 psig – Area 4

____**12.23.** CLOSE HV-0212 (Outer Jet High Flow Isolation Valve) – Area 4

____**12.24.** CLOSE HV-0213 (Outer Jet Low Flow Isolation Valve) – Area 4

____**12.25.** CLOSE HV-0206 (fine Outer Jet GN2 Throttle Valve) – Area 4

____**12.26.** CLOSE HV-0210 (coarse Outer Jet GN2 Throttle Valve) – Area 4

____**12.27.** Verify PG-0302 (Chamber Pressurization System Inlet Pressure Gauge) reads 0 psig – Area 4

____**12.28.** CLOSE HV-0301 (Chamber Pressurization Isolation Valve) – Area 4

____**12.29.** Fully DECREASE HR-0303 (Chamber Pressurization Regulator) – Area 4

____**12.30.** Verify PG-0304 (Chamber Pressure Regulated Pressure Gauge)reads 0 psig – Area 4

____**12.31.** CLOSE HV-0305 (Chamber Pressurization Throttle Valve) – Area 4

____**12.32.** Verify PG-0402 (LN2 Tank GN2 System Inlet Pressure Gauge) read 0 psig – Area 4

NOTE: Current readout sticks

____**12.33.** CLOSE HV-0401 (LN2 Tank Pressurization Isolation Valve) – Area 4

____**12.34.** Fully DECREASE HR-0403 (LN2 Tank GN2 Pressure Regulator) – Area 4

_____**12.35.** Verify PG-0404 (LN2 Tank Pressurization Pressure Gauge) reads 0 psig – Area 4

_____**12.36.** OPEN HV-0405 (LN2 Supply Tank Isolation Valve) – Area 4

_____**12.37.** OPEN/Verify OPEN HV-0406 (Tank GN2 Pressurization Isolation Valve) – Area 2

_____**12.38.** Verify PG-0504 (Window Purge Pressure Gauge) reads 0 psig – Area 5

_____**12.39.** CLOSE HV-0501 (Window Purge Isolation Valve) – Area 4

_____**12.40.** Fully DECREASE HR-0502 (Window Purge Pressure Regulator) – Area 4

_____**12.41.** OPEN HV-0608 (Gauge Vent Valve) – Area 5

_____**12.42.** Verify PG-0607 (Chamber Pressure Gauge) reads 0 psig – Area 5

_____**12.43.** CLOSE HV-0601 (PC Vent PG Isolation Valve) – Area 5

_____**12.44.** OPEN / Verify OPEN HV-0603 (Chamber Pressure Build Valve) – Area 4

_____**12.45.** OPEN HV-0604 (Primary Chamber Pressure Vent Valve) – Area 4

_____**12.46.** CLOSE HV-0605 (Secondary Chamber Pressure Vent Valve) – Area 4

_____**12.47.** CLOSE HV-0606 (Tertiary Chamber Pressure Vent Valve) – Area 4

_____**12.48.** OPEN HV-0708 (Heat Exchanger LN2 Throttle Vent Valve) – ceiling between Area 4&5

_____**12.49.** OPEN HV-0809 (Outer Heat Exchanger LN2 Throttle Vent Valve) – ceiling between Area 4&5

_____**12.50.** OPEN / Verify OPEN HV-0715 (Direct LN2 Supply Valve) - Area 2

_____**12.51.** Don Cryogenic PPE

____12.52. CLOSE HV-0804 (LN2 Tank Secondary Isolation Valve) – Area 1

____12.53. OPEN HV-0803 (LN2 Vent Isolation Valve - vent trapped LN2 between 0801 and 0804) - Area 1

____12.54. Remove Cryogenic PPE

____12.55. Verify PG-0417 (LN2 Tank Pressure Gauge) reads 0 psig – Area 5

____12.56. Notify SOCC EC-4 is going back to green condition

____12.57. Turn off portable O_2 sensors

____12.58. Turn EC-4 lights back to green

____12.59. Remove “DO NOT ENTER”, “Restricted Area” and “HEARING PROTECTION REQUIRED” signs

____12.60. Remove chain from entrance to horseshoe

____12.61. Turn off the acoustic drivers

____13. EMERGENCY PROCEDURE (GN_2 or LN_2 line leak or burst)

IF OXYGEN MONITORING ALARMS GO OFF:

____13.1. Exit the facility to a safe zone given in safety brief.

____13.2. Contact SOCC 5-5632 and report the emergency. Have SOCC contact the Fire Dept. 5-5181

____13.3. Contact the Facility Manager and isolate the cell or area.

IF POSSIBLE AND WHEN SAFE, DO THE FOLLOWING:

____**13.4.** CLOSE HV-0001 (EC-3, EC-4 Primary Facility Isolation Valve)

____**13.5.** CLOSE HV-0801 (Tank LN2 Isolation Valve)

NOTE: WHEN SAFE TO DO SO COMPLETE THE STEPS OF THE ”SHUT DOWN” SECTION 12

ACOUSTIC DRIVERS OPERATION

Settings to be verified every time something new is installed or there is an upgrade of the testing equipment that is directly involved with the operation of the acoustic drivers:

____**1.1.** Verify the wire from Channel 1 of the Tektronix oscilloscope (Model No. 2235A) comes from the strain gauge and during testing the signal should NEVER go over 43V peak-to-peak.

____**1.2.** Verify the setting of the Tektronix oscilloscope is such that Channel 1 has a range of 5V per division (for a total of 40V that can be seen on the screen, since there are 8 divisions)

____**1.3.** Verify the wire on Channel 1 of the Tenma oscilloscope (Model No. 72-6800) comes from the output voltage monitor on the Trek-1 amplifier and the wires on Channel 2 of the Tektronix and Tenma oscilloscopes come from the output voltage monitor on the Trek-2 amplifier

____**1.4.** Verify the setting of both oscilloscopes is such that Channel 2 has a range of 1V per division (for a total of 8V that can be seen on the screen, since the oscilloscope has 8 divisions)

____**1.5.** Verify the wire from Channel 1 of the Fluke Signal Generator goes to the Trek-1 amplifier and then the signal is amplified (200 times) and goes to the old (left as seen from the point where the high-speed camera is placed) acoustic driver (piezo-siren)

____**1.6.** Verify the wire from Channel 2 of the Fluke Signal Generator goes to the Trek-2 amplifier and then the signal is amplified (200 times) and goes to the new (right as seen from the point where the high-speed camera is placed) acoustic driver (piezo-siren)

____2. ACOUSTIC DRIVERS START UP

____**2.1.** Verify that the Fluke Signal Generator is on

____**2.2.** Verify that the Tektronix and Tenma oscilloscopes are on

____**2.3.** Lock Channel 1 to Channel 2 using the “Inter Channel” button on Fluke Signal Generator. Channel 1 setting is “Master/Frequency” and Channel 2 setting is “Slave”
NOTE: Make sure “Status” is ON after the appropriate mode settings on Channels 1 and 2

____**2.4.** Verify the phase difference between the two channels is 0 degrees

____**2.5.** Use the Fluke Signal Generator to assign Channel 1 an amplitude of 2 V peak-to-peak and a frequency of 3.00 kHz

____**2.6.** Verify that the signal (waveform) from Channel 1 is a sine function. [Use the “status” button on the Fluke Signal Generator]

____**2.7.** Use the Fluke Signal Generator to assign Channel 2 an amplitude of 2 V peak-to-peak (if there is an attempt to modify the frequency, a warning saying “Tracking Master Channel” should appear on the screen)

____**2.8.** Verify that the signal (waveform) from Channel 2 is a sine function. [Use the “status” button on the Fluke Signal Generator]

____**2.9.** Verify the LED lights of the Channel 1 and Channel 2 buttons of the Fluke Signal Generator are off. These buttons are used to send the signal to both amplifiers

____**2.10.** Verify the **output signal** and **high voltage connectors** of the acoustic drivers (piezo-siren) are **plugged in**

____**2.11.** Verify the Trek amplifiers are off and wall outlet power cords are disconnected

____**2.12.** Verify the wires of the input signal are disconnected and the wires of the output monitoring signal are connected

____**2.13.** Plug in high voltage connection of both Trek amplifiers (clear/red cable)

____**2.14.** Connect the wire from Channel 1 of the Fluke Signal Generator to the “Input Signal” slot on the Trek-1 amplifier and the wire from Channel 2 of the Fluke Signal Generator to the “Input Signal” slot on the Trek-2 amplifier

____**2.15.** Plug in wall outlet power cords of the Trek amplifiers

____**2.16.** Turn the (white) Trek amplifiers (switches) on

____**2.17.** Put on acoustic protection (ear plugs and ear muffs)

____**2.18.** Verify the **silver** acoustic-protection **foam door** is **in place**

____**2.19.** Pull gray high voltage enabling button of Trek amplifiers
NOTE: If the red light switch does not come on, push the start switch on the Trek amplifier

NOTES:

- Make sure waveforms are as expected on the Oscilloscope. The output signal from the strain gauge attached to the right acoustic driver (piezo-siren) should never go over 43V at any point during a test.
- Adjust driving frequency (selecting Channel 1 and using the "Frequency" button) and amplitude as needed for the particular test and case to be run.
- If there is an emergency and the room has to be evacuated: just leave. If there is time, press the grey button on the Trek amplifiers, and turn the main switches off.

____3. ACOUSTIC DRIVERS SHUT DOWN

____**3.1.** Once **acoustic testing** is **over**, verify that the lights of Channels 1 and 2 of the Fluke Signal Generator are off

____**3.2.** Press the grey button on the Trek amplifier

____**3.3.** Turn off the (white) main switch of the Trek amplifiers

____**3.4.** Disconnect the wall outlet power cord of the Trek amplifiers

____**3.5.** Disconnect the high voltage (clear/red) cable of the Trek amplifiers

____**3.6.** Disconnect the (input) cables from the Trek amplifiers

____**3.7.** Turn off Fluke Signal Generator

____**3.8.** **Uncouple connectors** from the right acoustic source (piezo-siren) and plug in 1 megaohm resistance connectors

APPENDIX C

Shear-Coaxial Jets Experiment:
Summary Tables of Flow Conditions

Table C.1: Summary table of flow conditions for the LAR-thin injector.

	J	R	S	T_c (K)	ρ_c (kg/m^3)	P_c (MPa)	T_o (K)	$\dot{m}_o$ (mg/s)	ρ_o (kg/m^3)	U_o (m/s)	Re_o (x10^{-4})	T_i (K)	$\dot{m}_i$ (mg/s)	ρ_i (kg/m^3)	U_i (m/s)	Re_i (x10^{-4})
P_r = 0.44	0.1	1.6	0.040	243	21	1.50	198	500	26	4.7	1.4	107	722	646	2.9	2.1
	0.5	3.5	0.042	217	24	1.50	204	1106	26	11	3.1	110	727	622	3.0	2.4
	2.1	7.4	0.039	220	23	1.50	205	2212	25	22	6.3	107	725	646	2.9	2.1
	5.2	11	0.041	221	23	1.50	203	3531	26	34	10	108	733	639	3.0	2.2
	11	17	0.040	216	24	1.51	204	4991	26	48	14	107	722	646	2.9	2.1
	14	19	0.041	221	23	1.50	201	3889	26	37	11	109	483	630	2.0	1.5
	20	22	0.042	220	23	1.50	204	4633	26	45	13	110	482	622	2.0	1.6
P_r = 1.05	0.1	0.9	0.11	252	49	3.57	195	773	67	2.8	2.2	114	725	613	3.1	2.5
	0.5	2.1	0.11	223	56	3.56	199	1742	65	6.6	4.8	115	724	605	3.1	2.5
	1.9	4.1	0.11	221	57	3.56	200	3479	65	13	9.6	118	724	577	3.3	2.8
	5.0	6.5	0.12	223	57	3.58	203	4189	64	16	11	122	511	531	2.5	2.4
	8.5	8.5	0.12	225	56	3.56	208	5135	61	21	14	123	483	515	2.4	2.4
	12	9.9	0.12	223	56	3.57	208	6217	62	25	17	124	482	497	2.5	2.5

Table C.2: Summary table of flow conditions for the SAR-thick injector.

	J	R	S	T_c (K)	ρ_c (kg/m^3)	P_c (MPa)	T_o (K)	$\dot{m}_o$ (mg/s)	ρ_o (kg/m^3)	U_o (m/s)	Re_o (x10^{-4})	T_i (K)	$\dot{m}_i$ (mg/s)	ρ_i (kg/m^3)	U_i (m/s)	Re_i (x10^{-4})
P_r = 0.44	0.1	1.6	0.043	242	21	1.50	192	404	27	3.0	3.1	110	1991	622	1.9	0.5
	0.5	3.4	0.043	218	24	1.50	196	928	27	6.9	1.0	110	2143	622	2.0	3.3
	2.1	7.3	0.039	205	25	1.50	212	1789	24	15	1.9	110	2130	622	2.0	3.3
	5.7	12	0.040	193	27	1.50	208	3008	25	24	3.2	110	2135	622	2.0	3.3
	10	16	0.040	194	27	1.50	208	4075	25	33	4.4	110	2153	622	2.0	3.3
	15	19	0.040	203	26	1.50	204	3604	26	28	3.9	107	1598	646	1.5	2.2
	21	23	0.039	196	27	1.50	206	4385	25	35	4.7	107	1658	646	1.5	2.3
P_r = 1.05	0.1	0.9	0.113	236	53	3.57	186	649	72	1.8	0.7	111	2126	636	2.0	3.1
	0.5	2.1	0.109	229	55	3.57	198	1400	66	4.3	1.5	115	2056	605	2.0	3.4
	2.1	4.4	0.106	208	61	3.56	202	2805	64	8.8	2.9	115	2041	605	2.0	3.4
	5.2	6.8	0.109	208	61	3.56	203	4219	63	13	4.4	118	1908	577	1.9	3.5
	9.2	9.0	0.113	205	63	3.56	203	5990	63	19	6.2	120	1985	556	2.1	4.0
	14	11	0.122	206	62	3.56	204	7154	63	23	7.5	123	1885	515	2.2	4.4
	21	14	0.104	205	63	3.57	206	7526	62	24	7.8	116	1724	596	1.7	3.0

Table C.3: Summary table of acoustic forcing conditions and dark-core length measurements for the LAR-thin injector.

	J	Baseline		f_F (kHz)	PAN		PN	
		$p'_{pk\text{-}pk}/P_c$	L_B/D_1		$p'_{pk\text{-}pk}/P_c$	L_{PAN}/D_1	$p'_{pk\text{-}pk}/P_c$	L_{PN}/D_1
$P_r = 0.44$	0.1	0.01%	-	3.13	0.82%	-	0.09%	-
	0.5	0.01%	-	3.14	0.96%	-	0.25%	-
	2.1	0.01%	18 ± 3	3.12	1.39%	15 ± 2	0.13%	11 ± 1
	5.2	0.01%	14 ± 2	3.12	1.42%	11 ± 1	0.23%	9.7 ± 0.9
	11	0.01%	11 ± 2	3.10	1.00%	10 ± 1	0.19%	10 ± 1
	14	0.01%	9 ± 2	3.11	1.04%	7.4 ± 0.9	0.30%	6.8 ± 0.6
	20	0.01%	8 ± 1	3.11	1.03%	6.7 ± 0.8	0.19%	6.8 ± 0.6
$P_r = 1.05$	0.1	0.01%	-	3.16	0.77%	-	-	-
	0.5	0.00%	-	3.10	0.98%	-	0.11%	-
	1.9	0.01%	11.9 ± 0.9	3.10	1.22%	8 ± 1	-	-
	5.0	0.01%	7.6 ± 0.7	3.41	0.54%	5.9 ± 0.5	0.05%	6.2 ± 0.4
	9	0.01%	5.9 ± 0.6	3.10	0.75%	5.0 ± 0.4	-	-
	12	0.01%	4.5 ± 0.4	3.10	1.02%	4.4 ± 0.4	-	-

Table C.4: Summary table of acoustic forcing conditions and dark-core length measurements for the SAR-thick injector.

	J	Baseline		f_F (kHz)	PAN		PN	
		$p'_{pk\text{-}pk}/P_c$	L_B/D_1		$p'_{pk\text{-}pk}/P_c$	L_{PAN}/D_1	$p'_{pk\text{-}pk}/P_c$	L_{PN}/D_1
$P_r = 0.44$	0.1	0.02%	-	3.10	1.32%	-	0.21%	-
	0.5	0.02%	-	3.04	1.27%	-	0.19%	-
	2.1	0.02%	10 ± 2	3.07	1.42%	10 ± 3	0.28%	8 ± 1
	5.7	0.02%	7 ± 1	3.11	1.06%	7 ± 1	0.14%	5.5 ± 0.8
	10	0.02%	5.2 ± 0.5	3.11	1.11%	5.4 ± 0.7	0.23%	4.7 ± 0.5
	15	0.02%	5.0 ± 0.5	3.04	1.48%	4.7 ± 0.5	0.25%	4.5 ± 0.5
	21	0.02%	4.6 ± 0.5	3.01	1.51%	4.1 ± 0.4	0.45%	4.3 ± 0.4
$P_r = 1.05$	0.1	0.01%	-	3.12	0.69%	-	0.13%	-
	0.5	0.01%	-	3.00	0.67%	-	0.40%	-
	2.1	0.01%	7 ± 1	3.04	1.17%	7.5 ± 1	0.23%	7.1 ± 0.8
	5.2	0.01%	5.1 ± 0.5	3.08	0.93%	5.3 ± 0.6	0.14%	3.8 ± 0.4
	9.2	0.01%	2.9 ± 0.2	3.11	0.99%	3.4 ± 0.4	0.19%	2.2 ± 0.2
	14	0.01%	2.4 ± 0.2	3.05	1.22%	2.8 ± 0.3	0.25%	2.1 ± 0.3
	21	0.01%	2.4 ± 0.2	3.12	1.11%	2.2 ± 0.3	0.13%	2.4 ± 0.3

REFERENCES

[1] A. R. Karagozian, W. J. A. Dahm, E. Glasgow, R. Howe, I. Kroo, R. Murray, and H. Shyu. Technology options for improved air vehicle fuel efficiency. Technical Report SAB-TR-06-04, Air Force Scientific Advisory Board Report, 2006.

[2] G. A. Mills and E. E. Ecklund. Alcohols as components of transportation fuels. *Annual review of energy*, 12(1):47–80, 1987.

[3] F. Fischer. *The Conversion of Coal*. Ernst Benn, Ltd., 1925.

[4] U.S. Air Force. B-52 flight uses synthetic fuel in all eight engines, 2006. http://www.af.mil/news/story.asp?id=123035568.

[5] J. Hernandez. Secaf certifies synthetic fuel blends for b-52h, 2007. http://www.af.mil/news/story.asp?id=123063866.

[6] A. Williams. Combustion of droplets of liquid fuels - a review. *Combustion and Flame*, 21, 1973.

[7] G. A. E. Godsave. Burning of fuel droplets. In *Combustion and Flame*, pages 818–830, Baltimore, 1953. Williams and Wilkins.

[8] C. K. Law and G. M. Faeth. Opportunities and challenges of combustion in microgravity. *Progress in Energy and Combustion Science*, 20, 1994.

[9] C. K. Law. Recent advances in droplet vaporization and combustion. *Progress in Energy and Combustion Science*, 8(3):171–201, 1982.

[10] S. R. Turns. *An Introduction to Combustion*. McGraw Hill, 2000.

[11] J. Blaszczyk. Acoustically disturbed fuel droplet combustion. *Fuel*, 70(9):1023 – 1025, 1991.

[12] S. Kumagai and H. Isoda. Combustion of fuel droplets in a vibrating air field. In *Fifth Symposium (International) on Combustion*, 1955.

[13] P. M. Struk, M. Ackerman, V. Nayagam, and D. L. Dietrich. On calculating burning rates during fibre supported droplet combustion. *Microgravity Science and Technology*, 11, 1998.

[14] M. Saito, M. Sato, and I. Suzuki. Evaporation and combustion of a single fuel droplet in acoustic fields. *Fuel*, 73, 1994.

[15] M. Saito, M. Hoshikawa, and M. Sato. Enhancement of evaporation/combustion rate coefficient of a single fuel droplet by acoustic oscillation. *Fuel*, 75, 1996.

[16] K. Okai, O. Moriue, M. Araki, M. Tsue, M. Kono, J. Sato, D. L. Dietrich, and F. A. Williams. Combustion of single droplets and droplet pairs in a vibrating field under microgravity. *Proceedings of the Combustion Institute*, 28, 200.

[17] M. Tanabe, T. Morita, K. Aoki, K. Satoh, T. Fujimori, and J. Sato. Influence of standing sound waves on droplet combustion. *Proceedings of the Combustion Institute*, 28, 2000.

[18] M. Tanabe, T. Kuwahara, K. Satoh, T. Fujimori, J. Sato, and M. Kono. Droplet combustion in standing sound waves. *Proceedings of the Combustion Institute*, 30, 2005.

[19] Lord Rayleigh. On the circulation of air observed in kundt's tubes, and some allied acoustical problems. *Philosophical Transactions of the Royal Society of London*, 175, 1884.

[20] S. Dattarajan, A. Lutomirski, R. Lobbia, O. I. Smith, and A. R. Karagozian. Acoustic excitation of droplet combustion in microgravity and normal gravity. *Combustion and Flame*, 144, 2006.

[21] S. Dattarajan. *Acoustically Excited Droplet Combustion in Normal Gravity and Microgravity*. Ph.d. dissertation, UCLA, 2004.

[22] D. B. Spalding. The combustion of liquid fuels. *Fourth Symposium (International) on Combsution*, 1953.

[23] G. A. Agoston, H. Wise, and W. A. Rosser. Dynamic factors affecting the combustion of liquid spheres. *Symposium (International) on Combustion*, 1957.

[24] D.T. Harrje and F.H. Reardon. Liquid propellant rocket combustion instability. nasa sp-194. *NASA Special Publication*, 194, 1972.

[25] K.C. Schadow, E. Gutmark, T.P. Parr, D.M. Parr, K.J. Wilson, and J.E. Crump. Large-scale coherent structures as drivers of combustion instability. *Combustion Science and Technology*, 64(4-6):167–186, 1989.

[26] N.A. Chigier and J.M. Beer. The flow region near the nozzle in double concentric jets. *Journal of Basic Engineering*, 86:797, 1964.

[27] W. Forstall and A.H. Shapiro. Momentum and mass transfer in coaxial gas jets. *Journal of Applied Mechanics*, pages 399–407, 1950.

[28] N.W.M. Ko and A.S.H. Kwan. The initial region of subsonic coaxial jets. *Journal of Fluid Mechanics*, 73(2):305–332, 1976.

[29] R.B. Wicker and J.K. Eaton. Near field of a coaxial jet with and without axial excitation. *AIAA Journal*, 32(3):542–546, 1994.

[30] E. Villermaux, H. Rehab, and E.J. Hopfinger. Breakup regimes and self-sustained pulsations in coaxial jets. *Meccanica*, 29(4):393–401, 1994.

[31] F.H. Champagne and I.J. Wygnanski. An experimental investigation of coaxial turbulent jets. *International Journal of Heat and Mass Transfer*, 14(9):1445–1464, 1971.

[32] H. Rehab, E. Villermaux, and E.J. Hopfinger. Flow regimes of large-velocity-ratio coaxial jets. *Journal of Fluid Mechanics*, 345:357–381, 1997.

[33] H. Au and N.W.M. Ko. Coaxial jets of different mean velocity ratios, part 2. *Journal of Sound and Vibration*, 116(3):427–443, 1987.

[34] A. Sevilla, J.M. Gordillo, and C. Martinez-Bazan. The effect of the diameter ratio on the absolute and convective instability of free coflowing jets. *Physics of Fluids*, 14:3028, 2002.

[35] N.W.M. Ko and H. Au. Coaxial jets of different mean velocity ratios. *Journal of Sound and Vibration*, 100(2):211–232, 1985.

[36] W.J.A. Dahm, C.E. Frieler, and G. Tryggvason. Vortex structure and dynamics in the near field of a coaxial jet. *Journal of Fluid Mechanics*, 241(1):371–402, 1992.

[37] H. Rehab, E. Villermaux, and E.J. Hopfinger. Geometrical effects on the near-field flow structure of coaxial jets. *AIAA Journal*, 36(5):867–869, 1998.

[38] P.G. Gladnick, A.C. Enotiadis, J.C. LaRue, and G.S. Samuelsen. Near-field characteristics of a turbulent coflowing jet. *AIAA Journal*, 28(8):1405–1414, 1990.

[39] M. Favre-Marinet, E.B. Camano, and J. Sarboch. Near-field of coaxial jets with large density differences. *Experiments in Fluids*, 26(1):97–106, 1999.

[40] M. Favre-Marinet and E.B. Camano Schettini. The density field of coaxial jets with large velocity ratio and large density differences. *International Hournal of Heat and Mass Transfer*, 44(10):1913–1924, 2001.

[41] P.E. Dimotakis. Two-dimensional shear-layer entrainment. *AIAA Journal*, 1986.

[42] H. Eroglu, N. Chigier, and Z. Farago. Coaxial atomizer liquid intact lengths. *Physics of Fluids A: Fluid Dynamics*, 3:303, 1991.

[43] J.C. Lasheras, E. Villermaux, and E.J. Hopfinger. Break-up and atomization of a round water jet by a high-speed annular air jet. *Journal of Fluid Mechanics*, 357(1):351–379, 1998.

[44] D.W. Davis and B. Chehroudi. Measurements in an acoustically driven coaxial jet under sub-, near-, and supercritical conditions. *Journal of Propulsion and Power*, 23(2):364–374, 2007.

[45] I.A. Leyva, B. Chehroudi, and D. Talley. Dark core analysis of coaxial injectors at sub-, near-, and supercritical pressures in a transverse acoustic field. In *43rd AIAA/ASME/SAE/ASEE Joint Propulsion Conference & Exhibit*, AIAA 2007-5456.

[46] J. I. Rodriguez. *Acoustic Excitation of Liquid Fuel Droplets and Coaxial Jets.* Ph.d. dissertation, UCLA, 2009.

[47] J. Cohen and I. Wygnanski. The evolution of instabilities in the axisymmetric jet. part 1. the linear growth of disturbances near the nozzle. *J. Fluid Mech*, 176:191–219, 1987.

[48] A. Michalke and G. Hermann. On the inviscid instability of a circular jet with external flow. *Journal of Fluid Mechanics*, 114(1):343–359, 1982.

[49] D. Perrault-Joncas and S.A. Maslowe. Linear stability of a compressible coaxial jet with continuous velocity and temperature profiles. *Physics of Fluids*, 20(7):074102, 2008.

[50] A. Talamelli and I. Gavarini. Linear instability characteristics of incompressible coaxial jets. *Flow, Turbulence and Combustion*, 76(3):221–240, 2006.

[51] C.C. Miesse. The effect of ambient pressure oscillations on the disintegration and dispersion of a liquid jet. *Jet Propulsion*, 25:525–530, 1955.

[52] J.A. Newman. A preliminary study of the effects of vaporization and transverse oscillations on liquid jet breakup. Technical Report CR-72258, NASA, 1967.

[53] M.F. Heidmann and J.F. Groeneweg. *Analysis of the dynamic response of liquid jet atomization to acoustic oscillations.* National Aeronautics and Space Administration, 1969.

[54] G. Balarac, O. Métais, and M. Lesieur. Mixing enhancement in coaxial jets through inflow forcing: A numerical study. *Physics of Fluids*, 19:075102, 2007.

[55] F. Richecoeur, P. Scouflaire, S. Ducruix, and S. Candel. Interactions between propellant jets and acoustic modes in liquid rocket engines: experiments and simulations. In *42nd AIAA/ASME/SAE/ASEE Joint Propulsion Conference & Exhibit*, AIAA 2006-4397.

[56] A. Ghosh, Q. Diao, G. Young, and K. Yu. Effect of density ratio on shear-coaxial injector flame-acoustic interaction. In *42nd AIAA/ASME/SAE/ASEE Joint Propulsion Conference & Exhibit*, AIAA 2006-4528.

[57] A. Ghosh. *The Role of Density Gradient in Liquid Rocket Engine Combustion Instability.* PhD thesis, University of Maryland, College Park.

[58] D.W. Davis. *On the Behavior of a Shear-Coaxial Jet, Spanning Sub- to Supercritical Pressures, with and without an Externally Imposed Transverse Acoustic Field.* Ph.d. dissertation, Pennsylvania State University, 2006.

[59] W. L. Nyborg. Radiation pressure on a small rigid sphere. *The Journal of the Acoustical Society of America*, 42(5), 1967.

[60] R. L. Panton. *Incompressible Flow.* John Wiley & Sons, Inc., Hoboken, NJ, third edition, 2005.

[61] National Institute of Standards and Technology. Thermophysical properties of fluid systems, 2011. http://webbook.nist.gov/chemistry/fluid/.

[62] N. Otsu. A threshold selection method from gray-level histograms. *IEEE Trans. Sys., Man., Cyber*, 1979.

[63] G. Berkooz, P. Holmes, and J.L. Lumley. The proper orthogonal decomposition in the analysis of turbulent flows. *Annual Review of Fluid Mechanics*, 25(1):539–575, 1993.

[64] A. Chatterjee. An introduction to the proper orthogonal decomposition. *Current Science*, 78(7):808–817, 2000.

[65] M. Arienti and M.C. Soteriou. Time-resolved proper orthogonal decomposition of liquid jet dynamics. *Physics of Fluids*, 21:112104, 2009.

[66] J.R. Taylor. *An Introduction to Error Analysis: The Study of Uncertainties in Physical Measurements.* University Science Books.

[67] A. F. Mills and B. H. Chang. Error analysis of experiments. UCLA, Los Angeles, CA, 2004.

[68] J.C. Lasheras and E.J. Hopfinger. Liquid jet instability and atomization in a coaxial gas stream. *Annual Review of Fluid Mechanics*, 32(1):275–308, 2000.

[69] J.J. Graham, I.A. Leyva, J.I. Rodriguez, and D. Talley. On the effect of a transverse acoustic field on a flush shear coaxial injector. In *45th AIAA/ASME/SAE/ASEE Joint Propulsion Conference & Exhibit*, AIAA 2009-5142.

[70] G.P. Sutton and O. Biblarz. *Rocket Propulsion Elements*. John Wiley & Sons, 2001.

[71] M.H. Yu and P.A. Monkewitz. The effect of nonuniform density on the absolute instability of two-dimensional inertial jets and wakes. *Physics of Fluids A: Fluid Dynamics*, 2:1175, 1990.

[72] P. Huerre and P.A. Monkewitz. Local and global instabilities in spatially developing flows. *Annual Review of Fluid Mechanics*, 22(1):473–537, 1990.

[73] P. Huerre. Open shear flow instabilities. *Perspectives in Fluid Dynamics*, pages 159–229, 2000.

[74] S. Jendoubi and P.J. Strykowski. Absolute and convective instability of axisymmetric jets with external flow. *Physics of Fluids*, 6:3000, 1994.

[75] S. Megerian, J. Davitian, L.S. de B. Alves, and A.R. Karagozian. Transverse-jet shear-layer instabilities. part 1. experimental studies. *Journal of Fluid Mechanics*, 593(1):93–129, 2007.